Uniwersytet Warszawski
Wydział Fizyki
Zakład Cząstek i Oddziaływań Fundamentalnych

Energy dependence of negatively charged pion production in proton-proton interactions at the CERN SPS

Rozprawa doktorska

Mgr Antoni Aduszkiewicz

Promotor:
Prof. dr hab. Wojciech Dominik

Warszawa, sierpień 2015

Acknowledgements

I would like to thank to people who helped me and contributed in completing this work.

Prof. dr hab. Wojciech Dominik and Prof. dr hab. Marek Gaździcki for a unique opportunity to participate in the NA61/SHINE experiment at CERN, for supervision of my work, inspiration and helpful ideas.

Dr Peter Seyboth and dr hab. Katarzyna Grebieszkow for weekly discussions and numerous helpful comments.

Dr Maja Maćkowiak-Pawłowska and Szymon Puławski for joint work, fruitful discussions and exchange of the experience.

Magdalena Kuich for valuable remarks and practical help.

My parents and sister for never ending support.

Project financed by Narodowe Centrum Nauki based on decision DEC-2012/05/N/ST2/02759, Europejski Fundusz Społeczny and the State Budget under "Zintegrowany Program Operacyjnego Rozwoju Regionalnego", Działania 2.6 "Regionalne Strategie Innowacyjne i transfer wiedzy" project of Mazowieckie voivodship "Mazowieckie Stypendium Doktoranckie".

Abstract

This thesis presents inclusive spectra of the negatively charged pions produced in inelastic proton-proton interactions measured at five beam momenta: 20, 31, 40, 80 and 158 GeV/*c*. The measurements were conducted in the NA61/SHINE experiment at CERN using a system of five Time Projection Chambers. The negatively charged pion spectra were calculated based on the negatively charged hadron spectra. Contribution of hadrons other than the primary pions was removed using EPOS simulations. The results were corrected for effects related to detection, acceptance, reconstruction efficiency and the analysis technique.

Two-dimensional spectra were derived as a function of rapidity and transverse momentum or transverse mass. The spectra were parametrised by widths of the rapidity distributions, inverse slope parameters of the transverse mass distributions, mean transverse masses and the total pion multiplicities.

The negatively charged pion spectra in proton-proton interactions belong to a broad NA61/SHINE programme of search of the onset of deconfinement of strongly interacting matter in collisions of light and intermediate-size ions. Spectra from this thesis were compared with the pion spectra in Pb+Pb collisions at the same beam momenta per nucleon measured by the NA49 experiment. The results, in particular the energy dependence of the mean pion multiplicity, support the interpretation of the onset of deconfinement in heavy ion collisions in the SPS energy range. However, unexpected similarities in energy dependences of the shapes of the spectra obtained in proton-proton interactions and Pb+Pb collisions are revealed.

Results presented in this thesis will serve for comparisons with other ongoing NA61/SHINE measurements of hadron production in p+p, Be+Be, Ar+Sc and Xe+La collisions. They widely extend the numerous, but mostly not detailed, low statistics existing p+p data.

Streszczenie

Praca przedstawia inkluzywne widma pionów ujemnych produkowanych w nieelastycznych oddziaływaniach proton-proton, zmierzone dla pięciu wartości pędu wiązki: 20, 31, 40, 80 i 158 GeV/c. Pomiary wykonano w eksperymencie NA61/SHINE w laboratorium CERN, z wykorzystaniem zespołu pięciu komór projekcji czasowej (TPC). Widma pionów ujemnych wyznaczono w oparciu o widma ujemnie naładowanych hadronów. Wkład hadronów innych niż piony pochodzące z pierwotnego oddziaływania dwóch protonów usunięto przy użyciu symulacji opartej o model EPOS. Wyniki poprawiono ze względu na efekty związane z detekcją, akceptacją detektora, wydajnością rekonstrukcji oraz techniką analizy danych.

Dwuwymiarowe widma wyznaczono w funkcji pospieszności oraz pędu poprzecznego i masy poprzecznej. Wyznaczono też parametry widm: szerokości rozkładów pospieszności, parametry nachylenia rozkładów masy poprzecznej, średnie masy poprzeczne oraz całkowite krotności pionów.

Widma pionów ujemnych w oddziaływaniach proton-proton należą do programu NA61/SHINE poszukiwań progu na produkcję plazmy kwarkowo-gluonowej (QGP) w zderzeniach lekkich i średnich jąder. Widma zostały porównane z widmami pionów w zderzeniach ołów-ołów przy tych samych pędach wiązki na nukleon, zmierzonymi w eksperymencie NA49. Wyniki, w szczególności zależność energetyczna całkowitej krotności pionów, potwierdzają interpretację obecności progu na produkcję QGP w zderzeniach ciężkich jąder w zakresie energii dostępnych w CERN SPS. Jednocześnie zauważono nieoczekiwane podobieństwo w zależnościach energetycznej kształtów widm w oddziaływaniach proton-proton i zderzeniach ołów-ołów.

Wyniki przedstawione w tej pracy posłużą do porównania z innymi pomiarami produkcji hadronów w zderzeniach p+p, Be+Be, Ar+Sc and Xe+La w ramach trwającego programu NA61/SHINE. W stosunku do licznych, lecz mało dokładnych dostępnych dotychczas danych pochodzących z oddziaływań proton-proton, przedstawiane tu wyniki znacznie pogłębiają szczegółowość widm ujemnych pionów.

Contents

1 Collisions of nuclei as a tool to study strongly interacting matter 1
- 1.1 High-energy nuclear collisions 1
- 1.2 Quark-gluon plasma phase transition 2
- 1.3 Programme of the NA61/SHINE experiment 5
- 1.4 Spectra of negatively charged pions in p+p interactions 7
- 1.5 NA61/SHINE experiment and this thesis 8

2 NA61/SHINE detector 9
- 2.1 NA49 detector and upgrades for NA61/SHINE 9
- 2.2 SPS beam and beam monitoring 10
- 2.3 Liquid hydrogen target 11
- 2.4 Spectrometer system 11
- 2.5 Time of Flight detectors 12
- 2.6 Projectile Spectator Detector 13

3 Time Projection Chambers 14
- 3.1 History and concepts 14
- 3.2 Principle of operation 15
- 3.3 Particle identification in TPC 18
- 3.4 NA61/SHINE Time Projection Chambers 18
  - 3.4.1 Construction 18
  - 3.4.2 Gas system 21
  - 3.4.3 Reconstruction of events and tracks 25

4 Monte Carlo simulation 28
- 4.1 Purpose of using simulations 28
- 4.2 Simulation of interaction and the detector response 28
- 4.3 Matching of the generated particles and reconstructed tracks 29
- 4.4 Data-based adjustments of the simulated spectra 31
- 4.5 Simulated and measured characteristics 35

5 Characteristics of the dataset 38
- 5.1 Data acquired and used in the analysis 38
- 5.2 Beam characteristics 39
  - 5.2.1 General properties 39
  - 5.2.2 Off-time beam particles 40
  - 5.2.3 Beam profile and divergence 43
- 5.3 Target density 44
- 5.4 Reconstruction efficiency and resolution 45

6 Data analysis **49**
- 6.1 Overview of the analysis procedure 49
- 6.2 Event selection 51
  - 6.2.1 List of event selection criteria 51
  - 6.2.2 Elastic event rejection 53
  - 6.2.3 Off-target interaction rejection 55
- 6.3 Track selection 55
  - 6.3.1 List of track selection criteria 55
  - 6.3.2 Classification of tracks due to their topology 58
  - 6.3.3 Selection of high reconstruction efficiency regions 59
  - 6.3.4 Correction for beam divergence 60
  - 6.3.5 Suppression of the electron tracks 60
  - 6.3.6 Uncorrected spectra of selected tracks 62
- 6.4 Corrections to the spectra 64
  - 6.4.1 Subtraction of the off-target interactions 64
  - 6.4.2 Correction for contamination of hadrons other than primary π^- mesons 66
  - 6.4.3 Correction for event losses as well as track losses and track migration between bins 67
  - 6.4.4 Rejection of poor quality bins of the final spectra 71
  - 6.4.5 Total correction 71
- 6.5 Statistical and systematic uncertainties 71
  - 6.5.1 Statistical uncertainties 71
  - 6.5.2 Systematic uncertainties 75
- 6.6 Cross checks of the final spectra 80
  - 6.6.1 Introduction 80
  - 6.6.2 Symmetries of the spectra 80
  - 6.6.3 Comparison with existing p+p data at 32 and 158 GeV/c . . . 83
  - 6.6.4 Comparison with existing p+p data at 12, 19 and 24 GeV/c . . 84

7 π^- spectra in p+p interactions and comparisons with Pb+Pb data and simulations **87**
- 7.1 Introduction 87
- 7.2 Double differential spectra 87
- 7.3 Transverse mass spectra 89
- 7.4 Rapidity spectra 91
- 7.5 Mean multiplicity 93
- 7.6 Comparison with simulated spectra 95

8 Summary and outlook **98**

A Coordinate system and kinematic variables **100**
- A.1 Introduction 100
- A.2 NA61/SHINE coordinate system 100
- A.3 Kinematic variables 101
  - A.3.1 Transverse variables 101
  - A.3.2 Rapidity 101

B Procedures of spectra extrapolation **104**
B.1 Transverse mass spectrum extrapolation 104
B.2 Rapidity spectrum extrapolation 106

C Tabulated results **109**
C.1 Introduction 109
C.2 Total multiplicities and rapidity distribution properties 109
C.3 Double differential spectra 109
C.3.1 p_{beam} = 20 GeV/c 110
C.3.2 p_{beam} = 31 GeV/c 111
C.3.3 p_{beam} = 40 GeV/c 112
C.3.4 p_{beam} = 80 GeV/c 113
C.3.5 p_{beam} = 158 GeV/c 114
C.4 Rapidity spectra 115
C.5 Inverse slope parameter 115
C.6 Mean transverse mass 115

Bibliography **116**

Chapter 1

Collisions of nuclei as a tool to study strongly interacting matter

1.1 High-energy nuclear collisions

What happens during collision of ultra-relativistic nuclei? Experiments detect large number of produced particles. The emitted particles carry information on course of the collision. Yet, despite studies of the high-energy nuclear collisions started more than 60 years ago, there are still many unknowns.

Nuclei are made of nucleons: protons (p) and neutrons (n), which are examples of hadrons, particles constituting of quarks and gluons. Six known types of quarks (and corresponding anti-quarks) form two types of hadrons: baryons (e.g. p, Λ) composed of three quarks (or three anti-quarks), and mesons (e.g. π, K) composed of a quark and an anti-quark. Gluons mediate in strong interactions between quarks. A particular feature of the strong interactions is that a quark cannot be separated from a hadron. Energy spent to pull a single quark is instead used to create a new pair of a quark and an anti-quark. This process is the most basic explanation of creation of new hadrons in high-energy hadron collisions.

Processes occurring in high-energy collisions of nuclei are dominated by the strong interactions. The theory of the strong interactions, quantum chromodynamics (QCD), explains production of hadrons with high transverse masses ($m_\mathrm{T} \gtrsim 2$ GeV/c^2, see Appendix A.3.1), which however constitute only a small fraction of percent of all produced particles at the energy range $\sqrt{s} = 5$–20 GeV, considered in this thesis [1]. Majority of hadrons, for which $m_\mathrm{T} \lesssim 2$ GeV/c^2 originate from interactions with low four-momentum transfer, q. For small q, the coupling constant is large, preventing the QCD perturbative calculations from converging in the higher orders. These interactions are called *soft* or *non-perturbative*.

An alternative to the QCD calculations is provided by models calculating statistical probability of hadron production from volume occupied by the colliding nuclei, filled with high energy density. The first model was proposed by Fermi in 1950 [2]. In 1965 Hagedorn found out, that temperature of matter composed of hadrons cannot exceed $T_\mathrm{H} \approx 158$ MeV [3].

A further step is a concept of quark-gluon plasma (QGP). At high energy densities hadrons start to overlap. The quarks and gluons, normally confined within hadrons, form a larger object. The process is called *deconfinement*. As QGP expands, it cools down. The moment when the inelastic interactions stop is called

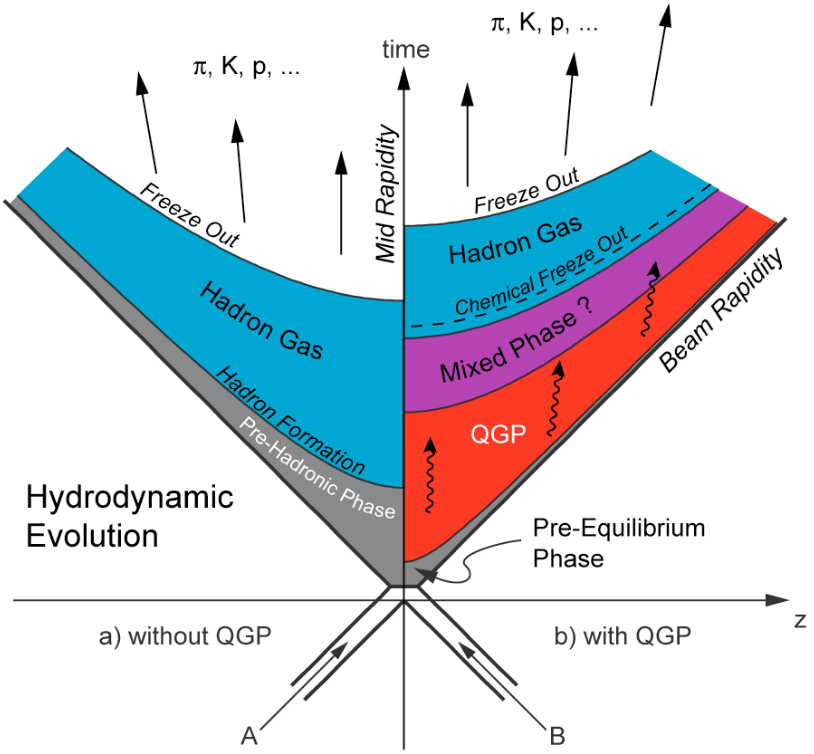

Figure 1.1: Two scenarios of collision of two relativistic nuclei ('A' and 'B'). The *left* side of the diagram shows direct formation of hadrons in series of the strong interactions. The *right* side shows creation of quark-gluon plasma phase, and subsequent phase transition and chemical freeze-out. Both scenarios are followed by the hadron gas phase and final release of the produced hadrons to the detector (thermal freeze-out). Figure taken from Ref. [4].

chemical freeze-out. The produced hadrons interact with each other elastically until the system reaches size exceeding their mean free path. The moment when the elastic interactions stop is called *thermal freeze-out*. In the detectors we observe these hadrons (mostly long-living $\pi^{\pm}$, K, p), or products of their decays. Two scenarios: with and without QGP creation are illustrated in Fig. 1.1.

QGP and gas of individual hadrons are two distinct phases of strongly interacting matter. The Statistical Model of Early Stage (SMES) [5, 6] relates hadron production to generation of new degrees of freedom. The number of degrees of freedom is higher in QGP, as they are connected with quarks and gluons, while in the hadron gas they are connected with hadrons. Moreover, masses of the light hadrons are primarily generated by the strong forces. Masses of the individual quarks ($m_{\mathrm{u}} = 2$ MeV, $m_{\mathrm{d}} = 5$ MeV, $m_{\mathrm{s}} = 95$ MeV) are much lower than masses of hadrons ($m_{\pi^-(\mathrm{d\bar{u}})} = 140$ MeV, $m_{\mathrm{K}^-(\mathrm{s\bar{u}})} = 494$ MeV, $m_{\mathrm{p(uud)}} = 938$ MeV) [7]. SMES predicts resulting differences in hadron production, which find experimental confirmation, as it will be described in the next section.

1.2 Quark-gluon plasma phase transition

Figure 1.2 shows the energy dependence of selected characteristics of hadron production and spectra [8, 9]. The spectra were measured in collisions of the heavy

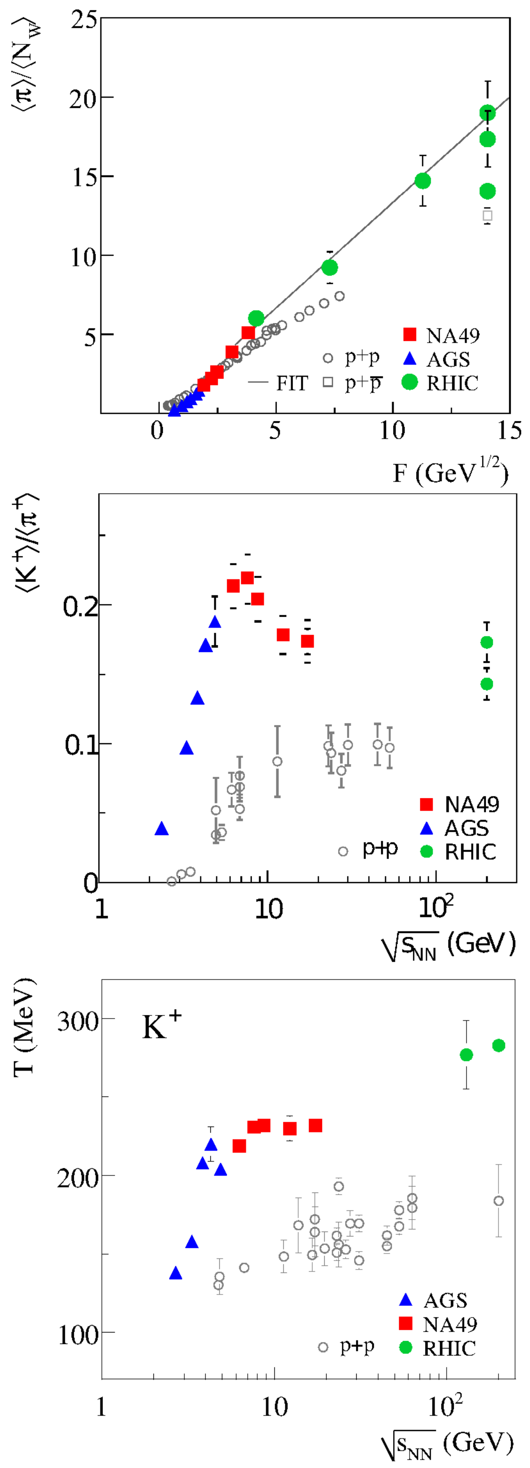

Figure 1.2: Set of plots presenting the onset of deconfinement. The full coloured points show properties of hadrons measured in heavy ion collisions in AGS (Au+Au), SPS (Pb+Pb in the NA49 experiment) and RHIC (Au+Au), while the open black points show the corresponding properties in p+p interactions. *Top:* “kink” – total pion multiplicity divided by the number of inelastically interacting nucleons (wounded nucleons, N_W) as a function of Fermi energy ($F \approx \sqrt[4]{s_{NN}}$, see Eq. (7.3)). *Middle:* “horn” – ratio of multiplicity of positively charged kaons and pions as a function of energy in the centre of mass frame $\sqrt{s_{NN}}$. *Bottom:* “step” – inverse slope parameter of the transverse mass spectrum of positively charged kaons. Figures taken from Refs. [8,9].

ions (Pb+Pb in the NA49 experiment at CERN Super Proton Synchrotron (SPS) and Au+Au in experiments at the Alternating Gradient Synchrotron (AGS) and Relativistic Heavy Ion Collider (RHIC)) and protons (various experiments). On each of the three plots three regions can be distinguished:

- No QGP production at $\sqrt{s} \lesssim 8$ GeV, $F \lesssim 2.3$ GeV$^{-1/2}$, corresponding to the blue triangles and first two red squares,
- QGP production, $\sqrt{s} \gtrsim 18$ GeV, $F \gtrsim 4$ GeV$^{-1/2}$, energies above the red squares,
- Production of mixed phase, where the QGP and hadron phases coexist, three top red squares at $8 \lesssim \sqrt{s} \lesssim 18$ GeV, $2.3 \lesssim F \lesssim 4$ GeV$^{-1/2}$.

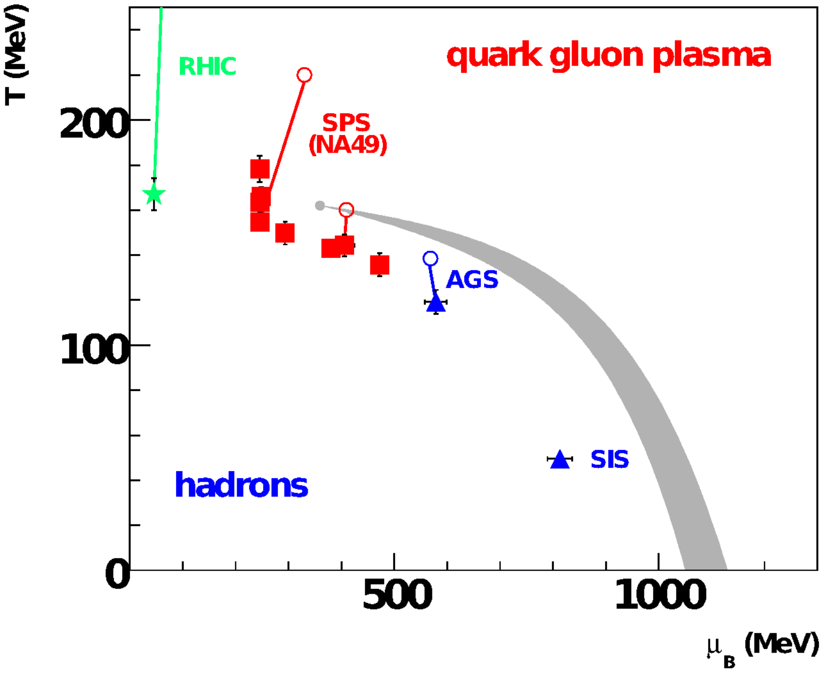

Figure 1.3: Phase diagram of strongly interacting matter in temperature T and baryonic chemical potential μ_B. The full colour points mark the chemical freeze-out points calculated in Refs. [10, 11] and based on existing ion-ion measurements at RHIC, SPS (NA49 experiment), AGS and SIS-18. The open points and the straight lines indicate possible evolution of the system from the early stage to the chemical freeze-out. The thick grey line shows the predicted first order phase transition between hadron gas and QGP, ending with a critical point [4, 12]. Figure taken from Ref. [13]

The hadron production properties in heavy ion collisions differ in the three regions. Slope of the total pion multiplicity $\langle\pi\rangle$ energy dependence is different in the three regions. The ratio of total multiplicity of the K^+ and π^+ mesons increases in the region with no QGP, then suddenly decreases in the mixed phase and finally shows almost no energy dependence in the QGP phase. Finally the inverse slope parameter of the transverse mass spectra of the K^+ mesons[1] increases at low energies, remains at constant level in the mixed phase, and then increases again, but slower in the QGP phase. These three dependences are predicted within SMES, as signatures of the QGP phase transition in the SPS energy range.

The corresponding energy dependences in p+p interactions show no distinct structures. This was explained that a system created by two protons is too small to form QGP. Also, the sizeable differences between hadron production in p+p interactions and heavy ion collisions demonstrate that collision of heavy ions cannot be treated as a simple superposition of many nucleon-nucleon interactions.

Figure 1.3 shows the phase-diagram of strongly interacting matter. The data points represents experimentally probed values of the chemical potential related to the barion number and the temperature of chemical freeze-out. Hadron gas and QGP phases are distinguished. First-order phase transition line sketched in the

---

[1] Procedure of derivation of the inverse slope parameter will be described in Sect. 7.3.

diagram might end with a critical point within the SPS energy range. Above the critical point the transition between the phases becomes smooth.

1.3 Programme of the NA61/SHINE experiment

The NA61/SHINE experiment (SPS Heavy Ion and Neutrino Experiment, the sixty-first experiment at the CERN North Area) studies hadron production in proton-proton, proton-nucleus, nucleus-nucleus and pion-nucleus collisions. The main goal is study of onset of deconfinement and search of critical point. This is being achieved by measurement of the energy dependence of hadron production properties in nucleus-nucleus collisions as well as p+p and p+Pb interactions. The π^- spectra in p+p collisions presented in this thesis belong to this part of the programme.

Two additional goals include:

- study of hadron production at high transverse momenta (p_T of up to 4.5 GeV/c) in high statistics of p+p and p+Pb interactions at 158 GeV/c. The data compared with the high p_T NA49 measurements of Pb+Pb collisions will allow for better understanding of the nucleus-nucleus reactions.
- precise hadron production measurements for the neutrino and cosmic ray experiments. The NA61/SHINE measurements of 31 GeV/c proton interaction with 2 cm-thick carbon target, and 90 cm-thick replica of the Tokai to Kamioka experiment (T2K) target help to calculate the T2K initial neutrino flux. The T2K analysis bases on comparison of the neutrino measurements in the far detector, Super-Kamiokande, with their initial flux, thus the NA61/SHINE role is of crucial importance [14–17].
  The Pierre Auger Observatory detects cosmic rays by measuring particles from atmospheric showers reaching detectors on the ground. π^++C interactions at 158 and 350 GeV/c measured in NA61/SHINE allow to reduce systematic uncertainties in simulations of the showers used to reconstruct properties of the initial cosmic ray particles [18,19].

NA61/SHINE aims to identify properties of the onset of deconfinement and to find the critical point of strongly interacting matter. This requires a comprehensive scan of the whole SPS beam momentum range from 13A to 158A GeV/c (A stands for the nucleus mass number) with light and intermediate mass nuclei. NA61/SHINE measures p+p, ^{7}Be+^{9}Be, ^{40}Ar+^{45}Sc, Xe+La (the choice of beam and target nuclei is dictated by technical capabilities of the ion source, and physical and chemical properties of the target element) and p+Pb collisions at six beam momenta with a typical number of recorded collision events of $2 \cdot 10^6$ at each reaction and energy. This number includes only the central collisions in which most of the nucleons participated in inelastic interaction. The programme is planned to be extended with the Pb+Pb energy scan.

Figure 1.4 lists the datasets being recorded by NA61/SHINE for the ion program. Figure 1.5 illustrates predicted region of the phase diagram explored by the two-dimensional scan, including also the data collected already by NA49.

The started two-dimensional scan of collision energy and colliding nuclei size is mainly motivated by the observation of the onset of deconfinement in central Pb+Pb collisions at beam momenta of about 30A GeV/c by the NA49 experi-

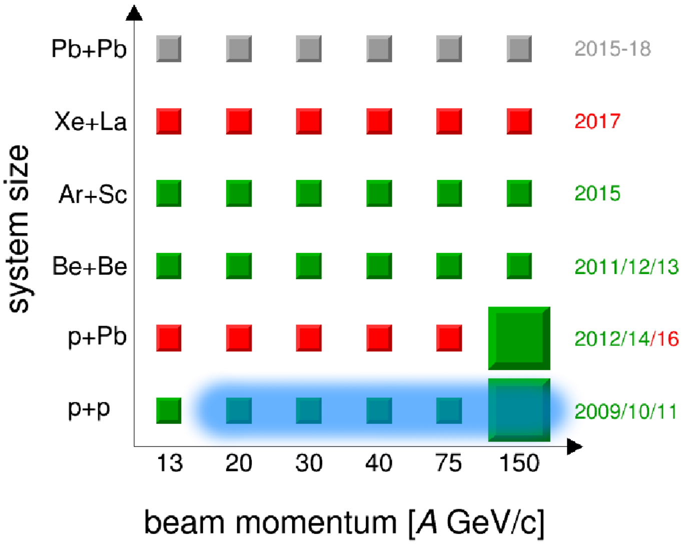

Figure 1.4: NA61/SHINE two-dimensional scan with the beam energy and the system size. The small boxes represent ~2·10^6 events, large boxes are ~50·10^6. The p+p, Be+Be, Ar+Sc and p+Pb data are collected as of summer 2015 (green boxes); the planned data are marked with red and grey. The blue area marks the p+p data at 20–158 GeV/*c* analysed in this thesis. Figure taken from Ref. [20].

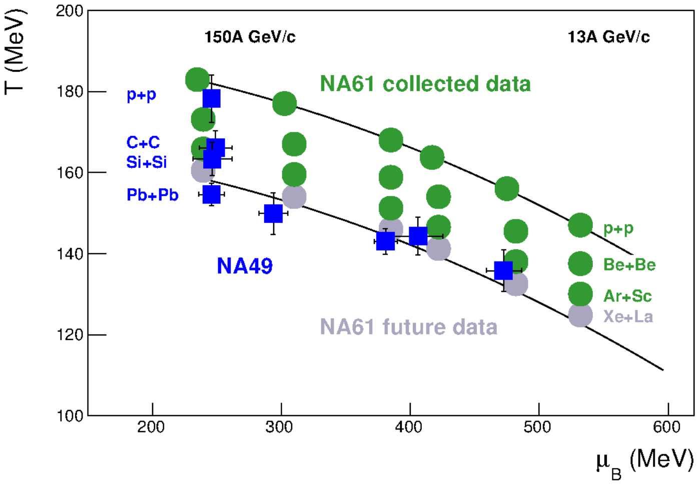

Figure 1.5: Coverage of the phase-space diagram by data measured by NA49 (blue squares) and measured (green circles) and planned to be measured (grey circles) by NA61/SHINE. Compare with Figs. 1.3 and 1.4 [21]. Figure taken from Ref. [20].

ment [8, 9]. Recently the NA49 results were confirmed by the RHIC Beam Energy Scan programme (BES) and their interpretation by the onset of deconfinement is consistent with the recent Large Hadron Collider (LHC) results (see Ref. [22] and references therein, and also more recent RHIC results in Refs. [23, 24]).

An interpretation of the experimental results on nucleus-nucleus collisions relies to a large extent on comparing them to the corresponding data on p+p and p+A interactions. The currently available p+p data originate mostly from bubble chamber experiments characterised by low statistics, typically of order of 10^4 events. While this suffices for the total multiplicity derivation, many needed results on differential properties of hadron production, fluctuations and correlations are missing. Detailed measurements of hadron spectra in a large acceptance in the beam momentum range covered by the data presented in this thesis exist only for inelastic p+p interactions at 158 GeV/*c* [25–27]. Attempts to extrapolate, or even interpolate measurements at different collision energies lead to large systematic uncertainties (see Sect. 6.6.4). This shows the importance of the detailed measurements of p+p interactions by NA61/SHINE in the study of the onset of deconfinement.

1.4 Spectra of negatively charged pions in p+p interactions

Pions are the lightest and by far the most abundant products of the high-energy nuclear collisions. Thus, data on pion production properties are crucial for constraining basic properties of models of the strong interactions. In particular, the most significant signals of the onset of deconfinement (the "kink" and "horn", see Fig. 1.2) [12] require precise measurements of the mean pion multiplicity at the same beam momenta per nucleon as the corresponding A+A data. Moreover, the NA61/SHINE data are taken with almost the same detector and similar acceptance as the NA49 Pb+Pb measurements, allowing to cancel possible systematic effects common to both experiments.

In the CERN SPS beam momentum range of 10–450 GeV/*c* the mean multiplicity of negatively charged pions in inelastic p+p interactions increases from about 0.7 at 10 GeV/*c* to about 3.5 at 450 GeV/*c* [28]. Among three charged states of pions the most straightforward measurements in the largest phase-space are usually possible for the π^- mesons. Neutral pions can be detected only indirectly, by measurement of invariant mass spectrum of two photons from their decays. The low mass NA61/SHINE detector is not well suited to detect photons; also sophistication of the analysis procedure limits precision of the results. Charged pions can be detected directly by ionisation detectors as they decay weakly with a relatively long lifetime. A significant fraction of positively charged hadrons are protons (25%) and kaons (5%) [25–27]. Therefore measurements of the π^+ mesons require their identification by measurements of the energy loss and/or time-of-flight. This identification is not as crucial for the π^- mesons because contribution of K^- and $\overline{\mathrm{p}}$ to the negatively charged hadrons is below 10% [25–27] and can be estimated reliably based on simulation. The latter method is used in this thesis and it allows to derive π^- spectra in a broad phase-space region using a uniform analysis method.

The thesis is organised as follows. Chapter 2 describes the NA61/SHINE experimental set-up. A detailed description of the main detector, Time Projection Chambers, is given in Chapter 3. The simulation used to correct the data is described in Chapter 4. Performance of the reconstruction and the detector is described in Chapter 5. The analysis technique is described in Chapter 6. The final results are presented in Chapter 7. The results are compared with the corresponding data on central Pb+Pb collisions and with Monte Carlo simulations. A summary in Chapter 8 closes the paper.

The appendices include definitions of the coordinate system and variables used in the analysis (Appendix A), details on calculations used to extrapolate the data to the non-measured regions (Appendix B) and tabulated results (Appendix C).

The thesis presents results on p+p at beam momenta of 20, 31, 40, 80 and 158 GeV/*c* measured by the NA61/SHINE detector. The results are inclusive π^- spectra – distributions of π^- produced in all inelastic p+p interactions as a function of rapidity (y) and the transverse momentum (p_T) as well as the transverse mass (m_T). These results published in a NA61/SHINE paper Ref. [29] of which I am the principal author. This thesis describes the analysis steps in much more detail, extends presentation of the results and provides additional comparisons and cross-checks.

1.5 NA61/SHINE experiment and this thesis

NA61/SHINE is an international collaboration, as of May 2015 numbering about 150 participants and 30 institutions, including 7 institutions from Poland. Polish groups contribute substantially to the detector operation and development, participation in data taking, data calibration and reconstruction, software development and conservation, simulations and analysis of particle spectra, fluctuations and correlations. Polish groups engage in the ion and neutrino programs.

The collaboration developed from collaboration of the NA49 experiment taking data in 1994–2002. In 2003 the Expression of Interest was formulated at CERN [30]. The Letter of Intent was submitted at the beginning of 2006 [31] for the "NA49-future" experiment using modernised NA49 detector for a broad program of hadron production measurements.

I joined the experimental group in 2006 under supervision of prof. Wojciech Dominik. Together with the initiators of the new experimental programme I participated in starting and testing the detector operation the shut-down in 2003. Following the successful tests the NA61/SHINE Collaboration was established in 2007. In the same year the first data on p+C interactions at 31 GeV/*c* was taken. Year 2008 was devoted for upgrade of the data acquisition system. In 2009 the p+p data at five beam momenta were collected, starting the ongoing two-dimensional scan of the beam momentum and the system size.

Since the beginning I work on operation and maintenance of the gas system of the NA61/SHINE Time Projection Chambers (TPCs), the main tracking detector. In the subsequent years my responsibility was broadened by operation of the TPCs and coordination of the experimental group. Since 2014 I have been entrusted with the task of NA61/SHINE deputy technical coordinator.

I worked on many levels of analysis of the p+p data presented in this thesis. From 2009 I work on calibration of the drift velocity in the TPCs for this, and subsequent datasets. I studied details of the simulation, in particular ambiguities in the matching procedure. In collaboration with Agnieszka Ilnicka we developed adjustments of the simulated spectra based on the experimental data. I cooperated with the NA61/SHINE Ion group in verification of validity of the data. I verified the reconstruction efficiency and momentum reconstruction resolution. I studied impact of the event and track selection properties on the analysis results, in particular the role of the off-time beam particles. Finally I developed the procedures for the data analysis and calculations of uncertainties, as well as I compared the results with data from other experiments and simulations.

Chapter 2

NA61/SHINE detector

2.1 NA49 detector and upgrades for NA61/SHINE

The data on p+p interactions at the beam momenta of 20, 31, 40, 80 and 158 GeV/*c* were collected in 2009 in the NA61/SHINE experiment at the CERN SPS accelerator. The NA61/SHINE detector structure is shown in Fig. 2.1 [32]. The coordinate system and the kinematic variables used in NA61/SHINE are explained in Appendix A. Many components were inherited from the previous experiment, NA49 [33]: the Time Projection Chambers (TPCs), magnets, side Time of Flight detectors (ToF-L and ToF-R) and the beam line detectors.

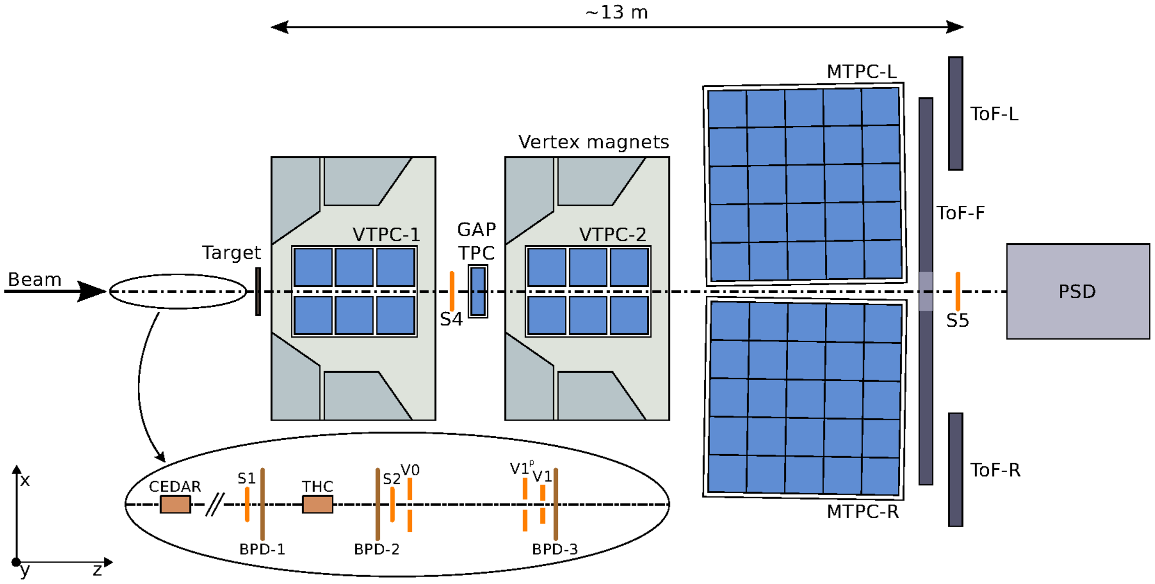

Figure 2.1: A schematic of the NA61/SHINE detector (horizontal cut, not to scale). The beam line set-up is magnified at the bottom of the figure. The spectrometer is formed by five Time Projection Chambers (TPC, blue). VTPCs are located inside VERTEX magnets. Behind the MTPCs there are three Time Of Flight (ToF) planes. On the right there is Projectile Spectator Detector (PSD) calorimeter. The coordinate system starts in the middle of VTPC-2; for clarity it is marked at the corner of the figure. Figure taken from Ref. [20].

The main detector upgrades for NA61/SHINE program include a new readout and data acquisition system, which increased the data taking rate by factor of 10 (to 80 events/s), new beam position detectors, new forward ToF detector and new forward calorimeter.

The main components are briefly presented below. A separate Chapter 3 is devoted to the TPCs. Detailed description of the NA61/SHINE beam line and detector system is given in Ref. [32].

2.2 SPS beam and beam monitoring

The CERN proton acceleration chain starts with linear accelerator LINAC2, which accelerates protons to 50 MeV/*c*. Next, they are injected into BOOSTER (1.4 GeV/*c*), the Proton Synchrotron (25 GeV/*c*), and finally into the Super Proton Synchrotron (SPS). SPS serves as an injector of 450 GeV/*c* protons into the Large Hadron Collider, but also delivers beams to fixed target experiments. Due to practical and safety reasons the fixed target experiments use secondary beams generated by the primary 400 GeV/*c* protons from SPS.

The secondary beam for the H2 line used by NA61/SHINE was produced in interactions of the primary protons with a beryllium target. The beam momenta of 20, 31, 40, 80 and 158 GeV/*c* were selected with a set of magnetic spectrometers and collimators. Details on the accelerator chain are given in Ref. [32, Sect. 2].

Schematic of the beam detectors is magnified on the bottom of Fig. 2.1. A pair of Cherenkov detectors: Cherenkov Differential Counters with Achromatic Ring Focus [34] (labelled CEDAR) and a threshold detector (labelled THC) was used to identify protons in the beams of momenta of 20–40 GeV/*c*. The number of misidentified beam particles is below 0.8% [32]. The beam particles were detected with two scintillator counters, S1 and S2, centred on the beam line. The large (6×6 cm^2) S1 counter defines the time reference for the detector. The small ($\varnothing = 2.8$ cm) S2 counter, and a set of counters with holes centred on the beam axis (V0, $\varnothing = 1.0$ cm; V1, $\varnothing = 0.8$ cm and V1$^\mathrm{p}$, $\varnothing = 2.0$ cm) select particles passing close to the nominal beam axis and rejects cases of beam scattering in the beam line.

A scintillator counter S4 is located behind the target on the extrapolated beam path, taking into account deflection in the magnetic field. This counter was used to detect interaction, as it is expected that the produced particles are unlikely to hit S4. In fact for the 80 and 158 GeV/*c* beams a non-negligible subclass of events contains a particle hitting S4. The correction for the related bias will be described in Sect. 6.4.3. In order to ensure the interaction detection efficiently, the beam was focused in the S4 counter region.

Incident protons were selected by coincidence

$$\mathrm{beam} \equiv \mathrm{S1} \wedge \mathrm{S2} \wedge \overline{\mathrm{V0}} \wedge \overline{\mathrm{V1}} \wedge \overline{\mathrm{V1^p}} \wedge \mathrm{CEDAR} \wedge \overline{\mathrm{THC}}\,. \tag{2.1}$$

Positive signal from S1 and S2 counters and lack of signal from V0, V1, and V1$^\mathrm{p}$ counters ensures proper beam alignment. Beam protons are identified by positive CEDAR signal, and lack of contamination of lighter particles ($\pi^\pm$, K$^\pm$) was ensured by lack of THC signal.

Interactions of the incident beams were identified by an additional requirement of lack of the S4 signal:

$$\mathrm{interaction} \equiv \mathrm{beam} \wedge \overline{\mathrm{S4}}\,. \tag{2.2}$$

These selection criteria were applied during data collection. Simultaneously a data sample with low statistics was collected with the beam trigger only for cross-checks.

The trajectory of each beam particle was measured with three Beam Position Detectors (BPD). They are gas detectors using Ar/CO_2 85/15 mixture, consisting of two perpendicularly aligned layers of readout strips. Each layer measures coordinate x or y of the beam position. The measurement allows to extrapolate the beam track to the target plane with precision of about 100 μm. For details see Ref. [32, Sect. 3.3].

2.3 Liquid hydrogen target

Liquid hydrogen was used as a proton target (LHT). The target system was used previously by the NA49 experiment [25]. It is located 88.4 cm upstream of VTPC-1 (target centre at $z = -581$ cm). The target cell was a cylinder of length of 20.29 cm (2.8% interaction length at 158 GeV/c) and 3 cm diameter. It was filled with liquid hydrogen at the pressure of 75 mbar above the air pressure. The target cell was surrounded by vacuum in order to minimise non-target interactions and secondary interactions of the produced particles.

The target system allowed to insert and remove[1] hydrogen from the cell. About 10% of the total statistics is collected with target removed, taken 2–3 times each day. The target removed data were used to correct for the beam interactions with the non-target material, mainly the target cell windows (see Sect. 6.4.1).

The liquid hydrogen density equalled $\rho_{\text{inserted}} \approx 0.07$ g/cm^3. The density ratio of target removed (gaseous residue) to inserted was estimated to $\rho_{\text{removed}}/\rho_{\text{inserted}} \approx$ 0.5%, see also Sect. 5.3 for detailed analysis.

2.4 Spectrometer system

Set of five Time Projection Chambers (TPCs) serves as the main spectrometer of the produced particles. TPCs measure three-dimensional tracks of charged particles, their momentum and the charge sign and allow to identify their mass.

The five detectors of total volume of about 40 m^3 are located downstream from the target. A detailed overview of TPCs is given in Sect. 3.

Two TPCs called Vertex TPC (VTPC) are located in the gap between upper and lower coils of two superconducting magnets: VERTEX-1 and VERTEX-2 [32, Sect. 4.3]. The magnets provide magnetic field polarised downwards (towards negative values of y), uniform in majority of the detector fiducial volume. Paths of the charged particles are bent in the horizontal plane. A detailed map of the magnetic field, including inhomogeneities measured at the VTPC corners is used to fit the particle tracks.

The maximum magnetic field: 1.5 T in VERTEX-1 and 1.1 T in VERTEX-2 corresponding to 9 Tm in total, was used with the 158 GeV/c beam. The TPC acceptance with this magnetic field setting covers the region of rapidities equal and greater

---

[1] The terms *inserted* and *removed* are used in NA61/SHINE in order to unify the naming for the liquid (e.g. hydrogen) and solid (e.g. beryllium) targets.

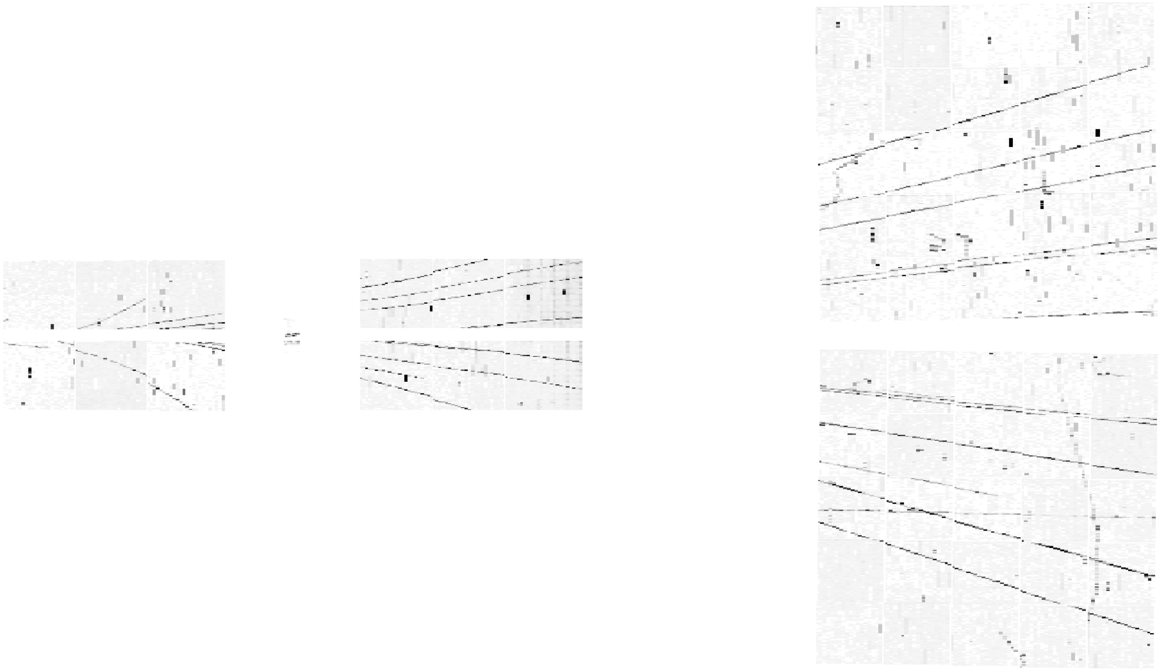

Figure 2.2: An example of a p+p interaction at 158 GeV/*c* measured in the NA61/SHINE spectrometer system (top view – projection on the x–z plane). The colours show unprocessed signals measured in the TPCs: light grey corresponding to electronic noise and black to tracks of charged particles. The positions of the detectors in the figure are approximate.

than 0 (see Appendix A.3 for definition). For the lower beam momenta the magnetic field was decreased proportionally to the beam momentum in order to maximise the detector acceptance at forward rapidity.

An example of a p+p interaction measured in the NA61/SHINE spectrometer is shown in Fig. 2.2.

2.5 Time of Flight detectors

The Time of Flight (ToF) detectors measure the time passing between interaction of the beam proton and the particle detection in the ToF detector [32, Sect. 5]. Together with the TPC measurement of trajectory and momentum of the particle, they provide an independent mass identification. Resolution of the time measurement limits maximum momentum of particles that can be distinguished to several GeV/*c*. The geometrical alignment of ToFs limits minimum particle momenta to about 0.5 GeV/*c* (2 GeV/*c*) at p_{beam} = 20 GeV/*c* (158 GeV/*c*).

There are three ToF walls located behind the TPCs:

- Two side ToF-L and ToF-R were built for the NA49 experiment to cover the mid-rapidity region for kaons. They consist of a two-dimensional arrays of 1782 scintillators in total, each of 34 mm height and 60–80 mm width read by a single photomultiplier. The detector covers the total area of 4.4 m^2.
- The forward ToF-F was built for NA61/SHINE in order to measure the π and K mesons produced in p+C interactions contributing to the neutrino beam in the T2K experiment [35]. The detector consists of 80 vertical scintillator

bars of length of 120 cm, covering the total area of 8.6 m^3. Each scintillator is read by two photo-multipliers at both ends. The time difference between the two signals allows to identify the hit position along the scintillator bar. The detector was used for measurements of p+p, p+C and π+C interactions, where the frequency of double hits in the scintillator bars was low due to low total produced particle multiplicity.

The ToF data was not used for the data analysis presented in this thesis. However the side ToFs served as a geometrical reference in calibration of the drift velocity of the TPCs.

2.6 Projectile Spectator Detector

Projectile Spectator Detector (PSD) is a sampling calorimeter designed and built for NA61/SHINE [36]. The University of Warsaw contributed in production of the detector. It is located behind all other detectors on the beam path. It counts the non-interacting nucleons (*spectators*) of the beam nucleus by measuring their total energy. Such precise measurement is necessary to determine the collision centrality needed in ion-ion collisions.

During the p+p data taking in 2009 a prototype of nine modules was tested. First physics data were obtained with detector of 36 modules in 2011; a complete detector of 44 modules was first used in 2012 to measure the Be+Be reactions.

Chapter 3

Time Projection Chambers

3.1 History and concepts

A Time Projection Chamber (TPC) is a detector of charged particles [37]. Their trajectories are measured in space. It was first proposed in 1976 by David Nygren and collaborators for the PEP-4 collider experiment at SLAC. The detector was completed in 1981 [38, 39]. This first TPC had volume of 6 m^3 and consisted of two cylindrical drift chambers arranged around the beam pipe, with multiwire proportional chambers (MWPC) reading signals at the end-caps. Since then, devices of a similar design were used in the collider experiments: 43 m^3 ALEPH TPC [40] and 10 m^3 DELPHI TPC [41] at LEP in CERN, 49 m^3 TPC of the STAR experiment at RHIC in BNL [42] and 90 m^3 TPC of the ALICE experiment at LHC in CERN [43]. A simpler, box-like TPCs were used in the fixed-target experiments. An example is the NA49 TPC system [33], later inherited and upgraded by the NA61/SHINE experiment. It was used to collect the data analysed in this thesis and it will be described in detail in this chapter.

A TPC is filled with a working medium which can be gas or liquid. Low density of the gas allows to achieve low rate of the secondary interactions. For this reason it is chosen typically in the accelerator experiments, as those listed above. On the contrary, large densities of liquids allow them to serve as targets for the ultra low cross-section interactions of neutrinos or hypothetical weakly interacting massive particles (WIMP). Examples include the liquid argon TPC of the ICARUS neutrino experiment [44] and the liquid xenon TPCs in the XENON experiment series [45]. In this thesis I will consider only the gas-filled TPCs.

Figure 3.1 shows a schematic of a TPC. A field cage encloses the active volume of a TPC, generating uniform electric field inside. Charged particles ionise the gas inside along their trajectories. Electrons (*blue circles*) freed in the process drift in presence of a uniform electric field towards the readout plane. As the number of electrons released in gas is relatively low (several to several hundreds per cm for relativistic particles), a charge amplification structure is located before the readout plane. This could be a MWPC, or developed in the last years gas electron multiplier (GEM).

The electrons are registered on a two-dimensional plane of readout pixels. Charge location on the readout plane is a projection of two coordinates (x and z in NA61/SHINE) of the track. Signal on the readout pixels is sampled many times during the charge collection from the drift volume. Measurement of the the drift

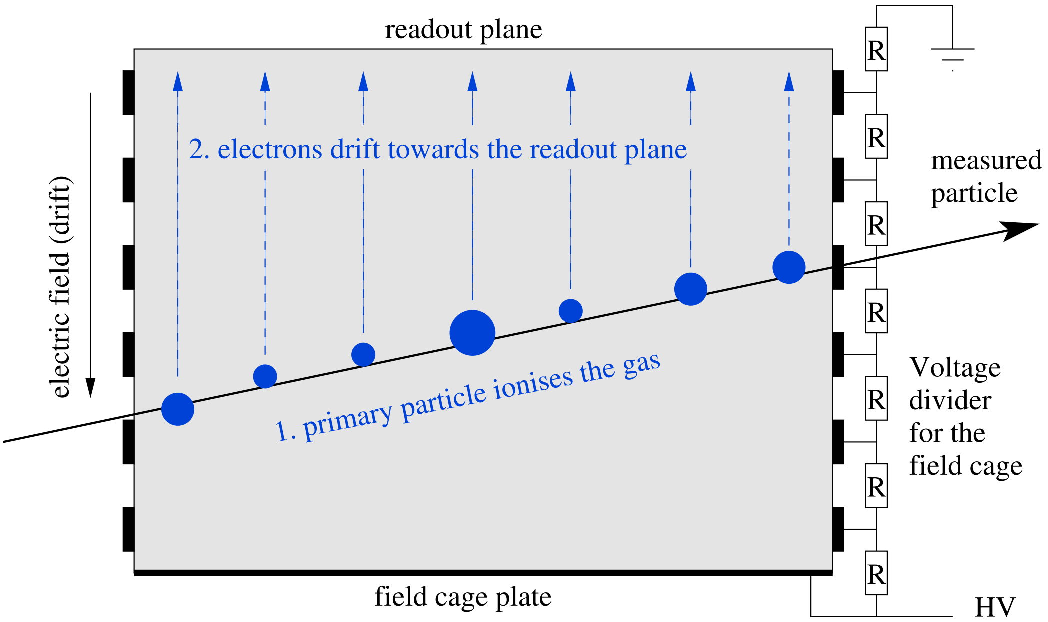

Figure 3.1: A schematic of a TPC. The active volume (*grey*) is enclosed in a field cage, consisting of an anode (*top*) and a cathode (*bottom*) plate, and a number of strips on the sides with gradually changing voltage. Electrons resulting from ionisation induced by the primary particle drift in presence of the electric field.

time t of the primary ionisation charge and knowledge of the drift velocity v_D allows to calculate the third coordinate:

$$y = y_0 - v_\mathrm{D} \cdot t\,, \tag{3.1}$$

where y_0 is the position of the readout plane.

A TPC enables measurement of the energy loss in gas (often referred to as $\mathrm{d}E/\mathrm{d}x$ – an energy loss per unit length). It allows to identify mass of the particle when combined with the momentum measurement. A TPC placed in a magnetic field can be also used to determine sign of the electrical charge q of the particle, and the track rigidity R, defined as:

$$R = B\rho = p/q\,, \tag{3.2}$$

where B is the magnetic field, ρ is the Larmor radius, and p is the particle momentum.

3.2 Principle of operation

Volume of a TPC is filled with gas. A charged particle passing through the chamber ionises atoms of the gas. The number of electrons in the primary ionisation clusters depends on the gas properties and on the energy lost by the particle. The mean energy loss per unit length, $-\langle \mathrm{d}E/\mathrm{d}x\rangle$, of a moderately relativistic particle ($0.5 < \beta\gamma < 500$) is described by the Bethe formula [7, Eq. (31.2)]:

$$-\left\langle \frac{\mathrm{d}E}{\mathrm{d}x} \right\rangle = Kz^2 \frac{Z}{A}\frac{1}{\beta^2} \cdot \left[\frac{1}{2} \ln \frac{2m_\mathrm{e}c^2\beta^2\gamma^2 T_\mathrm{max}}{I^2} - \beta^2 - \frac{\delta(\beta\gamma)}{2} \right], \tag{3.3}$$

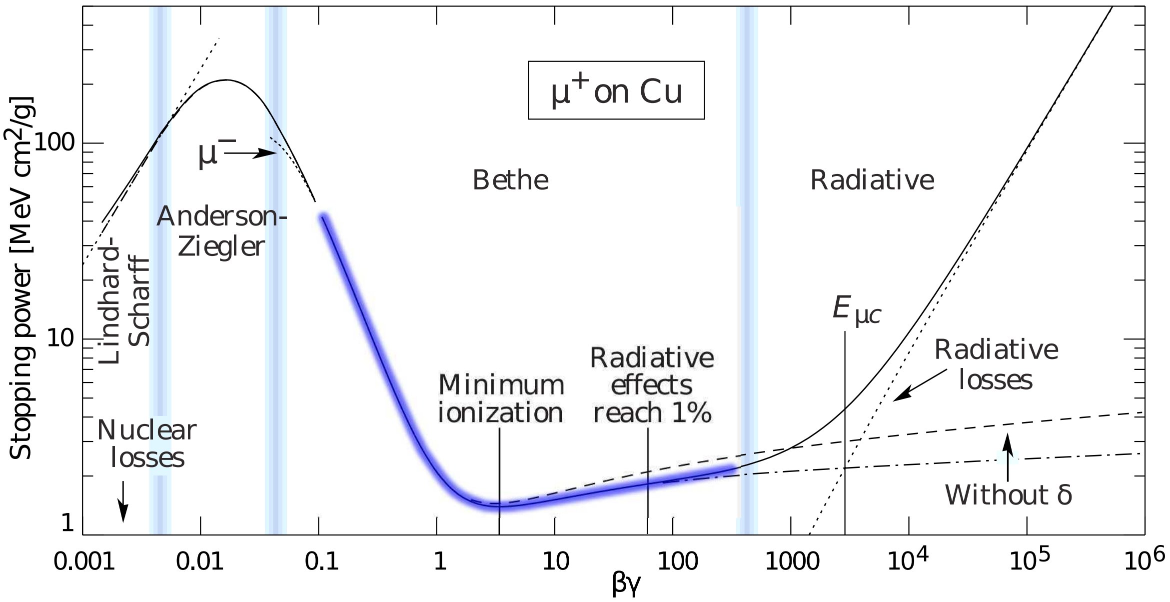

Figure 3.2: Energy loss per unit length, $-\langle dE/dx\rangle$, for muons in copper. The region relevant for TPCs in typical high-energy physics experiments is marked by the thick blue line. The characteristic properties of this region is the decrease proportional to $1/\beta^2$ at the low energies, a minimum at $\beta\gamma \approx 3$ and a slow increase at the higher energies. Figure taken from [46, Fig. 27.1].

where $\gamma = (1-\beta^2)^{-1/2}$, $\beta = v/c$, v – velocity of the particle, c – speed of light, x – distance travelled by the particle, z – particle charge in electron units, Z – atomic number of absorber, A – atomic mass of absorber, m_e – mass of the electron, T_{max} – maximum kinetic energy that can be imparted to a free electron in a single collision, I – mean excitation energy of absorber, $K = 0.307075$ MeV g^{-1}cm^2 (constant), $\delta(\beta\gamma)$ – density effect correction to ionization energy loss.

The formula Eq. (3.3) is a function of the particle velocity β. This dependence is visualised in Fig. 3.2. Particles of different masses m and the same momentum p have different velocities:

$$\beta = \frac{p}{mc} \, . \tag{3.4}$$

Hence, measurement of the energy loss and the momentum allows to identify mass of the particle.

The formula Eq. (3.3) describes the average energy loss per unit length, however actual value undergoes large statistical fluctuations. The energy loss needs to be measured on a long path in order to provide identification power.

The readout plane is divided into pixels allowing to select short track pieces corresponding to the energy losses in thin gas layers. Distribution of the energy deposit in a track piece is often parametrised with the Landau distribution [47]. An example is shown in Fig. 3.3 (*left*). A characteristic feature of this distribution is a long tail at the high values: occasionally the energy deposit is very large. As a result the mean value of the energy loss along the track fluctuates strongly. Impact of the fluctuations can be reduced by omitting the extreme values in the mean value calculation. For example, in NA61/SHINE only the 50% track pieces with the lowest energy loss is used to calculate the mean loss; this so-called *truncation*

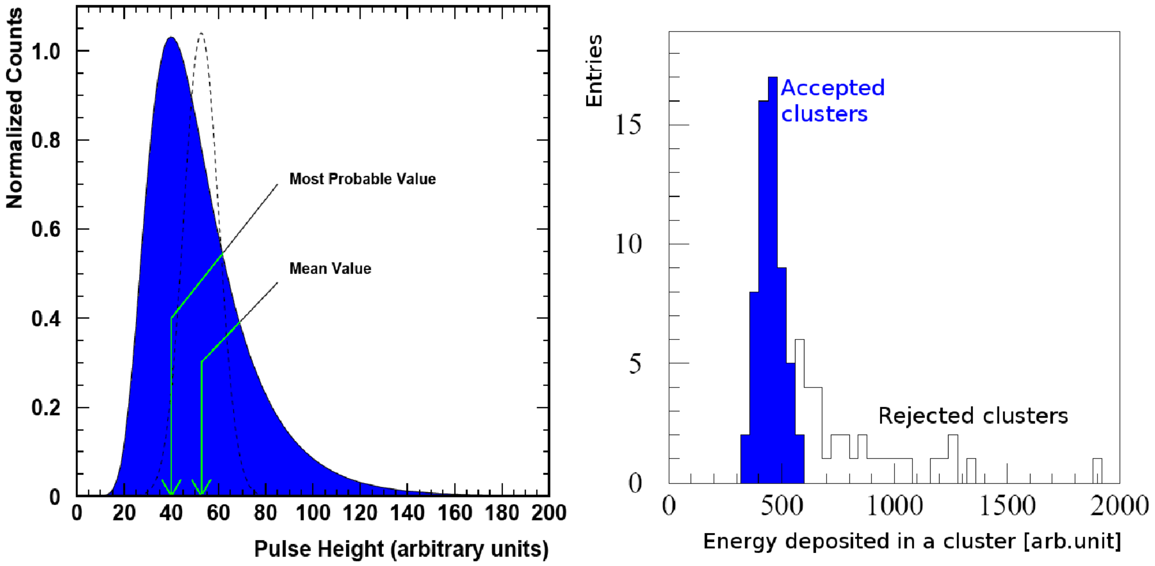

Figure 3.3: *Left:* Landau distribution. For comparison the dashed line shows Gaussian distribution with the same mean value and similar peak width. *Right:* example distribution of many measurements (called "clusters" in the figure) of the energy lost by a single particle. The blue area shows the truncated distribution. Figure taken from Ref. [20].

procedure is demonstrated in Fig. 3.3 (*right*). Truncation increases resolution of particle identification based on the dE/dx measurement.

The primary ionisation clusters drift in presence of the electric field towards the readout plane. The drift velocity depends on the gas mixture, its density, and the electric field strength [47]. Knowledge of the drift velocity value is crucial for precise position reconstruction in a TPC.

In absence of the magnetic field the drifting clusters follow straight paths. If a TPC is placed inside a magnet, the typically chosen alignment is that the magnetic field lines are parallel to the electric field lines. This way the drift direction is unaffected, and also the transverse diffusion of the drifting electron cloud is reduced.

The small primary ionisation charge in gases needs to be amplified internally in the detector before electronic registration. Available devices providing so-called *gas amplification* include MWPC and GEM; let us discuss the first one. Thin (typical diameter of 20 μm) high voltage wires form a plane next to the readout plane. In a small distance r to the wire centre the electric field increases proportionally to $1/r$. In presence of the high field the electrons accelerate and ionise atoms of the gas. The process repeats creating an avalanche of electrons which develops until all the electrons become collected on the wire. The voltage on the wires is adjusted so that the amplified charge is proportional to the primary charge. Sudden disappearance of the electrons, and movement of the positive ions repelled from the wire induce an electromagnetic pulse on the readout plane. Due to the gas amplification the amplitude of the signal suffices for electronic readout. A practical implementation of the gas amplification set-up in NA61/SHINE will be discussed in Sect. 3.4.1 (see Fig. 3.6).

Side effects of the gas amplification include sense wire ageing, and distortions of the drift field due to space charge from the positively charged ions, drifting about

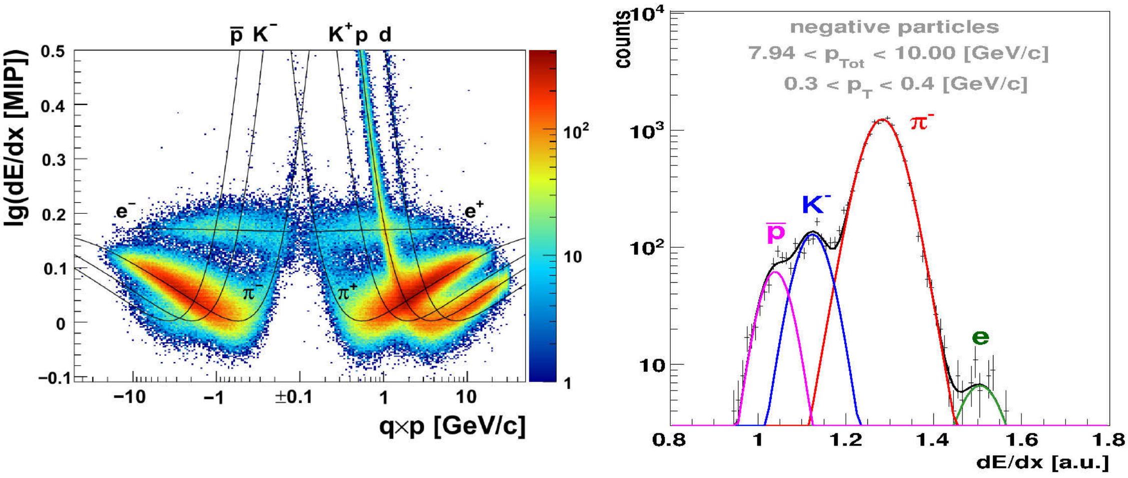

Figure 3.4: Particle identification in NA61/SHINE Time Projection Chambers. *Left:* logarithm of the measured energy loss in TPCs as a function of momentum times electric charge of the measured particle. Each entry on the histogram corresponds to a single particle. Theoretical Bethe curves are drawn over the measured data. *Right:* the dE/dx distribution in the selected momentum range of 7.94–10.00 GeV/c for the transverse momentum range of 0.3–0.4 GeV/c. The fitted lines indicate contributions of various particle types. Figures obtained from Ref. [48].

1000 times slower than the electrons. This effects need to be taken into account in design of high event rate TPC.

3.3 Particle identification in TPC

An experimental measurement of the energy loss as a function of particle momentum is shown in Fig. 3.4 (*left*). The measurements are consistent with the Bethe curves, but they are scattered due to fluctuations of the primary energy loss. An example of the energy loss measured in a selected narrow momentum range is shown in Fig. 3.4 (*right*). In many momentum regions the distributions from individual particle types overlap with each other making is impossible to identify each particle individually. However, the particle yields can be calculated by fitting the distribution.

At the momenta momenta of several GeV/c the Bethe curves for different particle types approach and cross each other. Below 5 GeV/c it becomes difficult to distinguish pions from deuterons, protons and kaons; the pion and the electron curves overlap below 400 MeV/c. Identification is possible again at the even lower momenta, where the Bethe curves separate again.

3.4 NA61/SHINE Time Projection Chambers

3.4.1 Construction

The main detector of the NA61/SHINE tracking spectrometer is a set of 5 TPCs: VTPC-1, VTPC-2, MTPC-L, MTPC-R and GAP TPC (see Fig. 2.1). The basic characteristics of the NA61/SHINE TPCs are listed in Table 3.1. The readout pad array

	VTPCs	MTPCs	GAP TPC
Width (x) [mm]	2 000	3 900	815
Length (z) [mm]	2 500	3 900	300
Number of padrows	72	90	7
Drift length (y) [mm]	666	1 117	590
Drift voltage [kV]	−13	−19	−10.2
Drift field [V/cm]	195	170	173
Drift velocity [cm/μs]	1.4	2.3	1.4
Ar/CO_2 mixture	90/10	95/5	90/10

Table 3.1: Characteristics of the NA61/SHINE TPCs: dimensions, drift voltages, fields and velocities and the gas mixture proportions.

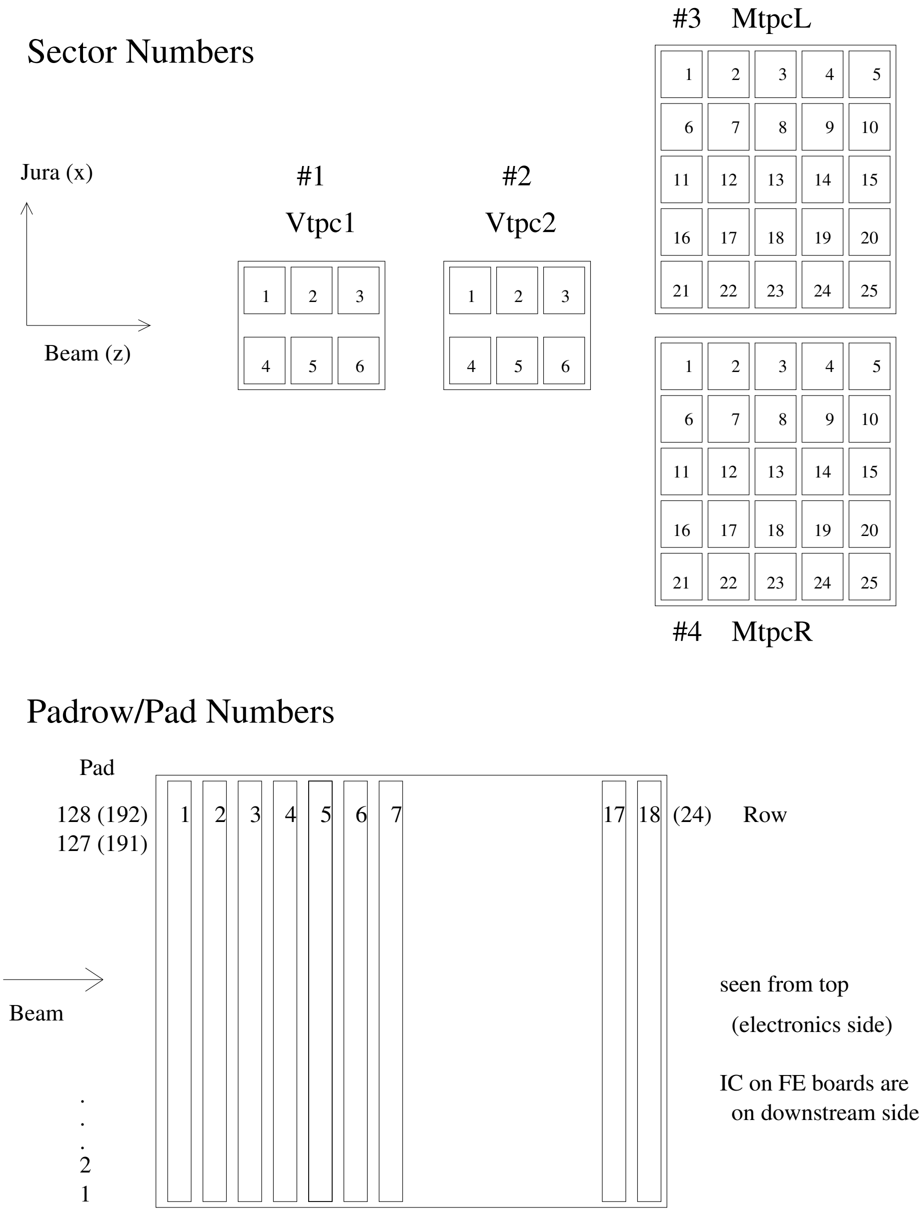

Figure 3.5: *Top:* NA61/SHINE TPC sector numbering convention. *Bottom:* Alignment and numbering convention of the NA61/SHINE TPC padrows and pads within a single sector. Drawing taken from [49].

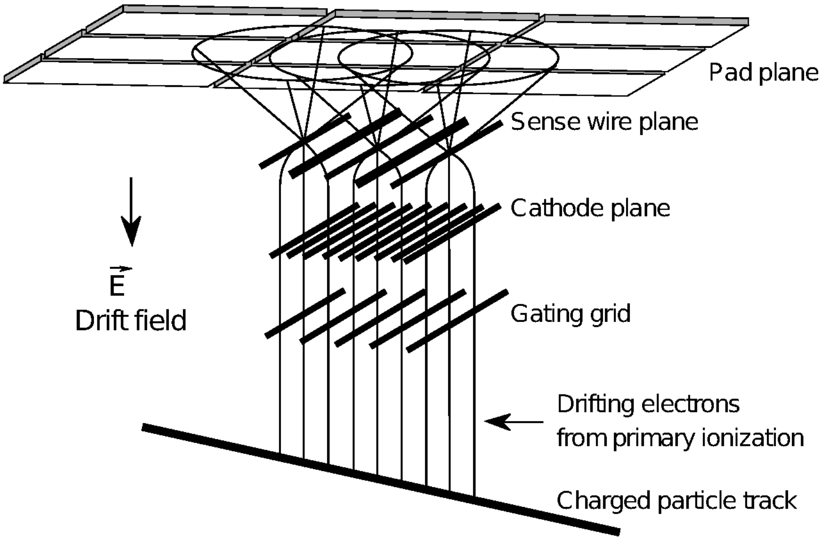

Figure 3.6: A schematic of the charge amplification and signal registration structure in the NA61/SHINE TPCs. Note the *cathode plane* serves as a negative electrode for the sense wires, but also as a positive electrode for the field cage. Figure taken from Ref. [20].

consists of over $181 \cdot 10^3$ pads organised as shown in Fig. 3.5: the TPCs are divided into sectors; the pads are located along the padrows perpendicular to the beam line. The number of padrows determines the maximum number of clusters that can be measured on a track passing through the whole detector length. The signal is sampled 256 times during the 50 μs charge collection time, with 8 bit final resolution after the ADC pedestal subtraction.

Figure 3.6 shows a schematic of the charge amplification and signal registration structure in the NA61/SHINE TPCs. The *cathode plane* wires at the ground potential separate the drift volume and the amplification region. The *sense wires* plane consist of 20 μm amplification wires at about +1 kV. They are interspaced by field wires at the ground potential, which helps to shape the electric field for the gas amplification. The *gating grid* separates the drift and the amplification regions. During the charge collection its voltage is adjusted in the way that it does not modify the drift field. Between the charge collection periods an additional voltage of about ±45 V is applied to each second wire. Electrons and positively charged ions cannot pass between the two regions, which reduces aging of the sense wires, and distortions of the drift field by the slowly drifting positively charged ions.

Both VTPCs are located inside two superconducting dipole magnets. The magnetic field bends tracks of charged particles in the horizontal plane (x–z) allowing to measure their momenta. Lines of the magnetic field are aligned along the y axis, parallel to the electric field lines and the drift direction. Only small corrections during track reconstruction are needed to take into account distortions due to inhomogeneities of the magnetic field in the corners of the VTPCs.

The MTPCs are located outside of the magnetic field. They can measure up to 90 clusters on a track, which enhances the $\mathrm{d}E/\mathrm{d}x$ measurement resolution.

The TPC system was designed to measure collisions of lead ions in the NA49 experiment. Very high track density in the forward region in such collisions limits the measurement possibility due to the two-track resolution of about 1 cm [33], rapid wire ageing and large amounts of the positively charged ions in the drift volume. In order to avoid these issues, the active sections of VTPCs are separated by a 25.5 cm wide uninstrumented gap on the beam axis.

The GAP TPC centred on the beam axis completes the acceptance in the smallest production angles in low multiplicity collisions of protons and light nuclei. Seven padrows of the GAP TPC are insufficient to reconstruct the tracks passing the GAP TPC alone. However it allows to reconstruct the tracks missing the VTPCs, which would otherwise leave only a straight track in one of the MTPCs.

3.4.2 Gas system

The detection properties of TPC strongly depend on the gas mixture choice [50]. Firstly, the drift velocity must be sufficiently high, to allow the charge to be collected from the full TPC volume within the event readout period, which is 50 μs in NA61/SHINE. Although for many gas mixtures the drift velocity can be increased in a large range by increasing the drift voltage, there are practical and safety limitations related to the chosen power supplies and cables, and heating of the voltage divider resistor chain; the NA61/SHINE TPCs are operated at voltages below 20 kV. Secondly, the gas amplification must be stable. An addition of so-called quenching gas helps to limit excessive and uncontrolled growth of the electron avalanches.

The mixtures chosen in NA49 were Ne/CO_2 90/10 in VTPCs and GAP TPC and Ar/CO_2/CH_4 90/5/5 in MTPCs, based on experimental measurements of properties of various mixtures [33, 51, 52]. Argon as a base component of the MTPC gas is characterised by large number of electrons produced in the primary ionisation. Lighter neon used in VTPCs and GAP TPC allowed to reduce the number of unwanted interactions with the gas, in particular production of δ-electrons of energies of fraction of GeV, which can be trapped in the magnetic field and produce high background signals. Methane and carbon dioxide served as quenching gases.

Table 3.1 lists the gas mixtures selected in NA61/SHINE, consisting of argon and carbon dioxide only. It was verified that the detection properties with the new mixtures satisfy the experimental requirements [53]. Absence of flammable methane and use of more similar mixture in all TPCs facilitates the detector operation and calibration of the data. The δ-electrons production was not of a concern with the proton and pion beams used in the first years of operation. Later, before the first data taking period with beams of heavier ions, a helium-filled pipe centred on the beam line was introduced in the VTPCs, reducing interactions with the TPC gas by factor of about 10 [32].

Stability and purity of the gas mixture are critical for the detector operation. The drift velocity and gas amplification strongly depend on the gas content (order of 1% change in the drift velocity per 0.1% change of the Ar/CO_2 proportion). Contamination of electronegative oxygen causes charge absorption along the drift path which is significant already at the levels of tens of ppm (parts per million). Water at the level of 100 ppm modifies the drift velocity by about 1% [33].

Gas in VTPCs and MTPCs is supplied by four independent, almost identical systems. Figure 3.7 presents the gas system of MTPC. The symbols used in the diagram are explained in Fig. 3.8. The fresh gas is mixed from the pure Ar and CO_2 using mass flow controllers. The gas is recirculated through set of filters with rate of about 20% detector volume per hour, i.e. 0.9 m^3/h for the VTPCs and and 3 m^3/h for the MTPCs. Only about 3% of this amount is a fresh gas.

In order to limit secondary interactions, side walls of the TPCs consist only of two layers of 125 μm-thick Mylar foils. The space between two foils is flushed with nitrogen to protect the gas from contamination by air due to diffusion through the walls and in case of leak. This fragile construction could be easily damaged by ex-

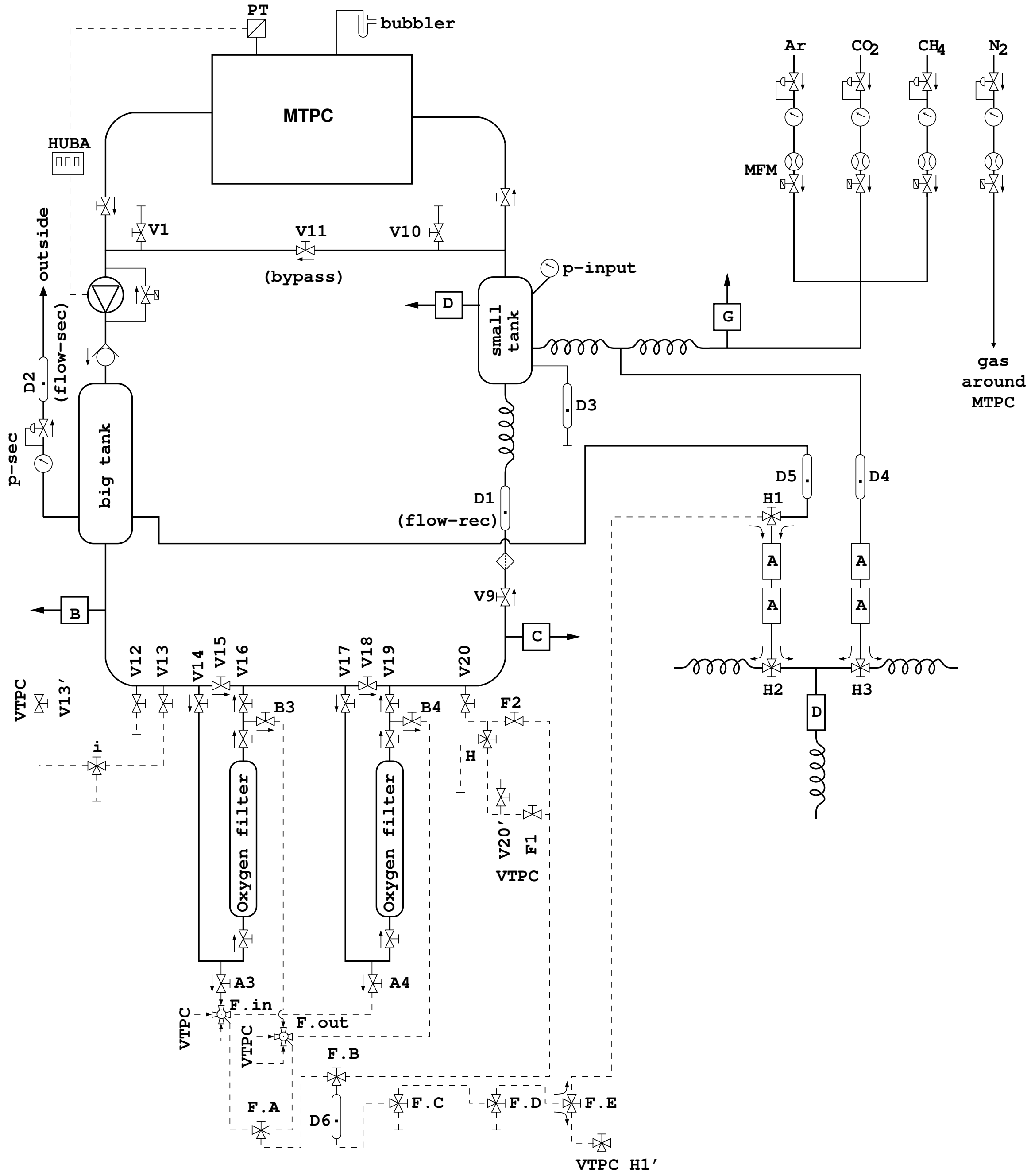

Figure 3.7: A schematic of the gas system of one of the MTPCs. The schematic for VTPCs is almost identical. The symbols used are explained in Fig. 3.8. The main parts are drawn with bold lines; the dashed lines show connections not used in the regular operation modes. The gas mixing system is shown in the upper right corner. The fresh gas enters the small buffer tank and then the TPC. A compressor pumps the gas out of the TPC and circulates it through the oxygen filter. The oxygen and water content in the gas can be monitored in points labelled B, C, D and G. The drift velocity and the gas amplification can be measured in fresh gas and in gas coming from the TPC in the monitors drawn on the right side, labelled D and A, respectively.

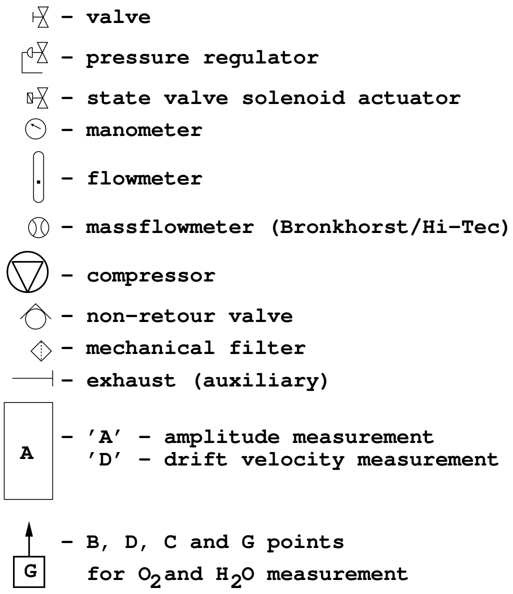

Figure 3.8: Descriptions of symbols used in Fig. 3.7.

cessive overpressure or underpressure of the gas in the TPC. The gas is circulated by a compressor, which circulation speed is adjusted automatically to maintain a constant overpressure of 0.50 ± 0.01 mbar in the chamber above the ambient pressure. The small overpressure additionally prevents contamination by air in case of leak. Safety bubbler protects the TPC from excessive overpressure in case of the compressor failure, or when the compressor is switched off.

The recirculated gas is flushed through a filter made of activated copper. The filter reduces the oxygen contamination to about 5 ppm. The water content is also removed, but after about 2 weeks of operation first signs of filter saturation are visible. Typically water levels of 20–100 ppm are achieved. The filters are regenerated after 4–6 months of operation by flushing them with the Ar/H_2 (97/3) mixture at 200°C for 2–3 days. The regeneration progress is monitored by measuring moisture in the outgoing gas. An additional filter is used to remove dust from the gas.

Quality of the gas mixture is monitored periodically in a set of detectors. Figure 3.9 shows example values measured in MTPC-R. For each TPC we monitor the drift velocity v_D, temperature T and drift voltage U (both in the drift monitor and in the TPC), air pressure p, and the oxygen and water content in the gas. For the gas mixtures used in NA61/SHINE, in the first approximation

$$v_D \sim \frac{T \cdot U}{p} \,, \tag{3.5}$$

where the T is given in Kelvin. While the temperature and the drift voltage is stabilised on a sub-permille level (panels c and d) most of the time, variations of the air pressure (panel b) change the drift velocity by several percent. The normalised drift velocity, corrected for changes of T, U and p allows to monitor stability of the gas mixture. Its increase visible in the panel a might be related to stability of the gas flow controllers and/or a decrease of the water level (panel e) caused by decrease of the air humidity in the autumn. Measurements of T and U in the TPCs allows to calculate the drift velocity in the TPC (panel a).

The calculated values of the drift velocity are used for the first calibration reconstruction of the data (details of reconstruction will be explained in the next section).

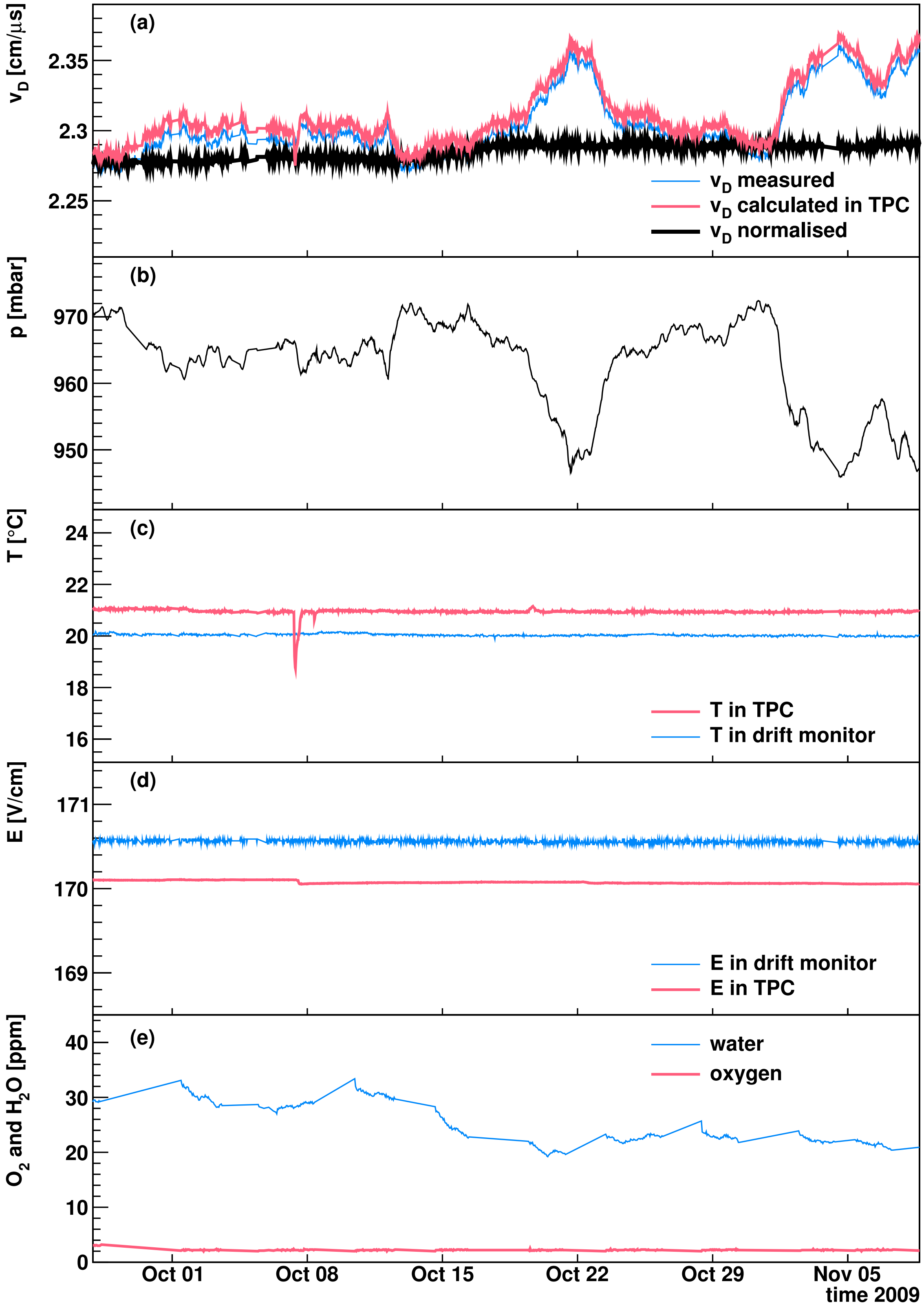

Figure 3.9: Parameters of the gas in MTPC-R monitored in a selected period of time. *a:* drift velocity measured in the drift monitor, normalised based on measurements of pressure, temperature and drift voltage, and calculated in the TPC conditions, *b:* air pressure, *c:* gas temperature in the drift monitor and in the TPC, *d:* electric field in the drift monitor and in the TPC, *e:* water and oxygen content in the TPC gas.

Comparison of positions of the tracks with positions of signals in TPCs and ToF allows to derive a correction factors for the drift velocity. Typically the correction factor is of order of several permille, and it changes very slowly in time. Possible reasons for the errors in the measurement could be unknown temperature distribution in the TPC, or precision of formulae used to calculated the drift velocity in TPC.

The GAP TPC of volume of only about 150 l uses a much simpler system. About 20 l/h of fresh gas mixture is flushed through the detector. The gas coming out from the TPC is measured only in a drift velocity monitor.

3.4.3 Reconstruction of events and tracks

Figure 3.10 shows an example of a reconstructed p+p event measured in NA61/SHINE. The track reconstruction consists of the following steps:

- **Finding points.** Points are searched in a two-dimensional array of signals collected in each individual row of pads in all 256 time slices, an example of which is shown in Fig. 3.11 (*left*). Signals in at least two adjacent cells of the array in both dimensions are required for a point to be found; typically the points are built from signals collected from 3–5 adjacent pads (x coordinate), and 2–4 time slices (y coordinate). Several effects broaden the signal: the drifting charge diffuses, the signal is induced on several pads within a pad row, and the preamplifier shapers elongate duration of the pulse. Precision of

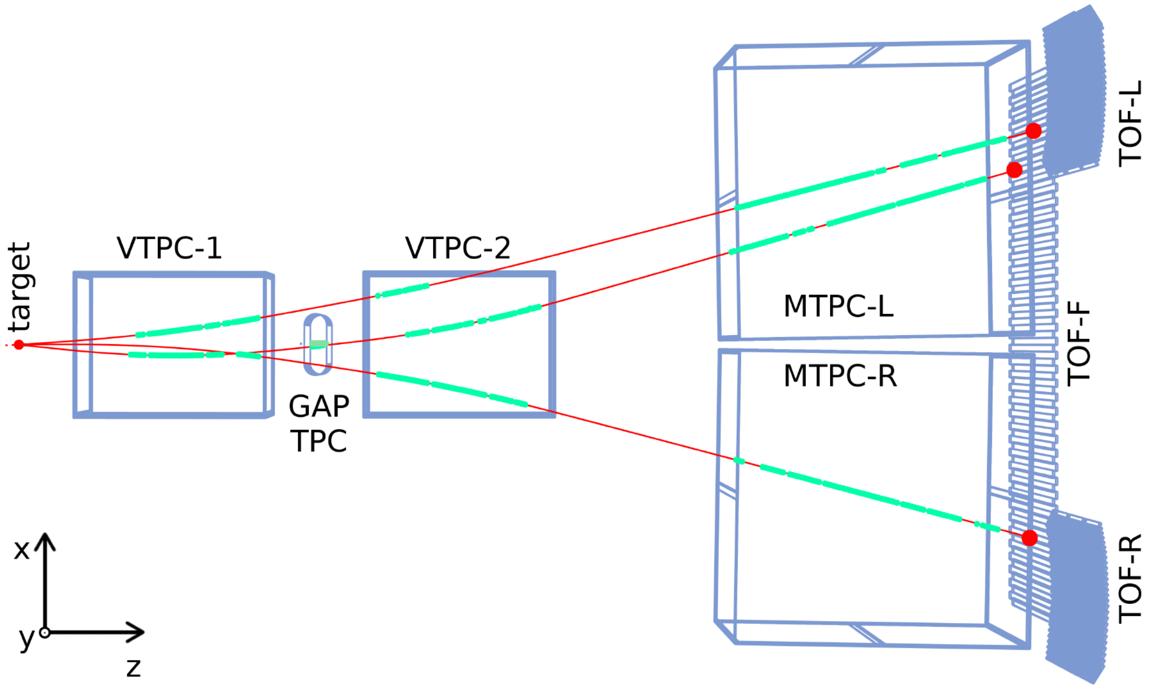

Figure 3.10: An example of a reconstructed p+p interaction at 40 GeV/c measured in the NA61/SHINE detector. The points measured in the TPCs (green) are connected with the reconstructed tracks (red), and fitted to the interaction point (red circle on the left). Also the ToF hits are shown. The track segments in the VTPCs are bent by the magnetic field. Two positively charged particles are bent upwards (in the figure) and a single negatively charged particle is bent downwards.

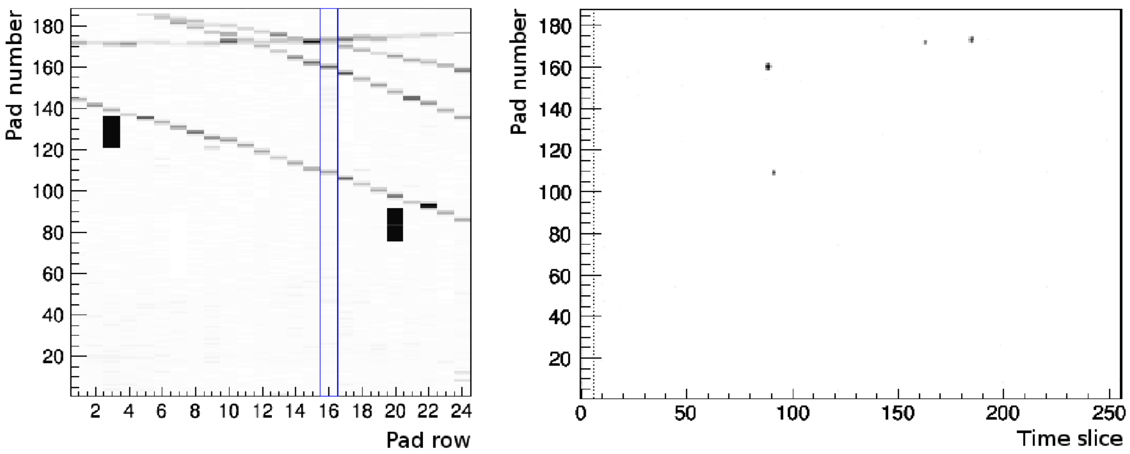

Figure 3.11: *Left:* Example signals measured in the VTPC-1 sector 5, top view. Four dark lines are tracks of four particles. The two black rectangles are electronic noises. *Right:* Signals collected on a padrow 16 (marked with a blue frame on the *left* panel) versus time slice in the same event. Four grey spots are charge clusters belonging to the four tracks.

the point position calculated with centre of gravity method is better than size of a single pad and a single time slice.

- **Fitting track pieces in each TPC separately.** In the MTPCs points aligned along straight lines are connected into track pieces. In VTPCs curved track pieces are searched. Momentum of the track pieces is determined according to their curvature and distribution of the magnetic field in the detectors.
- **Merging track pieces from all TPCs.** Matching track pieces from different TPCs are connected together. Momenta of the tracks including clusters found in all TPCs are fitted again, according to the magnetic field distribution within the TPC volumes and between them.
- **Determination of the interaction vertex.** The algorithm attempts to find a common vertex for all tracks extrapolated to the target region. The vertex z coordinate is fitted using tracks found in TPCs in given event. In case the vertex cannot be fitted, the geometrical centre of the target is used instead. The x and y coordinates of the vertex are calculated by extrapolating the beam track measured by the BPDs to the vertex z coordinate.

  Momenta of the TPC tracks are fitted again using the vertex point as an additional constrain.

  Figure 3.12 shows distribution of the fitted z coordinate of the reconstructed vertex. The distribution show location of the material along the beam line, in vicinity of the target.

  The distance in the x–y plane between the vertex point measured by the BPDs and the track extrapolated from TPCs is called *impact parameter*. Such defined impact parameter is a technical parameter determining how well the reconstructed track is extrapolated to the vertex point.
- **Determination of the secondary vertices.** For each pair of tracks the algorithm attempts to find a secondary vertex, indicating that the particles may originate from a decay, mostly of K^0_S or Λ. At the level of reconstruction a single track may be assigned to any number of vertices, e.g. both primary and

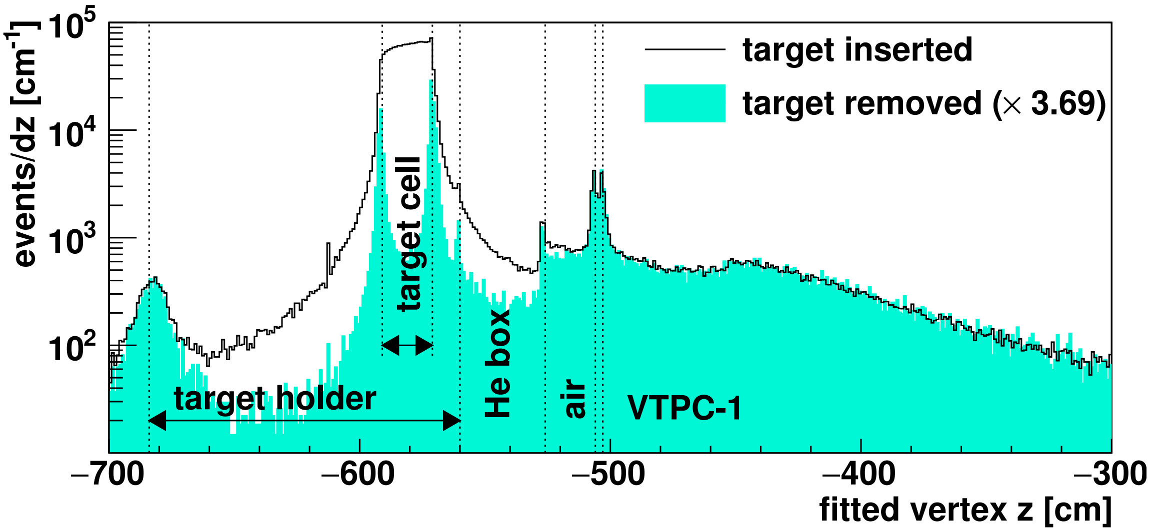

Figure 3.12: Distribution of the fitted vertex z coordinate for interactions of proton beam at 40 GeV/c with target inserted and removed. Peaks in the histogram reflect the distribution of the material along the beam line: liquid hydrogen, walls, vacuum, helium, and the TPC working gas.

secondary; a distinction must be done on the analysis level, for example by restricting the impact parameter range.

Information available for each track include:

- electric charge sign,
- momentum vector at the interaction vertex,
- average charge loss $\langle \mathrm{d}E/\mathrm{d}x \rangle$,
- number of points measured in each TPC,
- impact parameters in the x and y coordinates, b_x and b_y respectively.

During the analysis the events and tracks pass additional selection. Only events containing interaction of the beam particle with the target are accepted. Events with high background from the off-time particles are rejected. Tracks are required to be sufficiently long and precisely fitted to the interaction point. This ensures the parameters of the particles are well measured, and that background is suppressed. While the selection criteria will be described in detail in Sects. 6.2 and 6.3 devoted to the analysis method, in the subsequent Chapters 4 and 5 describing simulations and characteristics of the collected data I will often refer to tracks passing the selection criteria.

Typical spacial resolution, defined as an average distance between the points and tracks is several hundred μm, and two tracks distant by 1 cm can be distinguished. The resulting momentum resolution $\sigma_p/p^2 = 7.0 \cdot 10^{-4}$ (GeV/c)$^{-1}$ for tracks detected in VTPC-1 only, and $\sigma_p/p^2 = 0.3 \cdot 10^{-4}$ (GeV/c)$^{-1}$ for tracks detected in VTPC-2 and one of the MTPCs [33]. High precision of point identification with good two-track separation allowed to reconstruct high multiplicity (>1000 tracks) Pb+Pb collisions by the NA49 experiment.

Chapter 4

Monte Carlo simulation

4.1 Purpose of using simulations

The detector properties are studied using simulations. Dedicated software using Monte Carlo (MC) techniques simulated interactions of the beam particle with the target, propagation of the produced particles through the detector and processes related to detection.

In the analysis presented in this thesis the MC simulation is used:

- to study the detector resolution and detection properties (see Sect. 5.4),
- to identify regions with good geometrical acceptance and high reconstruction efficiency (see Sect. 6.3.3),
- to correct for the detection inefficiencies and other related effects (see Sect. 6.4.3),
- to identify contributions of various charged particles among the measured tracks (see Sects. 6.3.5 and 6.4.2).

The effects not included in the NA61/SHINE simulation yet are:

- the transmission of beam particle through the beam line including possible interactions outside of the target and deviation of the beam direction from the z axis (see Sect. 6.3.4),
- other beam particles arriving during the TPC readout (see Sect. 5.2.2),
- energy loss of the produced particles ($\mathrm{d}E/\mathrm{d}x$) in the TPCs.

The following naming convention is used in this thesis. The particle spectra from the generator, not reconstructed nor propagated through the detector are called *generated*, and labelled with a subscript $_{\mathrm{gen}}$ in formulae. The reconstructed spectra are labelled with a subscript $_{\mathrm{sel}}$, to emphasize that only tracks passing the selection criteria which will be described in Sect. 6.3 are considered. The MC simulated spectra are distinguished from the data spectra by a superscript $^{\mathrm{MC}}$, or a model name in the superscript.

4.2 Simulation of interaction and the detector response

First, an event generator simulates the initial proton-proton interaction. The event generator outputs list of primary produced particles and their momenta. The short-living particles decaying via strong and electromagnetic processes also decay at the generator level and the decay products are considered primary. The events are randomly rotated in the x–y (transverse) plane.

Several MC models were compared with the NA61/SHINE results on p+p, p+C and π+C interactions: FLUKA2008, URQMD1.3.1, VENUS4.12, EPOS1.99, GHEISHA2002, QGSJetII-3 and Sibyll2.1 [54–57]. Based on these comparisons and taking into account continuous support and documentation from the developers the EPOS model [58] was selected for the MC simulation used in this thesis. The VENUS model [59] was also used for supplementary calculations.

Second, the particles are propagated through the detector and the measured signals are simulated. At the beginning of the procedure the interaction point is randomly placed in the target volume, taking into account exponential beam attenuation. Then the particles from the event generator are propagated through the detector using GEANT 3.21 package [60]. The detailed model of the detector contains information about all materials, including the construction elements of detectors and magnets and different gases filling various volumes. Particles decay and interact with the material emitting secondary particles. The detector response is parametrised in order to speed up the calculations, which however is the reason for lack of information on the energy loss ($\mathrm{d}E/\mathrm{d}x$) for tracks simulated in the TPCs. Simulated points are generated along the particle paths and converted into signals in the detectors.

The output is saved in the same format as the real data. Then it is reconstructed with the same algorithms as described in Sect. 3.4.3.

4.3 Matching of the generated particles and reconstructed tracks

In the last stage of the Monte Carlo procedure the reconstructed tracks are assigned with the generated particles. The algorithm matches tracks with particles if the reconstructed points lie in a small distance to the generated points. The procedure succeeds in the p+p events as the track multiplicity is low and they are typically well separated. However, in several percent of the cases more than a single track and particle are matched. The matching algorithms provide information on all matched candidates and allow the person analysing the data select the best candidate.

In this thesis the matching information was used for two purposes:

- Determination of the good acceptance regions. The goal is to determine how the detector registers the tracks generated in the primary interaction.
- Identification of the reconstructed particles. The information is used to remove the electron contribution (see Sect. 6.3.5) and to distinguish various particle types for the h^- correction (see Sect. 6.4.2). As the $\mathrm{d}E/\mathrm{d}x$ information is not available, only matching allows to identify the reconstructed MC tracks. The goal is to determine what is the source of the tracks measured in the detector.

Events containing ambiguous matching cases were identified and examined visually. The major effects and their treatment are described below.

The parameters of the reconstructed track and the generated particle may differ substantially:

- the electric charge sign can be reconstructed incorrectly. This concerns about 1% of all tracks, but this fraction is reduced to 10^{-4}–10^{-3} for the well reconstructed tracks (the selection criteria will be described in Sects. 6.2 and 6.3). It was found that the charge is reconstructed incorrectly mostly for the poorly measured, very short tracks, which are rejected from the analysis anyhow.
- a secondary particle can be assigned to the main vertex. This effect concerns several percent of tracks (see Sect. 6.4.2).

In case of the acceptance study such tracks are rejected, as the experiment fails to reconstruct them properly. For the identification purposes such tracks are accepted, as the same effects occur in reconstruction of real events. The simulated data is used to correct for these effects during the analysis.

It was verified that each reconstructed track passing the selection criteria (see Sect. 6.3) is matched to some generated particle. However, in 4–6% cases a single reconstructed track is matched to several generated particles. The following most common sources of uncertainty were identified:

- A charged particle may produce a δ-electron. Its path is often very short and it is matched to the reconstructed track of the parent particle.
- In case of decays (mostly $\pi^{\pm} \rightarrow \mu^{\pm}\ (+\nu)$), angle between the parent and the child particles might be small and they can be reconstructed together as a single track.

The effect concerns a non-negligible fraction of tracks. In both cases identified above the ambiguity is solved by selecting the generated particle candidate with the highest number of generated points matched to the reconstructed ones.

In 0.1–0.2% cases a single generated particle is matched to several reconstructed tracks. Usually some of these tracks miss points in one of the TPCs. Therefore only tracks passing the selection criteria are considered as valid candidates for the matched track.

Summarising, the matching selection procedure for the acceptance study is the following:

(i) loop over the generated primary particles in the event,
(ii) for each particle get a list of the primary reconstructed candidates for the matched track,
(iii) reject the reconstructed candidates that do not pass the track cuts (excluding the acceptance cut),
(iv) out of the remaining candidates select the one with the best ratio of the number of matched points to the number of reconstructed points,
(v) reject tracks with charge reconstructed incorrectly.

Matching selection procedure used to identify the reconstructed tracks is the following:

(i) loop over the reconstructed primary tracks in the event,
(ii) for each track get a list of all generated candidates for the matched track (including the secondary particles),
(iii) select the candidate with the highest number of matched points.

The procedures described above attempt to mimic the particle detection in the real data. The δ-electrons leaving very short tracks are ignored. In case of decays the particle contributing to the largest track piece in the detector is used to identify it. A similar behaviour is expected in identification of the real data by the $\mathrm{d}E/\mathrm{d}x$

measurement. If a single generated particle yields several tracks reconstructed in the TPCs, all these tracks are matched to the same parent particle.

Given only several percent of tracks and particles is matched ambiguously, and majority of such cases was identified and treated correctly, as described in this section, matching has a negligible impact on the uncertainty of results of the data analysis.

4.4 Data-based adjustments of the simulated spectra

The h^- method of deriving the π^- spectra bases on the fact that majority of the produced negatively charged hadrons (h^-) are pions. Small contribution of other particles is corrected using Monte Carlo. These are mostly the primary negatively charged hadrons: K^- and $\overline{p}$, and the secondary π^- incorrectly reconstructed as primary, originating mostly from weak decays of K^0_S and Λ (marked as $\pi^-_{K^0_S}$ and π^-_{Λ}, respectively) and from secondary interactions. As the h^- correction is small (typically below 20%, see Sect. 6.4.5), the method is weakly sensitive to potential biases of the simulated spectra. Still, an effort was made to improve precision of the MC spectra basing on the preliminary NA61/SHINE results [61, 62] and sparse data available from other experiments [63, 64]. Large part of the analysis comes from MSc thesis of A. Ilnicka [57]. This section only summarises this work and provides details on extensions with respect to that work.

Spectra of the π^-, K^-, $\overline{p}$, K^0_S and Λ particles from VENUS and EPOS models were compared with the experimental data. The first observation was that the total multiplicities simulated by EPOS agree better with the data. Hence the EPOS model was selected to calculate the final results.

Then the adjustment factors $a[x]$ were derived for the primary charged particles, and for π^- from decays. Here x stands for the particle type: π^-, K^-, $\overline{p}$, $\pi^-_{K^0_S}$ and π^-_{Λ}. Depending on quality of the available reference data, the adjustment factor was assumed to be constant, or it was parametrised as a function of y and p_T or m_T. The adjustment factors were used to calculate the best estimate of the spectrum of reconstructed tracks $\mathsf{n}[x]^{MC}_{sel}$:

$$\mathsf{n}[x]^{MC}_{sel} = a[x] \cdot \mathsf{n}[x]^{uMC}_{sel} \,, \tag{4.1}$$

where $\mathsf{n}[x]^{uMC}_{sel}$ is the unadjusted reconstructed MC spectrum. Spectrum of particle x is defined as

$$\mathsf{n}[x] = \frac{t[x]}{N \cdot \Delta} \,, \tag{4.2}$$

where $t[x]$ is number of particles in given (y, p_T) or (y, m_T) bin, Δ is size of the bin and N is number of events. The binning schemes will be described in Sect. 6.1.

The adjustment factors were derived independently for each particle type, for both MC models and for five beam momenta:

- π^-: The datasets used were the preliminary NA61/SHINE (y, p_T) and (y, m_T) spectra $\mathsf{n}[\pi^-]^{NA61}$ [61], and compilation of measurements of the total multiplicities $\langle \mathsf{n}[\pi^-]^{ref} \rangle$, mostly from bubble chamber experiments [63]. In order to minimise potential normalisation bias, the preliminary NA61/SHINE spectra were scaled so that the total π^- multiplicity agreed with the bubble chamber

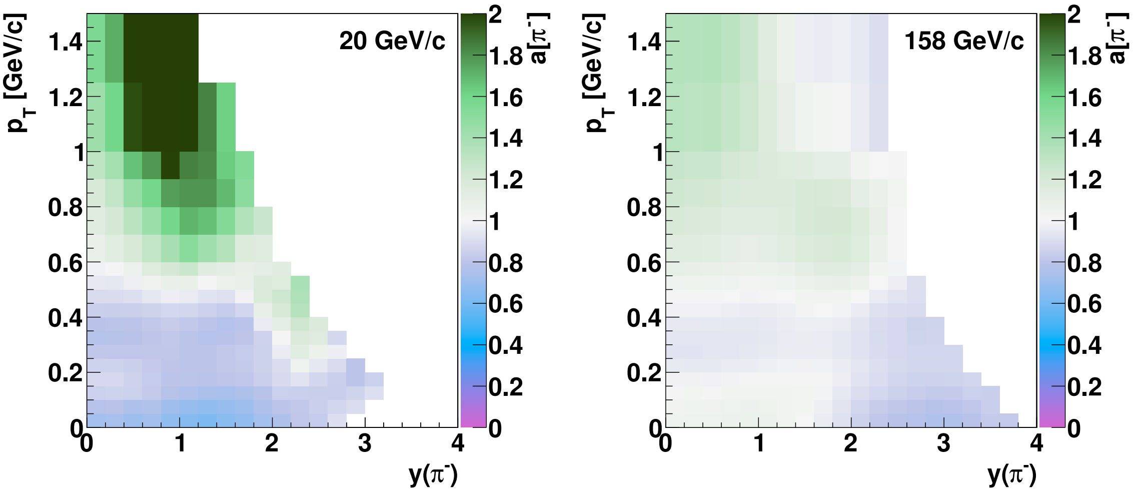

Figure 4.1: Bin-by-bin adjustment factors for π^- generated by the EPOS model at 20 (*left*) and 158 GeV/*c* (*right*).

reference. The adjustment factor was calculated in (y, p_T) and (y, m_T) bins independently:

$$a[x=\pi^-](y,\ p_\mathrm{T}/m_\mathrm{T}) = \frac{\mathsf{n}[x]^{\mathrm{NA61}}(y,\ p_\mathrm{T}/m_\mathrm{T})}{\mathsf{n}[x]^{\mathrm{uMC}}_{\mathrm{gen}}(y,\ p_\mathrm{T}/m_\mathrm{T})} \cdot \frac{\langle \mathsf{n}[x]^{\mathrm{ref}} \rangle}{\langle \mathsf{n}[x]^{\mathrm{NA61}} \rangle}\,, \tag{4.3}$$

where $\mathsf{n}[x]^{\mathrm{uMC}}_{\mathrm{gen}}$ is the generated unadjusted MC spectrum.
In order to reduce impact of the statistical fluctuations, the adjustment factor was smoothed in the adjacent y and p_T or m_T bins. Also, as the preliminary NA61/SHINE results were derived in slightly reduced acceptance, in the regions without experimental data the adjustment factors were copied from the adjacent bins. This concerns only several bins at the edge of the phase-space. The final bin-by-bin adjustment factors are shown in Fig. 4.1. The adjustment at 158 GeV/*c* ranges from −20% at low p_T and high y to +35% at high p_T; at 20 GeV/*c* the adjustment reaches −35% at low p_T and +100% at high p_T.

- K^- and $\overline{\mathrm{p}}$: The data used were the preliminary NA61/SHINE (y, p_T) spectra at 40, 80 and 158 GeV/*c* [62] and the total multiplicities [64]. In the first stage the adjustment factor was derived at 158 GeV/*c*, where the data covered the largest fraction of the phase-space. The ratio of the data to the MC spectrum

$$r[x=\mathrm{K}^-,\overline{\mathrm{p}}](y,\ p_\mathrm{T}) = \frac{\mathsf{n}[x]^{\mathrm{NA61}}(y_x,\ p_\mathrm{T})}{\mathsf{n}[x]^{\mathrm{uMC}}_{\mathrm{gen}}(y_x,\ p_\mathrm{T})} \tag{4.4}$$

was parametrised with a bilinear function:

$$a[x=\mathrm{K}^-,\overline{\mathrm{p}}]_{158\ \mathrm{GeV}/c}(y,\ p_\mathrm{T}) = A_x y_x + B_x p_\mathrm{T} + C_x\,, \tag{4.5}$$

where y_x is rapidity calculated using true mass of particle x, and the parameters A_x, B_x and C_x were fitted. The fitted values are listed in Table 4.1. Figure 4.2 shows the bin-by-bin adjustment factors at 158 GeV/*c*.
Data abundance at the lower beam momenta was smaller than for 158 GeV/*c*. It was concluded that the models agree with the data better at the lower beam

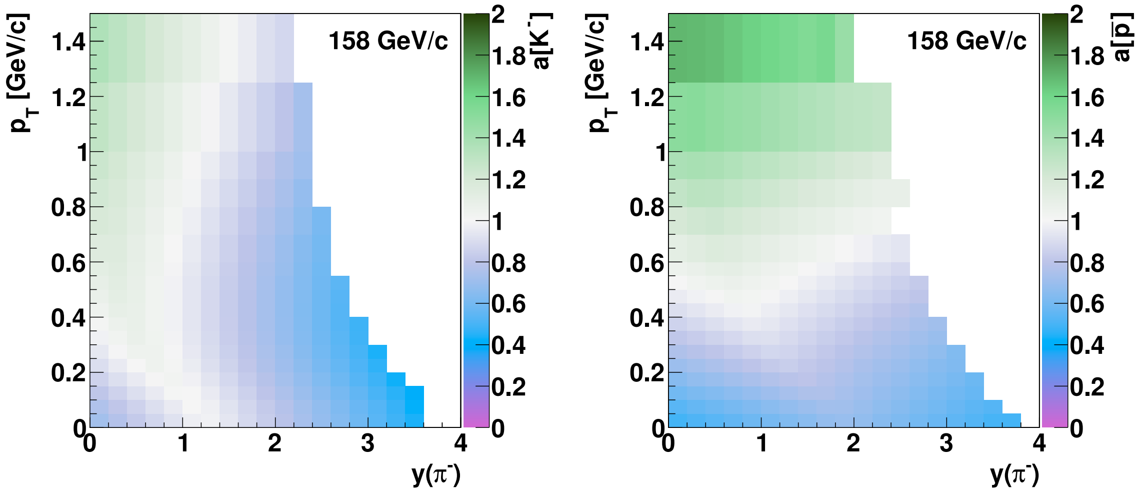

Figure 4.2: Bin-by-bin adjustment factors for K^- (*left*) and $\bar{p}$ (*right*) generated by the EPOS model at 158 GeV/c.

parameter	$x = K^-$	$x = \bar{p}$
A_x	−0.252	−0.124
B_x	0.281	0.766
C_x	0.995	0.675

Table 4.1: The adjustment parameters (see Eq. (4.5)) for the K^- and $\bar{p}$ particles generated in the EPOS model [57].

momenta based on comparison of the total multiplicities. The ratios of the experimental and the MC spectra at 40 and 80 GeV/c were fitted with a modified function (4.5):

$$a[x = K^-, \bar{p}](y,\ p_T) = 1 + D_x \cdot (A_x y_x + B_x p_T + C_x - 1)\,, \tag{4.6}$$

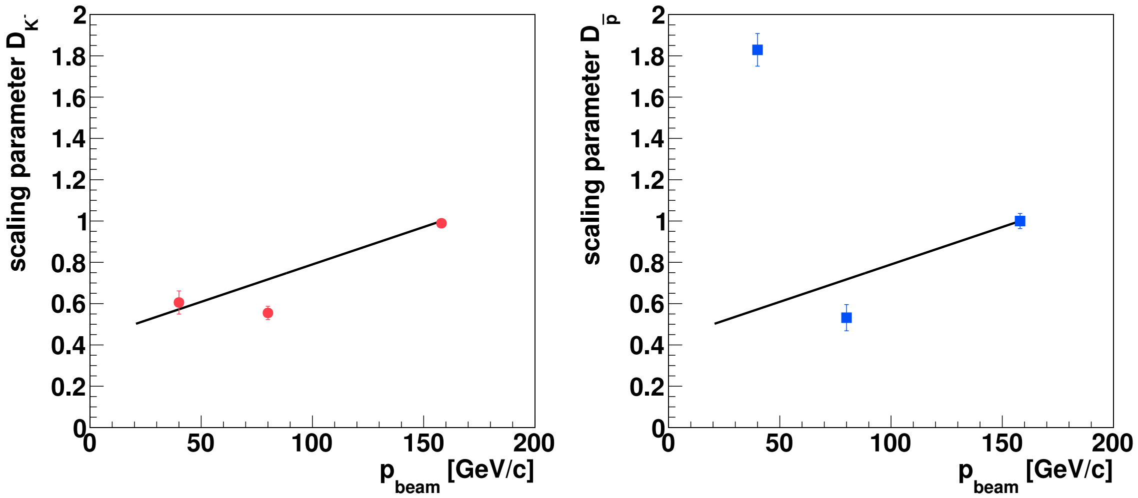

Figure 4.3: The scaling parameter D_x for $x = K^-$ (*left*) and $\bar{p}$ (*right*). The points show the fitted values as defined in Eq. (4.6), and the line shows the chosen parametrisation Eq. (4.7).

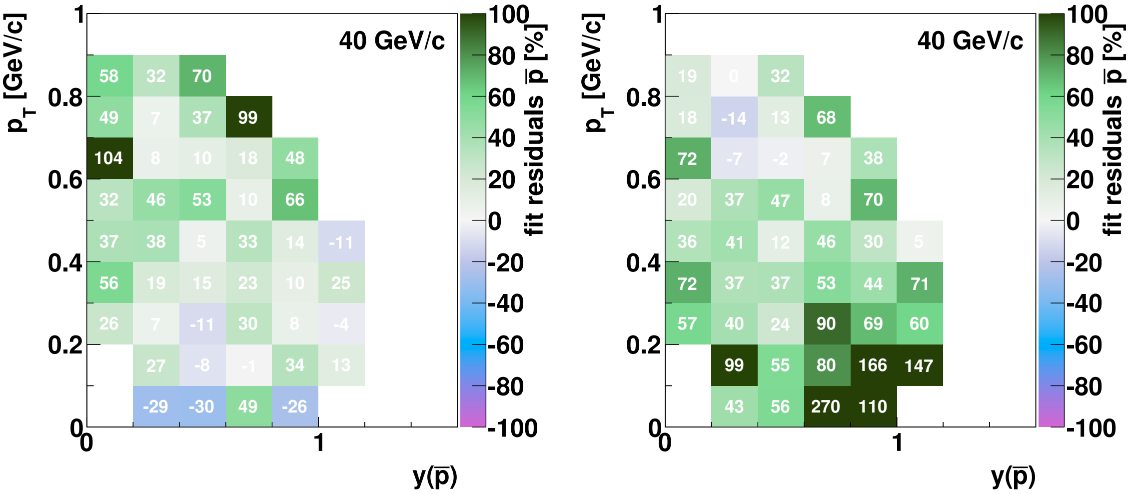

Figure 4.4: Residuals of the function $a[\overline{\mathrm{p}}]$ (Eq. (4.6)) and the data ratio $r[\overline{\mathrm{p}}]$ (Eq. (4.4)) using the best fit of the $D_{\overline{\mathrm{p}}}$ parameter (*left*, see Fig. 4.3), and $D_{\overline{\mathrm{p}}}$ calculated from Eq. (4.7) (*right*) at 40 GeV/c. The plotted residuals are defined as residuals $= (a[\overline{\mathrm{p}}]/r[\overline{\mathrm{p}}] - 1) \cdot 100\%$.

p_{beam} [GeV/c]	a[$\pi^-_{\mathrm{K}^0_\mathrm{S}}$]	a[π^-_Λ]
20	0.815	0.656
31	0.737	0.766
40	0.740	0.808
80	0.841	1.009
158	0.874	0.948

Table 4.2: The adjustment parameters for the secondary π^- from decays of K^0_S and Λ generated in the EPOS model [57].

where the parameters A_x, B_x and C_x were taken from the previous fit, and only D_x was fitted. It was verified that the fitted function describes the spectra well.

The fitted values of D_x are shown in Fig. 4.3. As only three data points were available it was decided to parametrise D_{K^-} and $D_{\overline{\mathrm{p}}}$ linearly with the beam momentum p_{beam}, so that it equals 0.5 at 20 GeV/c and 1 at 158 GeV/c:

$$D_x(p_{\mathrm{beam}}) = 0.5 + 0.5 \cdot \frac{p_{\mathrm{beam}} - 20\ \mathrm{GeV}/c}{158\ \mathrm{GeV}/c - 20\ \mathrm{GeV}/c} \,. \tag{4.7}$$

A single point for $\overline{\mathrm{p}}$ at 40 GeV/c does not support this choice. Figure 4.4 shows the fit residuals for $\overline{\mathrm{p}}$ at 40 GeV/c using the fitted and parametrised value of $D_{\overline{\mathrm{p}}}$. The overall agreement is better for fitted $D_{\overline{\mathrm{p}}}$ (*left*), however the parametrisation (*right*) provides better description of the high p_T region. As it will be shown in Sect. 6.4.2 the contribution of $\overline{\mathrm{p}}$ is the most significant in this region, thus the selected parametrisation of $D_{\overline{\mathrm{p}}}$ helps to reduce the systematic uncertainty of the final results introduced by MC. Also, the largest residuals occur in the bins with large statistical uncertainties, and thus they do not indicate firm problems with the parametrisation.

The final adjustment ranges from −30% at low p_T up to +30% at high p_T at 158 GeV/c. At the lower beam momenta it is scaled down by the D parameter.

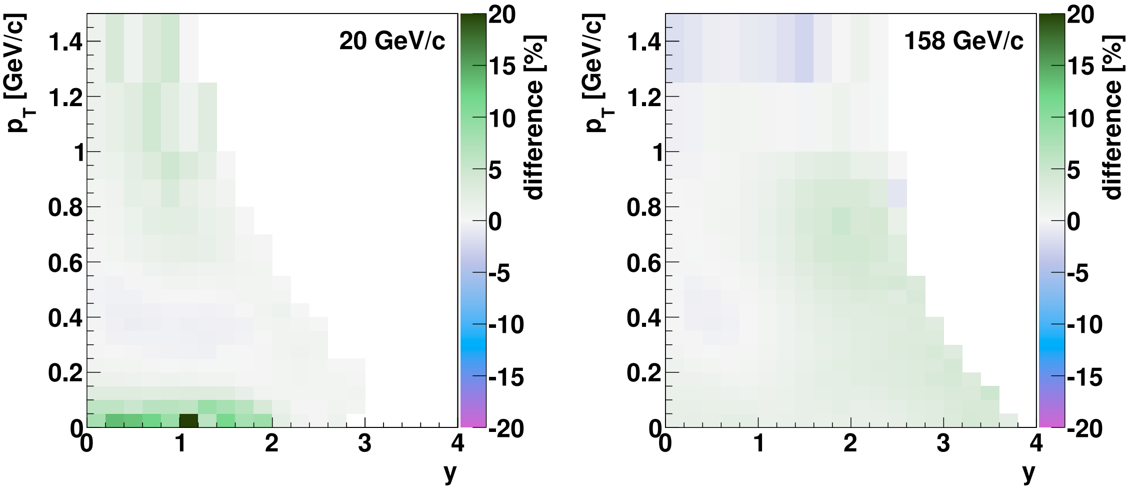

Figure 4.5: Impact of the adjustment on the final π^- spectra, defined as difference = $(\mathsf{n}[\pi^-]/\mathsf{n}[\pi^-]^{\mathrm{uMC}} - 1) \cdot 100\%$, for 20 (*left*) and 158 GeV/*c* (*right*).

- $\pi^-_{\mathrm{K^0_S}}$ and π^-_{Λ} (π^- from $\mathrm{K^0_S}$ and Λ decays): The data used were the total multiplicities of $\mathrm{K^0_S}$ and Λ [64]. The constant adjustment factors were derived at each beam momentum:

$$a[x = \pi^-_{\mathrm{K^0_S}}, \pi^-_{\Lambda}] = \frac{\langle \mathsf{n}[x]_{\mathrm{ref}} \rangle}{\langle \mathsf{n}[x]^{\mathrm{uMC}}_{\mathrm{gen}} \rangle} \,. \tag{4.8}$$

  The values are listed in Table 4.2. The adjustment for $\pi^-_{\mathrm{K^0_S}}$ equals about −20% and it is almost constant. The adjustment for π^-_{Λ} is only −5% at the high beam momenta, but reaches −35% at 20 GeV/*c*.

Figure 4.5 shows how much the final π^- spectra (obtained using procedures described in Chapter 6) change after applying the MC spectra adjustments. The impact of the adjustments on the final spectra ranges from −2% to +5% in most regions, except of a single bin at the low p_{T} region at 20 GeV/*c*, where it reaches +20%.

Validity of the adjustment procedure was verified by comparing different methods of calculating the h^- correction: by subtracting the non-primary-pion contribution, and by multiplying the h^- spectrum by a correction factor. Also results obtained using VENUS and EPOS corrections were compared. Without the adjustments the differences of tens of percent were present at the low beam momenta in the p_{T} region (where contribution of the secondary particles dominates). Also differences above 10% were present in the high p_{T} region (populated by K^- and Λ). The differences between the results obtained using the adjusted MC spectra were much smaller, and below 10% in almost all regions.

4.5 Simulated and measured characteristics

Monte Carlo simulation was validated in several tests. The simulated distributions of selected parameters were compared with the experimental ones. It is expected that if the simulation is accurate, these distribution should be equal.

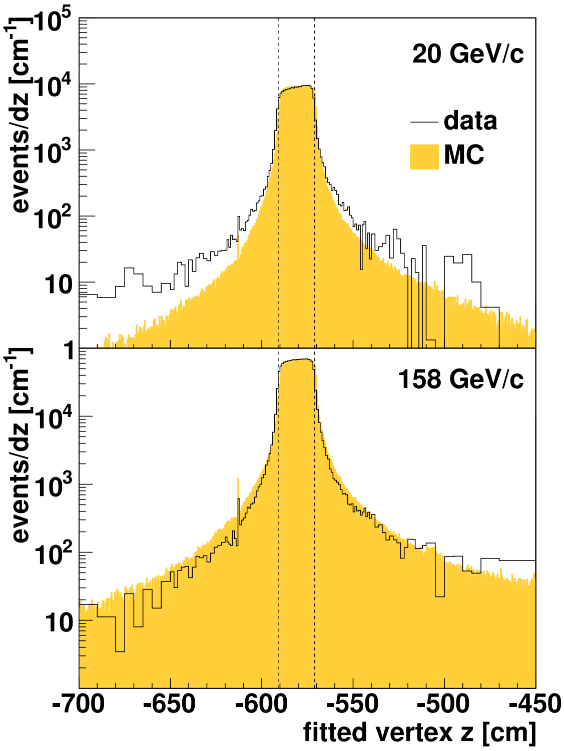

Figure 4.6: Distribution of fitted vertex z coordinate for p+p interactions at 20 (*top*) and 158 GeV/c (*bottom*) in the target vicinity ($-591 < z_{\text{target}} < -571$ cm, marked with vertical dashed lines). The solid line shows the distribution of interactions with the hydrogen target in the data. The filled area shows the distribution for the reconstructed Monte Carlo simulation. This distribution was normalised to the total integral of the data plot.

Figure 4.6 shows distribution of the fitted z coordinate of vertices originating from the beam interactions with target for data and MC. The simulation describes the peak region well. The tails of the distribution (present due to limited reconstruction resolution) differ, which is caused by imperfect simulation of the detector response. The differences are very small in comparison to the total statistics.

Figure 4.7 shows distribution of the impact parameter, as defined in Sect. 3.4.3. Small differences between the data and MC reveal limited accuracy of the detector simulation. The largest discrepancy visible for b_y at 20 GeV/c originates from interactions of beam particles close in time to the trigger particle (see Sect. 5.2.2), not simulated in MC. When much stricter rejection of events with such off-time beam particles is applied, the difference decreases by factor of several.

Figure 4.8 shows distribution of number of points allocated to a track. Maxima visible in the distribution correspond to tracks measured in two sectors of VTPC-1 (48 points), whole VTPC-1 (72 points), VTPC-2 and a MTPC (162 points) and both VTPCs and a MTPC (234 points). The maxima in the data distributions are less sharp and slightly shifted towards lower values. This suggests that the point reconstruction efficiency is somewhat overestimated in simulation.

The differences between data and simulation visible in Figs. 4.6–4.8 occur mostly at the tails of the distributions. Their overall contribution to the total statistics is small. Systematic bias due to limited precision of the simulation was estimated by varying the selection cuts and was found to be below 2% (see Sect. 6.5.2). It was always significantly smaller than the other sources of the systematic uncertainties.

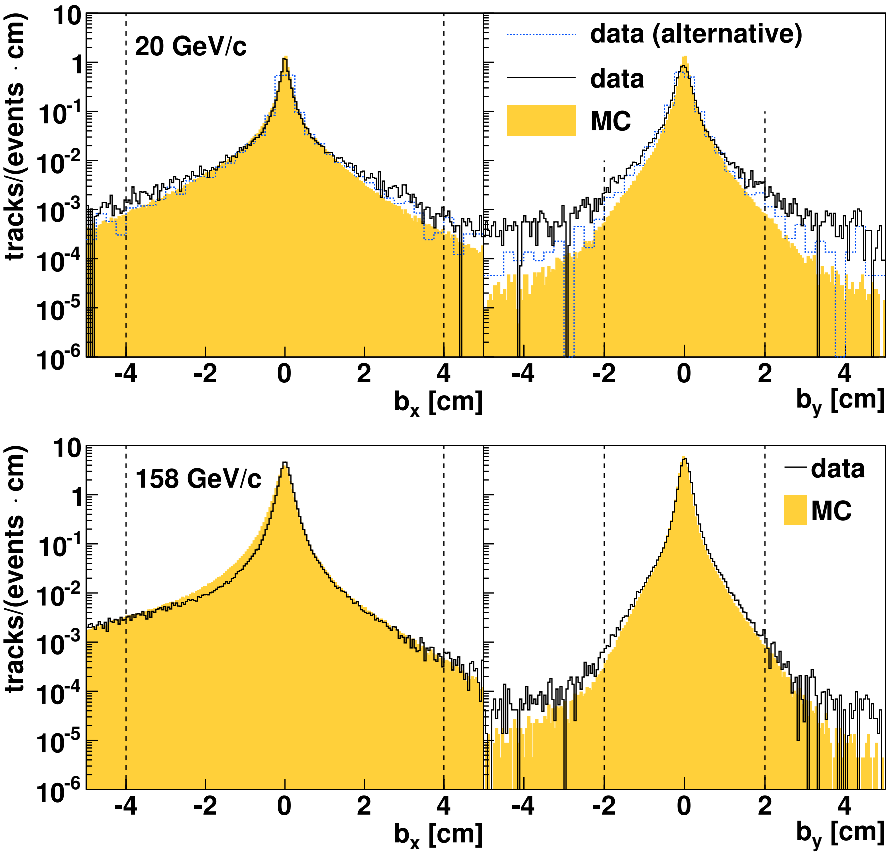

Figure 4.7: Distribution of the track impact parameter (see Sect. 3.4.3) in the x (*left*) and y (*right*) coordinate for p+p interactions at 20 (*top*) and 158 GeV/c (*bottom*). The black line shows the measured interactions with the hydrogen target. The filled area shows the reconstructed Monte Carlo simulation. The dashed vertical lines show the accepted range (see Sect. 6.3). The dotted blue line in the 20 GeV/c plots show the distribution obtained for events with no off-time beam particles within the time window of ±6 μs with respect to the trigger particle time.

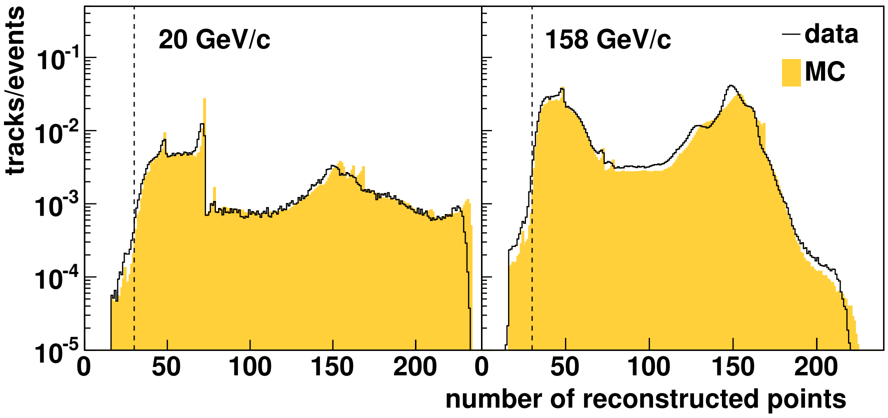

Figure 4.8: Distribution of the number of points allocated to a track at 20 (*left*) and 158 GeV/c (*right*). The black line shows the measured interactions with the hydrogen target. The filled area shows the reconstructed Monte Carlo simulation. The dashed vertical line shows the track selection threshold (see Sect. 6.3).

Chapter 5

Characteristics of the dataset

5.1 Data acquired and used in the analysis

The data on proton-proton interactions were collected at five momenta of the beam particles: p_{beam} = 20, 31, 40, 80 and 158 GeV/c with the NA61/SHINE detector in 2009. The data taking periods and numbers of events collected are listed in Table 5.1. About one week was devoted for each beam momentum. The data collection rate was lower at the lowest beam momenta due to the secondary beam properties (see Sect. 5.2). As a result the statistics available at 20 GeV/c is 2–3 times smaller than at the other beam momenta.

The analysis was based on the 12D002 (40 GeV/c) and 12E002 (other reactions) reconstructions. These two reconstructions are related to different software versions used for processing. The differences are irrelevant for the analysis presented in this thesis.

The data was collected within so-called *runs*. A run lasts from several minutes (if the data acquisition system stops unexpectedly, typically due to minor hardware or software faults) to several hours (optimally no more than two) and contains up to 100 k events.

An event corresponds to information read from all detectors synchronised by the trigger signal. Simultaneously with the interaction trigger (see Eq. (2.2)) 10–20% of events with the unbiased beam trigger (see Eq. (2.1)) were taken for test purposes. The runs were taken with target inserted and removed alternately, the latter contributing by 5–10% to the total statistics.

Table 5.1: Information about the data collection times at each beam momentum and the total number of all triggers and target inserted and removed together. The numbers of triggers are given before and after verification described in this section.

p_{beam} [GeV/c]	data taking period	first run	last run	statistics all	statistics verified
20	2009.09.21–2009.09.28	9265	9389	2.15 M	1.45 M
31	2009.09.05–2009.09.14	8947	9135	3.55 M	3.49 M
40	2009.10.12–2009.10.22	9451	9702	5.84 M	5.79 M
80	2009.11.09–2009.11.16	9996	10148	4.99 M	4.34 M
158	2009.11.05–2009.11.09	9910	9989	3.98 M	3.98 M

p_{beam} [GeV/c]	particles per spill	p fraction
20	1000 k	12%
30	1000 k	14%
40	1200 k	14%
80	460 k	28%
158	250 k	58%

Table 5.2: Basic beam properties. The first column gives the beam momentum. The second and third columns list typical numbers of beam particles per spill (~10 s) and fraction of protons in the beam, respectively.

The data collected was verified in various ways in order to reject runs of bad or uncertain quality. First, runs marked in the logbook as faulty were rejected. Second, it was verified if the fraction of events accepted by the event selection criteria used in the analysis (see Sect. 6.2) is consistent. For example, when the target is removed the interaction probability is lower, and thus the fraction of events with the interaction trigger is lower. Comparison of this fraction between all runs allowed to identify several runs incorrectly marked as inserted or removed (human mistake) and to assign them to correct sets. Similarly it was found that in runs 10022–10039 the beam track was not properly measured in BPDs in large fraction of events; these runs were rejected. Runs 9373–9382 were rejected as it was found the VTPC-2 sector 6 was inactive in this period.

The raw data before processing was stored in so-called *chunks* – files of about 1 GB, and containing several hundred events. Each event was reconstructed individually (see Sect. 3.4.3). The results were saved in format of DSPACK, a data handling software package [65]. The reconstructed data in DSPACK contain detailed event and track properties, in particular parameters of all points in the TPCs. A DSPACK chunk occupies typically 200 MB. For convenience selected data were then copied into files in format of ROOT61 [66], which is a set of data storage and analysis classes written for NA61/SHINE within the the ROOT framework [67]. Data in the ROOT61 format contains only the general event and track properties sufficient for most physics analyses, such as particle momentum at the interaction vertex and total numbers of points in each detector. A ROOT61 chunk occupies about 2 MB. Finally only the event and track properties necessary for the analysis performed in this thesis were extracted and saved in the ROOT format, resulting in further size reduction by factor of over 10. The whole dataset occupied several hundred MB for each beam momentum. The corresponding MC data, containing also information about the generated and matched particles occupied about 2 GB for each beam momentum.

5.2 Beam characteristics

5.2.1 General properties

The basic beam properties are listed in Table 5.2. The beam momentum is known with 0.5% precision. This was verified by measuring the momentum of the 31 GeV/c beam deflected into the TPCs using the maximum magnetic field [54].

The secondary proton beam was produced in interactions of 400 GeV/c protons from SPS with a beryllium target. With decreasing momentum of the secondary beam contamination of π^+ and K^+ increased. The beam particle content measured

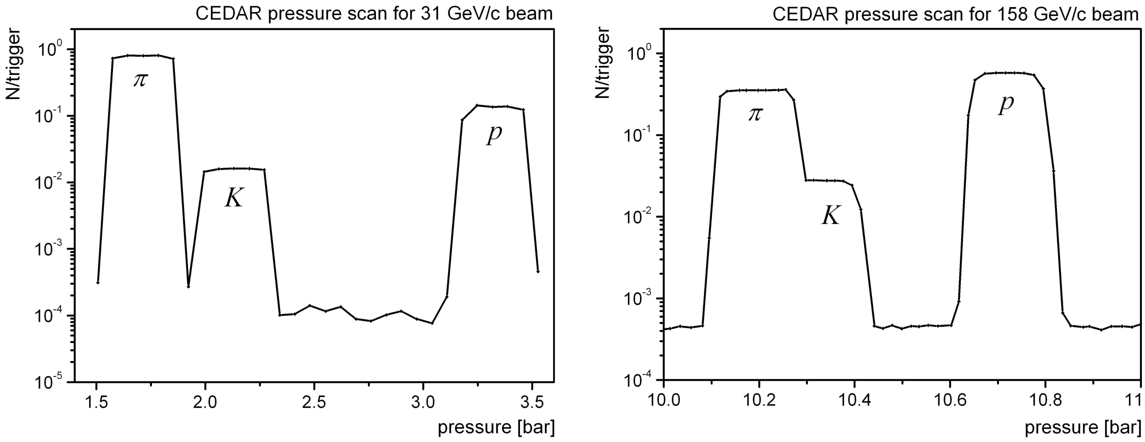

Figure 5.1: Fraction of hadrons of various species per incident beam particle from the CEDAR counter as a function of the gas pressure within the pressure range which covers maxima of π^+, K^+ and p at 31 (*left*) and 158 GeV/c (*right*). Figures taken from Ref. [32].

with CEDAR is shown in Fig. 5.1. In order to retain sufficient proton rate the low momenta beam intensities were increased by opening the collimators. As a result the beam width and divergence increased, leading to higher fraction of events rejected in the analysis. Also as the total beam intensity increased, more so-called *off-time* beam particles were arriving within the ±25 μs signal collection period of the TPCs. Some (about 2%) of these particles interacted and generated TPC tracks mistakenly fitted to the main vertex.

5.2.2 Off-time beam particles

Information of charged beam particles registered in the S1 counter within ±25 μs with respect to the trigger particle is saved in the event. The particle arrival times are measured with precision of 0.1 μs, with 0.2 μs two-particle resolution. The time distribution of the beam particles is shown in Fig. 5.2. Besides the trigger particle, large number of the off-time particles is present, in particular at the lowest beam momentum. Ratio of numbers of the on-time to off-time particles decreases by factor of 4 from 158 to 20 GeV/c.

Figure 5.3 shows the average number of the off-time beam particles per event. At 20–40 GeV/c there is in average one off-time beam particle in the ±5 μs range. As it will be shown the off-time beam particles within this range affect the results.

Due to electron drift in the TPCs tracks from the off-time interactions are vertically shifted with respect to the tracks originating from interaction of the trigger particle. This allows to distinguish them, however some them can be incorrectly fitted to the main vertex. This happens most often for the electrons, as they originate mostly from the secondary vertices. The largest effect is visible at the low azimuthal angles θ and particle momenta of several GeV/c.

Figure 5.4 shows the dE/dx distributions selected with two different off-time particle rejection criteria. When the off-time particles are rejected more strictly (*right* panel, with respect to the *left* one) the electron yield decreases, while yield of the negatively charged hadrons (h^-) remains constant. Figure 5.5 (*left*) shows the electron yield dependence on the off-time beam particles rejection range. At 20–

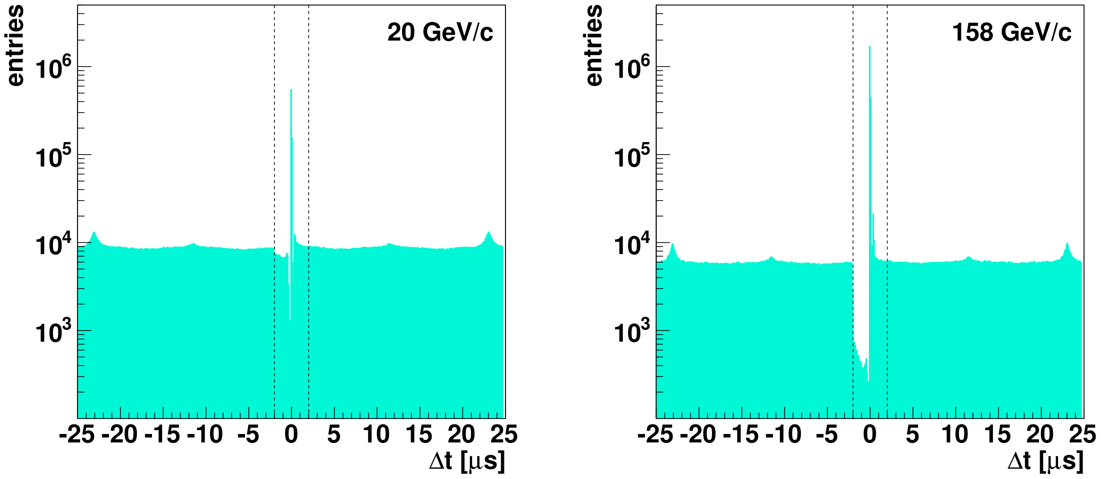

Figure 5.2: Time distribution of the beam particles measured in the S1 counter with respect to the trigger particle for 20 (*left*) and 158 GeV/*c* (*right*). The peak at $\Delta t = 0$ corresponds to the trigger particle. The rest of the distribution corresponds to the off-time beam particles. The minimum at $-2 < \Delta t < 0$ μs is a result of the hardware mechanism disabling the trigger for 2 μs after each non-interacting beam particle. The other small maxima (e.g. at $\Delta t = \pm 23$ μs) are related to the beam time structure in the SPS. The dashed vertical lines show the off-time particle cut window (see Sect. 6.2).

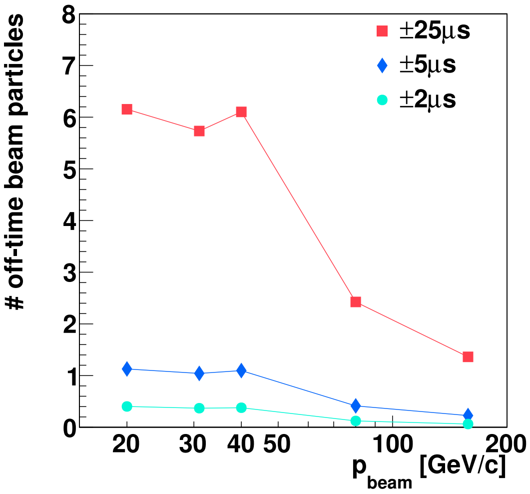

Figure 5.3: The average number of the off-time beam particles per event within ±2, ±5 and ±25 μs around the trigger particle, at five beam momenta.

40 GeV/*c* there is a systematic effect visible up to 5 μs, no effect at 80 and 158 GeV/*c*. This shows that the electron tracks are fitted more poorly and electrons originating from the off-time interactions are more likely to be fitted to the main vertex.

Rejecting all events with off-time beam particles within ±5 μs would imply discarding significant fraction of the statistics at the low beam momenta, as demonstrated in Fig. 5.5 (*right*). Instead, only events with off-time beam particles within ±2 μs window are rejected, which corresponds to ±2.8 cm vertical shift of the VTPC tracks. Hadrons originating from the accepted off-time interaction are rejected by the ±2 cm impact parameter cut. Electrons are rejected using dE/dx measurement (see Sect. 6.3.5).

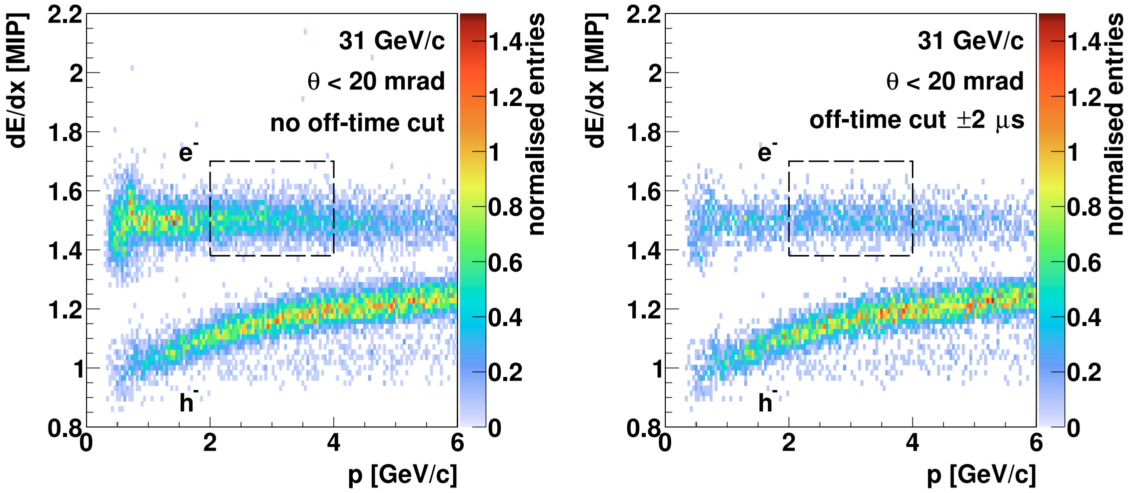

Figure 5.4: The dE/dx distribution of the negatively charged tracks selected with the event and track selection criteria described in Sects. 6.2 and 6.3, measured at 31 GeV/c. The tracks were selected in the azimuthal angle range $\theta = \arcsin(p_T/p) < 20$ mrad. No off-time particle rejection was used for the *left* panel, while only events with no off-time beam particles within ±2 μs are accepted in the *right* panel. The number of entries was divided by the number of events and by the p, dE/dx and θ bin size. The upper band on the plot corresponds to electrons, and the lower band to negatively charged hadrons (h^-), mostly π^-. The dashed rectangle shows the selection range used to count electrons in Fig. 5.5 (*left*).

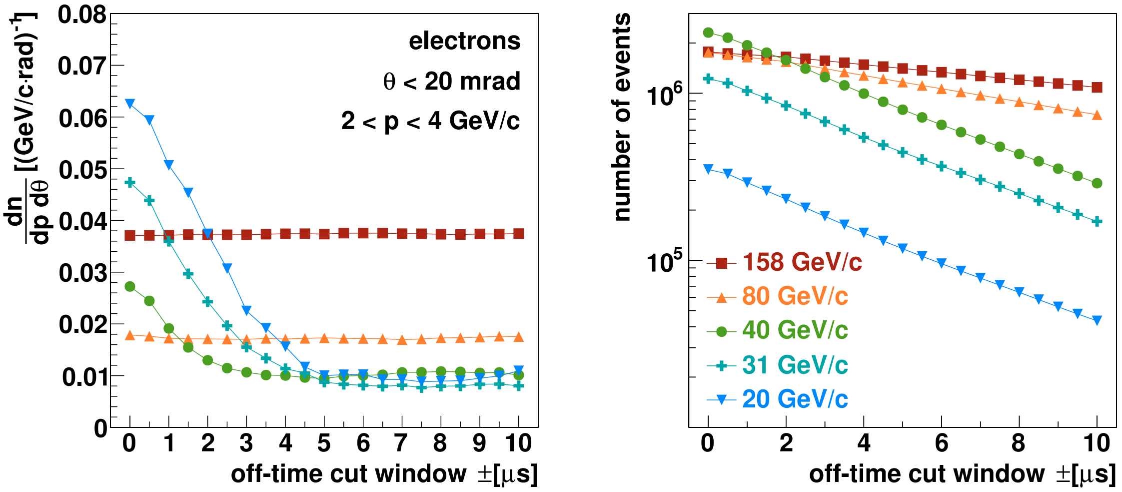

Figure 5.5: *Left:* The electron yield for $\theta < 20$ mrad and $2 < p < 4$ GeV/c at five beam momenta, for events selected with no off-time beam particle closer to the trigger particle than the time given on abscissa (0 μs corresponds to no event rejection). Electrons were identified using dE/dx measurement, as shown in Fig. 5.4. *Right:* Number of events as a function of the off-time beam particles rejection range.

Requirement of good quality of signal measured in the BPDs provide additional rejection of events with an off-time particle arriving within ±100 ns. As the BPD integration time equals approximately 300 ns, two particles would induce a double peak signal which cannot be reconstructed properly.

Any remaining effects related to the off-time beam particles are included in the systematic uncertainty (see Sect. 6.5.2).

5.2.3 Beam profile and divergence

The beam profiles measured in BPD-3 are shown in Fig. 5.6 (*top*). The beam width is much wider at the lowest momentum. The shape of the V1 counter is clearly visible, suggesting that the actual beam width is even larger than the accepted beam fraction.

Figure 5.6 (*bottom*) shows distribution of the beam angle with respect to the nominal beam axis measured in BPDs. The beam divergence is narrower at the high momenta. However, as it will be shown in Sect. 6.3.4 the particle momenta are more affected by the beam angle variation at the high beam momenta, as the effect concerns only the high momentum produced particles.

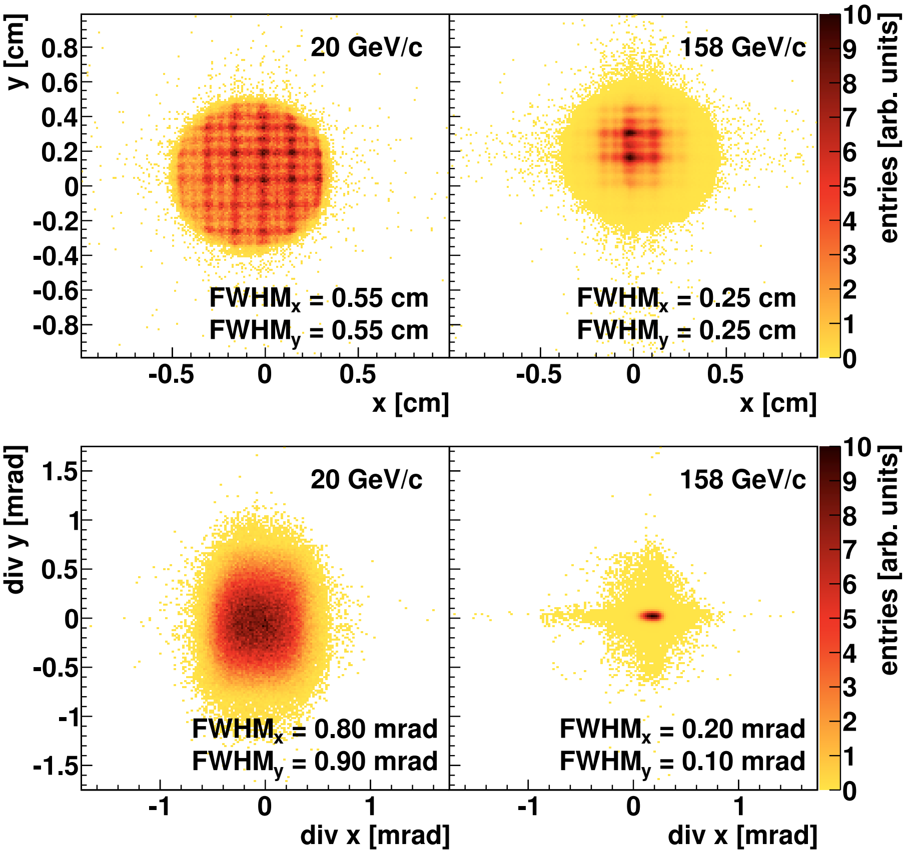

Figure 5.6: *Top:* The beam spot as measured by BPD-3 for 20 (*left*) and 158 GeV/c (*right*) beam momenta. The circular outline of the distribution corresponds to shape of the hole in the V1 counter. *Bottom:* The beam divergence in x and y for 20 (*left*) and 158 GeV/c (*right*) beam momenta. All distributions were arbitrarily scaled to the full colour scale. Widths of the distributions are given in the legend.

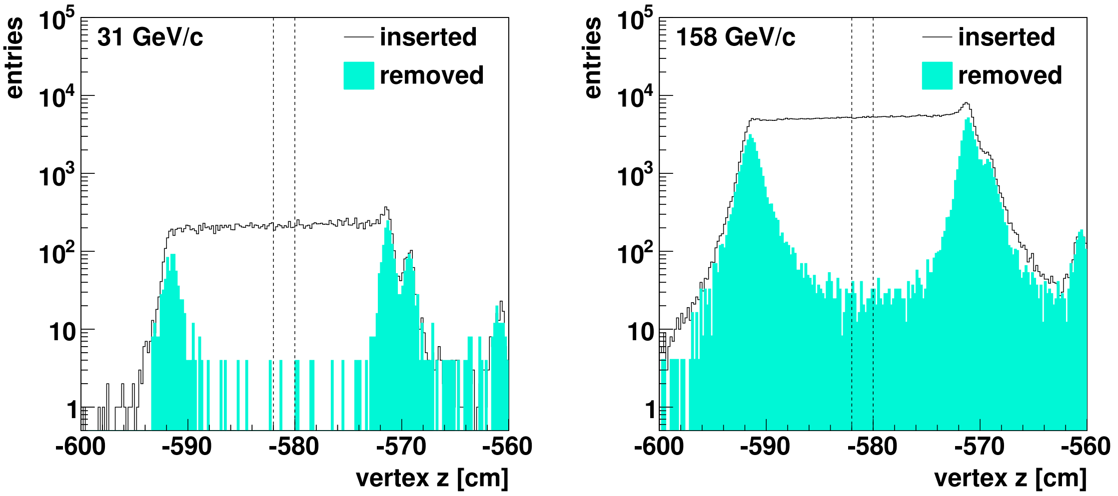

Figure 5.7: Distributions of the fitted vertex z coordinate for the target inserted and removed in events taken with an unbiased beam trigger at 31 GeV/c (*left*) and 158 GeV/c (*right*). For the best resolution, only events with at least 7 tracks were selected. The target removed distribution was normalised to the vertex distribution far away from the target cell, as described in Sect. 6.4.1. The vertical dashed lines show the z range used to calculate the interaction rates shown in Fig. 5.8.

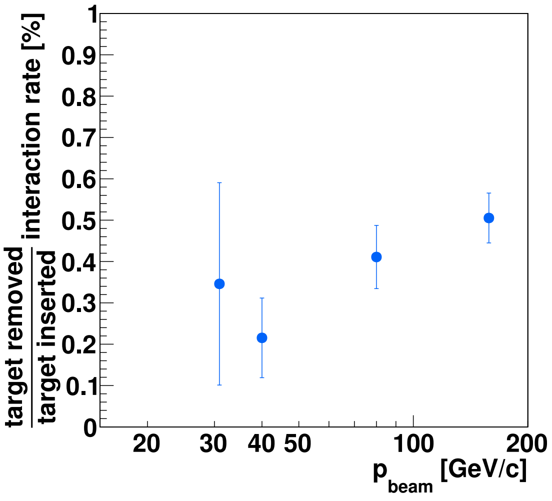

Figure 5.8: Ratio of interaction rates with hydrogen in the target cell in target removed (gaseous hydrogen residue) and inserted. It is calculated as a ratio of the number of entries with the vertex fitted within ±1 cm around the target centre ($z = -581$ cm) for target removed normalised, and target inserted, as shown in Fig. 5.7. Events with at least 7 tracks were selected. The analysis was not performed for 20 GeV/c due to insufficient data statistics.

5.3 Target density

An analysis described in Ref. [68] showed discrepancy of up to 7% at 80 GeV/c between the p+p interaction cross-section measured by NA61/SHINE and the literature values. A possible explanation was variation of the target density ratio between target inserted and removed, possibly due to boiling of the liquid hydrogen. Uncertainty of knowledge of this ratio affects the cross-section uncertainty proportionally.

The density ratio of the target removed and inserted was calculated from the relative interaction rates in the unbiased beam trigger data (see Eq. (2.1)). Figure 5.7 shows the fitted vertex z distributions for target removed and inserted. Only the high multiplicity events were selected to ensure good fit resolution. The maxima at $z = -591$ cm and $z = -571$ cm in the target removed distributions correspond to interactions with the target cell windows. Entries between the maxima correspond to interactions with the gaseous hydrogen residue. The numbers of events in this region for target removed (normalised) and inserted were divided to calculate the relative interaction rate with gaseous hydrogen, shown in Fig. 5.8 for various beam momenta. The ratio varies from 0.2% to 0.5%, which corresponds to about ±50% relative variation. This result agrees with the hypothesis that the difficulties to calculate the cross-section are related to variable target removed to inserted density ratio in various datasets. The other likely explanations of these difficulties were ruled out [68].

The ±50% uncertainty or variability of the target density significantly limits precision of determination of inelastic cross-section. The pion spectra presented in this thesis are determined from particle yields per selected event and thus they are independent of the target density.

5.4 Reconstruction efficiency and resolution

Properties of reconstruction were studied using MC. The simulated and reconstructed information of the matched tracks were compared.

The reconstruction efficiency was calculated by checking what fraction of the simulated π^- is reconstructed and passes the selection criteria. In order to limit impact of the possible imperfect implementation of the detector shape in simulation, only the regions with good reconstruction efficiency (>90%) are selected for the analysis (see Sect. 6.3.3). The reconstruction efficiency in these regions calculated using MC is close to 100%, as demonstrated in Fig. 5.9.

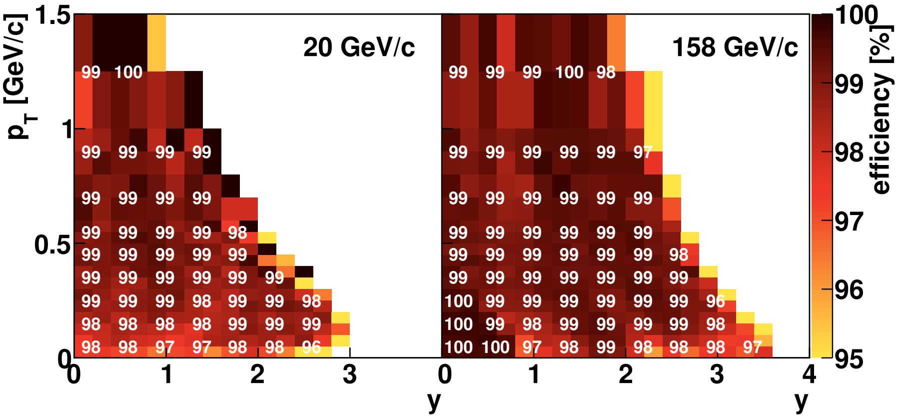

Figure 5.9: Reconstruction efficiency of negatively charged pions produced in p+p interactions simulated in EPOS at 20 (*left*) and 158 GeV/*c* (*right*) as a function of rapidity and the transverse momentum. It was calculated by dividing the number of tracks passing the track selection cuts specified in Sect. 6.3 by the number of the generated tracks. The selection criteria include selection of the azimuthal angle ϕ regions with at least 90% reconstruction efficiency. Only tracks with at least 25 generated points were used. For clarity, the numbers printed are averages calculated in four adjacent bins.

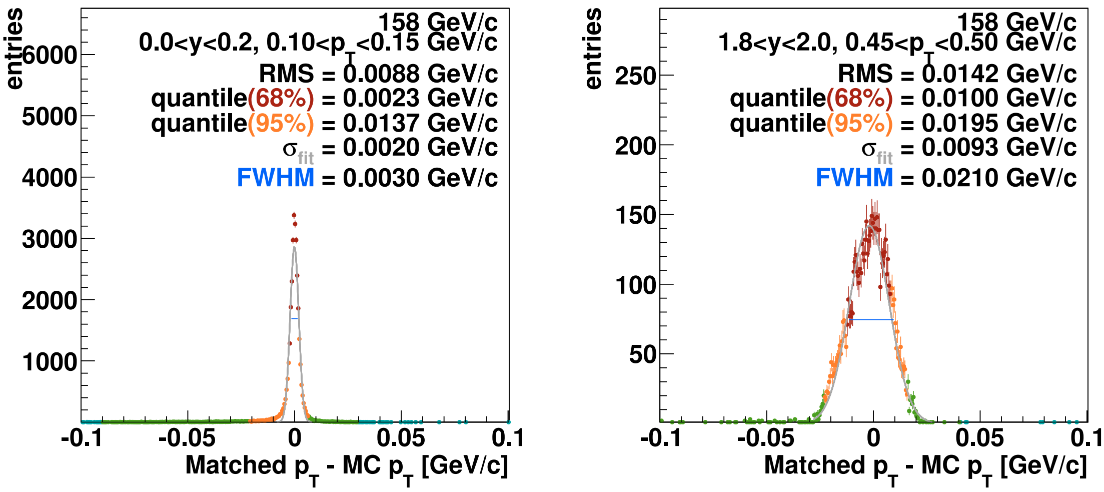

Figure 5.10: Distributions of differences between the generated and reconstructed transverse momentum of matched MC tracks in selected (y, p_T) bins. Results of several methods to estimate width of the peak are given in the legend (see text for explanation). The dark red, orange, green and aquamarine points distinguish quantiles covering 68%, 95%, 99.7% and 99.99% statistics in the middle, respectively. The horizontal blue line shows the full width at half maximum (FWHM).

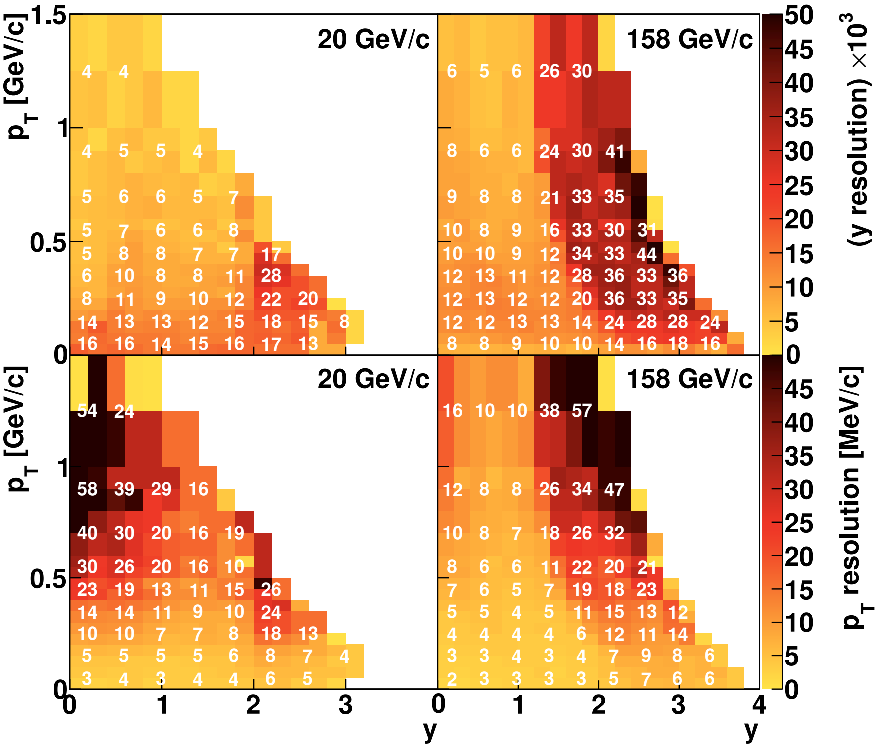

Figure 5.11: Resolution of rapidity (*top*, multiplied by 10^3) and the transverse momentum (*bottom*) measurements for negatively charged pions produced in p+p interactions at 20 (*left*) and 158 GeV/c (*right*) as a function of pion rapidity and the transverse momentum. The results are obtained using the track selection cuts specified in Sect. 6.3. For clarity, the numbers printed are averages calculated in four adjacent bins.

Resolution of rapidity and the transverse momentum was calculated as a width of the distribution of differences between y and p_{T} of the generated π^- particles and corresponding matched tracks. Figure 5.10 shows example distributions derived in selected (y, p_{T}) bins. Several methods to estimate width of the distribution were examined.

- Simple calculation of RMS often overestimated the value due to long tails of the distribution.
- The distribution were divided into quantiles covering to 68%, 95%, 99.7% and 99.99% statistics in the middle of the distribution, which would correspond to 1σ, 2σ, 3σ and 4σ respectively in case of Gaussian distribution. The *left* panel shows that the 95% quantile is often much more than twice wider than the 68% one.
- Gaussian distribution was fitted in region from -2RMS to $+2$RMS, and its width σ was taken as a width estimate.
- FWHM of the distribution was calculated. In the lowest statistics (y, p_{T}) bins the histogram bin widths were increased until FWHM could be calculated unambiguously.

Out of the method described above FWHM was chosen, as it was not sensitive to long tails of the distributions and yielded the most reasonable results in both low and high statistics bins. Resulting resolution of rapidity and the transverse momentum reconstruction is shown in Fig. 5.11.

Due to limited reconstruction resolution the reconstructed tracks can be assigned to incorrect (y, p_{T}) bin. This effect is called *bin migration*. In order to minimise this effect, the bin sizes were chosen larger than the reconstruction resolution.

Figure 5.12 shows distributions of the invariant mass of secondary $\pi^+\pi^-$ pairs in the measured data and in simulation. The difference between the peak position and the literature value of $\mathrm{K}^0_{\mathrm{S}}$ mass is below 1 MeV/c^2. This demonstrates resolution of the momentum reconstruction, and correctness of the magnetic field calibration. The width of the MC distribution is about 25% smaller than for the data. This implies that statistical or systematic uncertainties of track parameters reconstructed from the data are slightly underestimated in the simulation. As it will be demonstrated in Sect. 6.5.2 these imperfections have low impact on the final results.

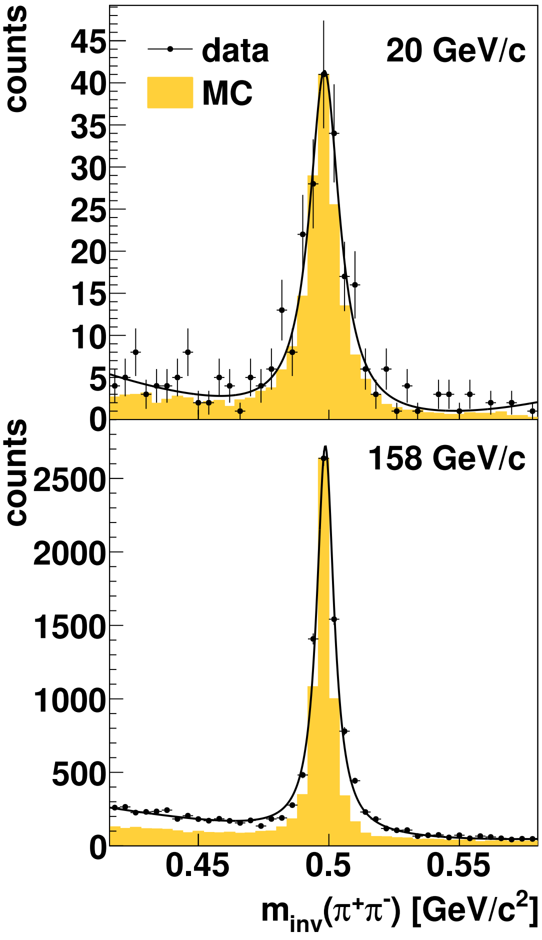

Figure 5.12: Invariant mass distribution of reconstructed $\pi^+\pi^-$ pairs in p+p interactions at 20 (*top*) and 158 GeV/c (*bottom*) for the measured data and EPOS model based Monte Carlo simulations. The peak at $m \approx 0.5$ GeV/c corresponds to K^0_S decays. The MC plot was normalised to the peak height of the data distribution. The K^0_S candidates were selected within $0 < y < 1$ and $0 < p_T < 0.5$ GeV/c for 20 GeV/c and $-1 < y < 0$ and $0 < p_T < 0.5$ GeV/c for 158 GeV/c. In order to reduce background, the secondary vertices were selected at $c\tau > 1.0$ cm for $y < 0.5$ and $c\tau > 1.5$ cm for $y > 0.5$. The data distribution was fitted with a sum of a Lorentzian function (signal) and a second order polynomial (background). Figure taken from Ref. [29].

Chapter 6

Data analysis

6.1 Overview of the analysis procedure

Spectra of the π^- mesons produced in p+p collisions at the beam momenta of 20, 31, 40, 80, and 158 GeV/c were obtained with so-called h^- method. The analysis is based on the fact that the majority of produced negatively charged hadrons (h^-) are pions [25–27]. The particle charge is measured and non-hadrons (i.e. electrons) are rejected based on the dE/dx measurement. Contribution of other particles (mostly K^-, $\overline{p}$ and secondary particles mistakenly fitted to the main vertex) is removed using the Monte Carlo (MC) simulation. MC is also used to correct for other experimental effects, which will be described in this chapter.

The final results refer to the π^- mesons produced in inelastic p+p interactions by the strong interaction processes and in electromagnetic decays of produced hadrons. Such pions are referred to as *primary* π^-. The term *primary* will be used in the above meaning also for other particles. Particles produced in weak decays or interactions of the produced particles are called *secondary*. The spectra represent the average number of particles produced in event in given bin of a two-dimensional histogram in rapidity y and the transverse momentum p_T or transverse mass m_T, divided by the size of the bin.

The procedure used for the data analysis consists of the following steps:

(i) applying event (Sect. 6.2) and track (Sect. 6.3) selection criteria,
(ii) determination of spectra of negatively charged hadrons using the selected events and tracks,
(iii) evaluation of corrections to the spectra, based on experimental data and simulations (see Sect. 6.4),
(iv) calculation of the corrected spectra,
(v) calculation of the statistical and systematic uncertainties (see Sect. 6.5).

Corrections for the following data biases were evaluated and applied:

(i) geometrical acceptance and impact of the beam angle variation,
(ii) contribution of off-target interactions,
(iii) contribution of the negatively charged particles other than π^- produced in inelastic p+p interactions,
(iv) rejection of some of the inelastic p+p interactions as well as of the π^- tracks produced in accepted interactions due to the trigger and the event and track selection criteria employed in the analysis, as well as the track migration be-

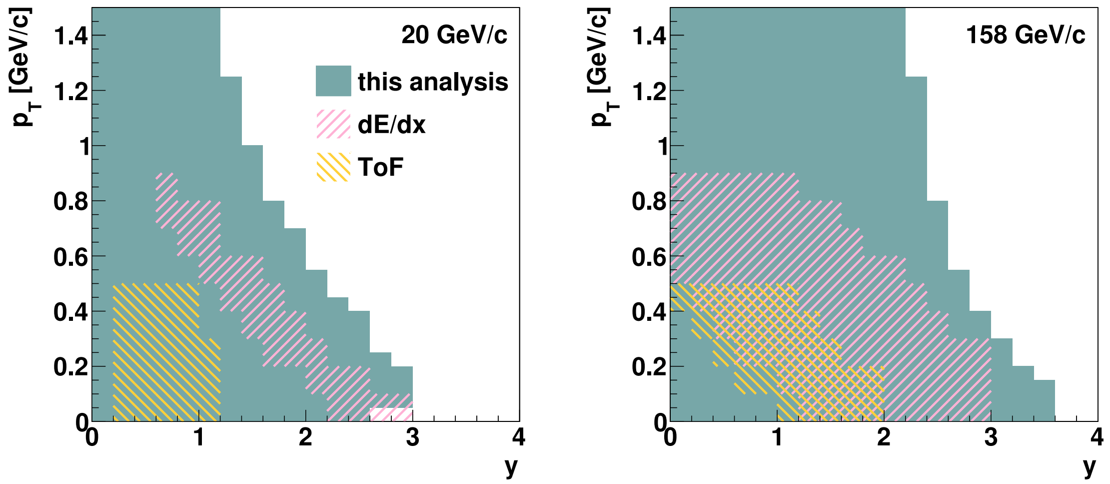

Figure 6.1: Typical acceptance regions for the π^- meson spectra in p+p interactions at 20 GeV/c (*left*) and 158 GeV/c (*right*) for different analysis methods: the method used in this thesis which does not require an explicit pion identification, the method which identifies pions via their energy loss (dE/dx) and time of flight (ToF) [48].

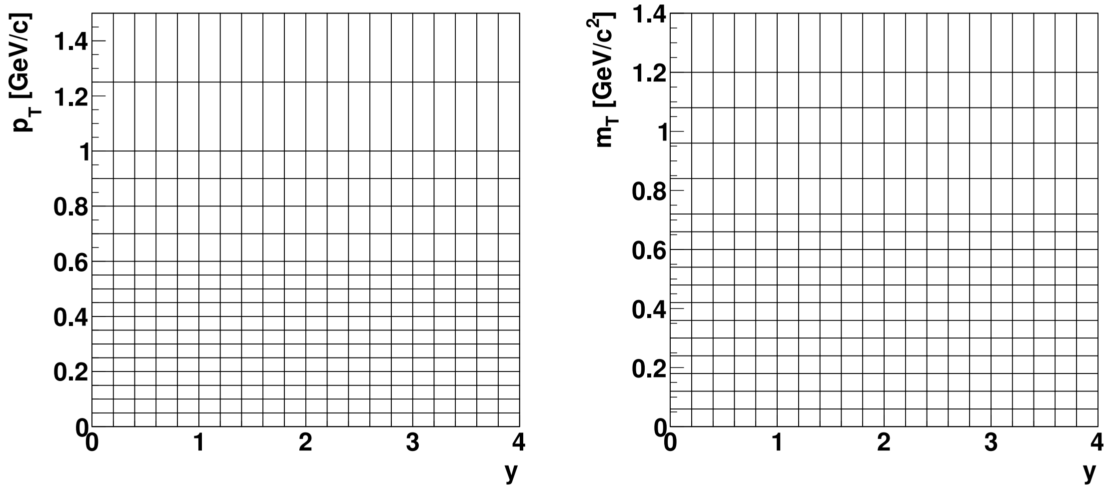

Figure 6.2: The histogram bin ranges used for (y, p_T) (*left*) and (y, m_T) (*right*).

tween the histogram bins due to finite momentum resolution and other effects related to detection and reconstruction.

These steps are described in the successive subsections.

The typical acceptance in rapidity and the transverse momentum for p+p interactions at 20 and 158 GeV/c is presented in Fig. 6.1. This figure also shows acceptance regions for methods based on explicit pion identification using dE/dx and time of flight measurements. They are limited due to the geometrical acceptance of the ToF detectors, the finite resolution of the dE/dx measurements and limited statistics of the experimental data.

The analysis was performed in (y, p_T) and (y, m_T) bins. Corrections as well as statistical and systematic uncertainties were calculated for each bin independently.

The binning scheme is shown in Fig. 6.2. The bin sizes were selected taking into account the statistical uncertainties as well as the resolution of the momentum reconstruction. The bins in rapidity are of constant width of 0.2. Widths of the p_T bins equal 0.05 GeV/c up to $p_T = 0.6$ GeV/c, 0.1 GeV/c for $0.6 < p_T < 1$ GeV/c, and 0.25 GeV/c up to $p_T = 1.5$ GeV/c.

The m_T bins were selected in order to match the binning used for the Pb+Pb experimental results at 20 and 30A GeV/c in Ref. [9], and extended above 0.96 GeV/c^2 up to 1.4 GeV/c^2. Widths of the bins equal 0.06 GeV/c^2 up to $m_T = 0.84$ GeV/c^2, and the further bins end at 0.90, 0.96, 1.08, 1.20 and 1.40 GeV/c^2. The spectra obtained in Pb+Pb collisions at 40, 80 and 158A GeV/c [8] were derived in different, 0.05 GeV/c constant size m_T bins, and extended only up to $m_T = 0.75$ GeV/c^2. In order to simplify comparison of the data it was decided to use the same binning for all beam momenta and to interpolate the Pb+Pb data at high beam momenta.

The data were analysed using ROOT and ROOT61 code dedicated for this task.

6.2 Event selection

6.2.1 List of event selection criteria

The following on-line (the interaction trigger condition) and off-line event selection criteria were applied to the events recorded with the interaction trigger:

(i) interaction is recognised by the trigger logic defined in Eq. (2.2),

(ii) no off-time beam particle is detected within ±2 μs with respect to the trigger particle S1 signal,

(iii) The beam particle trajectory is measured in BPD-3 and at least one of BPD-1 or BPD-2.

(iv) there is at least one track reconstructed in the TPCs and fitted to the interaction point (see Sect. 6.2.2),

(v) if the vertex is found by the reconstruction algorithms, its z position lies within ±40 cm from the LHT centre (see Sect. 6.2.2),

(vi) events with a single, positively charged primary hadron track of total momentum within several GeV/c with respect to the beam momentum are rejected (see Sect. 6.2.3).

The numbers of events selected for the analysis are shown in Table 6.1. At each beam momentum several millions events are collected for target inserted, except for 20 GeV/c due to slower data acquisition rate (see Sect. 5.2). The target removed statistics was aimed to be 5–10% of the total statistics, as this is sufficient to achieve the necessary statistical precision for the off-target interactions. This fraction is further reduced by the event selection criteria described above. About 5 millions of simulated events were generated at each beam momentum.

In the measured data p+p interactions were selected by the trigger logic (cut (i), see Sect. 2.2). In simulation however, all inelastic events are available. In order to mimic the trigger behaviour cut (i) is reproduced by requiring lack of the S4 signal. Fraction of events lost due to use of the S4 counter is of order of 1–2% at the low beam momenta, but increases to 16% at 158 GeV/c. This effect is corrected using MC (see Sect. 6.4.3).

Table 6.1: Numbers of events selected for analysis after consecutive selection criteria listed in Sect. 6.2.1, for target inserted, removed and EPOS MC. The first line (*) gives the number of events before S4 selection (cut (i)) for MC. Numbers are given in thousands (k = 10^3). The numbers in round brackets give the percentage with respect to cut (i), and numbers in the square brackets give the percentage with respect to the previous cut.

cut	target inserted			target removed			EPOS		
$p_{\text{beam}} = 20$ GeV/c									
(*)	–	–	–	–	–	–	4 975 k	(100.7)	–
(i)	1 257 k	(100.0)	–	109.2 k	(100.0)	–	4 939 k	(100.0)	[99.3]
(ii)	790 k	(62.8)	[62.8]	69.1 k	(63.3)	[63.3]	–	–	–
(iii)	477 k	(37.9)	[60.4]	25.1 k	(23.0)	[36.4]	–	–	–
(iv)	276 k	(22.0)	[57.9]	7.0 k	(6.4)	[27.8]	4 377 k	(88.6)	[88.6]
(v)	255 k	(20.3)	[92.4]	3.8 k	(3.5)	[54.1]	4 351 k	(88.1)	[99.4]
(vi)	233 k	(18.5)	[91.1]	3.6 k	(3.3)	[93.8]	4 274 k	(86.5)	[98.2]
$p_{\text{beam}} = 31$ GeV/c									
(*)	–	–	–	–	–	–	4 980 k	(101.5)	–
(i)	2 839 k	(100.0)	–	248.3 k	(100.0)	–	4 905 k	(100.0)	[98.5]
(ii)	1 839 k	(64.8)	[64.8]	156.1 k	(62.9)	[62.9]	–	–	–
(iii)	1 438 k	(50.7)	[78.2]	83.7 k	(33.7)	[53.6]	–	–	–
(iv)	955 k	(33.6)	[66.4]	31.3 k	(12.6)	[37.4]	4 432 k	(90.4)	[90.4]
(v)	875 k	(30.8)	[91.7]	14.9 k	(6.0)	[47.8]	4 404 k	(89.8)	[99.4]
(vi)	843 k	(29.7)	[96.3]	14.6 k	(5.9)	[97.6]	4 372 k	(89.1)	[99.3]
$p_{\text{beam}} = 40$ GeV/c									
(*)	–	–	–	–	–	–	4 992 k	(102.4)	–
(i)	4 684 k	(100.0)	–	364.9 k	(100.0)	–	4 874 k	(100.0)	[97.6]
(ii)	3 021 k	(64.5)	[64.5]	228.2 k	(62.5)	[62.5]	–	–	–
(iii)	2 529 k	(54.0)	[83.7]	150.2 k	(41.2)	[65.8]	–	–	–
(iv)	1 761 k	(37.6)	[69.6]	77.3 k	(21.2)	[51.5]	4 470 k	(91.7)	[91.7]
(v)	1 625 k	(34.7)	[92.2]	45.3 k	(12.4)	[58.5]	4 439 k	(91.1)	[99.3]
(vi)	1 578 k	(33.7)	[97.1]	44.3 k	(12.1)	[97.9]	4 404 k	(90.4)	[99.2]
$p_{\text{beam}} = 80$ GeV/c									
(*)	–	–	–	–	–	–	4 990 k	(107.7)	–
(i)	3 387 k	(100.0)	–	234.1 k	(100.0)	–	4 632 k	(100.0)	[92.8]
(ii)	2 955 k	(87.2)	[87.2]	202.5 k	(86.5)	[86.5]	–	–	–
(iii)	2 133 k	(63.0)	[72.2]	128.9 k	(55.1)	[63.7]	–	–	–
(iv)	1 675 k	(49.5)	[78.5]	86.7 k	(37.0)	[67.2]	4 373 k	(94.4)	[94.4]
(v)	1 546 k	(45.7)	[92.3]	54.5 k	(23.3)	[62.9]	4 337 k	(93.6)	[99.2]
(vi)	1 543 k	(45.6)	[99.8]	54.4 k	(23.3)	[99.8]	4 332 k	(93.5)	[99.9]
$p_{\text{beam}} = 158$ GeV/c									
(*)	–	–	–	–	–	–	4 984 k	(118.9)	–
(i)	2 828 k	(100.0)	–	159.9 k	(100.0)	–	4 193 k	(100.0)	[84.1]
(ii)	2 634 k	(93.2)	[93.2]	148.8 k	(93.1)	[93.1]	–	–	–
(iii)	1 981 k	(70.1)	[75.2]	103.5 k	(64.7)	[69.6]	–	–	–
(iv)	1 783 k	(63.1)	[90.0]	80.5 k	(50.3)	[77.8]	4 055 k	(96.7)	[96.7]
(v)	1 650 k	(58.4)	[92.5]	51.1 k	(32.0)	[63.5]	4 008 k	(95.6)	[98.8]
(vi)	1 650 k	(58.4)	[100.0]	51.1 k	(32.0)	[100.0]	4 008 k	(95.6)	[100.0]

Non-biasing cuts (ii) and (iii) reduce number of tracks from the off-time interactions and ensure good resolution of the interaction point position. Only 7% of events is removed by the off-time particle rejection (cut (ii)) at 158 GeV/c, but this fraction increases to almost 40% at 20 GeV/c due to higher beam intensity (see Sect. 5.2.2). Another 25–40% of events is removed by cut (iii). This is related to interactions between BPD-1 and BPD-3 and to the off-time beam particles closer than 100 μs to the beam particle.

Cuts (iv) and (vi) remove the elastic interactions. As it is estimated with the simulation, cut (iv) removes from 3% events at 158 GeV/c to 11% at 20 GeV/c of inelastic interactions. As the produced particle multiplicity is lower at the low beam momenta, the vertex point is less likely to be found. The elastic event rejection will be discussed in detail in Sect. 6.2.2.

Cut (v) is supposed to remove interactions outside the hydrogen in the target cell. The cut removes about 40% of events with the target removed. The remaining 60% correspond mostly to interactions with the target cell windows. The cut removes about 8% of the events with the target inserted (containing only small fraction of off-target interactions) and only 1% of the simulated events (containing exclusively interactions with the target). The off-target interaction rejection will be discussed in detail in Sect. 6.2.3.

The corrections for the remaining accepted contribution of interactions outside the hydrogen in the target cell and for the loss of inelastic events due to finite vertex position reconstruction are presented in Sects. 6.4.1 and 6.4.3.

6.2.2 Elastic event rejection

In case of an elastic interaction the beam proton might get deflected far enough to miss the S4 counter of 1 cm diameter, located at $z = -212$ cm, which is 359 cm from the target downstream window. The trigger logic accepts such events as interactions. The goal of the experiment is to measure characteristics of the inelastic interactions, therefore one needs to correct for contribution of the elastic interactions accepted by the trigger.

The possible strategy is to accept all events in the analysis, and correct the resulting cross-sections using MC. However, due to uncertainty of the cross-section measurement in the p+p data (see Sect. 5.3) this approach could not be used.

Instead, two cuts were used to reject the elastic events:

- **Requirement of tracks in the TPCs** (cut (iv)). In an elastic interaction no particles are produced and at most one track of the deflected beam proton is expected to be measured in the TPCs. With high probability the vertex point is not found, since the track may pass through the gap between the left and right sides of the TPCs undetected (GAP TPC alone does not allow to reconstruct a track). Part of the elastic events can be thus removed by requiring a successful vertex fit.
  It was however observed that for the low multiplicity events the vertex fit fails 2% more likely in the measured data than in the simulated. This is probably caused by slight overestimation of the reconstruction efficiency in simulation. Strict vertex fit requirement would bias the results in a way that could not be corrected with MC. Instead, events with an unsuccessful vertex fit are re-

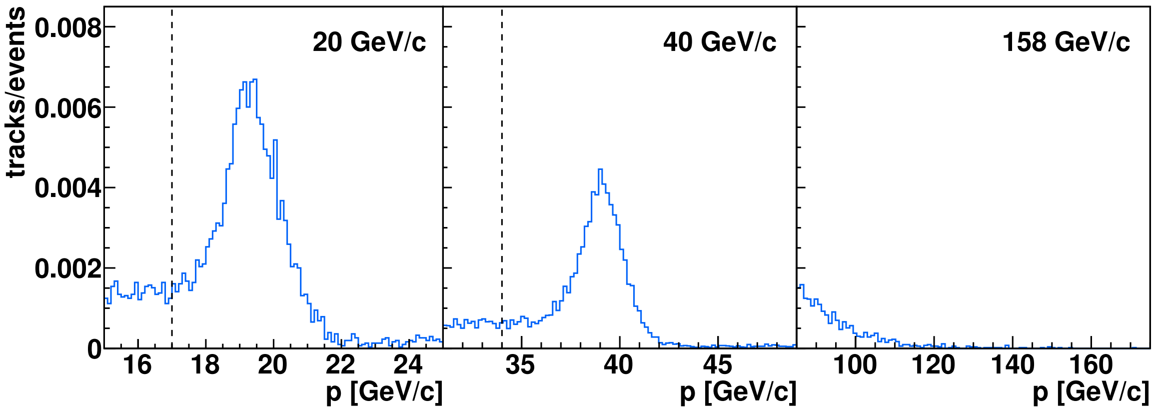

Figure 6.3: The momentum distributions of the positively charged particles for data obtained at 20 (*left*), 40 (*middle*) and 158 GeV/c (*right*) beam momenta. Only events passing the event cuts (ii)–(v) and containing a single track are accepted. The tracks are required to pass the selection cuts and to have at least 3 points measured in the GAP TPC. The maxima visible in the 20 and 40 GeV/c panels originate from elastic scattering of the beam particle. The vertical dashed lines show the threshold levels used to reject the elastic interactions, also listed in Table 6.2

p_{beam} [GeV/c]	p_{min} [GeV/c]
20	17
31	28
40	35
80	74
158	–

Table 6.2: Momentum thresholds p_{min} used to reject elastic interactions at each beam momentum, derived from the momentum distributions shown in Fig. 6.3. The threshold is not derived at 158 GeV/c where the elastically deflected beam remains outside of the TPC acceptance.

moved, only if they also contain no other hadron tracks in the TPCs ($e^{\pm}$ are distinguished with dE/dx (data) and matching (MC, see Sect. 4.3)).

- **Rejection of events with a single positively charged primary track with momentum close to the beam momentum** (cut (vi)). Figure 6.3 demonstrates that in the events passing cut (v) the total momentum distribution shows a maximum slightly below the beam momentum value. It is attributed to elastically deflected beam particles measured in the GAP TPC, MTPC-L and sometimes VTPC-2. Another cut is required to remove such events.
  An event is classified as an elastic interaction and thus rejected if it contains a single, positively charged primary hadron track passing track cuts with at least 3 points in the GAP TPC, and exceeding threshold momentum. The thresholds listed in Table 6.2 were derived from the momentum distributions exemplified in Fig. 6.3. As shown in the figure, at the beam momentum of 158 GeV/c almost no particles above 120 GeV/c are measured. For this reason the cut is not used at 158 GeV/c.

The two cuts described above remove some class of the inelastic interactions. This effect is corrected by applying the same cuts in the simulation used to derive the correction for event losses described in Sect. 6.4.3.

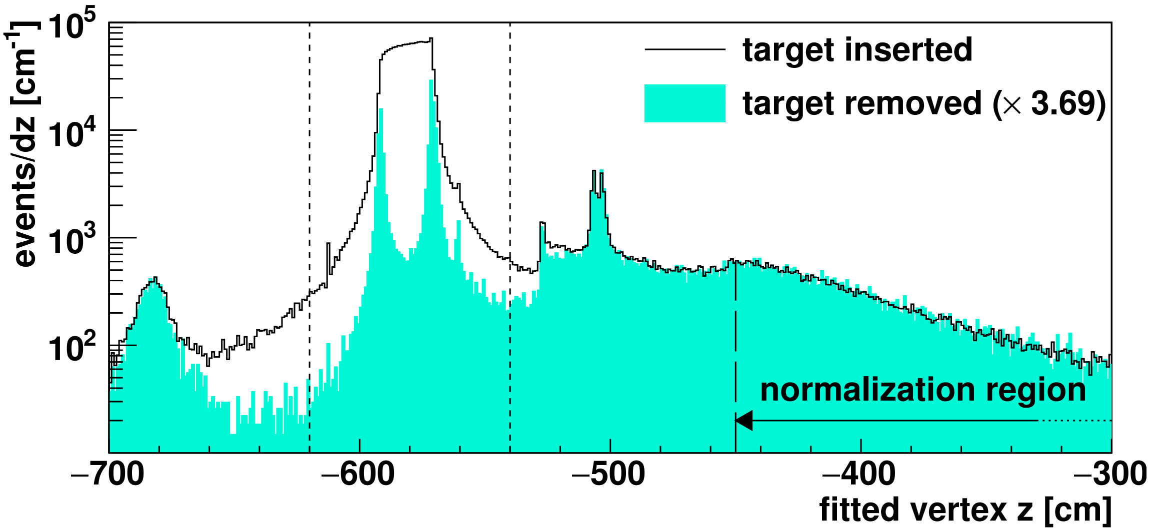

Figure 6.4: Distribution of fitted vertex z coordinate for target inserted and removed at 40 GeV/c. The distribution for the data recorded with the removed liquid hydrogen was multiplied by a factor equal to the ratio of events at $z > -450$ cm (region marked with a vertical arrow). The short-dashed vertical lines mark the selected z region.

The precision of the correction depends on the event generator. It is assumed that the fraction of events removed by the cut and their properties do not differ much in the simulation.

6.2.3 Off-target interaction rejection

In order to remove interactions occurring out of hydrogen target, events with the vertex fitted outside of the target were rejected (cut (v)). Example distributions of the fitted vertex z coordinate for target inserted and removed are shown in Fig. 6.4. The distributions are broadened due to limited reconstruction resolution. However, at the distances larger than 1 m from the target cell both distributions have the same shape, as the reconstructed vertices originate from interactions with the detector material only. It was therefore decided to remove the events with the vertex z position located outside of the $z \in [-620, -540]$ cm range, also marked in Fig. 6.4. The same cut was applied in the analysis of simulated events in order to correct for potential biases introduced by this cut. As stated in the previous subsection, events with the unsuccessful vertex fit are included in the analysis.

6.3 Track selection

6.3.1 List of track selection criteria

In order to select correctly reconstructed tracks of primary negatively charged hadrons as well as to reduce the contamination of tracks from secondary interactions, weak decays and off-time interactions the following track selection criteria were applied:

(i) the track is fitted to the main interaction vertex,
(ii) the track curvature corresponds to a negatively charged particle,
(iii) the fitted track momentum component p_x is negative (so-called *right side track*, see Sect. 6.3.2 for explanation),
(iv) the track is measured in a high (≥90%) reconstruction efficiency region of TPCs, which is defined Sect. 6.3.3,
(v) the total number of reconstructed points on the track is greater than 30,
(vi) the sum of the number of reconstructed points in VTPC-1 and VTPC-2 is greater than 15 or the number of reconstructed points in the GAP TPC is greater than 4,
(vii) the impact parameter (defined in Sect. 3.4.3) does not exceed 4 cm in the horizontal (bending) coordinate and 2 cm in the vertical (drift) coordinate,
(viii) tracks classified as electrons of momenta below 20 GeV/*c* are rejected (see Sect. 6.3.5).

Cuts (i), (v) and (vi) ensure the track was well measured and the momentum resolution is good, as shown in Sect. 5.4. In particular tracks with points in the GAP TPC only are rejected. Cuts (iii) and (iv) reduce the systematic biases related to the non-uniform detection efficiency which might be simulated inaccurately. Additionally cut (vii) helps to reject tracks which do not originate from the main vertex. It was found out that these three cuts are partially redundant [69]. Cuts (ii) and (viii) are necessary to select negatively charged hadrons.

Table 6.3 gives the numbers of tracks after consecutive cuts. The number of tracks decreases with decreasing momentum of the beam particles. This is due to lower particle multiplicity at lower collision energies and lower detector acceptance despite of the magnetic field adjustment. Additionally at $p_{\text{beam}} = 20$ GeV/*c* the number of events collected was 2–3 times smaller than for other datasets.

Negative charge selection (cut (ii)) removes more than half of the tracks: about 70% at 20 GeV/*c* and about 60% at 158 GeV/*c*. This is a result of the electric charge conservation in the two proton system. The average number of the negatively charged produced particles increases from $\langle n^- \rangle \simeq 1$ at 20 GeV/*c* to $\langle n^- \rangle \simeq 2.5$ at 158 GeV/*c* [63], while the number of the positively charged particles $\langle n^+ \rangle = \langle n^- \rangle + 2$ (where 2 is charge of two interacting protons).

Tracks with $p_x > 0$ removed by cut (iii) constitute about 51% of all tracks at 158 GeV/*c*, but this fraction decreases to about 45% at the lower beam momenta, due to different detector acceptance for wrong and right side tracks for different collision energies and magnetic field configurations.

The acceptance cut (iv) removes 30% tracks at 20 GeV/*c* and only 5% at 158 GeV/*c*.

Each of the cuts (v)–(vii) ensuring good reconstruction properties removes several percent tracks. Distributions of the impact parameter and number of points in the data and in MC generated tracks are shown in Figs. 4.7 and 4.8. The track loss is slightly higher for the target removed, as the tracks produced outside of the target region have worse reconstruction properties. The loss for MC is smaller which can be attributed to slight overestimation of detection efficiency in the simulation, but also the lack of the off-time beam particles and off-target interactions. The fraction of tracks removed is larger at the low beam momenta due to slightly worse reconstruction efficiency.

Table 6.3: Numbers of tracks in events selected for analysis after consecutive selection criteria listed in Sect. 6.3.1, for target inserted, removed and EPOS MC. Only tracks at $y > 0$ and $p_\mathrm{T} < 1.5$ GeV/c are considered. Numbers are given in thousands ($\mathrm{k} = 10^3$). The numbers in round brackets mean the percentage with respect to cut (i), and numbers in the square brackets mean the percentage with respect to the previous cut.

	cut	target inserted			target removed			EPOS		
$p_\mathrm{beam} = 20$ GeV/c	(i)	468 k	(100.0)	–	7.0 k	(100.0)	–	8 670 k	(100.0)	–
	(ii)	132 k	(28.3)	[28.3]	2.1 k	(29.4)	[29.4]	2 363 k	(27.3)	[27.3]
	(iii)	71 k	(15.1)	[53.3]	1.1 k	(15.1)	[51.3]	1 318 k	(15.2)	[55.8]
	(iv)	50 k	(10.6)	[70.6]	0.7 k	(10.6)	[70.5]	943 k	(10.9)	[71.5]
	(v)	48 k	(10.3)	[96.6]	0.7 k	(10.2)	[96.2]	931 k	(10.7)	[98.7]
	(vi)	47 k	(10.1)	[98.3]	0.7 k	(10.1)	[98.2]	925 k	(10.7)	[99.3]
	(vii)	46 k	(9.8)	[96.9]	0.7 k	(9.7)	[96.0]	916 k	(10.6)	[99.1]
	(viii)	43 k	(9.3)	[94.5]	0.6 k	(9.1)	[94.2]	888 k	(10.2)	[96.9]
$p_\mathrm{beam} = 31$ GeV/c	(i)	1 850 k	(100.0)	–	31.8 k	(100.0)	–	9 994 k	(100.0)	–
	(ii)	583 k	(31.5)	[31.5]	10.5 k	(33.0)	[33.0]	3 087 k	(30.9)	[30.9]
	(iii)	321 k	(17.4)	[55.1]	5.5 k	(17.1)	[51.9]	1 752 k	(17.5)	[56.8]
	(iv)	249 k	(13.5)	[77.6]	4.2 k	(13.3)	[77.6]	1 361 k	(13.6)	[77.7]
	(v)	242 k	(13.1)	[97.3]	4.1 k	(12.9)	[96.7]	1 347 k	(13.5)	[99.0]
	(vi)	239 k	(12.9)	[98.7]	4.0 k	(12.6)	[98.1]	1 339 k	(13.4)	[99.4]
	(vii)	235 k	(12.7)	[98.1]	3.9 k	(12.3)	[97.8]	1 329 k	(13.3)	[99.3]
	(viii)	225 k	(12.2)	[95.9]	3.8 k	(11.9)	[96.2]	1 291 k	(12.9)	[97.1]
$p_\mathrm{beam} = 40$ GeV/c	(i)	3 753 k	(100.0)	–	107.7 k	(100.0)	–	11 033 k	(100.0)	–
	(ii)	1 246 k	(33.2)	[33.2]	36.8 k	(34.2)	[34.2]	3 597 k	(32.6)	[32.6]
	(iii)	691 k	(18.4)	[55.4]	20.0 k	(18.5)	[54.2]	2 033 k	(18.4)	[56.5]
	(iv)	554 k	(14.8)	[80.2]	16.0 k	(14.8)	[80.0]	1 633 k	(14.8)	[80.3]
	(v)	542 k	(14.4)	[97.9]	15.6 k	(14.5)	[97.6]	1 619 k	(14.7)	[99.1]
	(vi)	536 k	(14.3)	[98.9]	15.4 k	(14.3)	[98.7]	1 611 k	(14.6)	[99.5]
	(vii)	530 k	(14.1)	[98.9]	15.2 k	(14.1)	[98.7]	1 602 k	(14.5)	[99.4]
	(viii)	513 k	(13.7)	[96.7]	14.8 k	(13.7)	[97.5]	1 558 k	(14.1)	[97.2]
$p_\mathrm{beam} = 80$ GeV/c	(i)	4 798 k	(100.0)	–	175.9 k	(100.0)	–	14 421 k	(100.0)	–
	(ii)	1 774 k	(37.0)	[37.0]	66.4 k	(37.8)	[37.8]	5 250 k	(36.4)	[36.4]
	(iii)	936 k	(19.5)	[52.8]	34.2 k	(19.5)	[51.5]	2 787 k	(19.3)	[53.1]
	(iv)	824 k	(17.2)	[88.1]	30.0 k	(17.1)	[87.7]	2 458 k	(17.0)	[88.2]
	(v)	815 k	(17.0)	[98.8]	29.6 k	(16.9)	[98.7]	2 443 k	(16.9)	[99.4]
	(vi)	810 k	(16.9)	[99.4]	29.5 k	(16.7)	[99.4]	2 437 k	(16.9)	[99.7]
	(vii)	807 k	(16.8)	[99.6]	29.3 k	(16.7)	[99.5]	2 430 k	(16.8)	[99.7]
	(viii)	788 k	(16.4)	[97.7]	28.9 k	(16.4)	[98.6]	2 374 k	(16.5)	[97.7]
$p_\mathrm{beam} = 158$ GeV/c	(i)	6 830 k	(100.0)	–	213.2 k	(100.0)	–	17 879 k	(100.0)	–
	(ii)	2 694 k	(39.4)	[39.4]	85.0 k	(39.9)	[39.9]	6 981 k	(39.0)	[39.0]
	(iii)	1 323 k	(19.4)	[49.1]	40.0 k	(18.8)	[47.0]	3 462 k	(19.4)	[49.6]
	(iv)	1 253 k	(18.4)	[94.7]	37.8 k	(17.7)	[94.6]	3 287 k	(18.4)	[94.9]
	(v)	1 243 k	(18.2)	[99.2]	37.5 k	(17.6)	[99.1]	3 272 k	(18.3)	[99.5]
	(vi)	1 240 k	(18.2)	[99.7]	37.3 k	(17.5)	[99.7]	3 267 k	(18.3)	[99.9]
	(vii)	1 237 k	(18.1)	[99.8]	37.2 k	(17.4)	[99.5]	3 262 k	(18.2)	[99.9]
	(viii)	1 214 k	(17.8)	[98.1]	36.8 k	(17.2)	[98.9]	3 197 k	(17.9)	[98.0]

The electron track cut (viii) removes 2–6% tracks, more for the low beam momentum data due to higher off-time interaction rate.

The spectra of negatively charged particles after track and event selections were obtained in two-dimensional bins of (y, p_T) and (y, m_T). The spectra were evaluated in the centre-of-mass frame of reference of the colliding protons after rotation of the z axis into the beam direction measured by the BPDs for each event.

6.3.2 Classification of tracks due to their topology

The reconstructed tracks are classified as *right side tracks* (RST) and *wrong side tracks* (WST). For the magnetic field polarisation used in NA61/SHINE the RST are defined as

$$q \cdot p_x > 0\,, \tag{6.1}$$

where q is the electric charge, and p_x is component x of the momentum vector. WST is the complementary class of $q \cdot p_x < 0$. Figure 6.5 shows an example of a WST.

The NA61/SHINE TPC pads are tilted with respect to the beam axis. The tilt angle is optimised to minimise the average angle between the pad and the RST in the horizontal (x–z) plane [33]. This reduces widths of the clusters measured on the padrows, reduces sensitivity of the reconstructed cluster position to the ionisation fluctuations along the pad row length and ensures constant dE/dx sensitivity.

Besides the mentioned worse cluster properties, a subclass of WST have segments measured on both left and right side of VTPCs. Formation of track out of such aligned segments is less efficient so the acceptance for such particles is lower. The only potential advantage of including WST in the analysis is increased acceptance for the very low momentum tracks, which are directed into the detector by the magnetic field. It has however low significance in analysis of spectra in collisions of identical particles, such as p+p, as these tracks lie in negative rapidity, where the spectrum is a symmetric reflection of the well measured positive rapidity region.

In order to minimise potential systematic biases, only RST are selected for the analysis (cut (iii)). As neither the beam nor the target are polarised the RST selection as defined in Eq. (6.1) removes exactly half of the phase-space. The track loss is compensated simply by multiplying the final results by factor of 2.

Unless stated otherwise, all plots show results for the RST only. Results using RST and WST are compared in Sect. 6.6.2.

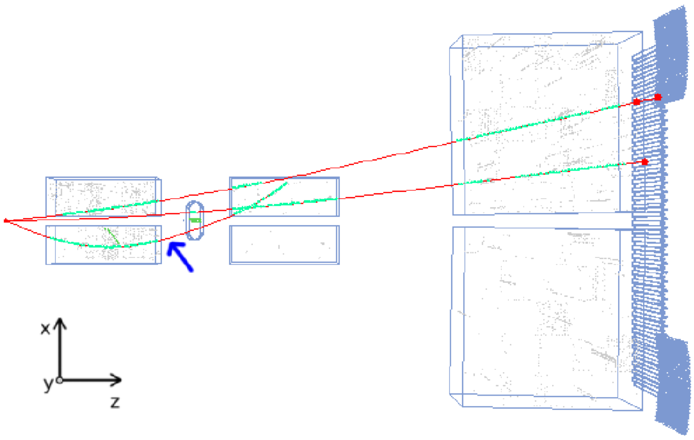

Figure 6.5: Example of a wrong side track, marked with the blue arrow. This positively charged particle has negative initial p_x momentum component, but the magnetic field bends it in the opposite direction, towards positive x. The two other visible tracks are right side tracks.

6.3.3 Selection of high reconstruction efficiency regions

The detection and reconstruction inefficiencies are corrected using the MC simulation. In order to limit the impact of possible inaccuracies of the detector simulation, only regions with high (≥90%) reconstruction efficiency are accepted (cut (iv)). The reconstruction efficiency is calculated as a ratio of the number of reconstructed and matched π^- tracks fulfilling the selection criteria to the number of generated π^- particles. Map of these regions was determined in three-dimensional bins of y, p_T (or m_T) and the azimuthal angle ϕ (5° bin width). Examples are shown in Fig. 6.6 (*top*). The accepted regions are not symmetric with respect to particles produced in the horizontal plane ($\phi = 180°$). The asymmetry is more pronounced at 20 GeV/c. It results from the detector asymmetry. The beam axis is aligned in the middle be-

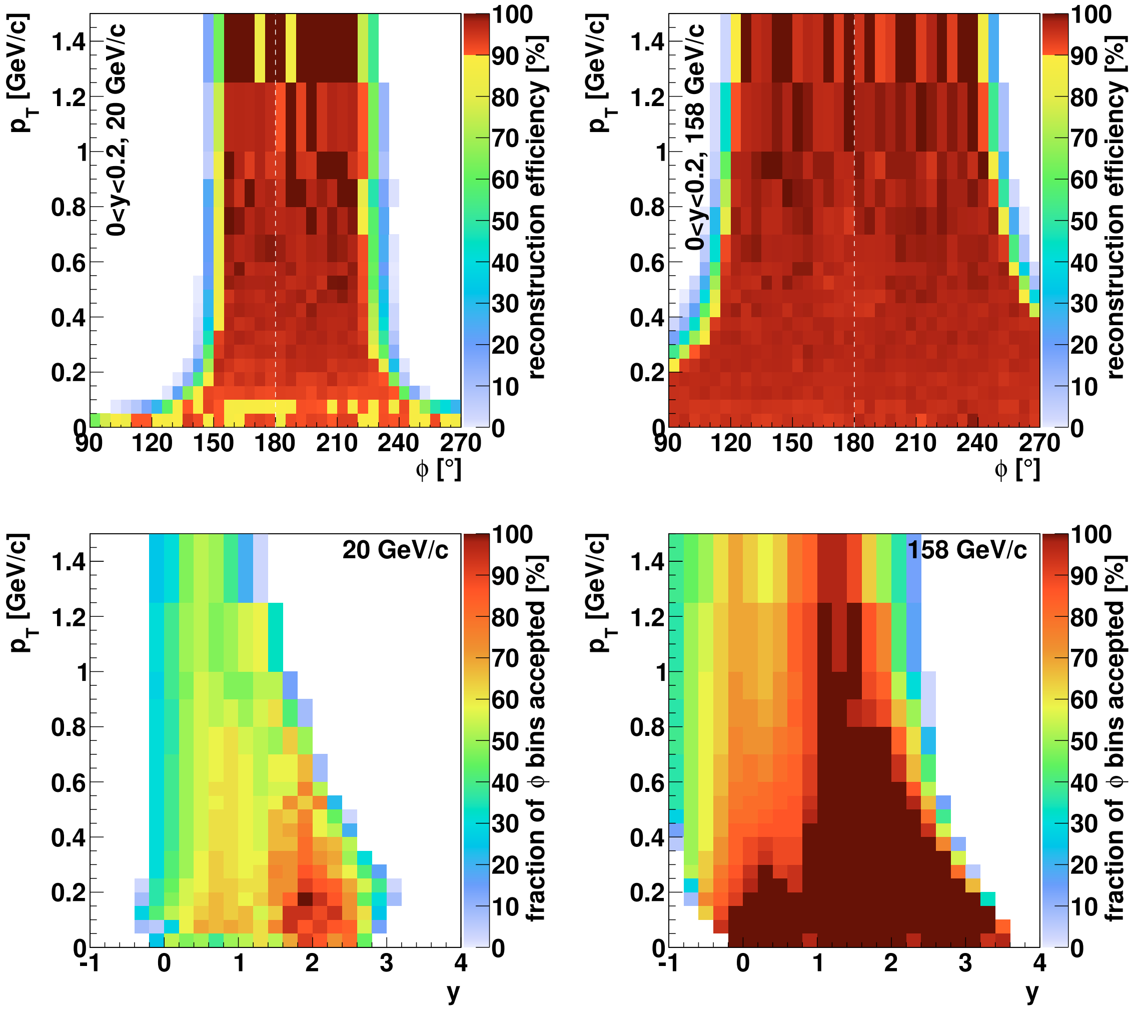

Figure 6.6: Calculation of the acceptance map for RST, at 20 (*left*) and 158 GeV/c (*right*) using EPOS simulation. *Top:* reconstruction efficiency in ϕ and p_T bins for $0 < y < 0.2$, calculated using EPOS simulation. Bins drawn in red colour, with efficiency above 90% are accepted. The vertical dashed line marks the particles produced in the horizontal plane, at $\phi = 180°$. *Bottom:* fraction of ϕ bins accepted in each (y, p_T) bin. The multiplicative correction for the acceptance is the reciprocal of the values shown.

tween the magnet cores, however the VTPC readout electronics occupies space on the top. As a result, the VTPC active volume is asymmetric: $-37 < y < +26$ cm with respect to the the beam axis ($y = 0$ cm).

Statistical fluctuations of the simulated particle distributions used to calculate the acceptance maps could bias results if used for analysis of the same distributions. In order to avoid this, VENUS simulation (which is a statistically independent dataset) was used to obtain the maps used with analysis done with the EPOS model, and *vice versa*.

Since neither target nor beam are polarised, we can assume a uniform distribution of particles in ϕ. The data is summed over the accepted ϕ bins. In order to compensate for the rejected regions, a correction factor c_{acc} is derived for each bin as:

$$c_{\text{acc}} = \frac{\text{total number of the } \phi \text{ bins}}{\text{number of accepted } \phi \text{ bins}} . \tag{6.2}$$

It is an inverse of the fraction of the ϕ bins accepted, shown in Fig. 6.6 (*bottom*). The procedure was developed in Ref. [70] and adapted for the needs of this analysis.

As it is shown in Fig. 6.6 fraction of the ϕ bins accepted is smaller at low beam momenta. The magnetic field is scaled down proportionally to the momentum of beam particles in order to retain acceptance. However the decreased magnetic field at the low beam momenta is insufficient to bend particles moving upwards ($\phi = 90°$) or downwards ($\phi = 270°$) into the TPC active volume.

6.3.4 Correction for beam divergence

Even a sub-milliradian deviation of the angle between the beam particle trajectory and the nominal axis (z) results in a non-negligible bias in the reconstructed transverse momentum. This may cause the tracks to migrate to neighbouring (y, p_{T}) bins. The trajectory of each beam particle is measured in the BPDs, and the reconstructed momenta of the produced particles are transformed to the frame of reference connected with direction of the beam particle. However, the detector acceptance depends on momentum in the frame of reference connected with the detector. Therefore the acceptance selection is done using momenta in the detector frame of reference, and the acceptance correction is applied as a weight to each track. The weights are used to fill the particle spectra histograms corrected for acceptance in the frame of reference connected with the beam direction.

Figure 6.7 demonstrates effective beam direction correction. The correction is the largest at large y and p_{T}, reaching several percent. At 158 GeV/c a diagonal structure is visible, which can be correlated with edge of the 100% acceptance region (see Fig. 6.6). This is because the beam direction effect is significant in the regions, where the corrections applied to the spectra change rapidly. The acceptance correction ranges from +0% (full acceptance) to +3500% (single ϕ bin accepted). All other corrections are of the order of single or tens of percent, thus they do not generate effect related to the beam divergence.

6.3.5 Suppression of the electron tracks

Production of electrons is considered difficult to describe in the VENUS and EPOS models. Also, as it was found in Sect. 5.2.2, majority of the electron tracks in the

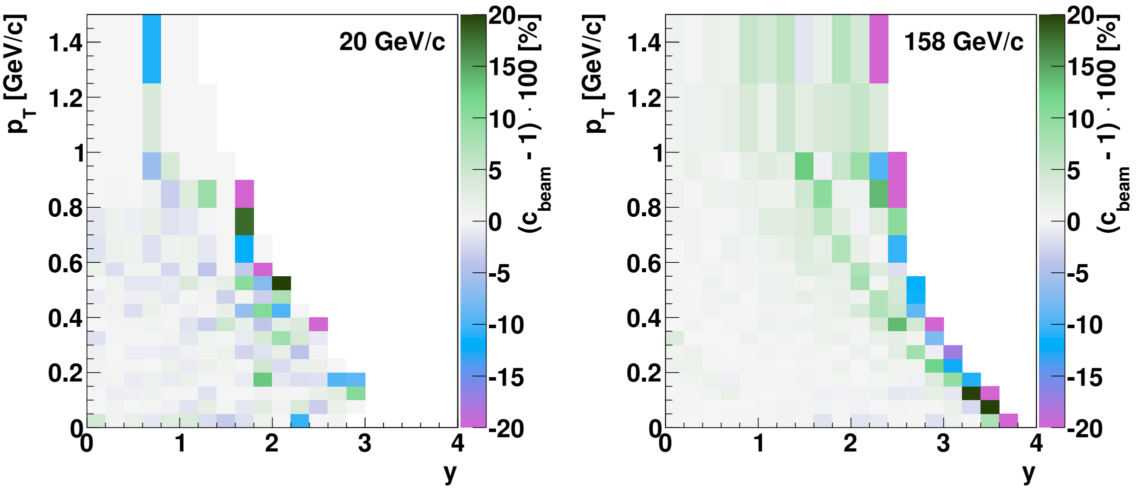

Figure 6.7: Effective correction for beam divergence c_{beam}, defined as a ratio of the corrected and uncorrected spectra, for 20 (*left*) and 158 GeV/*c* (*right*).

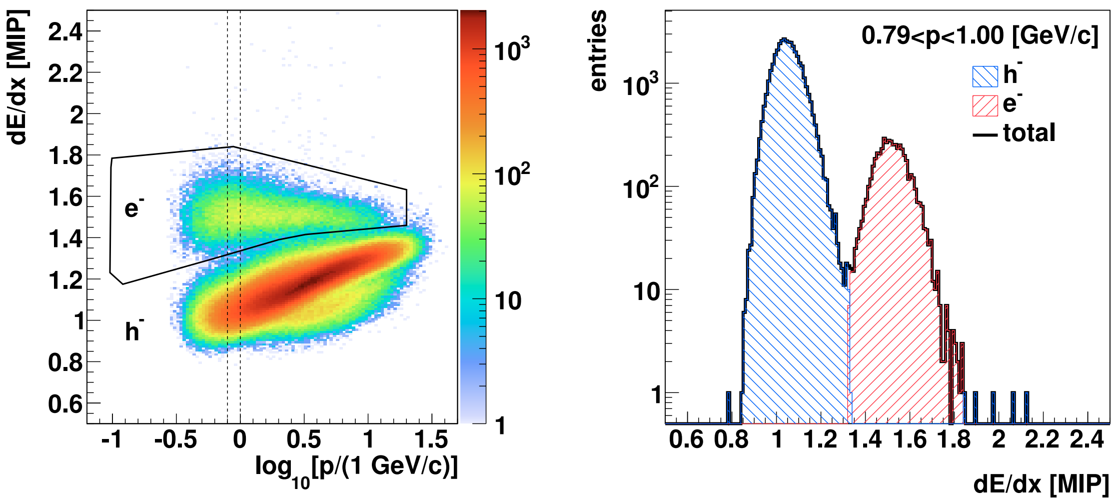

Figure 6.8: *Left:* Distribution of the energy loss as a function of logarithm of total momentum, for the negatively charged right side tracks produced at 40 GeV/*c*. The black contour shows the electron selection region. The two vertical dashed lines show the momentum range used to draw the d*E*/d*x* distribution shown in the *right* panel. Electrons and negatively charged hadrons are distinguished.

data originates from the off-time interactions, which are not simulated in MC. MC simulation cannot be used to correct for the electron contribution. Instead it was decided to suppress them completely (cut (viii)).

In the data the d*E*/d*x* information was used to separate electrons. Figure 6.8 (*left*) shows example distribution of the energy loss versus momentum. A contour was drawn around the well separated electron band. Validity of the selection was verified visually on the d*E*/d*x* distributions in small momenta ranges (see example in Fig. 6.8 (*right*)). Tracks falling inside this contour are rejected from the analysis.

At the produced particle momenta above 20 GeV/*c* electrons cannot be separated from pions via d*E*/d*x*. Correction for their contribution at the higher momenta is therefore included in the standard h$^-$ correction. The electron yield at the high momenta is very small.

In MC electrons (and scarce positrons with wrongly reconstructed charge) below 20 GeV/*c* are identified and rejected using matching. The uncertainty introduced by matching is negligible.

6.3.6 Uncorrected spectra of selected tracks

Figure 6.9 shows the uncorrected particle spectra before (*top*) and after (*bottom*) track selection. Entries at the edges of acceptance disappear after applying the selection criteria. They correspond to short tracks with the momentum reconstructed very poorly, rejected by the minimum number of points requirements. The histograms show the number of entries not divided by the bin size. Horizontal strips at $p_T = 0.6$ GeV/*c* and 1 GeV/*c* result from changes of the bin size at these p_T. At

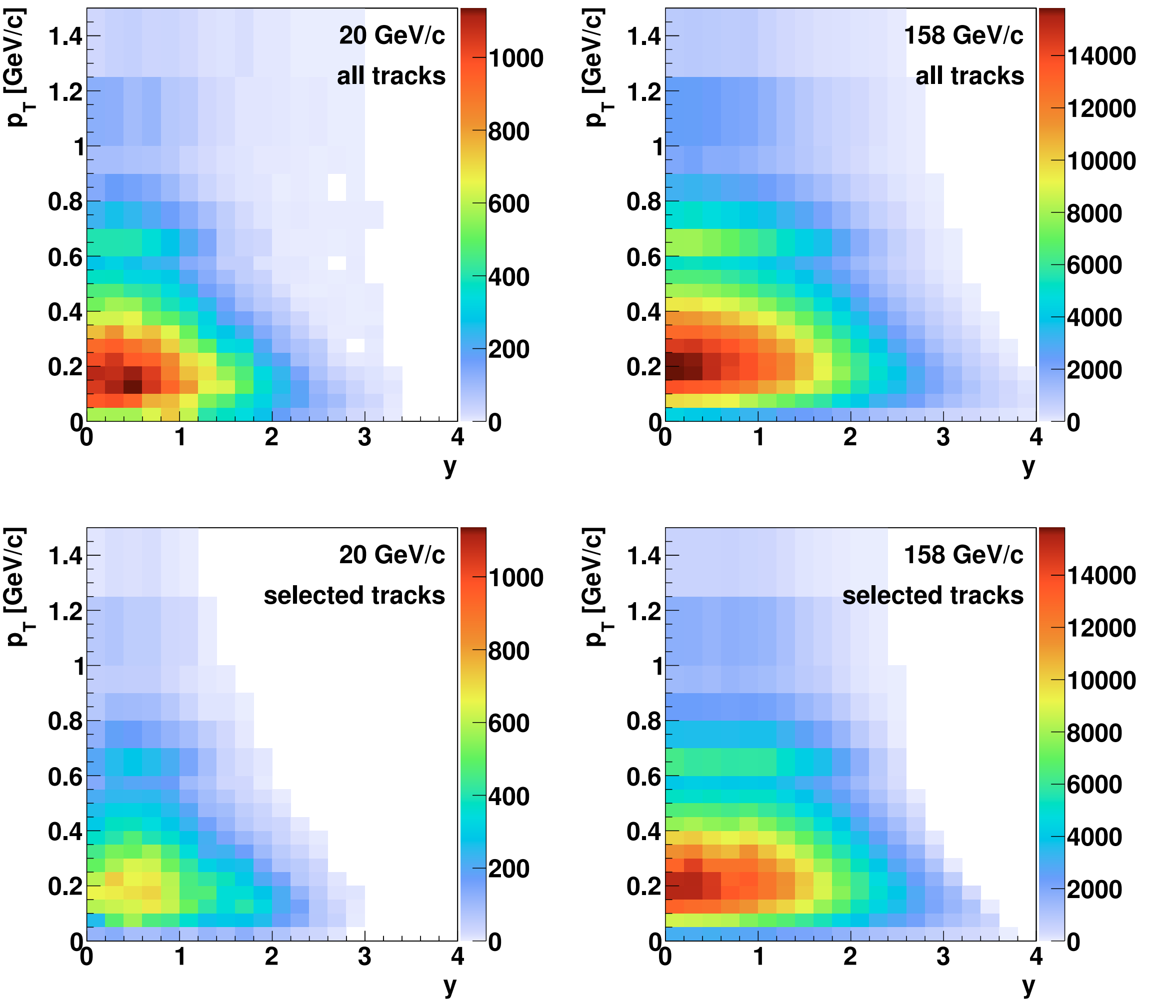

Figure 6.9: Uncorrected spectra of negatively charged right side tracks measured with 20 (*left*) and 158 GeV/*c* (*right*) beams with target inserted, without (*top*) and with (*bottom*) track selection. The plots present numbers of tracks in each bin, not normalised or divided by the bin size. Rapidity y used on this, and all other plots is calculated with charged pion mass assumption.

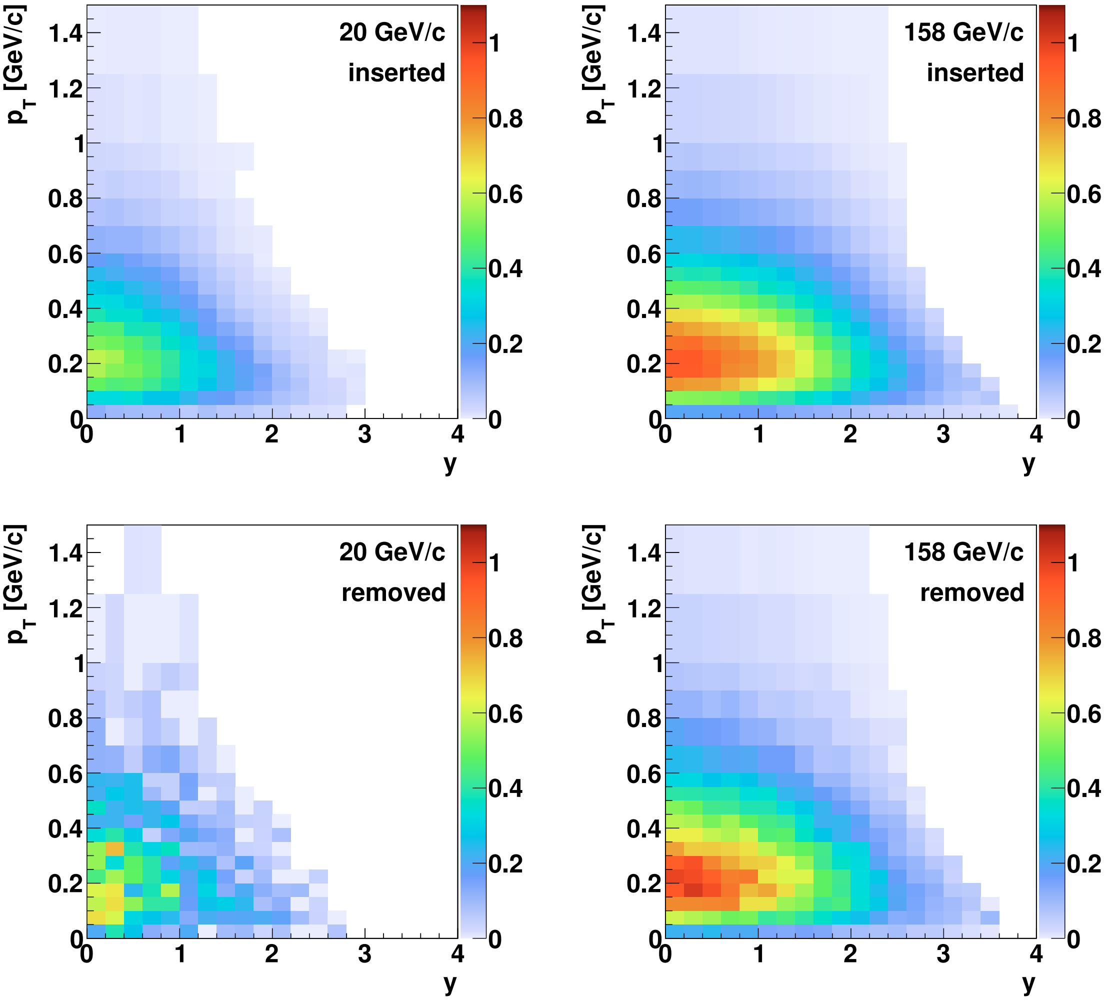

Figure 6.10: Negatively charged hadron spectra after event and track selection for target inserted $\mathsf{n}_{\mathrm{I}}[\mathrm{h}^-]$ (*top*) and removed $\mathsf{n}_{\mathrm{R}}[\mathrm{h}^-]$ (*bottom*) for 20 (*left*) and 158 GeV/*c* (*right*). The spectra are normalised to number of events and the bin size, as defined in Eq. (6.3), and corrected for the acceptance and beam divergence.

20 GeV/*c* the maximum of the distribution appears at $y \approx 0.5$, instead of expected $y = 0$. This results from a non-uniform acceptance (see Fig. 6.6 *bottom right*). Figure 6.10 shows the spectra for target inserted and removed normalised and corrected for acceptance. After applying the correction, the maximum at 20 GeV/*c* shifts to $y = 0$.

The analysis is performed in bins of (y, p_{T}) or (y, m_{T}) independently. Figure 6.11 (*top* and *middle*) shows the target inserted and removed (respectively) spectra corrected for acceptance and the beam direction effect as described in Sects. 6.3.3 and 6.3.4, divided by the number of events and by the bin size. The normalised bin content n shown in the figure is defined as as

$$\mathsf{n}[\mathrm{h}^-] = \frac{\sum_{i=1}^{t[\mathrm{h}^-]} c^i_{\mathrm{acc}}}{N \cdot \Delta}\,, \tag{6.3}$$

where $t[\mathrm{h}^-]$ is the number of tracks in given bin and c^i_{acc} is the acceptance correction for given track according to its momentum in the detector frame, N is the number

p_{beam} [GeV/c]	ε [%]
20	8.0 ± 0.3
31	7.1 ± 0.1
40	10.4 ± 0.1
80	12.7 ± 0.1
158	12.6 ± 0.1

Table 6.4: The ratio of the interaction probabilities, ε, for the removed and inserted target for p+p interactions measured at 20, 31, 40, 80 and 158 GeV/c.

of events selected. Depending on the variables used, the bin size Δ equals either $dy\,dp_{\mathrm{T}}$ or $dy\,dm_{\mathrm{T}}$.

The normalised bin content n is a function of the analysis variables $\mathsf{n} = \mathsf{n}(y, p_{\mathrm{T}})$ or $\mathsf{n} = \mathsf{n}(y, m_{\mathrm{T}})$. In order to unify the formulae for both pairs of the variables, the variables are omitted in Eq. (6.3) and all further equations.

6.4 Corrections to the spectra

6.4.1 Subtraction of the off-target interactions

The spectra were derived for events with liquid hydrogen inserted ($_{\mathrm{I}}$) and removed ($_{\mathrm{R}}$) from the target cell. The latter dataset represents interactions outside the liquid hydrogen (interactions with material downstream and upstream of the liquid hydrogen volume). The differential inclusive yield of negatively charged hadrons per event produced in interactions of beam protons with the liquid hydrogen ($\mathsf{n}_{\mathrm{T}}[\mathrm{h}^-]$) is calculated as:

$$\mathsf{n}_{\mathrm{T}}[\mathrm{h}^-] = \frac{1}{1-\varepsilon} \cdot (\mathsf{n}_{\mathrm{I}}[\mathrm{h}^-] - \varepsilon \cdot \mathsf{n}_{\mathrm{R}}[\mathrm{h}^-]) \ , \tag{6.4}$$

where:

(i) $\mathsf{n}_{\mathrm{I}}[\mathrm{h}^-]$ and $\mathsf{n}_{\mathrm{R}}[\mathrm{h}^-]$ is the normalised bin content, as defined in Eq. (6.3), for events and tracks selected for the analysis (see Sect. 6.3) for the data with the liquid hydrogen inserted and removed, respectively,

(ii) ε is the ratio of the interaction probabilities for the removed and inserted target operation.

The parameter ε was derived based on the distribution of the fitted z coordinate of the interaction vertex (see Fig. 6.4). All reconstructed vertices at distances of over 1 m from the target originate from interactions with the beam-line and detector materials. Neglecting the beam attenuation of about 2.8% in the target, ε can be calculated as:

$$\varepsilon = \left(\frac{N_{\mathrm{I}}[z > -450\ \mathrm{cm}]}{N_{\mathrm{I}}} \right) / \left(\frac{N_{\mathrm{R}}[z > -450\ \mathrm{cm}]}{N_{\mathrm{R}}} \right) , \tag{6.5}$$

where $N[z > -450\ \mathrm{cm}]$ is the number of events with fitted vertex $z > -450$ cm; these events were selected with vertex fit requirement. This procedure is insensitive to the target density uncertainty described in Sect. 5.3.

Values of ε are listed in Table 6.4. The strong dependence on the beam momentum might be caused by variation of the ratio of the target density in target removed and inserted (see Sect. 5.3), but also by the energy dependence of the cross-section for proton interactions with nuclei in the detector and by the beam profile.

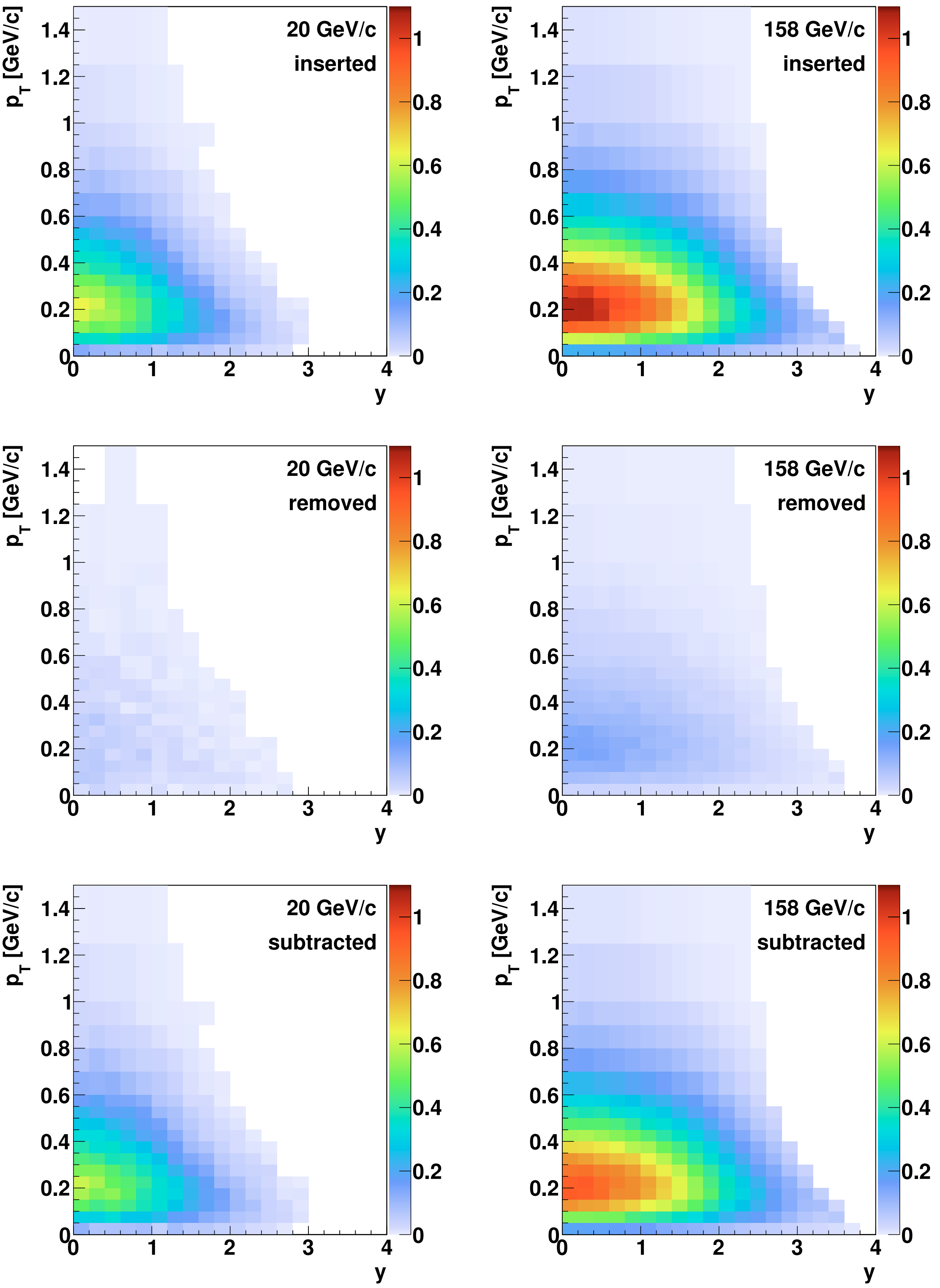

Figure 6.11: Negatively charged hadron spectra after event and track selection for target inserted $n_I[h^-]/(1-\varepsilon)$ (*top*), removed $n_R[h^-]\varepsilon/(1-\varepsilon)$ (*middle*) and their difference (*bottom*) $n_T[h^-]$, normalised as in Eq. (6.4), for 20 (*left*) and 158 GeV/*c* (*right*).

The normalised spectra of target inserted, removed and results of subtraction are shown in Fig. 6.11. As it will be shown in Fig. 6.15, the correction for the off-target interactions changes the yields obtained from the target inserted data by less than ±5%, except in the regions where the statistical uncertainty is high.

As shown in Fig. 6.10, in first approximation spectra of target inserted (proton interactions) and removed (interaction of protons with light nuclei) are similar. Results of the subtraction are thus weakly sensitive to uncertainty of ε.

6.4.2 Correction for contamination of hadrons other than primary π^- mesons

The track selection criteria described in Sect. 6.3 allow to derive spectra of negatively charged hadrons (h^-). It is known that majority of them are π^- [25–27]. The dominating sources of the primary negatively charged hadron tracks (h^-) were identified by examining the MC simulation results:

- primary π^-,
- primary K^-,
- primary $\overline{p}$,
- secondary π^- from K^0_S decays, assigned to the main vertex ($\pi^-_{K^0_S}$),
- secondary π^- from Λ decays, assigned to the main vertex (π^-_{Λ}),
- other particles, mostly products of secondary interactions of various particles (mostly p, π^- and π^+) assigned to the main vertex.

Figure 6.12 shows the h^- spectra from EPOS simulation. Figures 6.13 and 6.14 show relative contributions of π^-, K^-, $\overline{p}$, $\pi^-_{K^0_S}$, π^-_{Λ} and all other particles to h^-. Majority (70–90%) of the particles are primary π^-. Contributions of primary K^- and $\overline{p}$ are significant (~10%) at $p_T > 0.5$ GeV/c and $y > 2$; it is larger at the high beam momenta. On the contrary, contributions of $\pi^-_{K^0_S}$ and π^-_{Λ} and other particles are

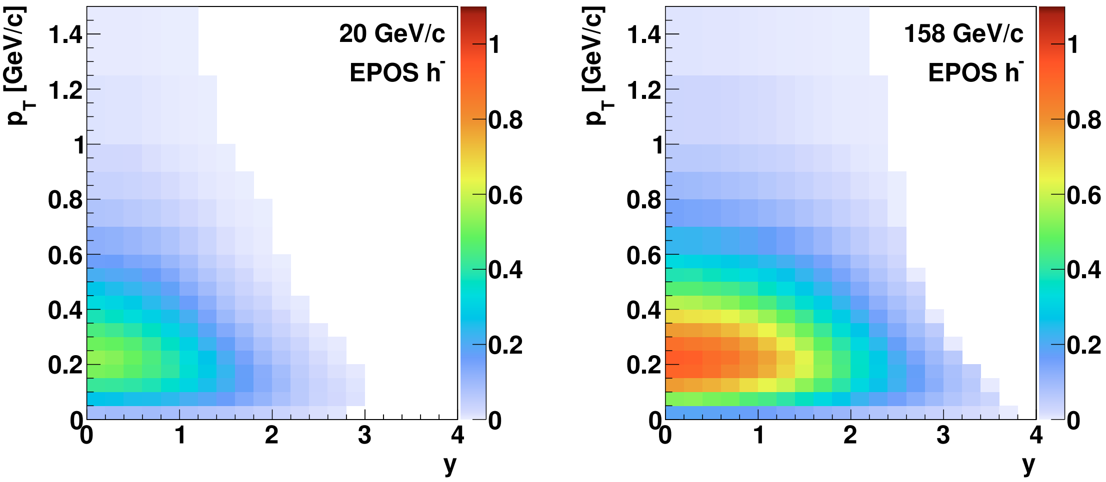

Figure 6.12: Adjusted spectra of negatively charged hadron tracks (h^-) obtained with EPOS simulation of p+p interactions at 20 (*left*) and 158 GeV/c (*right*) measured with the NA61/SHINE detector. The spectra were adjusted as described in Sect. 4.4. Rapidity y was calculated with charged pion mass assumption.

significant (also ∼10%) at the low beam momenta at $p_{\mathrm{T}} < 0.2$ GeV/c and $y < 2$. Contribution of other particles, is of the same order as $\pi^-_{\mathrm{K}^0_\mathrm{S}}$ and π^-_{Λ}. As it originates from numerous sources, mostly secondary interactions of various particles, it was decided not to subdivide this class of particles any further.

The identified particle spectra obtained with MC are used to suppress contribution of particles other than primary π^- from the h^- spectra.

As it was found in Ref. [57] the yields of K^- and $\overline{\mathrm{p}}$ are strongly correlated with the π^- yield. Thus correction for the contribution of primary hadrons is performed via the multiplicative factor c_{K}. On the contrary the weak decays and secondary interactions contribute mostly in the low p_{T} region, and they are weakly correlated with the primary pion yield in this region. Thus this contribution is corrected for using the additive correction c_{V}. The total correction is applied as:

$$\mathsf{n}_{\mathrm{prim}}[\pi^-] = (\mathsf{n}_{\mathrm{T}}[\mathrm{h}^-] - c_{\mathrm{V}}) \cdot c_{\mathrm{K}} \,, \tag{6.6}$$

where

$$c_{\mathrm{V}} = \left(\mathsf{n}[\pi^-_{\Lambda}] + \mathsf{n}[\pi^-_{\mathrm{K}^0_\mathrm{S}}] + \mathsf{n}[\mathrm{other}]\right)^{\mathrm{MC}}_{\mathrm{sel}} \,, \tag{6.7}$$

$$c_{\mathrm{K}} = \left(\frac{\mathsf{n}[\pi^-]}{\mathsf{n}[\mathrm{K}^-] + \mathsf{n}[\overline{\mathrm{p}}] + \mathsf{n}[\pi^-]}\right)^{\mathrm{MC}}_{\mathrm{sel}} \,. \tag{6.8}$$

The adjusted EPOS spectrum $\mathsf{n}[x]$ of a particle x is calculated similarly to Eq. (6.3) as:

$$\mathsf{n}[x] = \frac{t[x] \cdot a[x] \cdot c_{\mathrm{acc}}}{N \cdot \Delta} \,, \tag{6.9}$$

where $t[x]$ is the number of tracks in given bin, $a[x]$ is the adjustment, as defined in Sect. 4.4 and c_{acc} is the acceptance correction for given bin. The term $\mathsf{n}[\mathrm{other}]$ stands for all primary and secondary particles other than K^-, $\overline{\mathrm{p}}$, π^- and $\pi^-_{\mathrm{K}^0_\mathrm{S}}$ and π^-_{Λ}. It originates mostly from the secondary interactions. This contribution was taken from the simulations without adjustment. The superscript $^{\mathrm{MC}}$ marks spectra which were obtained using the Monte Carlo simulation. The subscript $_{\mathrm{sel}}$ indicates that the event and track selection criteria were applied and then the correction for the detector acceptance was performed; the reconstructed tracks were identified with the matching procedure (see Sect. 4.3). One has to note that similarly simple formula could not be written for the data spectrum (Eq. (6.3)), as due to the beam direction effects the acceptance correction is calculated independently for each track.

The correction for contamination of hadrons other than primary π^- mesons will be included in Fig. 6.15. In comparison to the h^- spectra, the corrected π^- spectra are lower by 10% in most regions, and by up to 20% in the high p_{T} region at high beam momenta, and up to 30% in the low p_{T} region at low beam momenta. The fluctuations visible at 20 GeV/c are statistical.

6.4.3 Correction for event losses as well as track losses and track migration between bins

This section describes correction for effects related to the detector and reconstruction inefficiencies, removal of inelastic events by the event selection criteria, removal of tracks by the track selection criteria, and track migration between the

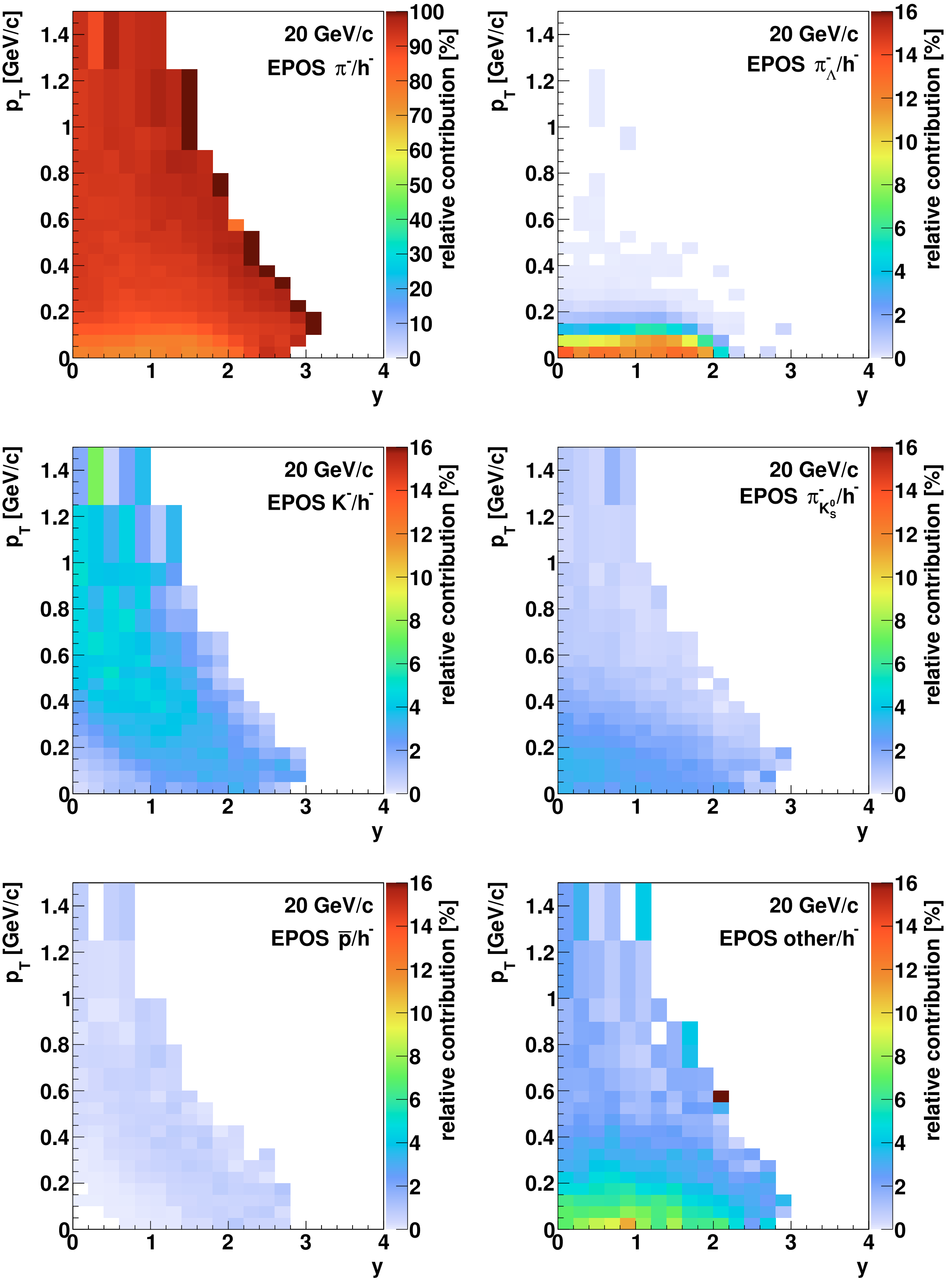

Figure 6.13: Spectra of primary π^-, K^-, $\overline{\mathrm{p}}$ (*left*), secondary π^- from K^0_S and Λ decays assigned to the main vertex ($\pi^-_{\mathrm{K}^0_\mathrm{S}}$ and π^-_Λ), and other reconstructed negatively charged hadron tracks (*right*) divided by sum of all of them (h^-). The results were obtained with EPOS simulation of p+p interactions at 20 GeV/c measured in the NA61/SHINE detector. The spectra were adjusted as described in Sect. 4.4. Note different range of the colour scale for π^-. For all particles rapidity y was calculated with the charged pion mass assumption.

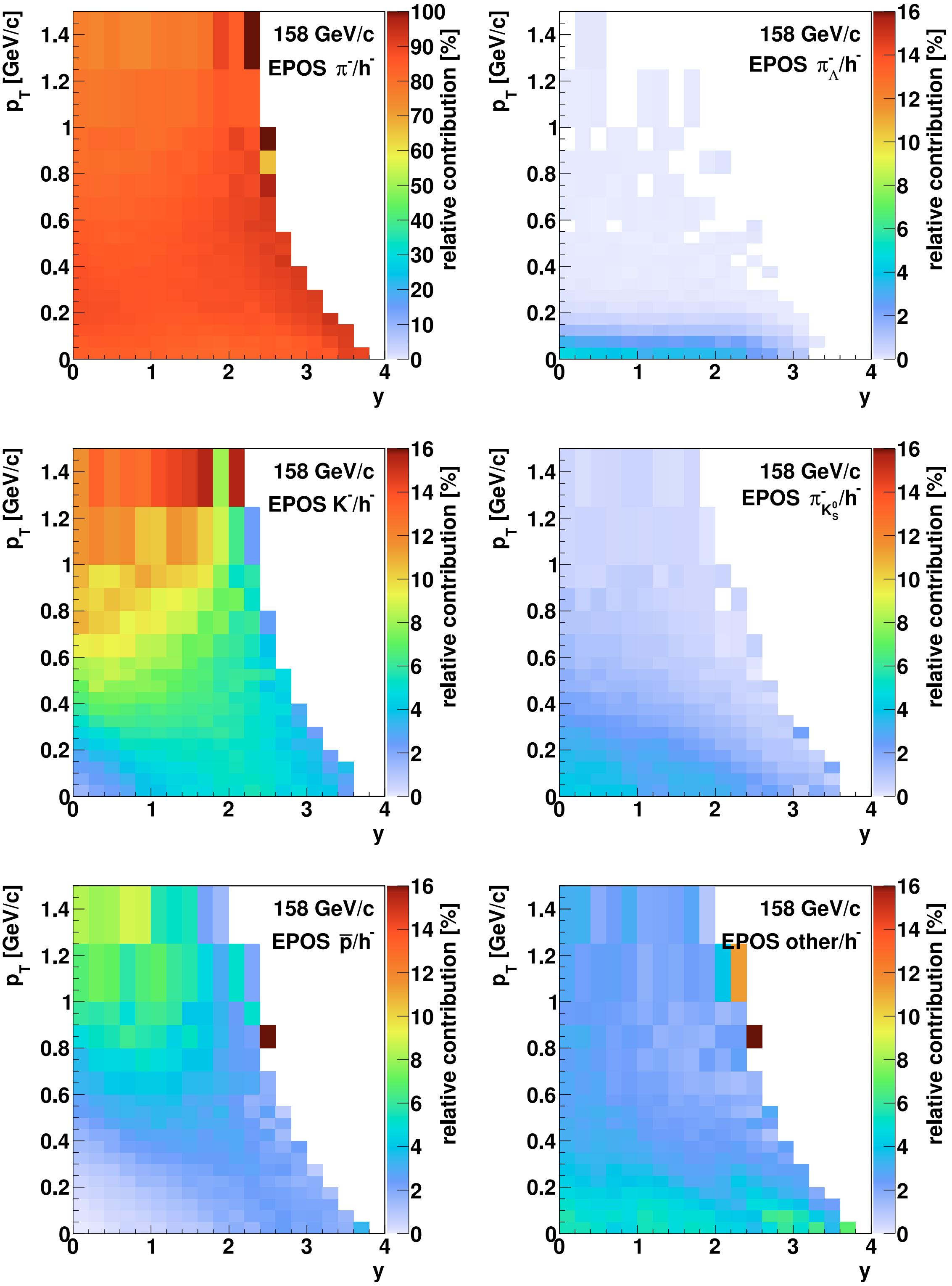

Figure 6.14: Spectra of primary π^-, K^-, $\bar{p}$ (*left*), secondary π^- from K^0_S and Λ decays assigned to the main vertex ($\pi^-_{K^0_S}$ and π^-_{Λ}), and other reconstructed negatively charged hadron tracks (*right*) divided by sum of all of them (h^-). The results were obtained with EPOS simulation of p+p interactions at 158 GeV/*c* measured in the NA61/SHINE detector. The spectra were adjusted as described in Sect. 4.4. Note different range of the colour scale for π^-. For all particles rapidity y was calculated with the charged pion mass assumption.

bins. The track migration effect refers to particles assigned to different (y, p_T) or (y, m_T) bins than if their true momenta were known, due to finite reconstruction resolution. The effect may play a non-negligible role in the regions where the spectrum changes rapidly between the adjacent bins.

The multiplicative correction c_{loss} for losses of inelastic events as well as losses and track migration of primary π^- mesons emitted within the acceptance is calculated using the Monte Carlo simulation as:

$$c_{\text{loss}} = \mathsf{n}[\pi^-]^{\text{MC}}_{\text{gen}} \,/\, \mathsf{n}[\pi^-]^{\text{MC}}_{\text{sel}} \,, \tag{6.10}$$

where

$$\mathsf{n}[\pi^-]^{\text{MC}}_{\text{gen}} = \frac{t[\pi^-]^{\text{MC}}_{\text{gen}}}{N^{\text{MC}}_{\text{gen}}} \,, \tag{6.11}$$

where $t[\pi^-]^{\text{MC}}_{\text{gen}}$ is the number of generated π^- tracks in given bin and $N^{\text{MC}}_{\text{gen}}$ is the number of generated events, while

$$\mathsf{n}[\pi^-]^{\text{MC}}_{\text{sel}} = \frac{t[\pi^-]^{\text{MC}}_{\text{sel}} \cdot c_{\text{acc}}}{N^{\text{MC}}_{\text{sel}}} \,, \tag{6.12}$$

where $t[\pi^-]^{\text{MC}}_{\text{sel}}$ is the number of reconstructed MC π^- tracks selected for the analysis in given bin and $N^{\text{MC}}_{\text{sel}}$ is the number of selected events; c_{acc} stands for the acceptance correction. Then the final, corrected π^- meson spectrum in inelastic p+p interactions is calculated as

$$\mathsf{n}[\pi^-] = c_{\text{loss}} \cdot \mathsf{n}_{\text{prim}}[\pi^-] \,. \tag{6.13}$$

The dominating effects contributing to the correction c_{loss} are

(i) pion migration between bins, c_{mig},
(ii) pion reconstruction inefficiency, c_{eff},
(iii) losses of inelastic events due to the trigger and off-line event selection, c_{sel}.

The correction c_{loss} can be thus factorised as

$$c_{\text{loss}} = c_{\text{mig}} \cdot c_{\text{eff}} \cdot c_{\text{sel}} \,. \tag{6.14}$$

The correction for pion migration is defined as

$$c_{\text{mig}} = \mathsf{n}[\pi^-]^{\text{MC}}_{\text{sel}}(\vec{p} = \vec{p}_{\text{gen}}) \,/\, \mathsf{n}[\pi^-]^{\text{MC}}_{\text{sel}} \,, \tag{6.15}$$

where $\mathsf{n}[\pi^-]^{\text{MC}}_{\text{sel}}(\vec{p} = \vec{p}_{\text{gen}})$ is the reconstructed MC π^- spectrum histogrammed using the simulated momentum, rather than the reconstructed one.

The correction for the reconstruction efficiency is defined as

$$c_{\text{eff}} = \mathsf{n}[\pi^-]^{\text{MC}}_{\text{gen}}(\overline{\text{S4}}) \,/\, \mathsf{n}[\pi^-]^{\text{MC}}_{\text{sel}}(\vec{p} = \vec{p}_{\text{gen}}) \,, \tag{6.16}$$

where $\mathsf{n}[\pi^-]^{\text{MC}}_{\text{gen}}(\overline{\text{S4}})$ is the generated π^- spectrum in events passing the event selection cuts. This includes selection of events with no signal in the S4 counter.

Finally the correction for event losses is defined as

$$c_{\text{sel}} = \mathsf{n}[\pi^-]^{\text{MC}}_{\text{gen}} \,/\, \mathsf{n}[\pi^-]^{\text{MC}}_{\text{gen}}(\overline{\text{S4}}) \,. \tag{6.17}$$

The total correction c_{loss} and its contributions c_{mig}, c_{eff} and c_{sel} are shown in Fig. 6.15.

6.4.4 Rejection of poor quality bins of the final spectra

The $(y,\ p_T)$ or $(y,\ m_T)$ bins were removed from the final results in the following cases:

(i) The relative statistical uncertainty of the bin content is greater than 100%. The reason is to avoid very large biases in the regions of the lowest statistics.

(ii) The relative statistical uncertainty introduced by the MC corrections (including the h^- correction and c_{loss}) is greater than 20%. The reason is to minimise systematic bias introduced by the MC corrections in the regions where their systematic uncertainties might be underestimated.

(iii) The bin is isolated in p_T or m_T from the rest of the spectrum. The missing bins in the middle of the spectra could hinder interpretation of the results by persons employing them in future analyses.

In all five dataset in total, out of 1148 non-empty $(y,\ p_T)$ RST bins at positive rapidity, 5 were rejected due to the criterion (i), 2 due to the criterion (ii) and 1 due to the criterion (iii).

6.4.5 Total correction

Figure 6.15 shows example magnitudes of corrections applied to the spectra. The fluctuations that can be observed at 20 GeV/c in particular in the low and the high p_T bin occur due to low statistics. This effect is included in the total statistical uncertainty. The target removed subtraction is in general very small. Correction for contamination of particles other than primary π^- ranges from −5% to −20% and it is the highest at 158 GeV/c in the high p_T region. Correction for event losses is of order of −10%. The total correction

$$c_{\mathrm{TOTAL}} = \mathsf{n}[\pi^-]/\mathsf{n}_{\mathrm{I}}[\mathrm{h}^-] \tag{6.18}$$

typically ranges from −15% to −30%.

Figure 6.16 shows the total correction c_{TOTAL} at 20, 31, 40, 80 and 158 GeV/c. The correction compared at $y \approx 1$ and $p_T \approx 0.5$ GeV/c changes from −15% at 20 GeV/c to −25% at 158 GeV/c. This change is mostly caused by the increase of c_{h^-} at higher beam momenta due to larger production of particles heavier than π: K^-, K^0_S, $\overline{\mathrm{p}}$ and Λ.

6.5 Statistical and systematic uncertainties

6.5.1 Statistical uncertainties

Statistical errors receive contributions from the finite statistics of both the data as well as the simulated events used to obtain the correction factors. The main assumption was that the numbers of tracks in each bin were undergoing Poisson distribution. This neglects correlations between the tracks in each event, which are expected to have low impact on the uncertainty.

The dominating contribution is the uncertainty of the measured data which is calculated in approximation of independent particles. The MC statistics was higher than the data statistics. Also the uncertainties of the MC corrections calculated

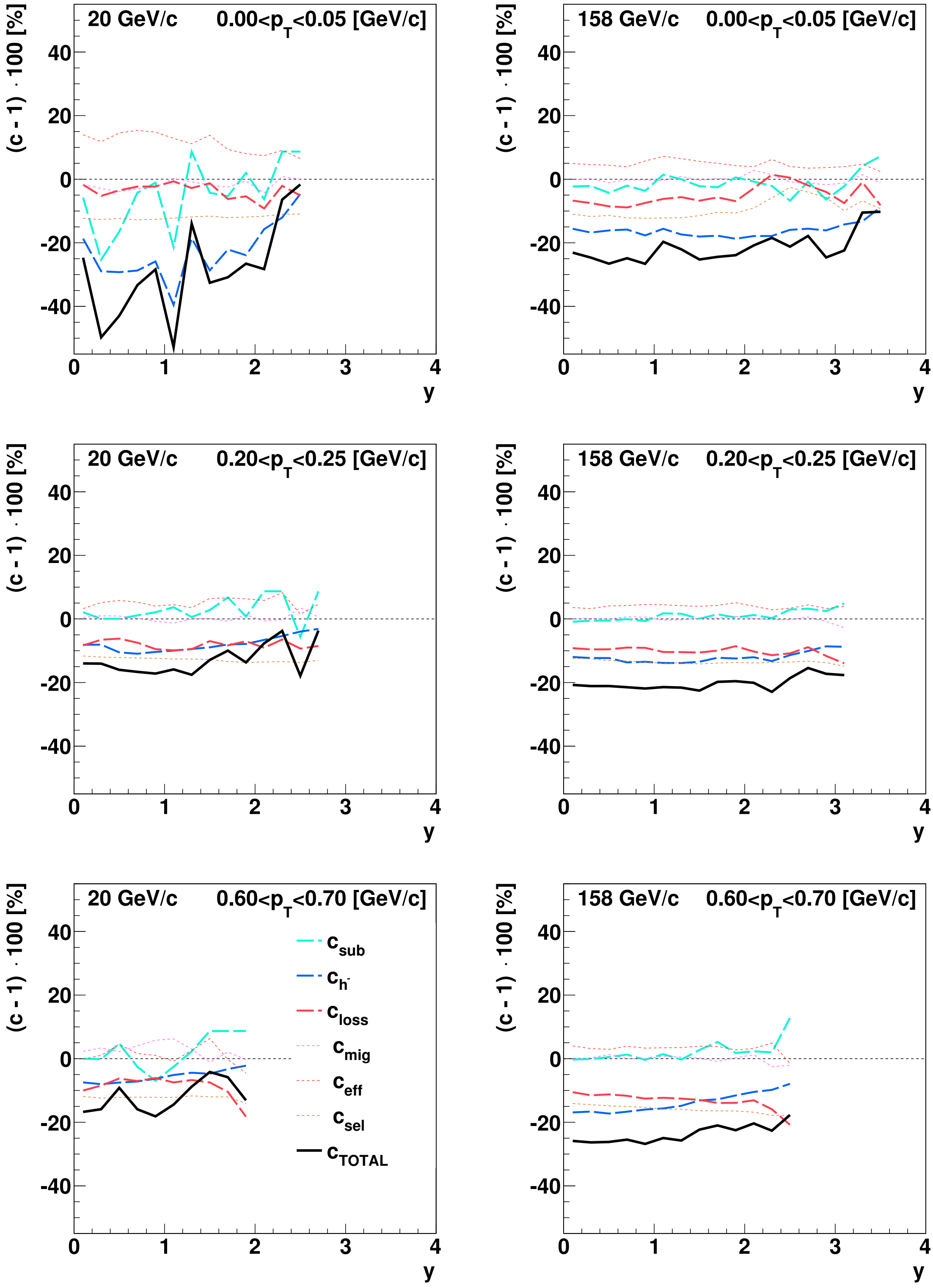

Figure 6.15: Relative corrections at 20 (*left*) and 158 GeV/c (*right*) in selected p_{T} bins. Thick coloured dashed lines show: effective correction from the target removed subtraction procedure $c_{\mathrm{sub}} \equiv \mathrm{n_T[h^-]/n_I[h^-]}$ (see Sect. 6.4.1), effective correction for contribution of particles other than primary π^-, $c_{\mathrm{h^-}} \equiv \mathrm{n_{prim}}[\pi^-]/\mathrm{n_T[h^-]}$ (see Sect. 6.4.2) and correction for event and track losses and migration c_{loss} (see Sect. 6.4.3) and its contributions c_{mig}, c_{eff} and c_{sel} drawn with thin dashed lines. The legend drawn in the *bottom left* panel concerns all panels. The thick continuous black line shows the effective total correction c_{TOTAL}, as defined in Eq. (6.18). A horizontal dashed line at 0 is drawn for reference.

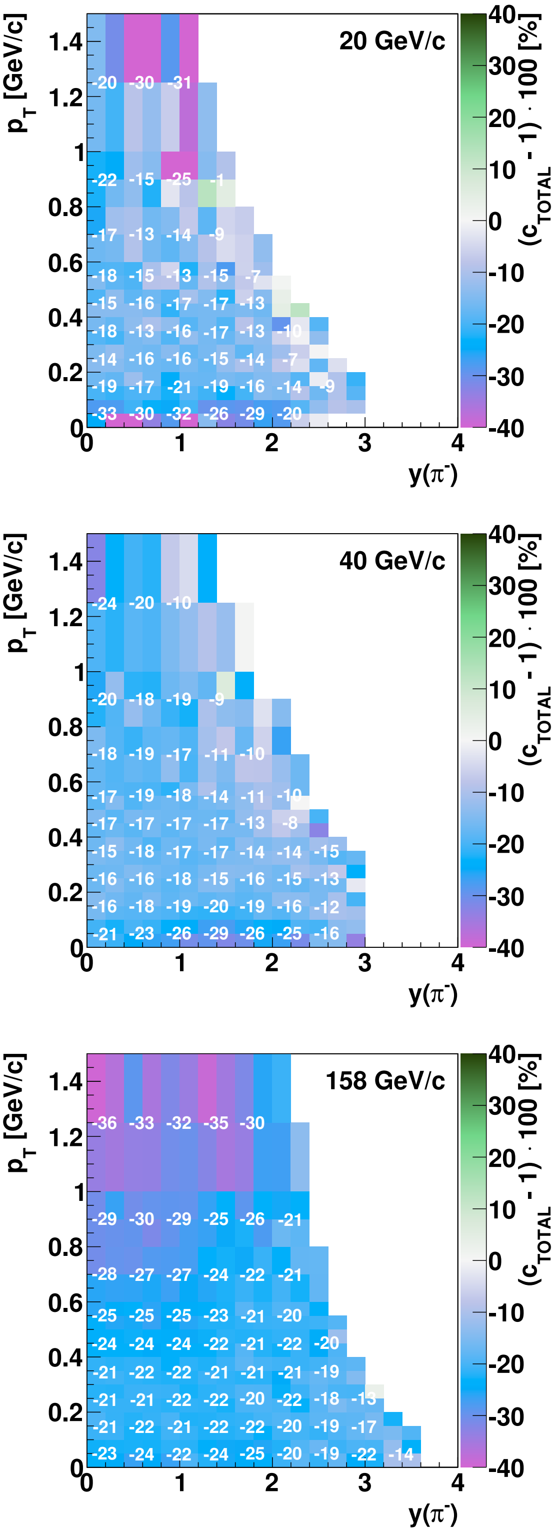

Figure 6.16: The total correction c_{TOTAL} (see Eq. (6.18)) at 20, 31, 40, 80 and 158 GeV/c. The numbers printed are averages for each four non-empty adjacent bins.

assuming binomial distribution are significantly smaller than the uncertainties of the number of entries in bins undergoing Poisson distribution.

Statistical uncertainties $\sigma_{\mathsf{n}_{\mathrm{I/R}}[\mathrm{h}^-]}$ of the uncorrected target inserted and removed spectra (Eq. (6.3)) were calculated assuming Poisson probability distribution for the number of entries (weighted by the acceptance correction) in a bin:

$$\sigma_{\mathsf{n}[\mathrm{h}^-]} = \frac{\sqrt{\sum_{i=1}^{t[\mathrm{h}^-]} (c^i_{\mathrm{acc}})^2}}{N} \,, \tag{6.19}$$

where $t[\mathrm{h}^-]$ is the number of tracks in given bin and c^i_{acc} is the acceptance correction calculated for each track. For the empty bins in the target removed histograms the uncertainty was calculated assuming a single entry, if at least three (out of eight) adjacent bins were not empty (i.e. they contained any measured tracks). This allowed for more realistic estimation of the uncertainties in these bins, without overestimating them at the far edges of the spectrum, where it is unlikely to find any tracks.

In the subtraction procedure (Eq. (6.4)) the uncertainty was calculated from independent uncertainties of target inserted and removed spectra. Uncertainty of ε was neglected, as it was of order of 1% only (see Table 6.4), and also the results were weakly sensitive to its small deviations:

$$\sigma_{\mathsf{n}_{\mathrm{T}}[\mathrm{h}^-]} = \frac{1}{1-\varepsilon} \cdot \sqrt{\sigma^2_{\mathsf{n}_{\mathrm{I}}[\mathrm{h}^-]} + \varepsilon \cdot \sigma^2_{\mathsf{n}_{\mathrm{R}}[\mathrm{h}^-]}} \,. \tag{6.20}$$

Uncertainty of the additive correction (c_{V}, see Eq. (6.7)) was calculated assuming Poisson distribution of the number of each particle type in given bin:

$$\sigma_{c_{\mathrm{V}}} = \sqrt{\sum_{x=\pi^-_{\Lambda},\ \pi^-_{\mathrm{K}^0_{\mathrm{S}}},\ \mathrm{other}} \sigma^2_{\mathsf{n}[x]}} \,, \tag{6.21}$$

where the uncertainty of spectrum of particle x (defined in Eq. (6.9)):

$$\sigma_{\mathsf{n}[x]} = \frac{\sqrt{t[x]} \cdot a[x] \cdot c_{\mathrm{acc}}}{N \cdot \Delta} \,. \tag{6.22}$$

The multiplicative correction (c_{K}, see Eq. (6.8)) is calculated by dividing $\mathsf{n}[\pi^-]$ by $\mathsf{n}[\mathrm{K}^-] + \mathsf{n}[\overline{\mathrm{p}}] + \mathsf{n}[\pi^-]$. As the component $\mathsf{n}[\pi^-]$ dominates over $\mathsf{n}[\mathrm{K}^-]$ and $\mathsf{n}[\overline{\mathrm{p}}]$, the nominator and the denominator are strongly correlated. Taking into account this correlation the uncertainty of c_{K} is much smaller than that of c_{V}:

$$\sigma_{c_{\mathrm{K}}} = c^2_{\mathrm{K}} \cdot \frac{\mathsf{n}[\mathrm{K}^-] + \mathsf{n}[\overline{\mathrm{p}}]}{\mathsf{n}[\pi^-]} \cdot \sqrt{\left(\frac{\sigma_{\mathsf{n}[\pi^-]}}{\mathsf{n}[\pi^-]}\right)^2 + \frac{\sigma^2_{\mathsf{n}[\mathrm{K}^-]} + \sigma^2_{\mathsf{n}[\overline{\mathrm{p}}]}}{(\mathsf{n}[\mathrm{K}^-] + \mathsf{n}[\overline{\mathrm{p}}])^2}} \,. \tag{6.23}$$

Uncertainty c_{loss} (see Eq. (6.10)) was calculated assuming the denominator $\mathsf{n}[\pi^-]^{\mathrm{MC}}_{\mathrm{sel}}$ is a subset of nominator $\mathsf{n}[\pi^-]^{\mathrm{MC}}_{\mathrm{gen}}$ and thus undergoes binomial distribution. This assumption is not exactly true as some of the reconstructed tracks assigned to given bin might originate from tracks generated in adjacent bins, due to finite reconstruction resolution and the track migration effect. This effect has negligible impact on the uncertainty $\sigma_{c_{\mathrm{loss}}}$. The uncertainty is calculated as follows:

$$\sigma_{c_{\mathrm{loss}}} = c_{\mathrm{loss}} \sqrt{\frac{t[\pi^-]_{\mathrm{gen}} - t[\pi^-]_{\mathrm{sel}}}{t[\pi^-]_{\mathrm{gen}} \cdot t[\pi^-]_{\mathrm{sel}}}} \,. \tag{6.24}$$

Potentially this formula could return nonsense results if the difference in the nominator under the square root would be less or equal zero but this has never happened.

The total statistical uncertainty is calculated as:

$$\begin{aligned} \sigma_{\mathrm{stat}} = \Big[& \left(\sigma_{c_{\mathrm{loss}}} \cdot c_{\mathrm{K}} \cdot (\mathrm{n_T}[\mathrm{h}^-] - c_{\mathrm{V}})\right)^2 + \left(\sigma_{c_{\mathrm{K}}} \cdot c_{\mathrm{loss}} \cdot (\mathrm{n_T}[\mathrm{h}^-] - c_{\mathrm{V}})\right)^2 \\ & + \left(\sigma_{\mathrm{n_T}[\mathrm{h}^-]} \cdot c_{\mathrm{K}} \cdot c_{\mathrm{loss}}\right)^2 + \left(\sigma_{c_{\mathrm{V}}} \cdot c_{\mathrm{K}} \cdot c_{\mathrm{loss}}\right)^2 \Big]^{1/2} \,, \end{aligned} \tag{6.25}$$

compare with Eqs. (6.6) and (6.10). The total statistical uncertainty is shown in Figs. 6.17 and 6.18. It is below 1% in the middle of the y–p_{T} phase-space, and stays below 10% except in the bins at the end of the measured spectrum at the largest y and p_{T}. The uncertainty is larger at the low beam momenta, in particular at 20 GeV/c, due to smaller number of events recorded and smaller number of particles produced per event.

6.5.2 Systematic uncertainties

Systematic uncertainties presented in this thesis were calculated independently in each bin. Figure 6.17 shows the total systematic uncertainties and the contributing effects, which are listed below.

(i) Possible biases due to event and track cuts which are not corrected for. These are:

- a possible bias due to the dE/dx cut applied to remove electrons,
- a possible bias related to insufficient rejection of events with off-time beam particles close in time to the trigger particle.

The magnitude σ_{i} of possible biases was estimated by varying values of the corresponding cuts. The dE/dx cut was shifted by ±0.01 dE/dx units (where 1.0 corresponds to minimum ionising particle, and 0.04 is a typical width of the dE/dx distribution in small momentum range for π^-, K^- and $\overline{\mathrm{p}}$), and the off-time interactions cut was varied from a ±1 μs to a ±3 μs time window. As the two sources of the uncertainty might be correlated the assigned systematic uncertainty was calculated as the maximum of the absolute differences between the results obtained for both values of the cut. This contribution is drawn with a long-dashed red line (– –) in Fig. 6.17. This is the dominating source of the systematic uncertainty at the low beam momenta, exceeding 10% at the edges of the phase-space. It might be however overestimated in these regions due to the statistical fluctuations.

(ii) Uncertainty of the correction for contamination of the h^- spectra by particles other than primary π^- mesons. The systematic uncertainty σ_{ii} of this correction was assumed as 20% (for 40, 80 and 158 GeV/c) and 40% (for 20

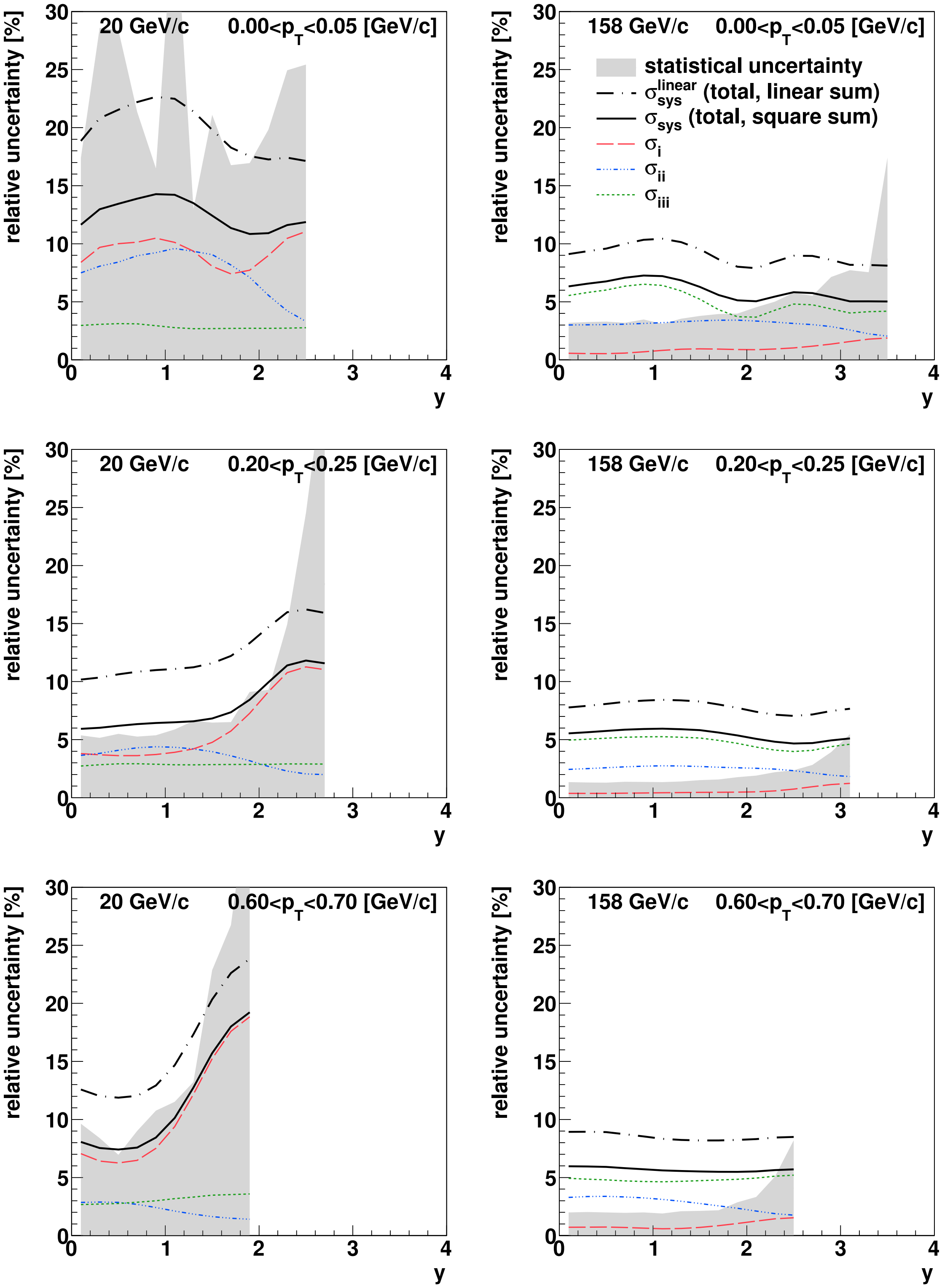

Figure 6.17: Statistical and systematic uncertainties in selected p_T bins for 20 (*left*) and 158 GeV/*c* (*right*) p+p data. The shaded band shows the statistical uncertainty; at 20 GeV/*c* the uncertainty exceeds the vertical scale on the plot in several bins. The coloured thin lines show the contributions to the systematic uncertainty listed in Sect. 6.5.2. The thick black lines show the total systematic uncertainty, which was calculated by adding the contributions in quadrature (continuous line) or linearly (dashed/dotted line).

and 31 GeV/c) of the absolute value of the correction. The increase of the uncertainty at the low beam momenta was arbitrary in order to reflect lower availability of the reference data to adjust the simulated spectra. This contribution is drawn with a dashed-dotted blue line (-····-) in Fig. 6.17. The absolute correction is typically of order of −5% to −15% thus the related systematic uncertainty is small.

(iii) Uncertainty of the correction for the event losses. The uncertainty was estimated using 20% of the correction magnitude and a comparison with the correction $c_{\mathrm{loss}}^{\mathrm{VENUS}}$ calculated using the VENUS model instead of EPOS:

$$\sigma_{\mathrm{iii}} = 0.2 \cdot |1 - c_{\mathrm{loss}}| + \left| c_{\mathrm{loss}} - c_{\mathrm{loss}}^{\mathrm{VENUS}} \right| . \tag{6.26}$$

This contribution is drawn with a short-dashed green line (- - -) in Fig. 6.17. This uncertainty typically does not exceed 5%.

(iv) Uncertainty related to the track selection method. It was estimated by varying the track selection cuts: removing the impact parameter cut and decreasing the minimum number of required points to 25 (total) and 10 (in VTPCs) and by checking symmetries with respect to $y = 0$ and $p_{\mathrm{T}} = 0$. The potential bias was found below 2% and the corresponding contribution was not taken into account in the total systematic uncertainty estimation.

The total systematic uncertainty was calculated by adding the contributions in quadrature:

$$\sigma_{\mathrm{sys}} = \sqrt{\sigma_{\mathrm{i}}^2 + \sigma_{\mathrm{ii}}^2 + \sigma_{\mathrm{iii}}^2} . \tag{6.27}$$

Finally the systematic uncertainty is averaged between the neighbouring bins. The reason is that the uncertainty is estimated rather than calculated. Results of the calculations described above might be overestimated or underestimated due to statistical fluctuations which do not have impact on the actual systematic error of the data, and are already included in the statistical uncertainty.

The systematic uncertainty is listed in the tables with the numerical values in Appendix C and it is visualised by a shaded band around the data points in plots presenting the results. Statistical and systematic uncertainties in selected example regions are shown in Fig. 6.17. For comparison, the figure includes the alternative systematic uncertainty estimate calculated as a linear sum $\sigma_{\mathrm{sys}}^{\mathrm{linear}} = \sigma_{\mathrm{i}} + \sigma_{\mathrm{ii}} + \sigma_{\mathrm{iii}}$, which is maximum value in case of full correlation of the three contributions. However, as the correlation appears to be unlike, the quadrature sum (Eq. (6.27)) was used as a final systematic uncertainty estimation.

Systematic biases in different bins are correlated, whereas statistical fluctuations are almost independent.

In order to calculate the systematic uncertainties of the integrated rapidity spectra and of the spectra parameters presented in Chapter 7 (like the inverse slope parameter T or average transverse mass $\langle m_{\mathrm{T}} \rangle$) the procedure described in this section was repeated independently for each value calculated. As the systematic uncertainties are strongly correlated between the adjacent bins it is impossible to propagate them similarly to the statistical uncertainties.

The total systematic uncertainty σ_{sys} is shown in Fig. 6.19. The systematic uncertainty is the lowest in the region of p_{T} from 0.1 GeV/c up to about 0.5 GeV/c below the maximum p_{T} measured. It increases at the low p_{T} due to contamination of the secondary particles, and at the high p_{T} due to contamination of primary K^-

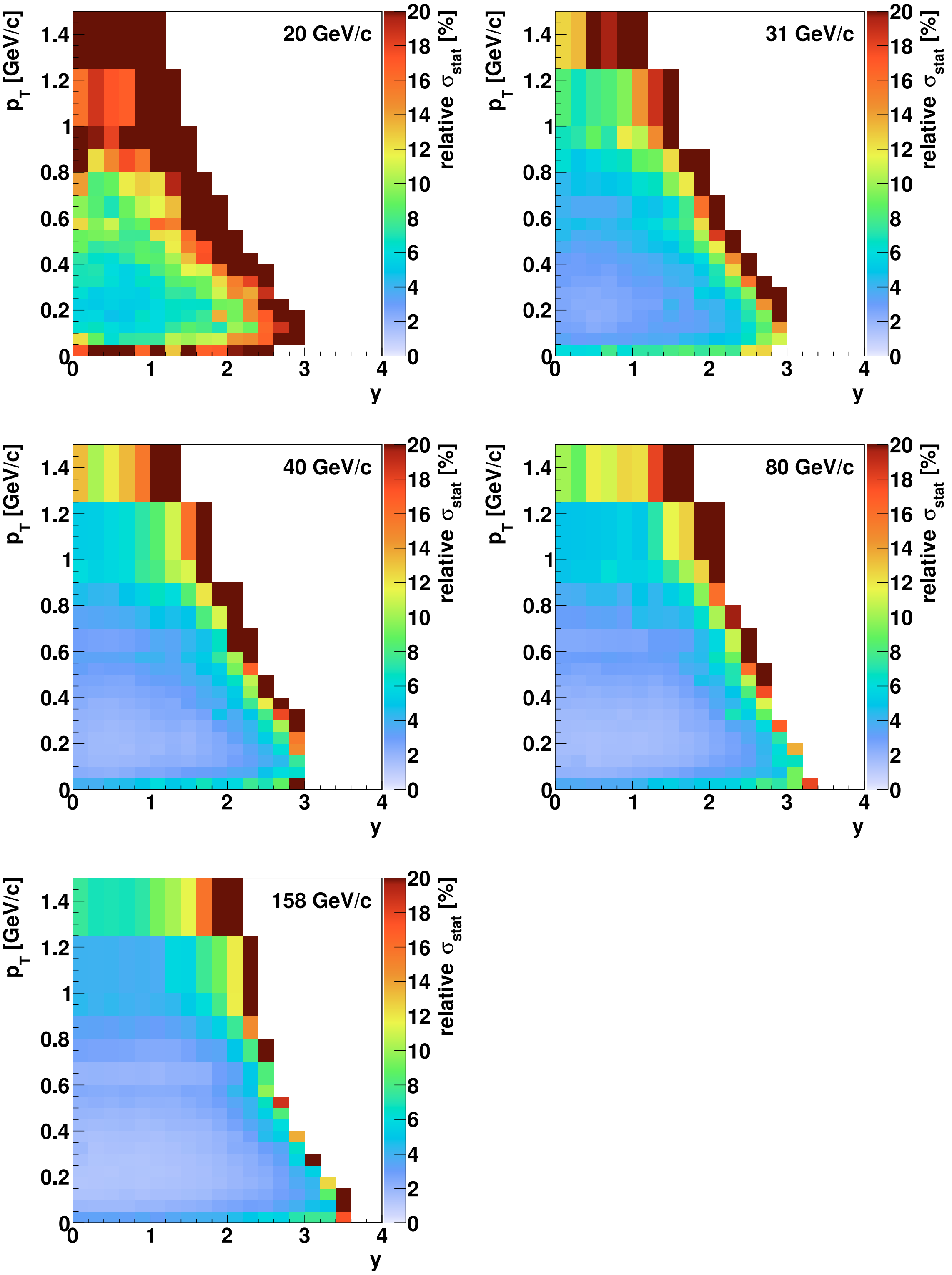

Figure 6.18: Relative statistical uncertainty σ_{stat} (see Eq. (6.25)) of the π^- spectra for 20, 31, 40, 80 and 158 GeV/*c*.

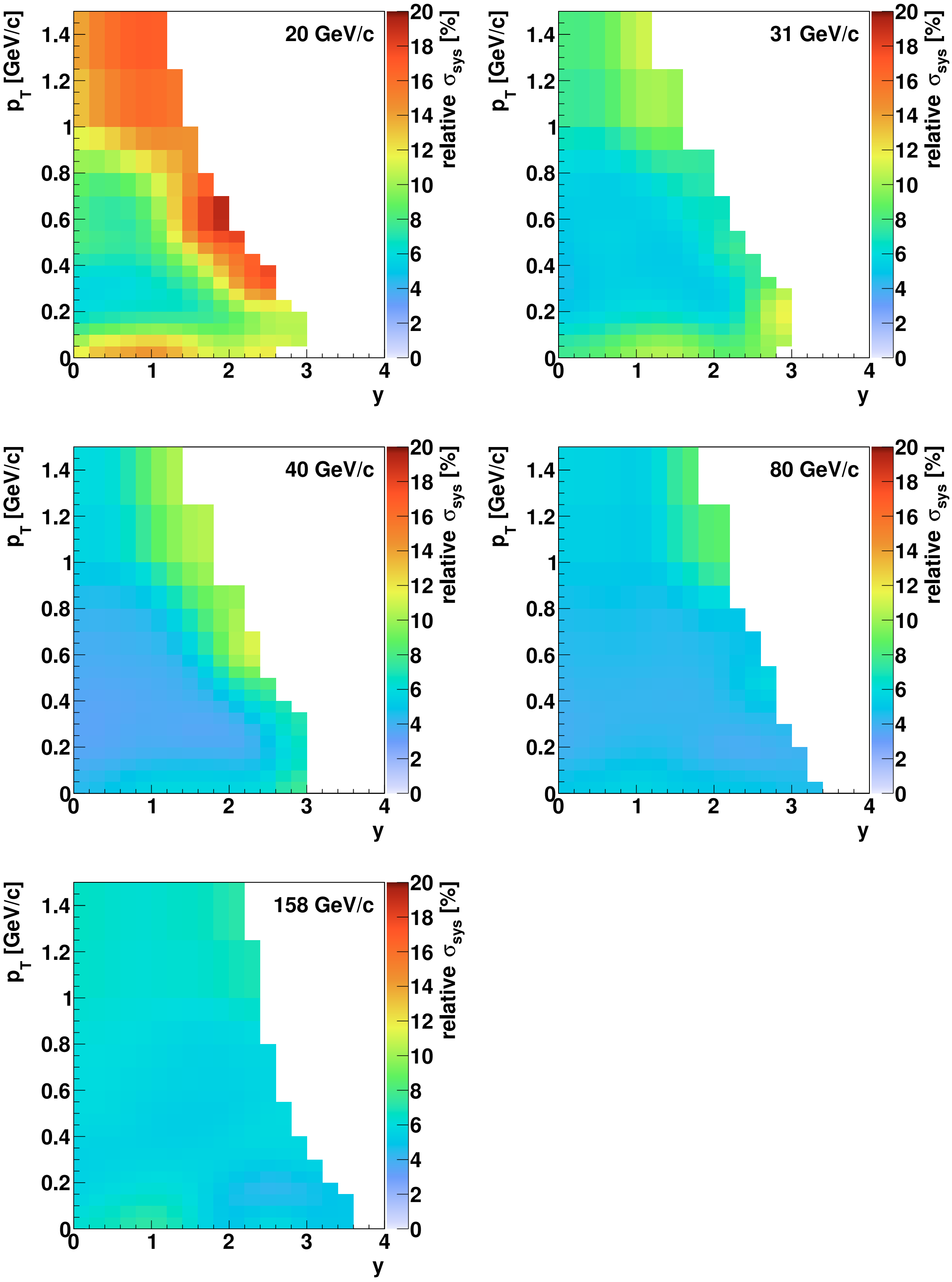

Figure 6.19: Relative systematic uncertainty σ_{sys} (see Eq. (6.27)) of the π^- spectra for 20, 31, 40, 80 and 158 GeV/c.

and $\overline{\mathrm{p}}$. The uncertainty is the lowest, down to 4%, at 40 GeV/c. It is higher at the lower beam momenta due to higher uncertainty of the h^- correction, and at the higher beam momenta due to the bias introduced by use of the S4 counter. In most regions it is below 10%, except at 20 GeV/c in the regions of the highest measured p_{T} where the low statistics limits the precision of the systematic uncertainty calculation.

6.6 Cross checks of the final spectra

6.6.1 Introduction

Validity of the final π^- spectra was verified in several tests. First, the expected symmetries of the spectra were evaluated. Second, the existing measurements of p+p interactions at 32 GeV/c [71] and 158 GeV/c [25] were compared with the NA61/SHINE results. Also the NA61/SHINE rapidity spectra were compared with the results at 12 and 24 GeV/c [72] and at 19 GeV/c [73]. This last comparison is rather inconclusive concerning correctness of the results, but rather reveals difficulty in comparing results obtained at different beam momenta.

The spectra used for the comparisons include all corrections. The method to obtain integrated rapidity spectra and their parametrisation will be explained in detail in Sect. 7.4.

6.6.2 Symmetries of the spectra

Spectra of the particles produced in collisions of non-polarised, identical particles are expected to obey reflection symmetry with respect to mid-rapidity and rotational symmetry around the beam axis. The latter symmetry imposes that the RST and WST spectra (as defined in Eq. (6.1)) are identical.

As the NA61/SHINE acceptance extends somewhat below mid-rapidity check of the reflection symmetry can be used to validate the measurements. This check is illustrated in Fig. 6.20, where the fully corrected spectra in y–p_{T} are shown above and below mid-rapidity. Yields measured for $y < 0$ agree within 1.5% with those measured for $y > 0$ in the reflected acceptance. A similar agreement was also found at the lower beam momenta. Only the measurements above mid-rapidity are taken as the final results. Nevertheless, for comparison the points at $y < 0$ are added in Figs. 6.22 and 7.6 in the regions where the measured p_{T} range extends to zero.

Figure 6.20 shows selected WST spectra in full rapidity range. The acceptance of the wrong side track spectra extends further in the backward rapidity, and a bit in the very forward rapidity. However, as shown in the figure, the acceptance of the wrong side tracks misses some regions at the forward rapidity, in particular at the low beam momenta. The missing regions at low p_{T} at 20 GeV/c and high p_{T} at 158 GeV/c correspond to particles passing through the uninstrumented gap around the beam line. Small differences between the forward an backward rapidity, and between RST and WST are due to statistical fluctuations.

Figure 6.21 shows ratios of spectra at $y > 0$ to the spectra reflected with respect to $y = 0$ and to the wrong side track spectra. The ratios are expected to equal 1. The phase-space available for the comparison is very limited, in particular at the low beam momenta. A bin-by-bin comparison is inconclusive due to statistical

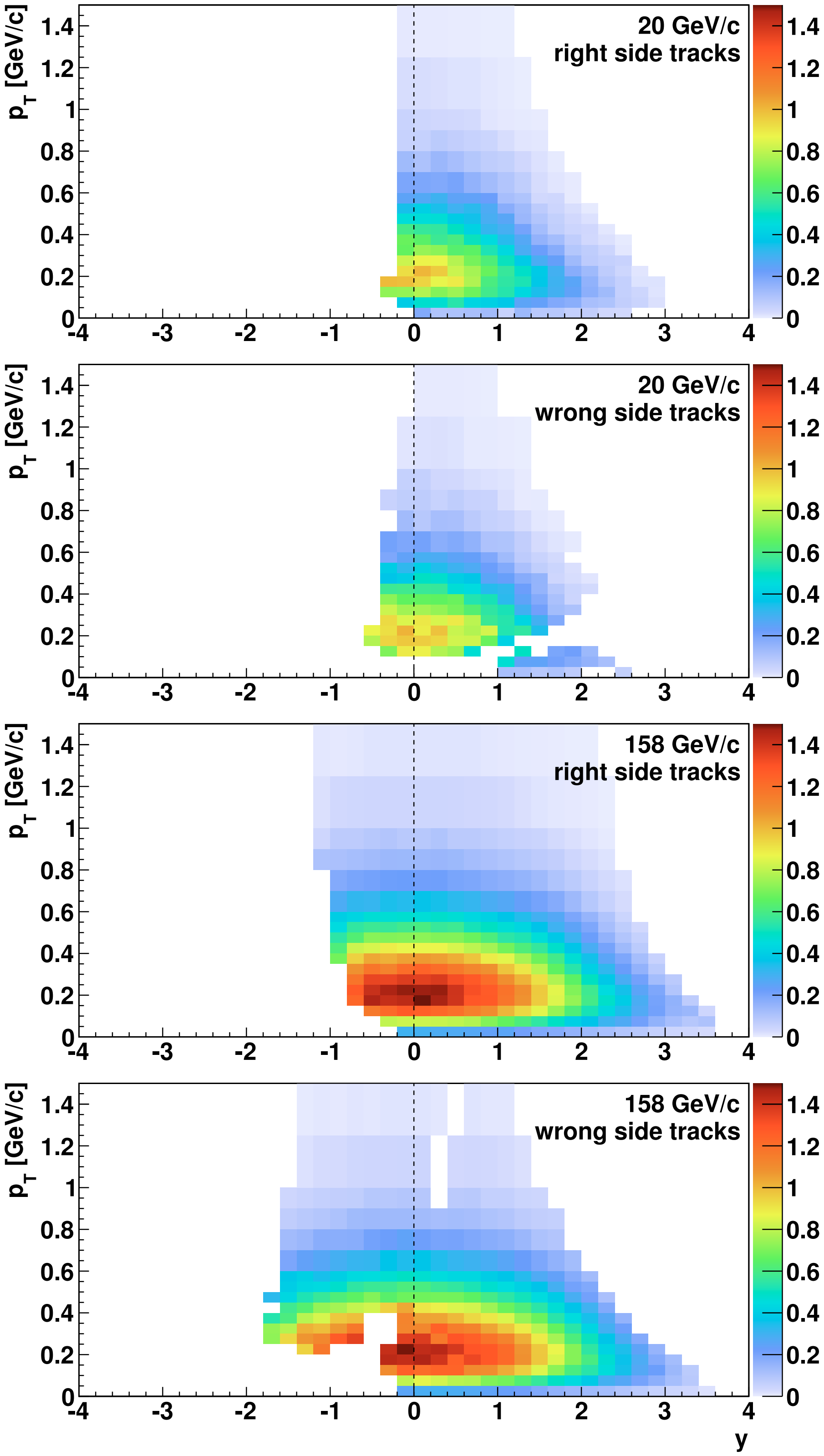

Figure 6.20: Fully corrected rapidity and the transverse momentum spectrum of the π^- mesons produced in inelastic p+p interactions at 20 (two *top* panels) 158 GeV/*c* (two *bottom* panels) obtained from the regular right side track analysis and wrong side tracks (marked in the legend). Data below and above mid-rapidity are shown to illustrate reflection symmetry of the measured spectrum with respect to $y = 0$ (as marked with the dashed line).

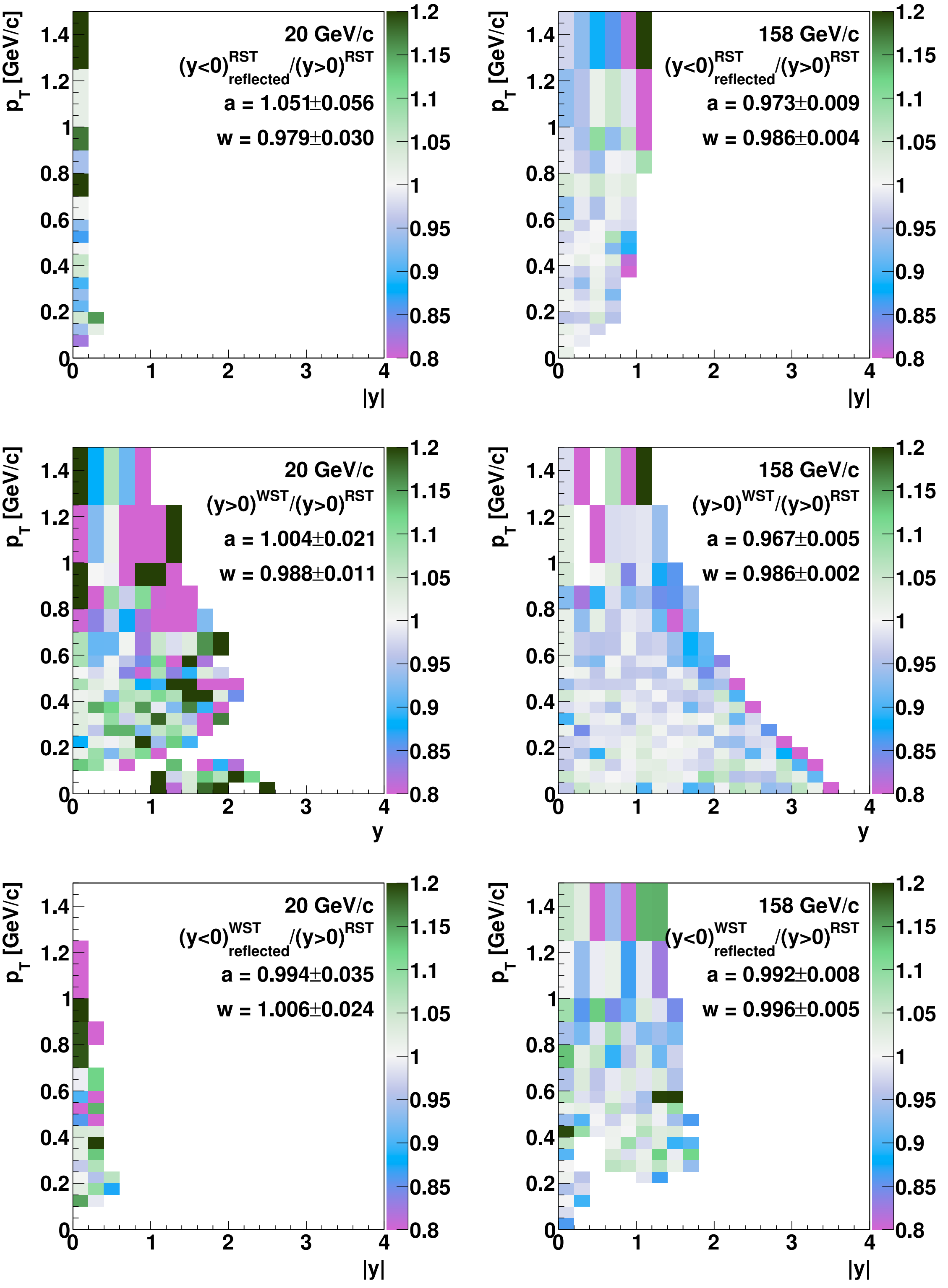

Figure 6.21: Verification of the symmetry between RST and WST and symmetry with respect to mid-rapidity at 20 (*left*) and 158 GeV/*c* (*right*). The plots of RST spectra at $y < 0$ reflected with respect to $y = 0$ (*top*), WST spectra (*middle*) and WST spectra at $y < 0$ reflected with respect to $y = 0$ (*bottom*) are divided by the RST spectra at $y > 0$. All these four spectra are expected to be identical thus the ratios should equal 1. Averages of the ratios: arithmetic a and weighted by the statistical uncertainties w are given in the legend.

fluctuations, however the average difference between the spectra typically does not exceed 2%. This result is consistent with expected symmetries of the spectra with respect to $y = 0$ and between WST and RST.

6.6.3 Comparison with existing p+p data at 32 and 158 GeV/*c*

Figure 6.22 (*left*) shows a comparison of the rapidity distribution at 31 GeV/*c* with the MIRABELLE results at 32 GeV/*c* [71]. A Gaussian parametrisation of the distribution and the total π^- multiplicity are provided. The normalisation of the parametrisation provided in Ref. [71] appears to be incorrect, possibly due to missing factor $1/(\sigma\sqrt{2\pi})$ in the Gaussian formula. The discrepancy was solved by normalising the parametrisation shown in Fig. 6.22 to the total multiplicity. The results agree within the NA61/SHINE systematic uncertainties.

Figure 6.22 (*right*) presents a comparison of the rapidity spectrum of the π^- mesons produced in inelastic p+p interactions at 158 GeV/*c* from the present analysis with the corresponding spectrum measured by NA49 [25]. Statistical and systematic uncertainties of the NA49 spectrum are not explicitly given but the published information implies that the systematic uncertainty dominates and amounts to several %. The results agree within the systematic uncertainties of the NA61/SHINE spectra.

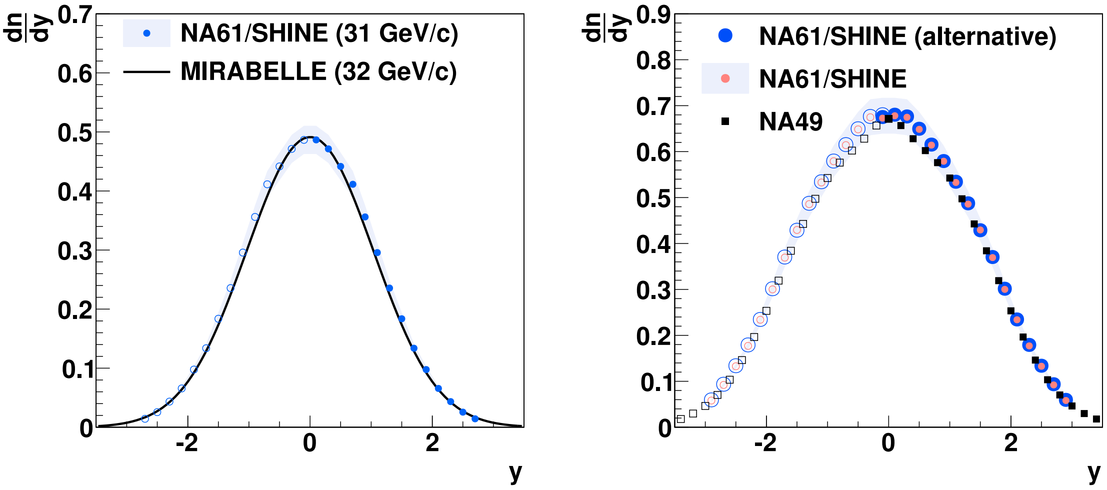

Figure 6.22: Comparisons of the rapidity distribution of the π^- mesons produced in inelastic p+p interactions. *Left:* The NA61/SHINE results at 31 GeV/*c* (blue points) are compared with the MIRABELLE measurement (parametrised by the black line) at 32 GeV/*c*. The shaded band shows the NA61/SHINE systematic uncertainty. *Right:* Rapidity distribution of the π^- mesons produced in inelastic p+p interactions at 158 GeV/*c*. The large blue points show the results obtained with an alternative method: without vertex fit requirement and rejection of events with a single very high momentum positively charged track. The results of NA61/SHINE (red dots) are compared with the NA49 measurements [25] (black squares). The open symbols show points reflected with respect to mid-rapidity. A single NA61/SHINE point measured at $y < 0$ is also shown for comparison. The shaded band shows the NA61/SHINE systematic uncertainty.

The analysis method of p+p interactions at 158 GeV/*c* performed by NA49 [25] differed from the one used in this thesis. In particular, pions were identified by dE/dx measurement and the NA49 event selection criteria did not include the selection according to the fitted z coordinate of the interaction vertex and the rejection of elastic interactions. Namely, all events passing the trigger selection and off-line quality cuts were used for the analysis. For comparison, this event selection procedure was applied to the NA61/SHINE data. As a result 20% more events were accepted. Approximately half of them were the elastic and off-target interactions and half were required inelastic interactions. Then the corrections corresponding to the changed selection criteria were applied (the contribution of elastic events was subtracted using the estimate from Ref. [25]). The fully corrected rapidity spectrum obtained using this alternative analysis is also shown in Fig. 6.22 (*right*). The differences between the results for the standard and alternative methods are below 0.5% at $y < 2$ and below 2% at higher y.

It should be noted that the complete NA49 normalisation method could not be used with the NA61/SHINE due to the difficulties with deriving the cross sections related to the uncertainty of the target removed to inserted ratio (see Sect. 5.3). The cross-sections used in the normalisation of the alternative analysis of the 158 GeV/*c* data, drawn with the blue points in Fig. 6.22 (*right*) were taken from the NA49 analysis in Ref. [25]. Corresponding cross-sections for the lower momenta of the beam particles are not available.

6.6.4 Comparison with existing p+p data at 12, 19 and 24 GeV/*c*

In this section the results of NA61/SHINE are compared with the bubble chamber results from p+p collisions at 12 and 24 GeV/*c* [72] and at 19 GeV/*c* [73]. The reference data were available only in form of histograms. The data points were read off from the scanned figures. In case the error bars were not visible, the printed point size was assumed as the uncertainty. This concerns several points in the mid-rapidity region in the 12 and 24 GeV/*c* datasets; their uncertainties are overestimated.

As the results of NA61/SHINE are obtained at different beam momenta, the comparison has to involve model-based scaling or interpolation. Two approaches were considered.

In the first approach a limiting fragmentation model [74] was assumed. The model predicts that the rapidity spectra in the laboratory frame of reference do not depend on the beam momentum in the region close to $y_{\mathrm{LAB}}(\equiv y + y_{\mathrm{CMS}}) \cong 0$. Figure 6.23 shows the NA61/SHINE results reflected with respect to $y = 0$ and transformed to the laboratory frame of reference. A function fitted to the 158 GeV/*c* points was used as a reference; the choice is arbitrary and does not affect the comparison. In general the particle yields in this region increase with decreasing beam momentum, thus the limiting fragmentation model is not valid for p+p interactions at the SPS energy range. The largest difference is observed at $y_{\mathrm{LAB}} = -0.5$. The 20 and 31 GeV/*c* data lie, respectively, 40% and 10% above the 24 GeV/*c* data. This could naively be interpreted as an inconsistency between the NA61/SHINE and the bubble chamber data. The 19 GeV/*c* reference data do not lie between the 12 and 24 GeV/*c* data. This can be partially explained by large statistical uncertainties

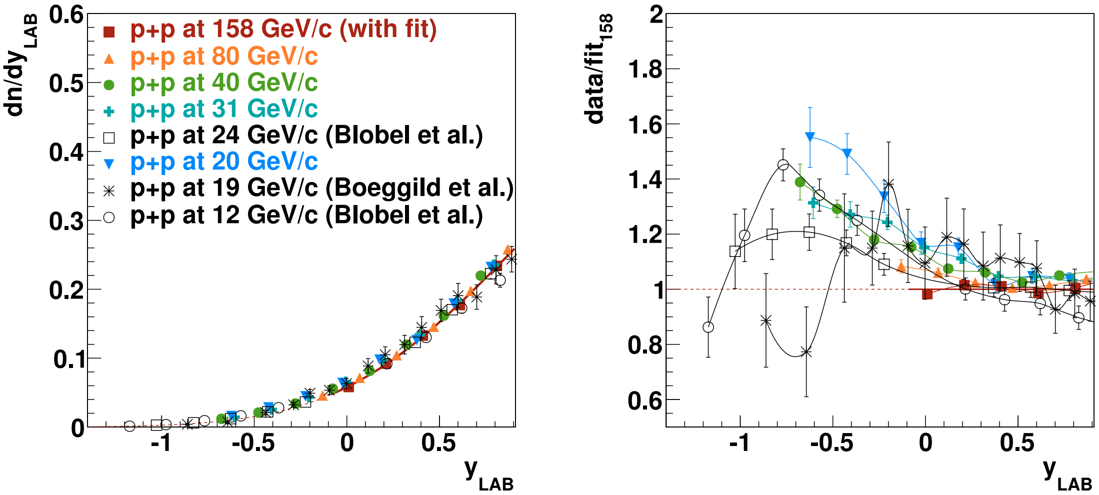

Figure 6.23: Comparison of the rapidity spectra from this thesis (filled symbols) with the p+p data at 12 and 24 GeV/*c* from Ref. [72] (Blobel *et al.*, open symbols) and with the p+p data at 19 GeV/*c* from Ref. [73] (Bøggild *et al.*, black stars). *Left:* The rapidity spectra in the laboratory frame of reference. The 158 GeV/*c* spectrum was fitted with the double Gaussian function (solid line, see Eq. (7.2)) in the region corresponding to $y > 2$ in the centre of mass frame; the dashed line shows extrapolated function. *Right:* the spectra divided by the fitted function, also in the extrapolated region. The data points were connected with lines to guide an eye.

of the data points, but also demonstrates inconsistency between results of various experiments.

In the second approach the comparison was done assuming scaling of the shape of rapidity spectra in relative rapidity y/y_{beam}. Figure 6.24 (*top*) shows the spectra in the relative rapidity normalised to unity in order to exclude trivial effect of an increase of mean pion multiplicity with collision energy. The data measured at 12 and 24 GeV/*c* are compared with the parametrised NA61/SHINE results at 20 (*left*) and 31 GeV/*c* (*right*). The ratios of the 12 and 24 GeV/*c* spectra to the NA61/SHINE fits are shown in the corresponding *bottom* panels. The spectra at $y/y_{\text{beam}} < 0.7$ agree better than 10%. At the higher rapidities however, the differences increase to almost 100%, both between the results from this thesis and the reference data, and between the reference data at different beam momenta. The 20 GeV/*c* points lie between the 12 and 24 GeV/*c* ones, while the 31 GeV/*c* lie below 24 GeV/*c*. Thus this comparison of the spectra does not indicate any inconsistency between them. In the region of $y/y_{\text{beam}} > 0.7$ the 19 GeV/*c* points lie between the 12 and 24 GeV/*c* points, closer to the 24 GeV/*c* points, which is consistent, as opposed to the comparison using the limiting fragmentation model scaling.

The two comparisons clearly demonstrate trivial fact that an interpolation between measurements may be strongly model dependent and lead to a significant bias. In the considered two examples even the qualitative conclusion whether or not the data are consistent depends on the model used for the comparison. This confirms importance of the NA61/SHINE scan of collisions of various ions at the same beam momenta. In particular the p+p data cannot be obtained by interpolat-

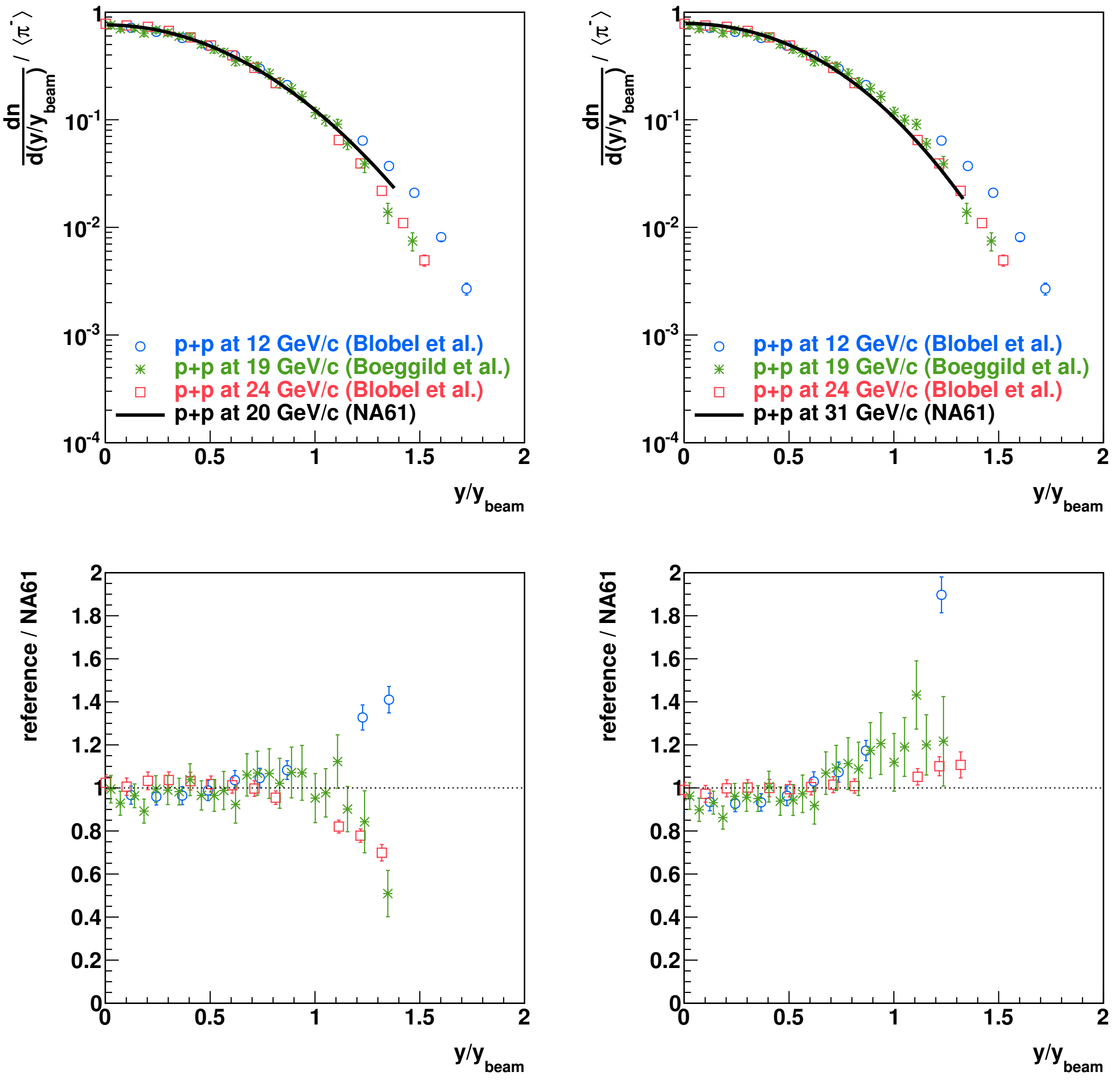

Figure 6.24: Comparison of the normalised rapidity spectra from this thesis (parametrised with a line) at 20 (*left*) and 31 GeV/*c* (*right*) with the p+p data at 12 and 24 GeV/*c* from Ref. [72] (Blobel *et al.*, open symbols) and with the p+p data at 19 GeV/*c* from Ref. [73] (Bøggild *et al.*, green stars). The *top* panels show the spectra and the *bottom* panels show the 12, 19 and 24 GeV/*c* spectra divided by the parametrised results from this thesis. The vertical dashed line at the ratio of 1 is drawn for reference. The data points were connected with solid lines to guide an eye.

ing the existing results. Also the data cannot be validated by comparison to data taken at different collision energies.

Chapter 7

π^- spectra in p+p interactions and comparisons with Pb+Pb data and simulations

7.1 Introduction

This chapter presents results on inclusive π^- meson spectra in inelastic p+p interactions at beam momenta of 20, 31, 40, 80 and 158 GeV/c. The spectra refer to pions produced by strong processes and in electromagnetic decays of produced hadrons. They are corrected for all effects related to detection and reconstruction, as described in Chapter 6.

Numerical results corresponding to the plotted spectra as well as their statistical and systematic uncertainties are given in Appendix C, as well in Ref. [29] in plain text format and in ROOT format.

The results are compared with existing p+p data [25, 63, 71, 75] and with the corresponding data on central Pb+Pb collisions at the same beam momenta per nucleon (except of 30A GeV/c instead of 31 for Pb+Pb) published by NA49 [8, 9], as well as results on central Au+Au collisions from AGS [76, 77] and RHIC [78–82], as processed in Ref. [9]. Here, centrality is a parameter determining number of nucleons of the projectile and the target nuclei participating in the collision. The central collisions selected by NA49 refer to 7% (5%) of the collisions at 20–80A GeV/c (158A GeV/c) for which the number of participating nucleons was the highest. Pion production characteristics in p+p interactions and central Pb+Pb collisions are identified and compared.

The chapter ends with comparisons of the measured π^- spectra with predictions of theoretical models: EPOS and VENUS.

7.2 Double differential spectra

The double differential spectra derived in bins of rapidity and the transverse momentum $d^2n/(dy\,dp_T)$, and rapidity and the transverse mass $d^2n/(dy\,dm_T)$ are equal to the fully corrected bin contents $\mathsf{n}[\pi^-]$ defined in Eq. (6.13). The spectra in rapidity and the transverse momentum produced in inelastic p+p interactions at 20, 31, 40, 80 and 158 GeV/c are shown in Fig. 7.1.

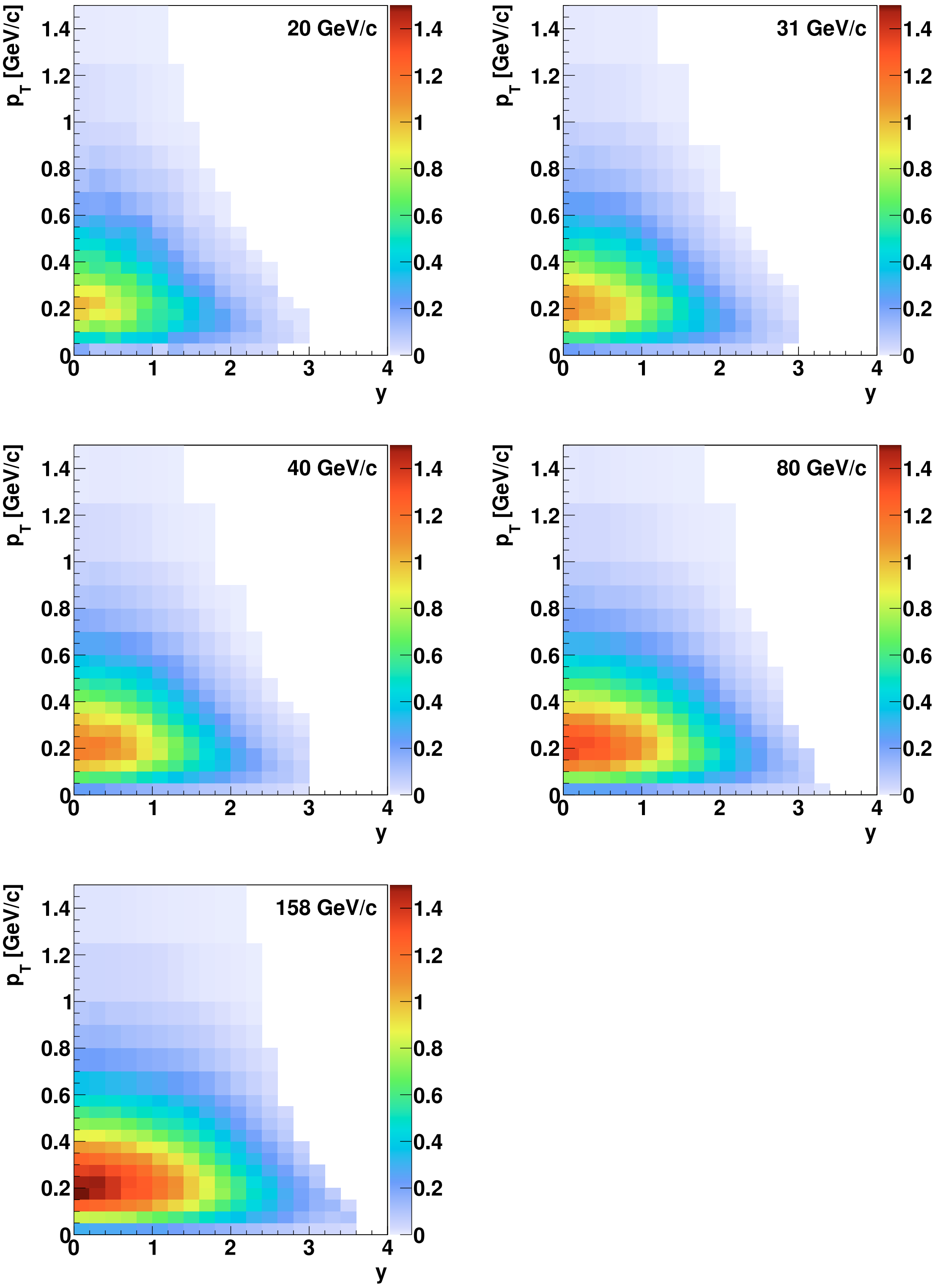

Figure 7.1: Double differential spectra $d^2n/(dy\,dp_T)$ $[(\mathrm{GeV}/c)^{-1}]$ of the π^- mesons produced in inelastic p+p interactions at 20, 31, 40, 80 and 158 GeV/c.

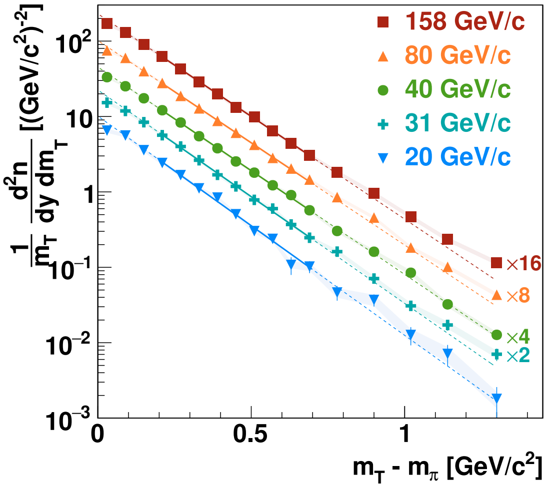

Figure 7.2: Transverse mass spectra at mid-rapidity ($0 < y < 0.2$). The fitted exponential function Eq. (7.1) is indicated by solid lines in the fit range $0.2 < (m_T - m_\pi) < 0.7$ GeV/c^2 and dashed lines outside the fit range. The data points for different beam momenta were scaled for better readability.

Table 7.1: Numerical values of the parameters fitted to the transverse mass spectra (see Eq. (7.1)) of the π^- mesons produced in inelastic p+p interactions at 20, 31, 40, 80 and 158 GeV/c. The uncertainty values provided correspond to the statistical and systematic uncertainties, respectively.

p_{beam} [GeV/c]	T($y = 0$) [MeV/c^2]	$\langle m_T\rangle(y = 0) - m_\pi$ [MeV/c^2]
20	$149.1 \pm 5.0 \pm 4.8$	$237.8 \pm 6.4 \pm 2.3$
31	$153.3 \pm 2.2 \pm 1.2$	$246.1 \pm 2.7 \pm 0.9$
40	$157.7 \pm 1.7 \pm 2.1$	$247.3 \pm 2.0 \pm 0.9$
80	$159.9 \pm 1.5 \pm 4.1$	$253.5 \pm 1.9 \pm 1.1$
158	$159.3 \pm 1.3 \pm 2.6$	$253.6 \pm 1.6 \pm 1.4$

7.3 Transverse mass spectra

Figure 7.2 shows the transverse mass spectra at mid-rapidity ($0 < y < 0.2$). A function

$$\frac{dn}{dm_T} = A \cdot m_T \cdot \exp\left(-\frac{m_T}{T}\right) \tag{7.1}$$

was fitted in the range $0.2 < (m_T - m_\pi) < 0.7$ GeV/c^2 and is indicated by lines in Fig. 7.2. The normalisation coefficient A and the inverse slope T were the fitted parameters. The fit minimises the χ^2 function calculated using statistical errors only. In the χ^2 calculation for each bin the measured bin content (dn/dm_T) was compared with integral of the fitted function over the bin, divided by the bin width. The fit m_T range was chosen the same as for the Pb+Pb results [8,9] in order to allow for comparison.

Table 7.1 lists the fitted values of T at mid-rapidity, and the mean transverse mass $\langle m_T\rangle$. In order to calculate $\langle m_T\rangle$ the spectra were extrapolated exponentially beyond the measured part of high m_T spectrum. The extrapolated function together with the measured data was used to calculate the $\langle m_T\rangle$ value, see Appendix B.1 for details. Half of the resulting correction is added to the systematic uncertainty in quadrature.

Figure 7.3 shows the inverse slope parameter T (*left*) and the mean transverse mass (*right*) calculated in all rapidity bins containing sufficient measured points.

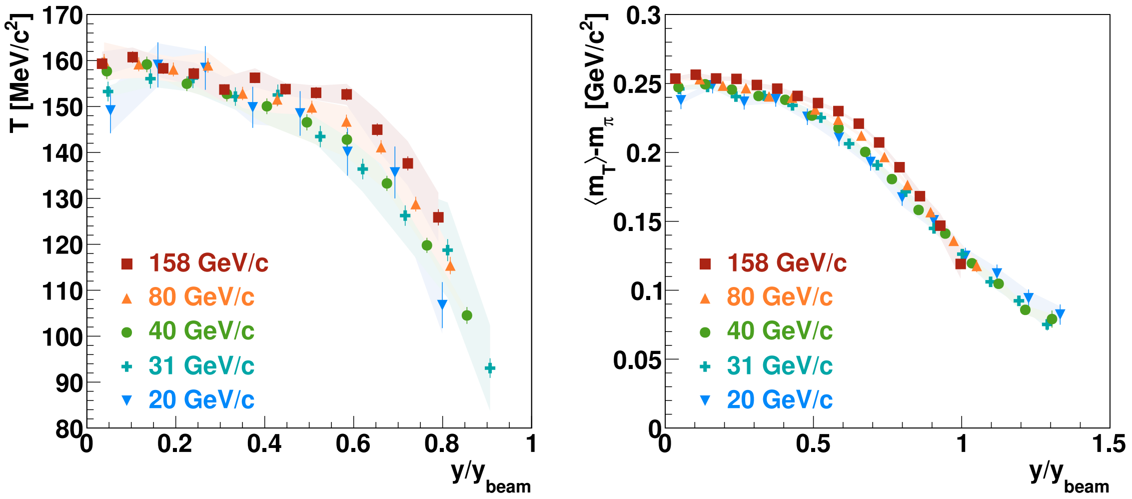

Figure 7.3: *Left:* The inverse slope parameter T of the transverse mass spectra as a function of rapidity divided by the projectile rapidity $y_{\text{beam}}(=1.877, 2.094, 2.223, 2.569$ and 2.909 at 20, 31, 40, 80 and 158 GeV/c, respectively). The fit range is $0.2 < (m_{\text{T}} - m_{\pi}) < 0.7$ GeV/c^2. *Right:* The mean transverse mass $\langle m_{\text{T}} \rangle$ as a function of rapidity divided by the projectile rapidity. The results in both panels refer to the π^- mesons produced in inelastic p+p interactions at 20, 31, 40, 80 and 158 GeV/c.

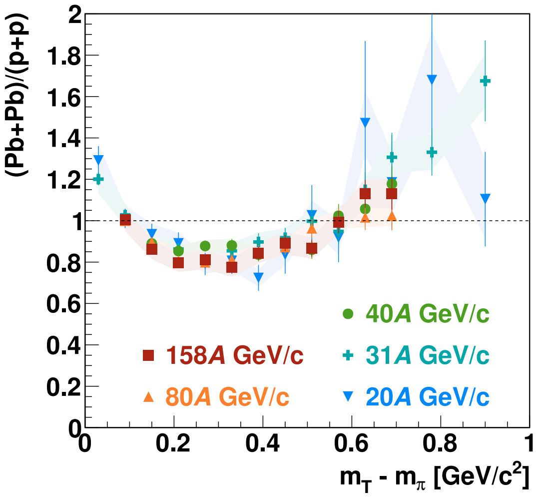

Figure 7.4: Ratio of the normalised transverse mass spectra of the π^- mesons at mid-rapidity produced in central Pb+Pb collisions and inelastic p+p interactions at the same collision energy per nucleon. The systematic uncertainty of the ratio represented by the coloured bands was calculated using uncertainty of the p+p data only.

For all beam momenta both parameters decrease significantly with rapidity increasing from mid-rapidity to the projectile rapidity y_{beam}. For $y/y_{\text{beam}} < 1$ they increase slightly with increasing beam momentum, but shape of the dependence on y/y_{beam} is rather similar at all energies.

Figure 7.4 shows ratio of the transverse mass spectra of the π^- mesons produced at mid-rapidity ($0 < y < 0.2$) in central Pb+Pb collisions and p+p interactions at the same collision energy per nucleon. As the Pb+Pb data at 40, 80 and 158 GeV/c was derived in different bins of m_{T}, the Pb+Pb points were interpolated to the binning used in this thesis assuming exponential behaviour, as in Eq. (7.1). The spectra were normalised to unity before calculating the ratio. The ratio is not constant implying the the spectral shapes are different in p+p interactions and central Pb+Pb collisions. Also, the ratio does not depend on the collision energy. The ratio is larger

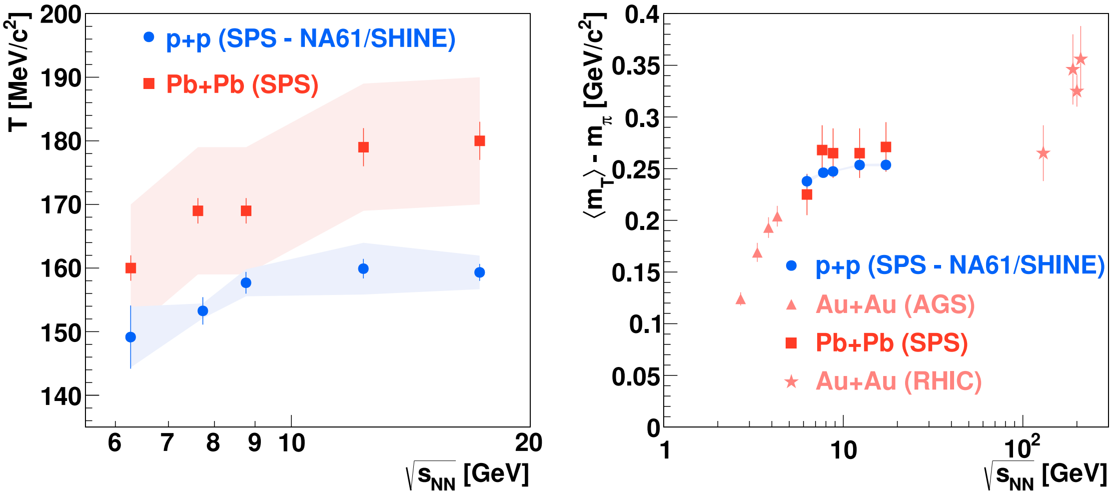

Figure 7.5: *Left:* Inverse slope parameter T of the transverse mass spectra at mid-rapidity ($0 < y < 0.2$) plotted against the collision energy per nucleon. The parameter T was fitted in the range $0.2 < (m_T - m_\pi) < 0.7$ GeV/c^2. The systematic uncertainty is shown with faded bands. As for the two lowest energy points for Pb+Pb, the systematic uncertainty was not given in [9], it is assumed to be the same as for the higher energies [8]. *Right:* The mean transverse mass $\langle m_T \rangle$ at mid-rapidity ($0 < y < 0.2$) versus the collision energy. The results on inelastic p+p interactions are compared with the corresponding data on central Pb+Pb and Au+Au collisions.

than unity for $(m_T - m_\pi) < 0.1$ GeV/c^2 and $(m_T - m_\pi) > 0.5$ GeV/c^2. It is smaller than unity in the region of $0.1 < (m_T - m_\pi) < 0.5$ GeV/c^2.

Figure 7.5 (*left*) shows the inverse slope parameter T of the transverse mass spectra at mid-rapidity as a function of the collision energy. The T parameter is larger by about 10–20 MeV/c^2 in central Pb+Pb collisions than in p+p interactions. Figure 7.5 (*right*) shows comparison for the mean transverse mass $\langle m_T \rangle$ parameter in the p+p and Pb+Pb data. In spite of different shapes of the m_T spectra, $\langle m_T \rangle$ is similar. This is because the differences in shapes of the m_T spectra at low m_T and high m_T shown in Fig. 7.4 cancel each other when calculating $\langle m_T \rangle$. Thus, the mean transverse mass appears to be insensitive to the apparent changes of the pion production properties observed between p+p interactions and central Pb+Pb collisions.

7.4 Rapidity spectra

Figure 7.6 shows the rapidity spectra. They were obtained by summing the m_T spectra in the measured range with the exponential function Eq. (7.1) extrapolating the spectrum (see Appendix B.1 for details). The correction is typically below 0.2% and becomes significant (a few %) only at $y > 2.4$. Half of the correction is added in quadrature to the systematic uncertainty.

The pion yield increases with increasing collision energy at all measured rapidities.

The rapidity spectra are approximately Gaussian, but as demonstrated in Appendix B.2, sum of two Gaussian functions symmetrically displaced with respect

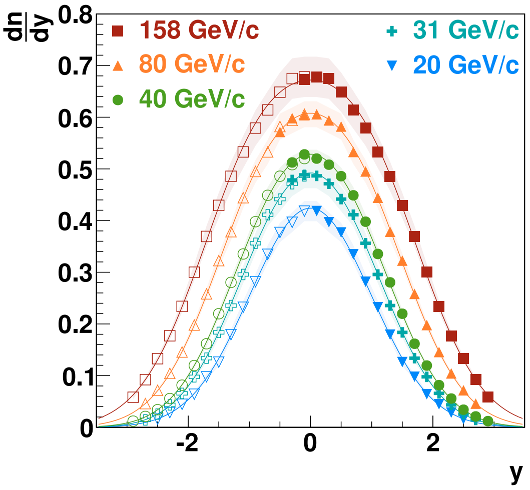

Figure 7.6: Rapidity spectra obtained from sums of the measured and extrapolated m_T spectra. Closed symbols indicate measured points, open points are reflected with respect to $y = 0$. The measured points at $y < 0$ are shown for systematic comparison only. The plotted statistical errors are almost always smaller than the symbol size. The systematic uncertainties are indicated by the coloured bands. The lines indicate fits of function Eq. (7.2) to the spectra. The results refer to the π^- mesons produced in inelastic p+p interactions at 20, 31, 40, 80 and 158 GeV/c.

Table 7.2: Numerical values of the parameters fitted to rapidity spectra (see Eq. (7.2)) of the π^- mesons produced in inelastic p+p interactions at 20, 31, 40, 80 and 158 GeV/c. As the systematic uncertainty dominates over the statistical one, the uncertainties written in the table are the square root of sum of squares of the statistical and systematic uncertainties. All uncertainties are given numerically in Appendix C.2.

p_{beam} [GeV/c]	$\langle\pi^-\rangle$	σ	σ_0	y_0
20	1.047 ± 0.051	0.981 ± 0.017	0.921 ± 0.118	0.337 ± 0.406
31	1.312 ± 0.069	1.031 ± 0.016	0.875 ± 0.050	0.545 ± 0.055
40	1.478 ± 0.051	1.069 ± 0.014	0.882 ± 0.045	0.604 ± 0.044
80	1.938 ± 0.080	1.189 ± 0.026	0.937 ± 0.019	0.733 ± 0.010
158	2.444 ± 0.130	1.325 ± 0.042	1.007 ± 0.051	0.860 ± 0.021

to mid-rapidity gives much better description:

$$\frac{dn}{dy} = \frac{\langle\pi^-\rangle(y_0,\sigma_0)}{2\sigma_0\sqrt{2\pi}} \cdot \left[\exp\left(-\frac{(y-y_0)^2}{2\sigma_0^2}\right) + \exp\left(-\frac{(y+y_0)^2}{2\sigma_0^2}\right)\right]. \tag{7.2}$$

The y_0 and σ_0 are fit parameters, and the total multiplicity $\langle\pi^-\rangle(y_0,\sigma_0)$ is calculated from the requirement that the integral over the measured spectrum equals the integral of the fitted function Eq. (7.2) in the range covered by the measurements (see Appendix B.2 for details). The χ^2 function was minimised in a similar way as in case of the m_T spectra, using the integral of the function in given rapidity bin. The numerical values of the fitted parameters as well as the RMS width $\sigma = \sqrt{y_0^2 + \sigma_0^2}$ are given in Table 7.2. The fitted parameters y_0 and σ_0 are strongly anticorrelated. As a result their individual uncertainties are large, while the value of σ is weakly sensitive to small deviations of the fit and its uncertainty is much smaller.

Figure 7.7 (*left*) presents ratio of the normalised π^- rapidity spectra produced in central Pb+Pb and inelastic p+p interactions at the same collision energy per nucleon. The spectra are plotted versus normalised rapidity. The ratio is close to unity in the central rapidity region ($y/y_{\text{beam}} < 0.6$), whereas it is higher for the

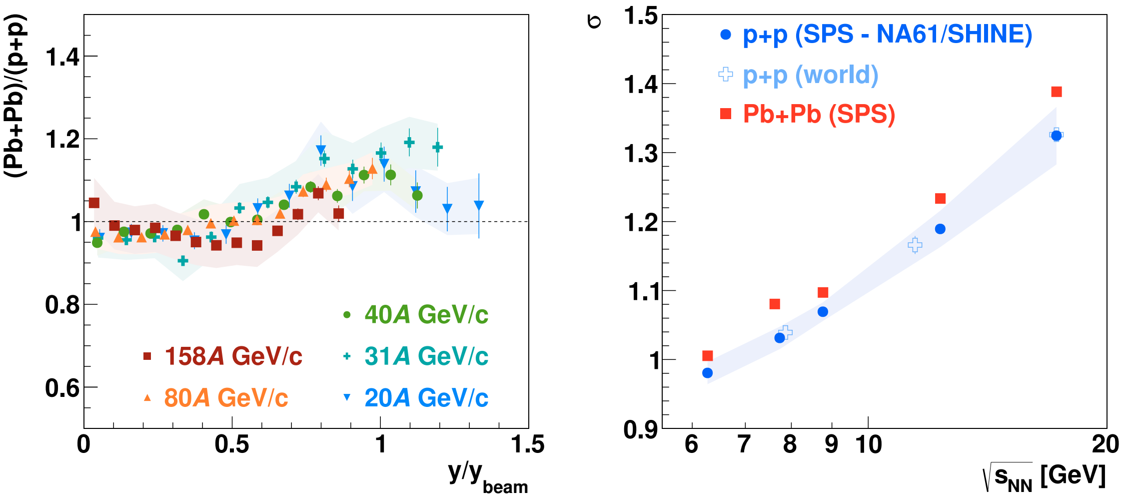

Figure 7.7: *Left:* Ratio of normalised rapidity spectra of the π^- mesons produced in central Pb+Pb collisions and inelastic p+p interactions at the same collision energy per nucleon plotted versus the rapidity scaled by the beam rapidity. The coloured bands represent the NA61/SHINE systematic uncertainty. *Right:* Energy dependence of the width of the rapidity distribution of the π^- mesons produced in p+p interactions and central Pb+Pb collisions. The systematic uncertainty for the Pb+Pb points is not given.

rapidity approaching the beam rapidity ($y/y_{\text{beam}} > 0.6$). The energy dependence of the ratio is small in comparison to the systematic uncertainties: at $y/y_{\text{beam}} < 0.3$ the ratio increases by 10–20% from 20A to 158 GeV/c; at $y/y_{\text{beam}} > 0.5$ the ratio decreases by about 20% from 20A to 158A GeV/c.

Consequently, the RMS width σ of the rapidity distributions of the π^- mesons produced in p+p interactions is smaller than in central Pb+Pb collisions, as shown in Fig. 7.7. Additionally, p+p data from Refs. [25,71,75] are shown; they agree with the NA61/SHINE results.

7.5 Mean multiplicity

Mean multiplicities of the π^- mesons, $\langle\pi^-\rangle$, produced in inelastic p+p interactions at 20, 31, 40, 80 and 158 GeV/c were calculated using Eq. (7.2). The extrapolation into the unmeasured region at large y contributes below 2% (see Appendix. B.2). Half of it is added in quadrature to the systematic uncertainty. The $\langle\pi^-\rangle$ values are given in Table 7.2

Figure 7.8 shows the dependence of the produced average $\langle\pi^-\rangle$ multiplicity per inelastic p+p collision on the Fermi energy

$$F \equiv \left[\frac{(\sqrt{s_{\text{NN}}} - 2m_{\text{N}})^3}{\sqrt{s_{\text{NN}}}}\right]^{1/4} \approx s_{\text{NN}}^{1/4}\,, \tag{7.3}$$

where $\sqrt{s_{\text{NN}}}$ is energy per nucleon available in centre of mass. Reference [2] predicts a linear dependence of the pion multiplicity in function of F. The results of NA61/SHINE are in agreement with a compilation of the world data [25,63].

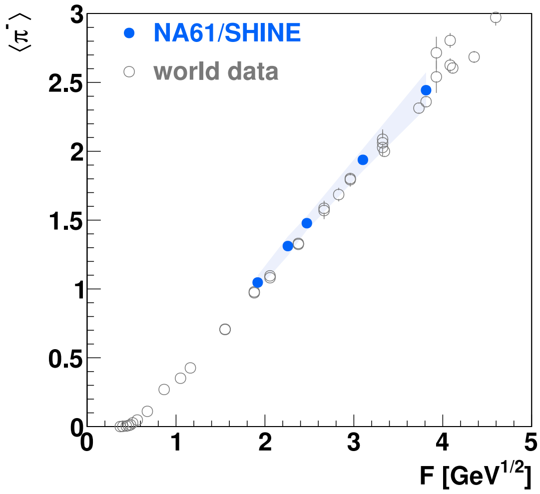

Figure 7.8: Dependence of the mean total multiplicity of the π^- mesons produced in inelastic p+p interactions on Fermi energy F (see Eq. (7.3)). The results of NA61/SHINE are indicated by filled circles and the compilation of the world data [25, 63] by open circles. The statistical errors are smaller than the symbol size. The systematic uncertainties are indicated by the coloured band.

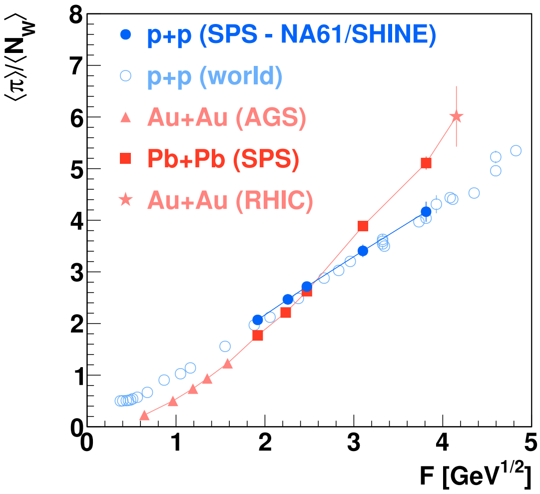

Figure 7.9: Mean multiplicity of all pions per wounded nucleon produced in inelastic p+p interactions and central Pb+Pb (Au+Au) collisions. The vertical lines show the total uncertainty, calculated as a square root of sum of the systematic and statistical (much smaller) uncertainties. To guide an eye, a line connects the ion-ion results, and separately the p+p results from this thesis.

Note, that the isospin effects should be taken into account in interpretation of differences between results obtained for inelastic p+p interactions and central Pb+Pb collisions. In order to reduce influence of the isospin effects the mean multiplicity of pions is obtained from a sum of mean multiplicities of negatively and positively charged pions using the phenomenological formula [28]:

$$\langle\pi\rangle = \frac{3}{2}\left(\langle\pi^+\rangle + \langle\pi^-\rangle\right) . \tag{7.4}$$

The mean π multiplicities are shown in Fig. 7.9 as a function of the Fermi energy F (see Eq. (7.3)). They are divided by the mean number of wounded nucleons, defined as the number of nucleons interacting inelastically ($N_W = 2$ for p+p). The value of $\langle\pi^+\rangle$ for the NA61/SHINE results on inelastic p+p interactions was estimated from the measured $\langle\pi^-\rangle$ multiplicity assuming $\langle\pi^+\rangle = \langle\pi^-\rangle + 2/3$. This assumption is based on the compilation of the world data presented in Ref. [28] and the model presented therein.

At the beam momenta lower than 40A GeV/c ($F < 2.5$ GeV$^{1/2}$) the $\langle\pi\rangle/\langle N_W\rangle$ ratio is higher in p+p interactions than in central Pb+Pb collisions. The opposite relation holds for beam momenta larger than 40A GeV/c. The energy dependence of the total π multiplicity for inelastic p+p interactions crosses the one for central Pb+Pb (Au+Au) collisions at about 40A GeV/c.

7.6 Comparison with simulated spectra

Figures 7.10 and 7.11 compare the π^- spectra generated by, respectively, EPOS and VENUS models and results of the data analysis. Both models overestimate the π^- production in the low p_T and high y region, and underestimate it at high p_T. The VENUS spectra are almost twice too large at rapidities between 2.5 and 3.5. The EPOS spectra agree better with data in general except at the lowest beam momenta where the π^- yield at high p_T is 50% too small. This is consistent with the fact that EPOS is a newer and better developed model. The EPOS spectra agree with data within ±20% at 158 GeV/c and within ±50% at 20 GeV/c.

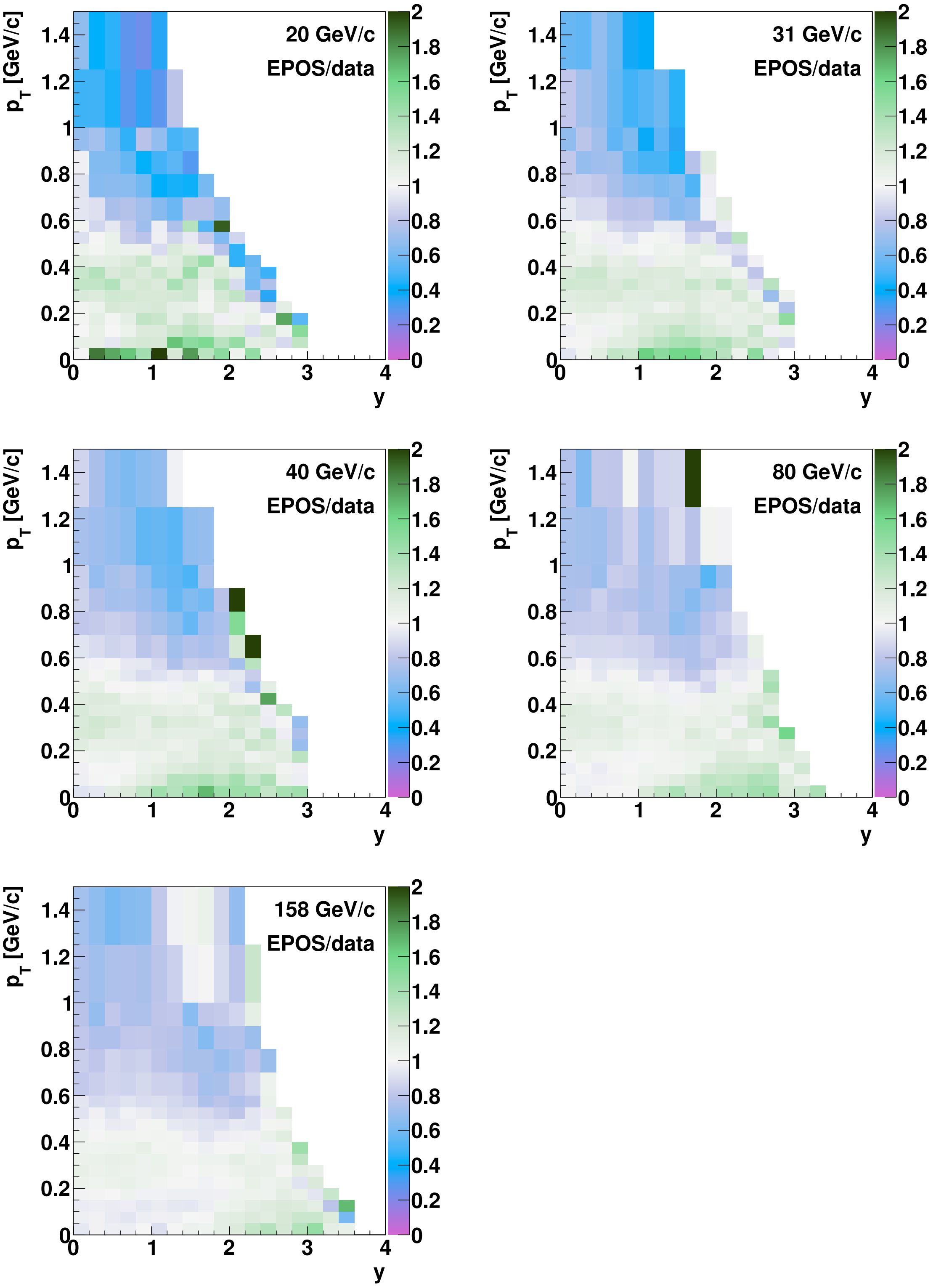

Figure 7.10: Double differential spectra of the π^- mesons produced in inelastic p+p interactions at 20, 31, 40, 80 and 158 GeV/*c* generated by EPOS divided by the NA61/SHINE measurement results.

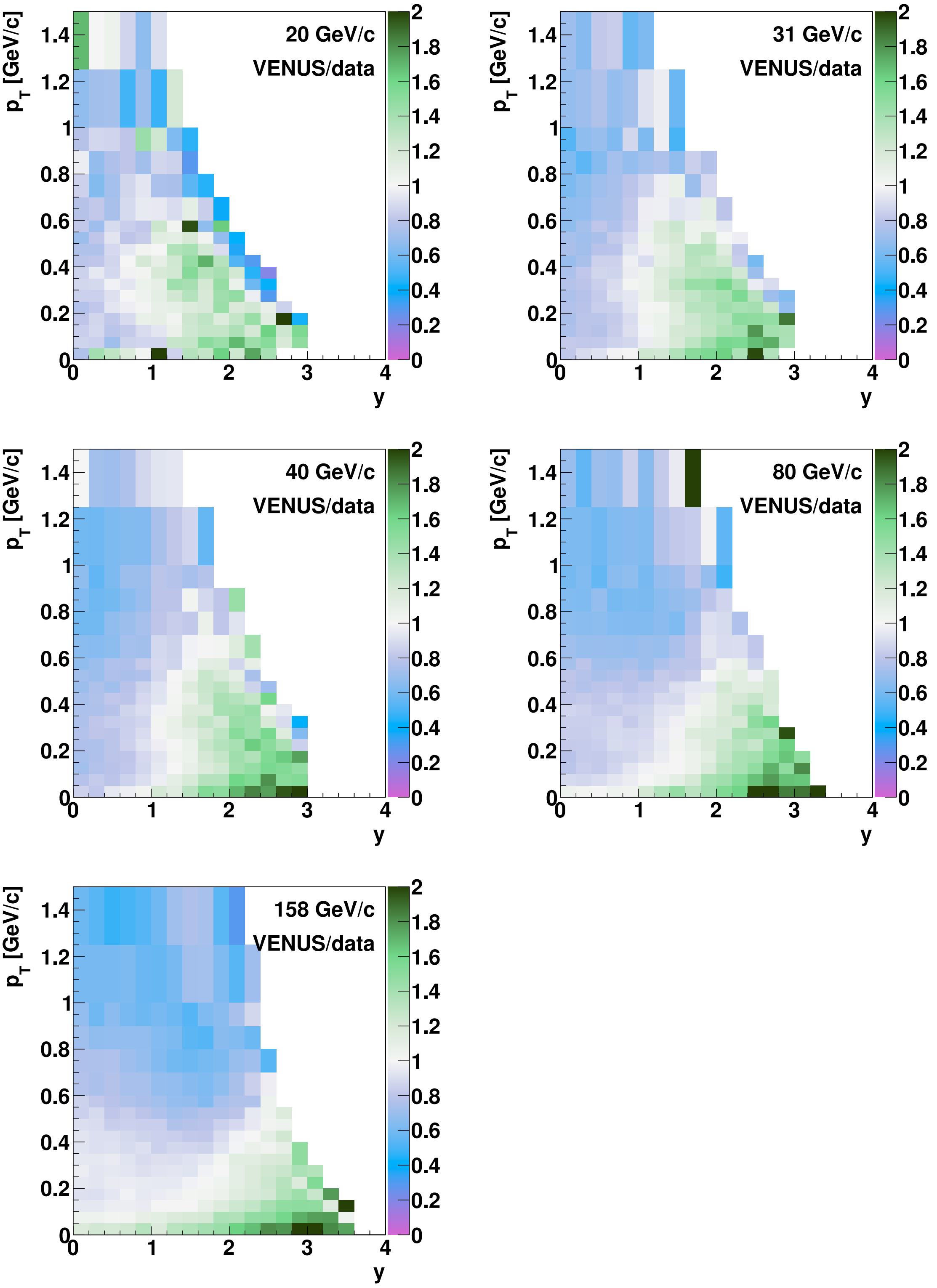

Figure 7.11: Double differential spectra of the π^- mesons produced in inelastic p+p interactions at 20, 31, 40, 80 and 158 GeV/c generated by VENUS divided by the NA61/SHINE measurement results.

Chapter 8

Summary and outlook

This thesis presents experimental results on inclusive spectra and mean multiplicities of negatively charged pions produced in inelastic p+p interactions at 20, 31, 40, 80 and 158 GeV/c by strong interaction processes and in electromagnetic decays of produced hadrons. The measurements were performed using the large acceptance NA61/SHINE hadron spectrometer at the CERN Super Proton Synchrotron based on a system of five Time Projection Chambers. Two-dimensional spectra were determined in terms of rapidity and transverse momentum or transverse mass with statistical and systematic uncertainties below 10% in large part of the phase-space. Characteristics of the spectra such as the width of rapidity distributions σ and the inverse slope parameter T of the transverse mass spectra were extracted and their collision energy dependences were presented.

The results were obtained by deriving spectra of unidentified negatively charged hadrons and removing contribution of hadrons other than primary π^- using EPOS simulation adjusted based on existing experimental data. Magnitudes of possible biases introduced by this and other corrections applied in the analysis were studied and included in the systematic uncertainty.

The results agree with the existing measurements of p+p interactions from MIRABELLE at 32 GeV/c [71] and NA49 at 158 GeV/c [25] and other experiments [63]. In majority of the existing datasets low statistics limits possibilities to study properties of the spectra. The NA61/SHINE measurement provide detailed spectra derived in broad phase-space region.

Comparison with the spectra predicted by the EPOS and VENUS models reveals differences of up to factor of 2. The obtained results might serve as a reference to improve the models.

The π^- spectra in p+p interactions belong to the NA61/SHINE programme of a two-dimensional scan of the collision energy and in the system size to study properties of onset of deconfinement. They were compared with the data on central Pb+Pb collisions at the same beam momenta per nucleon obtained by the NA49 experiment. The spectra in p+p interactions are narrower both in rapidity and in the transverse mass, which however might be related to isospin effects. The mean pion multiplicity per wounded nucleon in p+p interactions increases slower with energy in the SPS range and crosses the corresponding dependence measured in the Pb+Pb collisions at about 40A GeV/c, which supports interpretation of the onset of deconfinement in Pb+Pb collisions. Surprisingly, the energy dependences of

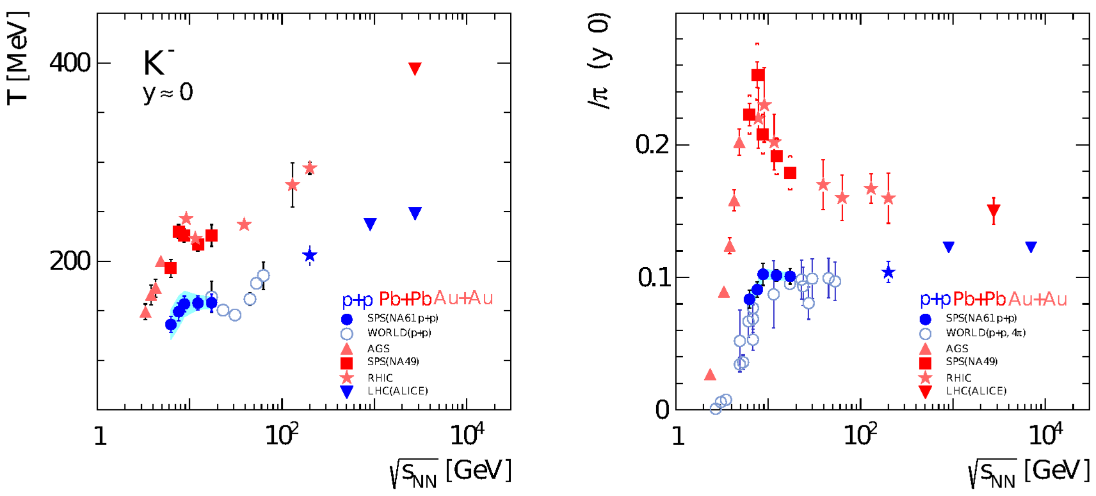

Figure 8.1: Energy dependence of the inverse slope parameter of the transverse mass spectra at mid-rapidity of the K^- mesons (*left*) and ratio of the K^+ and π^+ yields at mid-rapidity. The most recent results from NA61/SHINE as well as experiments at RHIC and LHC are included. The new NA61/SHINE points show sharp change at $p_{\text{beam}} = 40$ GeV/c ($\sqrt{s_{\text{NN}}} \approx 9$ GeV). Figures taken from Ref. [83].

shapes of the spectra and values of their parameters (σ, T) in p+p interactions and Pb+Pb collisions are very similar.

The most recent NA61/SHINE results on π^+, K^- and K^+ spectra [83] in p+p interactions show that some of the features in the energy dependence of the spectra produced in Pb+Pb collisions are also visible in p+p interactions. Figure 8.1 shows distinct structures in the energy dependence, which were not visible in the low statistics p+p data from bubble chamber experiments (compare with Fig. 1.2). The similarity of the energy dependence of shapes of the π^- spectra in p+p interactions and Pb+Pb collisions agrees with these findings.

Full interpretation of the results presented in this thesis requires comparison with other hadron spectra produced in collisions of p+p, Be+Be, Ar+Sc, Xe+La and Pb+Pb at the SPS energies, measured during the ongoing NA61/SHINE programme. Analyses based on identification method using dE/dx and ToF information, such as in Ref. [83], reduce systematic uncertainties related to simulation models used in the h^- method used in this thesis. On the other hand, results of the h^- method cover the broadest region of the phase-space. They allow to cross-check the dE/dx and ToF results, combine the results of these two identification analyses and clarify uncertainties related to normalisation. The h^-, dE/dx and ToF methods complement each other.

The results on p+p interactions at 20–158 GeV/c will be extended by analysis of p+p interactions at 13 GeV/c collected two years later after the main part of the beam momentum scan, and 350 GeV/c which were recently decided to be measured in autumn 2015.

Appendix A

Coordinate system and kinematic variables

A.1 Introduction

This appendix introduces the standard detector coordinate system used in this thesis as well as the definition of the kinematic variables. The reconstruction algorithms calculate the momentum vector of each particle at the interaction vertex. Various kinematic variables used in this thesis facilitate analysis of various track characteristics.

A.2 NA61/SHINE coordinate system

The coordinate system used in NA61/SHINE and in this thesis is shown in Fig. 2.1 on page 9. The origin of the system is located in the centre of VTPC-2, on the beam line. The system is right-handed. The z axis is horizontal, coincidental with the beam line. The y axis is vertical, pointing up, parallel to the electron drift direction in the TPC. The x axis is horizontal.

The azimuthal angle ϕ is defined in the x–y plane, so that $\phi = 0$ corresponds to the x axis, $\phi = 90°$ – the y axis, and it ranges from 0 to 360°.

$$\phi \equiv \operatorname{atan} \frac{p_y}{p_x} \,. \tag{A.1}$$

The polar angle θ is the angle from the z axis:

$$\theta \equiv \operatorname{asin} \frac{p_\mathrm{T}}{p} \,. \tag{A.2}$$

$\theta = 0$ corresponds to particles produced parallel to the beam particle, in the forward direction (towards the positive z values). The θ angle ranges from 0 to 180°.

The z axis defines two directions called *upstream*, towards negative z, from which the beam particles arrive and *downstream*, towards positive z.

A.3 Kinematic variables

A.3.1 Transverse variables

The transverse momentum is defined as

$$p_{\mathrm{T}} = \sqrt{p_x^2 + p_y^2} \,, \tag{A.3}$$

where p_x and p_y are the particle momentum components in the plane transverse to the beam axis (z).

The transverse mass is defined as

$$m_{\mathrm{T}} = \sqrt{p_{\mathrm{T}}^2 c^{-2} + m^2} \,, \tag{A.4}$$

where m is mass of given particle. By definition $m_{\mathrm{T}} \geq m$ thus the spectra are typically presented as a function of $(m_{\mathrm{T}} - m)$.

A.3.2 Rapidity

A.3.2.1 Definition

The rapidity definition used in this thesis is

$$y = \frac{1}{2} \log \frac{E + p_z c}{E - p_z c} \,, \tag{A.5}$$

where E is energy of the particle and p_z is its momentum component parallel to the beam line; log stands for the natural logarithm. It differs from the general rapidity definition which uses total momentum p instead of p_z. However, the definition given in Eq. (A.5) is widely used in the accelerator experiments. Such defined rapidity takes the observer to a frame in which the particle has only the transverse momentum component p_{T}.

Eq. (A.5) is equivalent to

$$y = \log \frac{E + p_z c}{m_{\mathrm{T}} c^2} \,. \tag{A.6}$$

In the denominator the often used Eq. (A.5), E and $p_z c$ are subtracted. For particles with high p and low p_{T} the values of E and $p_z c$ are very similar. As they are both known with limited precision, the subtraction leads to significant loss of numerical precision, regardless of the computing precision. For this reason the Eq. (A.6) was used instead in this thesis.

Rapidity is a dimensionless variable invariant with respect to the Lorentz transformation. It can be transformed from the laboratory frame of reference ($_{\mathrm{LAB}}$) to the centre of mass frame of reference ($_{\mathrm{CMS}}$) by subtracting a constant y_{CMS}:

$$y_{\mathrm{CMS\ frame}} = y_{\mathrm{LAB\ frame}} + y_{\mathrm{CMS}} \,, \tag{A.7}$$

where

$$y_{\mathrm{CMS}} = \operatorname{atanh} \frac{p_{\mathrm{beam}} c}{E_{\mathrm{beam}} + m_{\mathrm{p}} c^2} \,, \tag{A.8}$$

Table A.1: Kinematic variables in interactions of proton beam at the stationary proton target at 5 beam momenta: beam momentum p_{beam}, beam energy E_{beam}, rapidity of the centre of mass system y_{CMS} in the laboratory frame, which is equal to the beam rapidity in the centre of mass system y_{beam}, total energy $\sqrt{s}$ available in the centre of mass and the Fermi energy F (see Eq. (7.3)). A dedicated precise beam momentum measurement was performed for the 31 GeV/c beam. The decimal digits given for the other datasets are excessive, but are provided in order to avoid numerical errors in calculations.

p_{beam} [GeV/c]	E_{beam} [GeV]	$y_{\text{CMS}} = y_{\text{beam}}$	$\sqrt{s}$ [GeV]	F [GeV$^{1/2}$]
20.00	20.02	1.877	6.27	1.918
30.92	30.93	2.094	7.73	2.258
40.00	40.01	2.223	8.77	2.471
80.00	80.01	2.569	12.32	3.102
158.00	158.00	2.910	17.27	3.812

p_{beam} is the beam momentum, $E_{\text{beam}} = \sqrt{p_{\text{beam}}^2 c^2 + m_{\text{p}}^2 c^4}$ is the beam energy and m_{p} is mass of the beam particle: proton. In this thesis rapidity is always given in the centre of mass frame of reference.

The region close to $y = 0$, corresponding to particles produced perpendicularly to the beam line in the centre of mass system is called *mid-rapidity*, while the regions at $y > 0$ and $y < 0$ are called *forward* and *backward* rapidities, respectively.

The values of the kinematic variables for each analysed beam momentum are summarised in Table A.1.

A.3.2.2 Momentum and rapidity comparison

Figure A.1 shows lines of constant momentum in the y–p_{T} space. In collisions of identical nuclei, like p+p, the particle spectrum is symmetric with respect to $y = 0$. It is therefore sufficient to measure the spectrum only in the forward hemisphere ($y > 0$).

The h^- analysis method used in this thesis is restricted to particles of momenta above 0.4 GeV/c, where electrons can be distinguished from pions using the dE/dx measurement. Even at the lowest beam momentum, 20 GeV/c, this does not limit the acceptance at positive rapidity. In comparison, for the analysis method identifying all particles with dE/dx, the acceptance is limited to the region of $p > 5$ GeV/c.

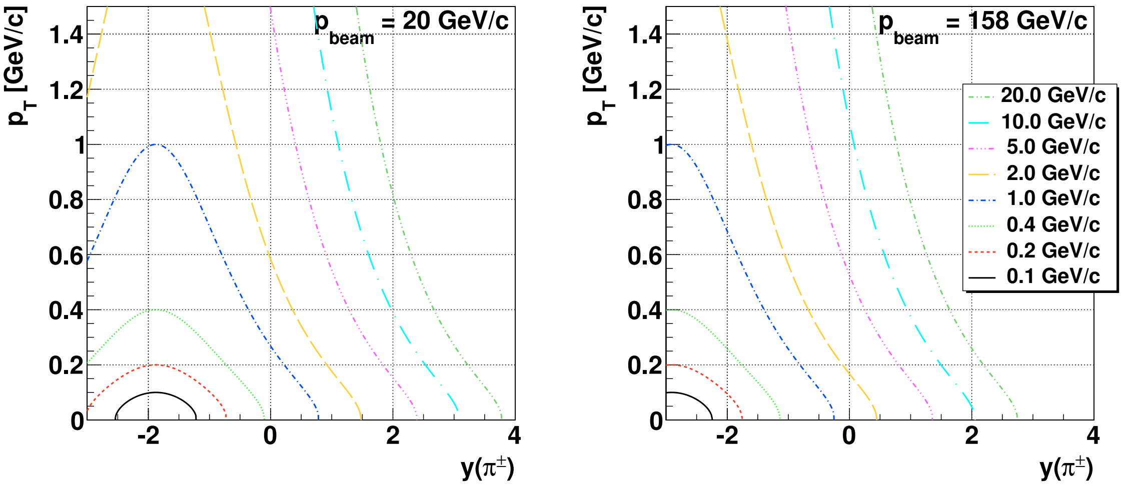

Figure A.1: Constant momentum lines drawn in the y–p_{T} space for the beam momenta of 20 (*left*) and 158 GeV/c (*right*). The green and the pink lines corresponds to the particle momenta of 0.4 and 5 GeV/c which are the low momentum limits for, respectively, electron and pion identification by the dE/dx method. Rapidity y is calculated in the centre of mass frame of reference using charged pion mass.

Appendix B

Procedures of spectra extrapolation

B.1 Transverse mass spectrum extrapolation

The π^- spectra were derived up to maximum transverse mass m_{Tmax} of 1.5 GeV/c^2 at rapidities close to 0, and even less at high y. Figure B.1 shows example spectra. They are approximately exponential.

A function

$$f(m_\mathrm{T}) = \frac{\mathrm{d}^2 n}{\mathrm{d}y\,\mathrm{d}m_\mathrm{T}} = A \cdot m_\mathrm{T} \cdot \exp\left(-\frac{m_\mathrm{T}}{T}\right), \tag{B.1}$$

is fitted to the m_T spectrum. In order to take into account small deviations from the exponential dependence at high rapidities, the fit range is limited from ($m_{\mathrm{Tmax}}-$ 0.9 GeV/c^2) to m_{Tmax}.

In the calculation of the integrated rapidity spectra, integral I_{ex} over the extrapolated part of the spectrum

$$I_{\mathrm{ex}} = \int_{m_{\mathrm{Tmax}}}^{\infty} f(m_\mathrm{T})\,\mathrm{d}m_\mathrm{T} = A \cdot T \cdot (m_{\mathrm{Tmax}} + T) \cdot \exp\left(-\frac{m_{\mathrm{Tmax}}}{T}\right). \tag{B.2}$$

is added to sum of the data in the measured range:

$$\frac{\mathrm{d}n}{\mathrm{d}y} = \sum_{m_\mathrm{T}=0}^{m_{\mathrm{Tmax}}} \frac{\mathrm{d}^2 n}{\mathrm{d}y\,\mathrm{d}m_\mathrm{T}} + I_{\mathrm{ex}}\,. \tag{B.3}$$

Half of I_{ex} is added in quadrature to the systematic uncertainty of dn/dy. Magnitude of the correction is shown in Fig. B.2 (*left*); it is below 1% at $y < 2$ and it increases up to 10% at higher rapidities, where it becomes the dominating source of the systematic uncertainty.

The mean transverse mass $\langle m_\mathrm{T}\rangle$ is calculated as:

$$\langle m_\mathrm{T}\rangle = \frac{v_{\mathrm{meas}} + v_{\mathrm{ex}}}{w_{\mathrm{meas}} + w_{ex}}\,. \tag{B.4}$$

The measured part is summed as

$$v_{\mathrm{meas}} = \sum_{m_\mathrm{T}=0}^{m_{\mathrm{Tmax}}} \frac{\mathrm{d}^2 n}{\mathrm{d}y\,\mathrm{d}m_\mathrm{T}} \cdot m_\mathrm{T} \cdot \Delta m_\mathrm{T}\,, \tag{B.5}$$

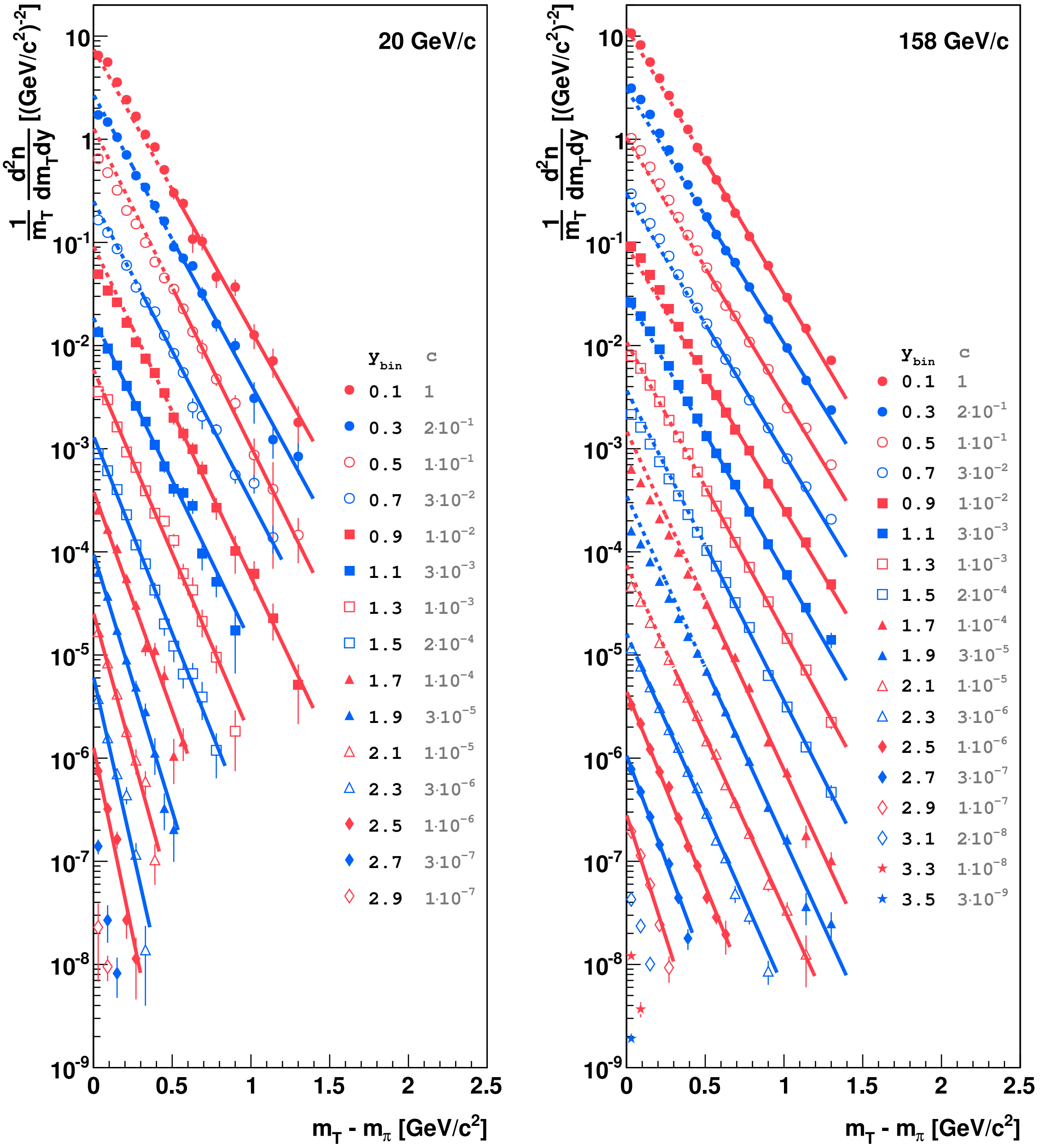

Figure B.1: Transverse mass spectra of the π^- mesons produced in inelastic p+p interactions at 20 (*left*) and 158 GeV/*c* (*right*) in various rapidity ranges. The legend provides the centres of the rapidity bins, y_{bin} and the scaling factor c used to separate the spectra visually. Exponential functions (Eq. (B.1)) were fitted to the tails of the spectra, in the ranges marked with continuous lines. The function at higher m_T was used to calculate the integrated rapidity spectra dn/dy and the average transverse mass $\langle m_T \rangle$.

$$w_{\text{meas}} = \sum_{m_T=0}^{m_{\text{Tmax}}} \frac{d^2 n}{dy\, dm_T} \cdot \Delta m_T \,, \tag{B.6}$$

where Δm_T is the bin size. The extrapolated part is calculated as

$$v_{\text{ex}} = \int_{m_{\text{Tmax}}}^{\infty} f(m_T) m_T \, dm_T = A \cdot T \cdot \exp\left(-\frac{m_{\text{Tmax}}}{T}\right) \cdot (m_{\text{Tmax}}^2 + 2T m_{\text{Tmax}} + 2T^2) \,, \tag{B.7}$$

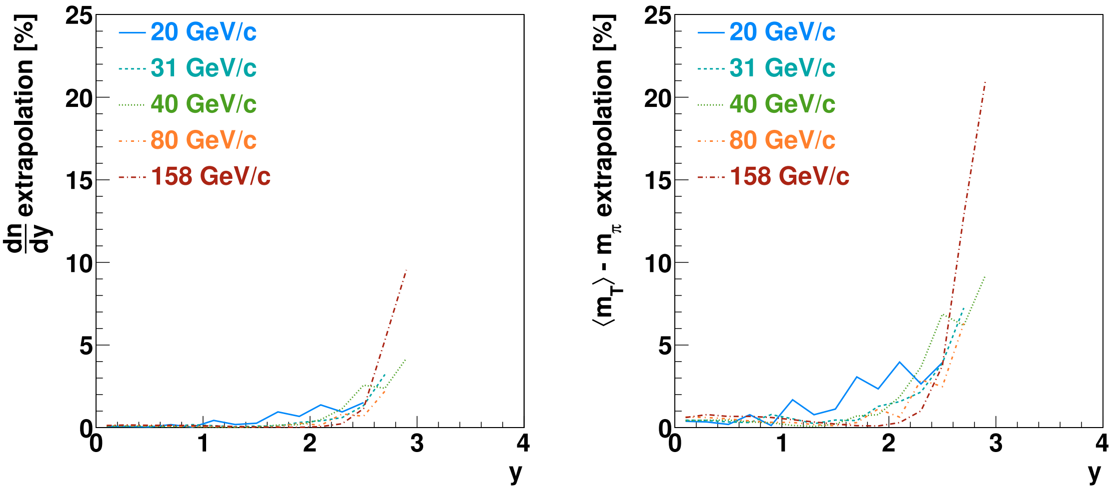

Figure B.2: Impact of the m_T spectrum extrapolation on the values of integrated rapidity $\mathrm{d}n/\mathrm{d}y$ (*left*) and the average transverse mass $\langle m_\mathrm{T} \rangle$ (*right*) at five beam momenta, defined as

$$\text{extrapolation} = \frac{\text{corrected value} - \text{uncorrected value}}{\text{uncorrected value}} \cdot 100\% \, .$$

$$w_\mathrm{ex} = \int_{m_\mathrm{Tmax}}^{\infty} f(m_\mathrm{T})\, \mathrm{d}m_\mathrm{T} = A \cdot T \cdot \exp\left(-\frac{m_\mathrm{Tmax}}{T}\right) \cdot (m_\mathrm{Tmax} + T)\, . \tag{B.8}$$

Half of the difference between $\langle m_\mathrm{T} \rangle$ calculated with and without extrapolation (i.e. for $w_\mathrm{ex} = v_\mathrm{ex} = 0$) is added in quadrature to the systematic uncertainty of $\langle m_\mathrm{T} \rangle$. Magnitude of the correction is shown in Fig. B.2 (*right*); it is below 3% at $y < 2$ and it increases up to 20% at higher rapidities, where it becomes the dominating source of the systematic uncertainty.

B.2 Rapidity spectrum extrapolation

The rapidity spectra are approximately Gaussian. However, as shown in Fig. B.3 the Gaussian function describes the data points worse at the higher beam momenta. A better description is provided by sum of two symmetrically displaced Gaussian functions:

$$\frac{\mathrm{d}n}{\mathrm{d}y} = \frac{\langle \pi^- \rangle(y_0, \sigma_0)}{2\sigma_0\sqrt{2\pi}} \cdot \left[\exp\left(-\frac{(y-y_0)^2}{2\sigma_0^2}\right) + \exp\left(-\frac{(y+y_0)^2}{2\sigma_0^2}\right)\right] \tag{B.9}$$

The total multiplicity $\langle \pi^- \rangle(y_0, \sigma_0)$ is defined so that the integral over the function in the measured range equals to the integral over the data:

$$\langle \pi^- \rangle(y_0, \sigma_0) = 4\left[\mathrm{erf}\left(\frac{y_\mathrm{h} - \mu_0}{\sigma_0\sqrt{2}}\right) - \mathrm{erf}\left(\frac{y_\mathrm{l} - \mu_0}{\sigma_0\sqrt{2}}\right) + \mathrm{erf}\left(\frac{y_\mathrm{h} + \mu_0}{\sigma_0\sqrt{2}}\right) - \mathrm{erf}\left(\frac{y_\mathrm{l} + \mu_0}{\sigma_0\sqrt{2}}\right)\right]^{-1} , \tag{B.10}$$

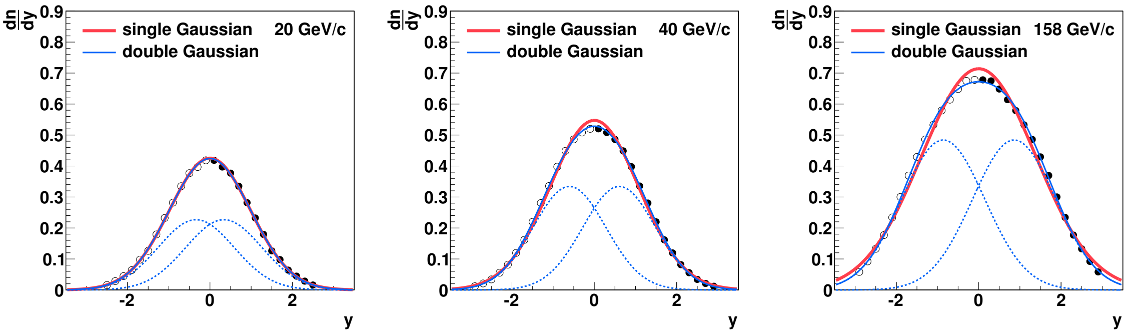

Figure B.3: Integrated rapidity spectra at 20, 40 and 158 GeV/c. The open points are reflection with respect to $y = 0$ of the measured full points. The thick solid red line shows parametrisation with a single Gaussian function. The solid blue line shows parametrisation with sum of two symmetrically displaced Gaussian functions; the added functions are drawn with dashed blue lines.

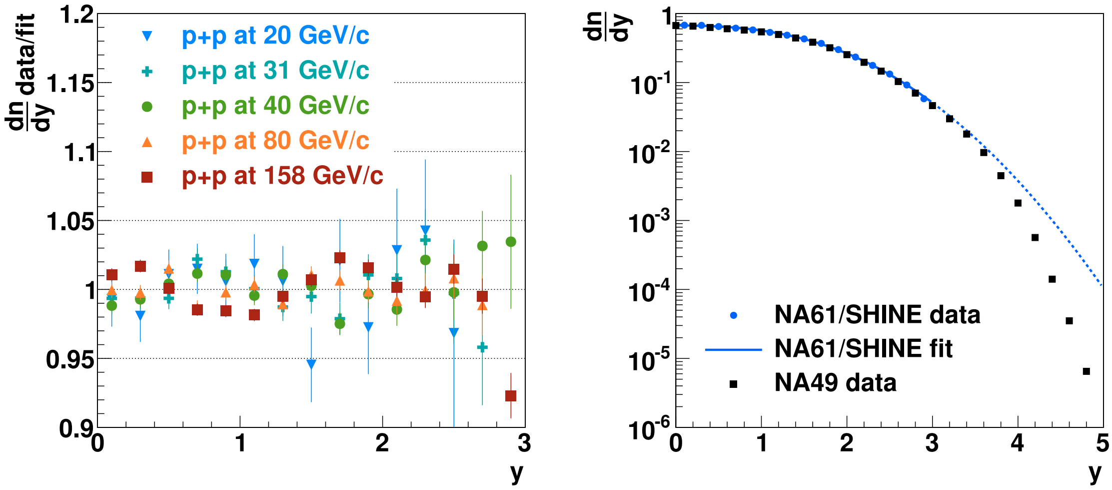

Figure B.4: Comparison of parametrisation of the rapidity distribution (Eq. (B.9)) and the measured data points. *Left:* Data divided by the parametrisation at five beam momenta. *Right:* comparison of the data on p+p interactions at 158 GeV/c measured by NA61/SHINE and NA49 [25] with the fitted parametrisation (solid line) and extrapolated parametrisation (dashed line).

where $y_{\mathrm{l}} = 0$ and y_{h} are, respectively, low and high edges of the measured rapidity range, and erf is the error defined in the standard way:

$$\mathrm{erf}(x) \equiv \frac{2}{\sqrt{\pi}} \int_x^{\infty} e^{-t^2}\, \mathrm{d}t\,. \tag{B.11}$$

Residuals of the fit are shown in Fig. B.4 (*left*). The parametrisation describes the data with ±5% precision except two points (at 20 and 158 GeV/c). Comparison with the NA49 data at 158 GeV/c [25] shows that the parametrisation overestimates the data beyond the fit range, as it is shown in Fig. B.4 (*right*). As only small fraction of all particles lies in the non-measured range, the extrapolated function appears to be sufficient to correct the spectrum parameters. The fitted function can be reliably used to parametrise the NA61/SHINE data within the measured range. Large

p_{beam} [GeV/c]	correction $\langle\pi^-\rangle$	σ
20	0.8%	1.4%
31	0.5%	0.6%
40	0.3%	1.0%
80	1.4%	2.1%
158	1.7%	2.4%

Table B.1: Correction to the total multiplicity $\langle\pi^-\rangle$ and the rapidity distribution width σ from the rapidity spectrum extrapolation, defined as

$$\text{correction} = \frac{\text{corrected value} - \text{uncorrected value}}{\text{uncorrected value}} \cdot 100\% \,.$$

systematic uncertainty of 50% of the extrapolation correction is attributed to the extrapolation procedure.

The extrapolated spectrum is used to calculate the total multiplicity $\langle\pi^-\rangle$, and the rapidity distribution width σ. The magnitudes of the corrections are listed in Table B.1. They are below 2% for $\langle\pi^-\rangle$ and below 2.5% for σ.

Appendix C

Tabulated results

C.1 Introduction

This appendix contains the numerical values of the spectra of the π^- mesons produced in inelastic p+p interactions at 20, 31, 40, 80 and 158 GeV/c and parameters of the spectra. For each value the statistical (σ_{stat}) and systematic uncertainties (σ_{sys}) are given as a percent fraction of the value. All the values can be also found in Ref. [29] in ROOT and ASCII formats.

C.2 Total multiplicities and rapidity distribution properties

Numerical values of the parameters fitted to the rapidity spectra (see Eq. (7.2)).

p_{beam} [GeV/c]	$\langle\pi^-\rangle$	σ_{stat}	σ_{sys}	σ	σ_{stat}	σ_{sys}	σ_0	σ_{stat}	σ_{sys}	y_0	σ_{stat}	σ_{sys}
20	1.0470	0.044	4.890	0.981	0.54	1.67	0.921	6.25	11.17	0.337	44.38	1.12
31	1.3115	0.011	5.298	1.031	0.22	1.57	0.875	0.97	5.64	0.545	2.24	0.10
40	1.4777	0.005	3.429	1.069	0.15	1.26	0.882	0.57	5.09	0.604	1.10	0.07
80	1.9379	0.015	4.150	1.189	0.17	2.21	0.937	0.51	1.91	0.733	0.64	0.01
158	2.4437	0.014	5.329	1.325	0.13	3.15	1.007	0.37	5.03	0.860	0.37	0.02

C.3 Double differential spectra

This section presents numerical values of the double differential π^- spectra

$$\frac{\mathrm{d}^2 n}{\mathrm{d}y\,\mathrm{d}p_{\mathrm{T}}}\ [(\mathrm{GeV}/c)^{-1}] \tag{C.1}$$

of the π^- mesons produced at five beam momenta.

C.3.1 $p_{\mathrm{beam}} = 20$ GeV/c

p_{T}[GeV/c]		$0.0 < y < 0.2$			$0.2 < y < 0.4$			$0.4 < y < 0.6$			$0.6 < y < 0.8$			$0.8 < y < 1.0$		
min	max	$\frac{\mathrm{d}^2 n}{\mathrm{d}y\,\mathrm{d}p_{\mathrm{T}}}$	σ_{stat}	σ_{sys}	$\frac{\mathrm{d}^2 n}{\mathrm{d}y\,\mathrm{d}p_{\mathrm{T}}}$	σ_{stat}	σ_{sys}	$\frac{\mathrm{d}^2 n}{\mathrm{d}y\,\mathrm{d}p_{\mathrm{T}}}$	σ_{stat}	σ_{sys}	$\frac{\mathrm{d}^2 n}{\mathrm{d}y\,\mathrm{d}p_{\mathrm{T}}}$	σ_{stat}	σ_{sys}	$\frac{\mathrm{d}^2 n}{\mathrm{d}y\,\mathrm{d}p_{\mathrm{T}}}$	σ_{stat}	σ_{sys}
0.00	0.05	0.183	17.4	11.6	0.099	28.6	13.0	0.107	28.4	13.4	0.114	21.4	13.9	0.129	16.5	14.3
0.05	0.10	0.480	12.2	10.1	0.471	8.8	11.3	0.539	6.3	11.7	0.427	7.3	12.1	0.408	7.5	12.5
0.10	0.15	0.779	6.3	7.9	0.713	6.7	8.6	0.747	6.1	9.0	0.681	5.6	9.3	0.586	6.2	9.5
0.15	0.20	0.944	5.7	6.6	0.862	5.8	6.8	0.893	4.8	7.0	0.776	5.1	7.2	0.606	6.5	7.4
0.20	0.25	1.009	5.4	5.9	0.964	5.2	6.0	0.816	5.5	6.2	0.760	5.3	6.3	0.673	5.4	6.4
0.25	0.30	0.874	6.3	5.7	0.870	5.3	5.8	0.785	5.6	5.9	0.694	5.6	6.0	0.620	5.4	6.2
0.30	0.35	0.739	6.8	5.8	0.723	6.9	5.8	0.635	6.2	5.9	0.650	5.5	6.0	0.523	6.6	6.2
0.35	0.40	0.645	6.9	6.3	0.574	7.0	6.2	0.603	6.0	6.2	0.507	5.6	6.3	0.447	6.4	6.6
0.40	0.45	0.562	7.3	7.1	0.556	6.5	7.0	0.499	6.2	6.9	0.416	7.2	6.8	0.317	8.7	7.2
0.45	0.50	0.461	8.9	7.9	0.467	7.3	7.7	0.396	7.7	7.5	0.355	7.9	7.4	0.288	8.5	7.7
0.50	0.55	0.408	9.0	8.1	0.348	9.2	7.8	0.301	9.4	7.6	0.330	7.7	7.4	0.277	7.7	7.9
0.55	0.60	0.268	12.5	8.0	0.303	9.5	7.5	0.247	10.9	7.3	0.243	8.3	7.3	0.223	8.9	8.0
0.60	0.70	0.194	9.6	8.1	0.187	8.4	7.5	0.202	7.0	7.4	0.157	9.0	7.6	0.126	10.8	8.4
0.70	0.80	0.107	14.1	8.7	0.140	8.3	8.2	0.118	8.9	8.3	0.091	11.9	8.8	0.0693	12.8	9.8
0.80	0.90	0.057	20.5	9.9	0.0769	12.3	9.8	0.0645	14.9	10.3	0.0534	17.6	11.1	0.0444	15.7	12.0
0.90	1.00	0.0419	20.7	11.5	0.0357	19.8	11.9	0.0342	18.0	12.7	0.0291	21.6	13.6	0.0111	60.0	14.3
1.00	1.25	0.0230	15.9	13.2	0.0200	18.7	14.2	0.0161	17.3	15.1	0.0160	16.9	15.9	0.0077	27.4	16.2
1.25	1.50	0.0033	37.4	14.0	0.0040	26.5	15.3	0.0028	74.5	16.1	0.0023	62.8	16.7	0.00147	38.7	16.9

p_{T}[GeV/c]		$1.0 < y < 1.2$			$1.2 < y < 1.4$			$1.4 < y < 1.6$			$1.6 < y < 1.8$			$1.8 < y < 2.0$		
min	max	$\frac{\mathrm{d}^2 n}{\mathrm{d}y\,\mathrm{d}p_{\mathrm{T}}}$	σ_{stat}	σ_{sys}	$\frac{\mathrm{d}^2 n}{\mathrm{d}y\,\mathrm{d}p_{\mathrm{T}}}$	σ_{stat}	σ_{sys}	$\frac{\mathrm{d}^2 n}{\mathrm{d}y\,\mathrm{d}p_{\mathrm{T}}}$	σ_{stat}	σ_{sys}	$\frac{\mathrm{d}^2 n}{\mathrm{d}y\,\mathrm{d}p_{\mathrm{T}}}$	σ_{stat}	σ_{sys}	$\frac{\mathrm{d}^2 n}{\mathrm{d}y\,\mathrm{d}p_{\mathrm{T}}}$	σ_{stat}	σ_{sys}
0.00	0.05	0.055	40.0	14.2	0.138	13.0	13.5	0.083	21.1	12.4	0.087	16.8	11.4	0.060	17.0	10.8
0.05	0.10	0.382	7.6	12.5	0.252	10.5	12.1	0.236	10.0	11.3	0.187	10.7	10.5	0.171	10.9	10.1
0.10	0.15	0.535	5.9	9.6	0.437	7.4	9.5	0.346	8.5	9.2	0.296	8.0	8.9	0.242	7.0	8.8
0.15	0.20	0.549	5.9	7.5	0.521	6.5	7.5	0.382	6.8	7.5	0.302	7.6	7.6	0.254	13.6	8.0
0.20	0.25	0.563	5.9	6.5	0.489	6.6	6.6	0.386	6.5	6.8	0.294	6.5	7.4	0.174	9.1	8.4
0.25	0.30	0.507	6.4	6.4	0.392	7.4	6.6	0.283	7.3	7.1	0.233	9.1	8.1	0.132	11.0	9.8
0.30	0.35	0.439	6.3	6.6	0.283	8.4	7.2	0.223	8.8	8.0	0.177	9.1	9.4	0.091	12.3	11.6
0.35	0.40	0.333	8.0	7.1	0.266	9.0	8.0	0.155	11.5	9.1	0.122	11.2	10.8	0.068	15.5	12.9
0.40	0.45	0.290	8.5	7.9	0.207	10.3	9.0	0.123	13.2	10.5	0.067	17.5	12.4	0.0434	22.0	14.2
0.45	0.50	0.256	8.1	8.6	0.141	11.8	10.2	0.096	15.5	12.2	0.062	17.3	14.3	0.0337	28.6	15.9
0.50	0.55	0.171	12.3	9.2	0.133	12.1	11.5	0.074	16.2	14.3	0.043	23.8	16.6	0.0212	26.8	17.7
0.55	0.60	0.117	16.3	9.5	0.101	15.3	12.3	0.032	31.6	15.5	0.0362	20.3	18.1	0.0034	60.0	19.1
0.60	0.70	0.096	11.5	10.1	0.0661	13.2	12.8	0.0254	22.9	15.7	0.0109	26.7	18.0	0.0041	38.8	19.2
0.70	0.80	0.0622	12.3	11.2	0.0353	19.4	12.9	0.0167	21.2	14.9	0.0047	43.1	16.8			
0.80	0.90	0.0236	23.2	12.9	0.0112	31.2	13.6	0.0085	31.5	14.5						
0.90	1.00	0.0070	74.9	14.7	0.0046	39.2	14.6	0.0020	58.9	14.5						
1.00	1.25	0.0048	37.2	16.1	0.00063	71.9	15.7									
1.25	1.50	0.00036	73.2	16.8												

p_{T}[GeV/c]		$2.0 < y < 2.2$			$2.2 < y < 2.4$			$2.4 < y < 2.6$			$2.6 < y < 2.8$			$2.8 < y < 3.0$		
min	max	$\frac{\mathrm{d}^2 n}{\mathrm{d}y\,\mathrm{d}p_{\mathrm{T}}}$	σ_{stat}	σ_{sys}	$\frac{\mathrm{d}^2 n}{\mathrm{d}y\,\mathrm{d}p_{\mathrm{T}}}$	σ_{stat}	σ_{sys}	$\frac{\mathrm{d}^2 n}{\mathrm{d}y\,\mathrm{d}p_{\mathrm{T}}}$	σ_{stat}	σ_{sys}	$\frac{\mathrm{d}^2 n}{\mathrm{d}y\,\mathrm{d}p_{\mathrm{T}}}$	σ_{stat}	σ_{sys}	$\frac{\mathrm{d}^2 n}{\mathrm{d}y\,\mathrm{d}p_{\mathrm{T}}}$	σ_{stat}	σ_{sys}
0.00	0.05	0.065	19.8	10.9	0.0349	24.9	11.6	0.0326	25.4	11.9						
0.05	0.10	0.114	14.4	10.2	0.103	14.7	10.8	0.063	16.6	11.1	0.048	21.5	11.1	0.0185	51.5	10.6
0.10	0.15	0.168	10.0	9.1	0.130	9.0	9.7	0.0587	16.4	10.3	0.0412	18.8	10.5	0.0127	44.7	10.5
0.15	0.20	0.160	9.2	8.7	0.092	14.7	9.7	0.061	17.0	10.4	0.0157	30.7	10.6	0.0163	32.7	10.6
0.20	0.25	0.133	9.3	9.9	0.072	14.9	11.4	0.042	24.5	11.8	0.0119	36.9	11.6			
0.25	0.30	0.076	14.8	12.0	0.0586	13.8	14.0	0.0516	18.9	14.4						
0.30	0.35	0.069	15.4	14.1	0.0426	18.0	16.2	0.0097	36.7	17.2						
0.35	0.40	0.032	37.1	15.1	0.0190	27.6	16.8	0.0050	59.3	17.7						
0.40	0.45	0.0349	27.1	15.6	0.0087	45.7	16.7									
0.45	0.50	0.0173	31.3	16.5												
0.50	0.55	0.0052	61.1	18.0												

C.3.2 $p_{\mathrm{beam}} = 31$ GeV/c

p_{T}[GeV/c]		$0.0 < y < 0.2$			$0.2 < y < 0.4$			$0.4 < y < 0.6$			$0.6 < y < 0.8$			$0.8 < y < 1.0$		
min	max	$\frac{\mathrm{d}^2 n}{\mathrm{d}y\,\mathrm{d}p_{\mathrm{T}}}$	σ_{stat}	σ_{sys}	$\frac{\mathrm{d}^2 n}{\mathrm{d}y\,\mathrm{d}p_{\mathrm{T}}}$	σ_{stat}	σ_{sys}	$\frac{\mathrm{d}^2 n}{\mathrm{d}y\,\mathrm{d}p_{\mathrm{T}}}$	σ_{stat}	σ_{sys}	$\frac{\mathrm{d}^2 n}{\mathrm{d}y\,\mathrm{d}p_{\mathrm{T}}}$	σ_{stat}	σ_{sys}	$\frac{\mathrm{d}^2 n}{\mathrm{d}y\,\mathrm{d}p_{\mathrm{T}}}$	σ_{stat}	σ_{sys}
0.00	0.05	0.220	6.1	7.7	0.199	5.9	8.0	0.178	6.1	8.4	0.157	7.8	9.0	0.1580	6.2	9.6
0.05	0.10	0.580	3.4	7.3	0.578	3.0	7.4	0.542	3.1	7.8	0.503	3.3	8.3	0.471	3.2	8.9
0.10	0.15	0.922	2.7	6.3	0.870	2.7	6.5	0.880	2.4	6.8	0.786	2.5	7.2	0.687	2.9	7.6
0.15	0.20	1.095	2.6	5.5	1.027	2.4	5.7	1.015	2.2	6.0	0.945	2.3	6.2	0.836	2.5	6.5
0.20	0.25	1.080	2.6	5.0	1.052	2.3	5.2	0.993	2.4	5.5	0.952	2.3	5.8	0.831	2.6	5.9
0.25	0.30	1.037	2.5	4.8	0.994	2.4	5.1	0.936	2.4	5.4	0.834	2.5	5.6	0.775	2.6	5.6
0.30	0.35	0.884	2.9	4.7	0.862	2.7	5.0	0.803	2.7	5.3	0.748	2.6	5.5	0.626	3.0	5.5
0.35	0.40	0.775	2.9	4.8	0.719	2.9	5.1	0.668	3.0	5.3	0.653	2.8	5.4	0.555	3.1	5.4
0.40	0.45	0.680	3.1	4.8	0.649	2.9	5.2	0.555	3.1	5.4	0.538	3.2	5.4	0.439	3.4	5.3
0.45	0.50	0.512	3.8	5.0	0.529	3.3	5.3	0.475	3.4	5.4	0.461	3.3	5.5	0.366	3.9	5.4
0.50	0.55	0.398	4.5	5.1	0.417	3.8	5.3	0.400	3.8	5.5	0.353	4.2	5.5	0.312	4.3	5.5
0.55	0.60	0.342	4.4	5.2	0.314	4.7	5.4	0.280	4.5	5.4	0.292	4.2	5.4	0.249	4.6	5.4
0.60	0.70	0.2362	4.1	5.3	0.2385	3.7	5.3	0.2147	3.7	5.3	0.2046	3.7	5.3	0.1720	4.1	5.4
0.70	0.80	0.1541	4.3	5.5	0.1444	4.8	5.4	0.1334	4.7	5.4	0.1226	4.9	5.4	0.1012	5.3	5.5
0.80	0.90	0.0906	6.3	6.0	0.1010	5.0	5.8	0.0878	5.6	5.8	0.0691	6.4	6.0	0.0652	6.7	6.4
0.90	1.00	0.0637	6.8	6.7	0.0515	7.2	6.6	0.0477	8.8	6.7	0.0479	7.2	7.1	0.0290	11.9	7.8
1.00	1.25	0.0217	8.3	7.7	0.0216	6.8	7.6	0.0184	7.8	7.8	0.0168	8.3	8.5	0.0127	9.4	9.5
1.25	1.50	0.00728	12.6	8.1	0.00662	13.4	8.0	0.0045	23.1	8.3	0.00333	19.7	9.2	0.00312	24.2	10.4

p_{T}[GeV/c]		$1.0 < y < 1.2$			$1.2 < y < 1.4$			$1.4 < y < 1.6$			$1.6 < y < 1.8$			$1.8 < y < 2.0$		
min	max	$\frac{\mathrm{d}^2 n}{\mathrm{d}y\,\mathrm{d}p_{\mathrm{T}}}$	σ_{stat}	σ_{sys}	$\frac{\mathrm{d}^2 n}{\mathrm{d}y\,\mathrm{d}p_{\mathrm{T}}}$	σ_{stat}	σ_{sys}	$\frac{\mathrm{d}^2 n}{\mathrm{d}y\,\mathrm{d}p_{\mathrm{T}}}$	σ_{stat}	σ_{sys}	$\frac{\mathrm{d}^2 n}{\mathrm{d}y\,\mathrm{d}p_{\mathrm{T}}}$	σ_{stat}	σ_{sys}	$\frac{\mathrm{d}^2 n}{\mathrm{d}y\,\mathrm{d}p_{\mathrm{T}}}$	σ_{stat}	σ_{sys}
0.00	0.05	0.1209	7.3	10.2	0.1190	7.3	10.4	0.1034	7.9	10.3	0.0919	8.4	9.8	0.0819	7.5	9.1
0.05	0.10	0.407	3.5	9.4	0.352	3.7	9.6	0.304	3.6	9.5	0.255	4.3	9.0	0.218	4.6	8.4
0.10	0.15	0.601	2.9	8.0	0.513	3.3	8.1	0.423	3.1	8.0	0.368	3.2	7.6	0.308	3.3	7.1
0.15	0.20	0.694	2.8	6.7	0.597	3.1	6.8	0.502	3.6	6.6	0.387	3.1	6.3	0.312	3.3	6.0
0.20	0.25	0.715	2.7	6.0	0.641	2.7	6.0	0.492	4.1	5.8	0.355	3.2	5.6	0.277	4.3	5.3
0.25	0.30	0.639	2.9	5.6	0.510	2.9	5.6	0.407	3.3	5.5	0.3009	3.3	5.3	0.217	5.4	5.1
0.30	0.35	0.554	3.2	5.4	0.442	3.1	5.4	0.324	3.9	5.3	0.2188	4.1	5.2	0.1591	4.4	5.2
0.35	0.40	0.445	3.5	5.3	0.352	3.6	5.2	0.263	4.1	5.2	0.1953	4.1	5.3	0.1249	5.2	5.6
0.40	0.45	0.422	3.5	5.2	0.298	3.8	5.2	0.2148	4.5	5.2	0.1419	5.0	5.4	0.0950	6.0	6.0
0.45	0.50	0.310	4.5	5.3	0.226	4.8	5.2	0.1662	4.9	5.3	0.1003	6.8	5.7	0.0561	8.5	6.3
0.50	0.55	0.227	4.5	5.3	0.1684	5.3	5.3	0.1212	6.0	5.4	0.0840	6.9	5.8	0.0388	10.3	6.4
0.55	0.60	0.191	5.5	5.4	0.1272	5.9	5.4	0.0859	7.0	5.7	0.0589	8.0	6.1	0.0276	12.3	6.5
0.60	0.70	0.1246	5.1	5.4	0.0955	4.8	5.6	0.0656	5.8	6.1	0.0344	7.9	6.5	0.0103	15.9	6.7
0.70	0.80	0.0758	6.3	5.8	0.0508	6.7	6.2	0.0268	9.5	6.7	0.0166	12.0	7.0	0.0037	29.5	7.1
0.80	0.90	0.0456	8.8	6.9	0.0292	9.1	7.3	0.0171	12.4	7.5	0.0043	27.7	7.5	0.00106	48.4	7.4
0.90	1.00	0.0287	10.6	8.5	0.0115	14.8	8.9	0.0078	21.9	8.9						
1.00	1.25	0.00689	14.4	10.1	0.00290	18.8	10.2	0.00156	28.0	9.9						
1.25	1.50	0.00152	34.9	11.0												

p_{T}[GeV/c]		$2.0 < y < 2.2$			$2.2 < y < 2.4$			$2.4 < y < 2.6$			$2.6 < y < 2.8$			$2.8 < y < 3.0$		
min	max	$\frac{\mathrm{d}^2 n}{\mathrm{d}y\,\mathrm{d}p_{\mathrm{T}}}$	σ_{stat}	σ_{sys}	$\frac{\mathrm{d}^2 n}{\mathrm{d}y\,\mathrm{d}p_{\mathrm{T}}}$	σ_{stat}	σ_{sys}	$\frac{\mathrm{d}^2 n}{\mathrm{d}y\,\mathrm{d}p_{\mathrm{T}}}$	σ_{stat}	σ_{sys}	$\frac{\mathrm{d}^2 n}{\mathrm{d}y\,\mathrm{d}p_{\mathrm{T}}}$	σ_{stat}	σ_{sys}	$\frac{\mathrm{d}^2 n}{\mathrm{d}y\,\mathrm{d}p_{\mathrm{T}}}$	σ_{stat}	σ_{sys}
0.00	0.05	0.0684	8.3	8.6	0.0645	7.7	8.6	0.0331	12.1	9.2	0.0346	12.6	9.8			
0.05	0.10	0.1653	4.9	8.0	0.1369	5.2	8.2	0.0950	6.6	9.0	0.0583	9.6	9.9	0.0457	11.0	10.4
0.10	0.15	0.2369	4.0	6.9	0.1732	4.7	7.5	0.0981	6.3	8.8	0.0729	8.4	10.4	0.0396	14.2	11.1
0.15	0.20	0.2338	4.1	6.0	0.1474	4.7	6.8	0.0915	7.0	8.6	0.0510	9.3	10.6	0.0193	31.7	11.6
0.20	0.25	0.1809	4.1	5.4	0.1203	5.3	6.4	0.0665	7.6	8.3	0.0360	14.5	10.5	0.0190	43.7	11.5
0.25	0.30	0.1431	4.9	5.3	0.0759	6.9	6.3	0.0465	9.6	7.9	0.0289	20.0	9.6	0.0061	44.5	10.6
0.30	0.35	0.0901	6.8	5.5	0.0555	9.0	6.4	0.0304	15.7	7.4	0.0070	28.4	8.6			
0.35	0.40	0.0710	7.0	6.1	0.0360	12.5	6.9	0.0167	23.3	7.4						
0.40	0.45	0.0490	9.4	6.7	0.0253	14.7	7.3	0.0070	28.6	7.6						
0.45	0.50	0.0306	11.8	7.1	0.0111	25.6	7.6									
0.50	0.55	0.0180	18.4	7.0	0.0043	49.1	7.3									
0.55	0.60	0.0085	26.9	6.9												
0.60	0.70	0.00353	24.5	6.7												

C.3.3 $p_{\text{beam}} = 40$ GeV/c

p_{T}[GeV/c]		$0.0 < y < 0.2$			$0.2 < y < 0.4$			$0.4 < y < 0.6$			$0.6 < y < 0.8$			$0.8 < y < 1.0$		
min	max	$\frac{\mathrm{d}^2n}{\mathrm{d}y\,\mathrm{d}p_{\mathrm{T}}}$	σ_{stat}	σ_{sys}	$\frac{\mathrm{d}^2n}{\mathrm{d}y\,\mathrm{d}p_{\mathrm{T}}}$	σ_{stat}	σ_{sys}	$\frac{\mathrm{d}^2n}{\mathrm{d}y\,\mathrm{d}p_{\mathrm{T}}}$	σ_{stat}	σ_{sys}	$\frac{\mathrm{d}^2n}{\mathrm{d}y\,\mathrm{d}p_{\mathrm{T}}}$	σ_{stat}	σ_{sys}	$\frac{\mathrm{d}^2n}{\mathrm{d}y\,\mathrm{d}p_{\mathrm{T}}}$	σ_{stat}	σ_{sys}
0.00	0.05	0.2357	3.9	4.4	0.2318	3.9	4.6	0.1951	4.4	4.9	0.1801	4.6	5.2	0.1601	5.0	5.5
0.05	0.10	0.646	2.3	4.2	0.615	2.2	4.4	0.613	2.1	4.6	0.561	2.3	4.9	0.506	2.6	5.1
0.10	0.15	0.983	2.0	3.8	0.952	1.8	3.9	0.914	1.9	4.1	0.864	1.9	4.3	0.764	2.0	4.5
0.15	0.20	1.145	2.0	3.5	1.125	1.7	3.6	1.068	1.7	3.7	1.030	1.7	3.8	0.906	1.9	4.0
0.20	0.25	1.134	1.9	3.4	1.150	1.8	3.4	1.101	1.7	3.6	1.008	1.8	3.7	0.898	1.9	3.8
0.25	0.30	1.064	2.0	3.4	1.018	1.9	3.4	1.027	1.8	3.5	0.941	1.9	3.6	0.866	2.0	3.7
0.30	0.35	0.966	2.1	3.4	0.906	2.0	3.4	0.875	2.0	3.5	0.829	2.1	3.6	0.765	2.1	3.7
0.35	0.40	0.816	2.3	3.4	0.822	2.1	3.4	0.780	2.1	3.5	0.691	2.2	3.5	0.621	2.4	3.6
0.40	0.45	0.678	2.5	3.5	0.650	2.5	3.5	0.609	2.4	3.5	0.596	2.4	3.6	0.516	2.6	3.6
0.45	0.50	0.576	2.7	3.6	0.535	2.7	3.6	0.546	2.6	3.6	0.491	2.5	3.7	0.413	2.9	3.7
0.50	0.55	0.432	3.1	3.7	0.448	2.8	3.7	0.409	2.9	3.7	0.399	2.9	3.8	0.360	3.2	3.8
0.55	0.60	0.369	3.3	3.8	0.353	3.3	3.8	0.317	3.4	3.8	0.302	3.5	3.9	0.256	4.1	3.9
0.60	0.70	0.2630	2.8	3.9	0.2619	2.7	3.9	0.2500	2.7	4.0	0.2158	2.8	4.0	0.1992	3.1	4.1
0.70	0.80	0.1741	3.4	4.1	0.1650	3.5	4.1	0.1437	3.6	4.2	0.1297	3.8	4.2	0.1105	4.2	4.4
0.80	0.90	0.0973	4.6	4.6	0.1030	4.3	4.5	0.0966	4.2	4.6	0.0826	4.9	4.7	0.0666	5.5	5.0
0.90	1.00	0.0573	6.0	5.1	0.0673	5.6	5.1	0.0563	5.8	5.2	0.0438	6.1	5.5	0.0377	7.6	6.1
1.00	1.25	0.0279	5.3	5.7	0.0267	5.4	5.6	0.0242	5.8	5.8	0.0203	6.2	6.5	0.0169	7.3	7.6
1.25	1.50	0.00580	13.3	6.0	0.00638	10.3	5.9	0.00620	11.9	6.2	0.00463	13.4	7.0	0.00301	15.6	8.3

p_{T}[GeV/c]		$1.0 < y < 1.2$			$1.2 < y < 1.4$			$1.4 < y < 1.6$			$1.6 < y < 1.8$			$1.8 < y < 2.0$		
min	max	$\frac{\mathrm{d}^2n}{\mathrm{d}y\,\mathrm{d}p_{\mathrm{T}}}$	σ_{stat}	σ_{sys}	$\frac{\mathrm{d}^2n}{\mathrm{d}y\,\mathrm{d}p_{\mathrm{T}}}$	σ_{stat}	σ_{sys}	$\frac{\mathrm{d}^2n}{\mathrm{d}y\,\mathrm{d}p_{\mathrm{T}}}$	σ_{stat}	σ_{sys}	$\frac{\mathrm{d}^2n}{\mathrm{d}y\,\mathrm{d}p_{\mathrm{T}}}$	σ_{stat}	σ_{sys}	$\frac{\mathrm{d}^2n}{\mathrm{d}y\,\mathrm{d}p_{\mathrm{T}}}$	σ_{stat}	σ_{sys}
0.00	0.05	0.1392	6.0	5.7	0.1382	5.1	5.8	0.1193	5.6	5.8	0.0935	6.8	5.7	0.0913	5.5	5.7
0.05	0.10	0.444	2.5	5.3	0.3696	2.7	5.4	0.3326	3.0	5.4	0.2828	3.1	5.3	0.2490	3.2	5.3
0.10	0.15	0.677	2.2	4.6	0.594	2.2	4.6	0.505	2.2	4.7	0.4258	2.3	4.6	0.3541	2.5	4.6
0.15	0.20	0.819	1.8	4.0	0.681	2.1	4.0	0.588	1.9	4.0	0.4527	2.2	4.0	0.3603	2.5	4.0
0.20	0.25	0.798	1.9	3.8	0.699	2.1	3.7	0.568	1.9	3.7	0.4219	2.3	3.7	0.3187	2.5	3.7
0.25	0.30	0.722	2.2	3.7	0.609	2.3	3.6	0.492	2.1	3.5	0.3741	2.3	3.5	0.2683	3.1	3.6
0.30	0.35	0.592	2.4	3.7	0.508	2.5	3.6	0.3956	2.4	3.6	0.2942	2.7	3.6	0.224	4.8	3.7
0.35	0.40	0.523	2.5	3.7	0.433	2.4	3.7	0.3230	3.1	3.8	0.2452	3.5	3.8	0.1486	3.6	4.2
0.40	0.45	0.448	2.7	3.7	0.3498	2.8	3.8	0.2665	3.0	4.0	0.1764	3.7	4.3	0.1130	4.2	4.9
0.45	0.50	0.354	3.1	3.8	0.2797	3.2	3.9	0.1957	3.7	4.2	0.1342	4.0	4.7	0.0851	5.0	5.8
0.50	0.55	0.285	3.5	3.9	0.2146	3.5	4.0	0.1576	3.8	4.4	0.0987	4.9	5.4	0.0631	5.4	6.9
0.55	0.60	0.2215	4.0	4.0	0.1938	3.5	4.3	0.1243	4.6	4.9	0.0789	5.2	6.2	0.0438	7.4	8.1
0.60	0.70	0.1473	3.6	4.3	0.1226	3.4	4.7	0.0790	4.2	5.7	0.0486	4.7	7.2	0.0228	6.7	8.9
0.70	0.80	0.0883	4.9	4.7	0.0652	4.7	5.5	0.0486	4.9	6.8	0.0201	8.2	8.2	0.0094	11.2	9.4
0.80	0.90	0.0497	6.6	5.7	0.0374	6.1	6.8	0.0179	8.4	8.1	0.0098	12.1	9.0	0.00334	23.1	9.6
0.90	1.00	0.0284	8.0	7.1	0.0186	10.5	8.3	0.0112	11.2	9.4	0.00349	25.1	9.9			
1.00	1.25	0.01016	8.5	8.8	0.00577	11.0	9.6	0.00242	16.0	10.2	0.00108	24.6	10.5			
1.25	1.50	0.00156	23.5	9.6	0.00062	36.2	10.3									

p_{T}[GeV/c]		$2.0 < y < 2.2$			$2.2 < y < 2.4$			$2.4 < y < 2.6$			$2.6 < y < 2.8$			$2.8 < y < 3.0$		
min	max	$\frac{\mathrm{d}^2n}{\mathrm{d}y\,\mathrm{d}p_{\mathrm{T}}}$	σ_{stat}	σ_{sys}	$\frac{\mathrm{d}^2n}{\mathrm{d}y\,\mathrm{d}p_{\mathrm{T}}}$	σ_{stat}	σ_{sys}	$\frac{\mathrm{d}^2n}{\mathrm{d}y\,\mathrm{d}p_{\mathrm{T}}}$	σ_{stat}	σ_{sys}	$\frac{\mathrm{d}^2n}{\mathrm{d}y\,\mathrm{d}p_{\mathrm{T}}}$	σ_{stat}	σ_{sys}	$\frac{\mathrm{d}^2n}{\mathrm{d}y\,\mathrm{d}p_{\mathrm{T}}}$	σ_{stat}	σ_{sys}
0.00	0.05	0.0724	5.9	5.7	0.0561	7.7	5.8	0.0466	6.9	6.2	0.0322	8.7	7.1	0.0190	36.1	7.6
0.05	0.10	0.1874	3.6	5.3	0.1612	3.7	5.4	0.1064	4.8	5.8	0.0927	6.0	6.7	0.0582	6.4	7.2
0.10	0.15	0.2631	2.8	4.5	0.2036	3.2	4.7	0.1413	3.8	5.1	0.0959	4.4	6.1	0.0580	7.5	6.6
0.15	0.20	0.2673	2.7	4.0	0.2021	3.4	4.2	0.1230	4.2	4.8	0.0711	6.2	5.9	0.0342	14.9	6.4
0.20	0.25	0.2321	3.2	3.7	0.1341	4.0	4.1	0.0886	5.3	4.9	0.0547	7.6	6.0	0.0392	15.6	6.6
0.25	0.30	0.1661	3.6	3.8	0.1167	4.2	4.3	0.0617	6.7	5.3	0.0395	10.2	6.4	0.0177	39.0	6.9
0.30	0.35	0.1332	3.8	4.1	0.0832	5.0	5.0	0.0492	7.9	5.9	0.0187	17.8	6.7	0.0089	42.3	7.0
0.35	0.40	0.0951	4.9	4.8	0.0512	7.7	5.8	0.0278	11.9	6.5	0.0071	32.4	7.0			
0.40	0.45	0.0708	5.3	5.8	0.0361	9.9	6.8	0.0086	30.6	7.3						
0.45	0.50	0.0526	6.6	7.0	0.0262	10.7	7.8	0.0065	28.2	8.1						
0.50	0.55	0.0310	9.3	8.5	0.0137	16.6	9.2									
0.55	0.60	0.0221	10.2	9.9	0.0043	34.7	10.7									
0.60	0.70	0.0067	21.6	10.4	0.00100	38.6	11.2									
0.70	0.80	0.00141	37.0	10.2												
0.80	0.90	0.00035	59.2	9.8												

C.3.4 $p_{\text{beam}} = 80$ GeV/c

p_T[GeV/c]		$0.0 < y < 0.2$			$0.2 < y < 0.4$			$0.4 < y < 0.6$			$0.6 < y < 0.8$			$0.8 < y < 1.0$		
min	max	$\frac{d^2n}{dy\,dp_T}$	σ_{stat}	σ_{sys}	$\frac{d^2n}{dy\,dp_T}$	σ_{stat}	σ_{sys}	$\frac{d^2n}{dy\,dp_T}$	σ_{stat}	σ_{sys}	$\frac{d^2n}{dy\,dp_T}$	σ_{stat}	σ_{sys}	$\frac{d^2n}{dy\,dp_T}$	σ_{stat}	σ_{sys}
0.00	0.05	0.2504	3.7	5.0	0.2544	3.6	5.1	0.2495	3.5	5.3	0.2324	3.7	5.4	0.2252	3.7	5.6
0.05	0.10	0.721	2.1	4.8	0.725	2.1	4.9	0.709	2.0	5.0	0.674	2.0	5.2	0.618	2.2	5.3
0.10	0.15	1.139	1.7	4.4	1.081	1.9	4.5	1.092	1.6	4.7	1.006	1.7	4.8	0.929	1.7	5.0
0.15	0.20	1.341	1.6	4.1	1.265	1.6	4.2	1.257	1.5	4.4	1.188	1.6	4.5	1.121	1.6	4.6
0.20	0.25	1.315	1.7	4.0	1.318	1.6	4.1	1.271	1.5	4.2	1.163	1.6	4.4	1.121	1.6	4.4
0.25	0.30	1.250	1.7	3.9	1.225	1.7	4.0	1.184	1.6	4.1	1.097	1.7	4.3	1.030	1.8	4.3
0.30	0.35	1.097	1.8	4.0	1.084	1.8	4.0	1.043	1.8	4.1	0.962	1.8	4.2	0.957	1.7	4.2
0.35	0.40	0.916	2.1	4.0	0.917	2.0	4.1	0.898	1.9	4.2	0.856	2.0	4.2	0.768	2.0	4.2
0.40	0.45	0.802	2.1	4.1	0.773	2.2	4.2	0.765	2.1	4.2	0.678	2.3	4.2	0.646	2.2	4.2
0.45	0.50	0.649	2.4	4.2	0.647	2.3	4.3	0.618	2.5	4.3	0.566	2.5	4.3	0.523	2.4	4.3
0.50	0.55	0.511	2.8	4.3	0.515	2.6	4.4	0.520	2.6	4.4	0.461	2.8	4.4	0.406	2.8	4.4
0.55	0.60	0.439	2.9	4.4	0.402	3.0	4.4	0.409	3.0	4.5	0.381	3.2	4.5	0.334	3.0	4.5
0.60	0.70	0.3074	2.4	4.5	0.3085	2.5	4.5	0.2940	2.5	4.5	0.2716	2.6	4.6	0.2432	2.6	4.6
0.70	0.80	0.2001	3.1	4.6	0.1954	3.0	4.6	0.1837	3.3	4.7	0.1719	3.4	4.7	0.1502	3.1	4.7
0.80	0.90	0.1298	3.8	4.7	0.1238	3.9	4.8	0.1068	4.3	4.8	0.1050	4.4	4.9	0.0953	3.8	4.8
0.90	1.00	0.0791	4.8	5.1	0.0776	5.2	5.1	0.0763	5.2	5.1	0.0577	6.1	5.1	0.0513	5.5	5.0
1.00	1.25	0.0355	4.9	5.4	0.0336	4.9	5.4	0.0325	5.0	5.4	0.0268	5.2	5.4	0.0211	5.5	5.2
1.25	1.50	0.00951	10.1	5.6	0.01097	8.9	5.6	0.00789	11.8	5.6	0.00700	11.1	5.5	0.00457	12.5	5.3

p_T[GeV/c]		$1.0 < y < 1.2$			$1.2 < y < 1.4$			$1.4 < y < 1.6$			$1.6 < y < 1.8$			$1.8 < y < 2.0$		
min	max	$\frac{d^2n}{dy\,dp_T}$	σ_{stat}	σ_{sys}	$\frac{d^2n}{dy\,dp_T}$	σ_{stat}	σ_{sys}	$\frac{d^2n}{dy\,dp_T}$	σ_{stat}	σ_{sys}	$\frac{d^2n}{dy\,dp_T}$	σ_{stat}	σ_{sys}	$\frac{d^2n}{dy\,dp_T}$	σ_{stat}	σ_{sys}
0.00	0.05	0.1820	4.1	5.6	0.1552	4.9	5.5	0.1377	5.3	5.3	0.1390	4.7	5.2	0.1219	5.1	5.1
0.05	0.10	0.564	2.3	5.4	0.497	2.4	5.3	0.442	2.6	5.1	0.377	2.8	4.9	0.3063	3.2	4.8
0.10	0.15	0.828	1.9	5.0	0.755	1.9	4.9	0.677	1.9	4.7	0.579	2.1	4.5	0.464	2.3	4.4
0.15	0.20	1.006	1.6	4.7	0.880	1.7	4.6	0.768	1.8	4.5	0.647	1.9	4.3	0.540	2.1	4.1
0.20	0.25	1.031	1.5	4.5	0.895	1.7	4.4	0.747	1.8	4.4	0.617	1.9	4.2	0.492	2.1	4.0
0.25	0.30	0.952	1.7	4.3	0.808	1.7	4.3	0.696	1.8	4.3	0.523	2.2	4.2	0.4288	2.3	4.1
0.30	0.35	0.836	1.9	4.2	0.704	1.8	4.2	0.600	1.9	4.2	0.468	2.2	4.2	0.3682	2.4	4.2
0.35	0.40	0.695	2.1	4.2	0.588	2.0	4.2	0.503	2.1	4.2	0.3967	2.4	4.2	0.2972	2.7	4.2
0.40	0.45	0.576	2.3	4.2	0.485	2.2	4.2	0.4156	2.3	4.2	0.3222	2.7	4.2	0.2267	3.2	4.3
0.45	0.50	0.469	2.5	4.2	0.3997	2.4	4.2	0.3196	2.7	4.2	0.2579	2.9	4.2	0.2044	4.7	4.3
0.50	0.55	0.394	2.8	4.3	0.3071	2.8	4.3	0.2759	2.9	4.3	0.2237	3.7	4.3	0.1410	4.0	4.4
0.55	0.60	0.3103	2.9	4.4	0.2550	3.1	4.4	0.2097	3.2	4.4	0.1702	4.1	4.4	0.1123	4.5	4.5
0.60	0.70	0.2097	2.6	4.5	0.1836	3.0	4.4	0.1448	3.0	4.4	0.1062	3.2	4.5	0.0651	4.4	4.6
0.70	0.80	0.1341	4.5	4.6	0.1084	4.3	4.5	0.0901	4.2	4.5	0.0567	4.5	4.7	0.0323	6.4	5.0
0.80	0.90	0.0808	4.9	4.7	0.0595	4.3	4.7	0.0449	5.3	5.0	0.0318	6.3	5.4	0.0160	9.6	5.9
0.90	1.00	0.0467	5.6	5.0	0.0323	6.1	5.2	0.0244	7.5	5.8	0.0141	10.2	6.5	0.0102	12.6	7.4
1.00	1.25	0.01817	5.1	5.3	0.01166	7.2	5.8	0.00679	11.6	6.9	0.00449	12.7	7.6	0.00154	22.6	8.4
1.25	1.50	0.00433	12.3	5.5	0.00234	18.0	6.1	0.00124	26.0	7.4	0.00025	95.5	8.3			

p_T[GeV/c]		$2.0 < y < 2.2$			$2.2 < y < 2.4$			$2.4 < y < 2.6$			$2.6 < y < 2.8$			$2.8 < y < 3.0$		
min	max	$\frac{d^2n}{dy\,dp_T}$	σ_{stat}	σ_{sys}	$\frac{d^2n}{dy\,dp_T}$	σ_{stat}	σ_{sys}	$\frac{d^2n}{dy\,dp_T}$	σ_{stat}	σ_{sys}	$\frac{d^2n}{dy\,dp_T}$	σ_{stat}	σ_{sys}	$\frac{d^2n}{dy\,dp_T}$	σ_{stat}	σ_{sys}
0.00	0.05	0.1050	5.5	5.1	0.0890	5.5	5.0	0.0630	6.5	4.9	0.0487	7.9	4.8	0.0433	7.3	4.7
0.05	0.10	0.2737	3.2	4.8	0.2248	3.5	4.7	0.1692	3.9	4.6	0.1319	4.3	4.5	0.1068	4.7	4.5
0.10	0.15	0.3676	2.7	4.3	0.3031	2.8	4.2	0.2313	3.2	4.1	0.1592	4.1	4.1	0.1297	6.4	4.2
0.15	0.20	0.4000	2.4	3.9	0.3086	2.7	3.8	0.2366	3.1	3.8	0.1589	4.3	3.9	0.0966	6.1	4.0
0.20	0.25	0.3826	2.4	3.9	0.2874	2.7	3.8	0.2153	3.5	3.9	0.1243	4.3	4.0	0.0703	7.2	4.1
0.25	0.30	0.3391	2.5	4.1	0.2211	3.5	4.1	0.1492	3.8	4.2	0.0944	5.9	4.3	0.0367	16.9	4.4
0.30	0.35	0.2627	3.1	4.2	0.198	6.9	4.3	0.1020	5.4	4.4	0.0535	8.8	4.5			
0.35	0.40	0.2125	3.6	4.3	0.1294	4.3	4.5	0.0739	6.4	4.8	0.0444	11.3	5.0			
0.40	0.45	0.1558	3.8	4.4	0.0998	4.9	4.7	0.0534	8.2	5.2	0.0236	17.6	5.4			
0.45	0.50	0.1101	4.4	4.6	0.0712	7.0	5.0	0.0379	10.7	5.5	0.0112	38.5	5.8			
0.50	0.55	0.0859	5.5	4.6	0.0508	7.1	4.9	0.0227	16.1	5.3	0.0065	49.2	5.6			
0.55	0.60	0.0618	6.7	4.6	0.0328	9.0	4.8	0.0146	23.0	5.1						
0.60	0.70	0.0393	5.8	4.7	0.0179	10.8	4.8	0.0061	22.8	4.9						
0.70	0.80	0.0164	10.3	5.0	0.0069	19.7	5.0									
0.80	0.90	0.0069	16.0	6.0												
0.90	1.00	0.00401	22.0	7.7												
1.00	1.25	0.00071	31.7	8.6												

p_T[GeV/c]		$3.0 < y < 3.2$			$3.2 < y < 3.4$		
min	max	$\frac{d^2n}{dy\,dp_T}$	σ_{stat}	σ_{sys}	$\frac{d^2n}{dy\,dp_T}$	σ_{stat}	σ_{sys}
0.00	0.05	0.0302	9.2	4.6	0.0154	17.9	4.6
0.05	0.10	0.0739	9.2	4.5			
0.10	0.15	0.0675	6.7	4.2			
0.15	0.20	0.0588	13.6	4.1			

C.3.5 $p_{\text{beam}} = 158$ GeV/c

p_T[GeV/c]		$0.0 < y < 0.2$			$0.2 < y < 0.4$			$0.4 < y < 0.6$			$0.6 < y < 0.8$			$0.8 < y < 1.0$		
min	max	$\frac{d^2n}{dy\,dp_T}$	σ_{stat}	σ_{sys}	$\frac{d^2n}{dy\,dp_T}$	σ_{stat}	σ_{sys}	$\frac{d^2n}{dy\,dp_T}$	σ_{stat}	σ_{sys}	$\frac{d^2n}{dy\,dp_T}$	σ_{stat}	σ_{sys}	$\frac{d^2n}{dy\,dp_T}$	σ_{stat}	σ_{sys}
0.00	0.05	0.2965	3.2	6.3	0.2805	3.3	6.6	0.2750	3.3	6.8	0.2661	3.2	7.1	0.2410	3.5	7.3
0.05	0.10	0.818	1.9	6.1	0.810	1.8	6.3	0.798	1.8	6.5	0.781	1.8	6.8	0.711	1.9	7.0
0.10	0.15	1.256	1.4	5.8	1.230	1.4	6.0	1.198	1.4	6.2	1.144	1.6	6.4	1.101	1.5	6.5
0.15	0.20	1.497	1.3	5.6	1.471	1.3	5.8	1.402	1.3	5.9	1.287	1.4	6.1	1.274	1.3	6.2
0.20	0.25	1.477	1.3	5.5	1.480	1.3	5.6	1.403	1.3	5.8	1.315	1.4	5.9	1.269	1.4	5.9
0.25	0.30	1.359	1.5	5.5	1.379	1.4	5.5	1.318	1.4	5.6	1.277	1.4	5.7	1.210	1.3	5.7
0.30	0.35	1.242	1.8	5.5	1.212	1.4	5.5	1.163	1.5	5.6	1.122	1.5	5.6	1.088	1.4	5.6
0.35	0.40	1.067	1.5	5.6	1.054	1.5	5.6	1.025	1.5	5.6	0.978	1.6	5.5	0.891	1.6	5.5
0.40	0.45	0.866	1.8	5.7	0.870	1.7	5.7	0.837	1.7	5.7	0.796	1.8	5.6	0.760	1.7	5.5
0.45	0.50	0.724	2.0	5.8	0.710	1.9	5.8	0.711	1.9	5.8	0.674	1.9	5.7	0.614	1.9	5.5
0.50	0.55	0.604	2.1	5.9	0.566	2.2	5.9	0.577	2.1	5.8	0.516	2.2	5.7	0.498	2.1	5.6
0.55	0.60	0.465	2.4	5.9	0.482	2.4	5.9	0.468	2.3	5.9	0.432	2.4	5.7	0.4108	2.4	5.6
0.60	0.70	0.3604	2.0	6.0	0.3520	2.0	6.0	0.3301	2.0	5.9	0.3163	2.0	5.8	0.2833	2.0	5.7
0.70	0.80	0.2148	2.7	6.0	0.2164	2.7	6.0	0.1987	2.7	6.0	0.1950	2.6	5.9	0.1771	2.5	5.8
0.80	0.90	0.1385	3.3	6.1	0.1440	3.3	6.1	0.1368	3.2	6.1	0.1202	3.5	6.0	0.1107	3.2	6.0
0.90	1.00	0.0855	4.4	6.3	0.0993	4.1	6.2	0.0782	4.3	6.2	0.0791	4.0	6.1	0.0702	3.9	6.1
1.00	1.25	0.0412	4.1	6.5	0.0416	4.0	6.4	0.0386	4.1	6.3	0.0354	3.8	6.2	0.0322	3.9	6.2
1.25	1.50	0.01302	7.5	6.6	0.01348	6.9	6.5	0.01414	7.0	6.4	0.01201	6.8	6.3	0.01017	7.3	6.3

p_T[GeV/c]		$1.0 < y < 1.2$			$1.2 < y < 1.4$			$1.4 < y < 1.6$			$1.6 < y < 1.8$			$1.8 < y < 2.0$		
min	max	$\frac{d^2n}{dy\,dp_T}$	σ_{stat}	σ_{sys}	$\frac{d^2n}{dy\,dp_T}$	σ_{stat}	σ_{sys}	$\frac{d^2n}{dy\,dp_T}$	σ_{stat}	σ_{sys}	$\frac{d^2n}{dy\,dp_T}$	σ_{stat}	σ_{sys}	$\frac{d^2n}{dy\,dp_T}$	σ_{stat}	σ_{sys}
0.00	0.05	0.2549	3.1	7.2	0.2127	3.5	6.8	0.1906	3.8	6.3	0.1788	3.9	5.6	0.1552	4.0	5.1
0.05	0.10	0.664	1.9	7.0	0.612	2.1	6.7	0.550	2.1	6.2	0.496	2.3	5.5	0.408	2.5	5.1
0.10	0.15	1.005	1.6	6.5	0.934	1.6	6.4	0.853	1.6	6.0	0.738	1.7	5.5	0.620	2.0	5.0
0.15	0.20	1.174	1.4	6.2	1.081	1.5	6.1	0.963	1.5	5.9	0.847	1.6	5.6	0.736	1.7	5.2
0.20	0.25	1.187	1.3	5.9	1.095	1.4	5.9	0.966	1.5	5.8	0.855	1.6	5.6	0.708	1.8	5.4
0.25	0.30	1.095	1.4	5.7	1.013	1.5	5.7	0.917	1.5	5.7	0.776	1.6	5.6	0.650	1.8	5.5
0.30	0.35	0.978	1.5	5.6	0.905	1.5	5.6	0.788	1.6	5.6	0.655	1.8	5.6	0.540	1.9	5.6
0.35	0.40	0.856	1.5	5.5	0.765	1.7	5.4	0.681	1.7	5.5	0.589	1.8	5.5	0.4698	2.0	5.6
0.40	0.45	0.689	1.7	5.4	0.616	1.9	5.4	0.562	1.9	5.4	0.4861	2.0	5.4	0.3745	2.3	5.5
0.45	0.50	0.544	2.0	5.4	0.525	2.0	5.4	0.4596	2.1	5.3	0.3825	2.3	5.3	0.3068	2.5	5.4
0.50	0.55	0.466	2.1	5.5	0.4303	2.1	5.4	0.3655	2.3	5.4	0.3018	2.5	5.4	0.2472	2.8	5.4
0.55	0.60	0.3705	2.3	5.5	0.3385	2.4	5.5	0.2960	2.6	5.5	0.2667	2.6	5.4	0.1960	3.1	5.4
0.60	0.70	0.2661	1.9	5.6	0.2323	2.1	5.6	0.2060	2.1	5.5	0.1795	2.2	5.5	0.1351	2.9	5.5
0.70	0.80	0.1662	2.4	5.7	0.1528	2.5	5.6	0.1314	2.7	5.6	0.1012	3.3	5.5	0.0770	3.4	5.6
0.80	0.90	0.0995	3.0	5.9	0.0879	3.4	5.8	0.0745	3.7	5.7	0.0647	4.5	5.7	0.0387	5.5	5.7
0.90	1.00	0.0593	4.1	6.1	0.0512	4.3	6.0	0.0478	5.2	5.9	0.0291	6.1	6.0	0.0202	7.9	6.1
1.00	1.25	0.0271	3.8	6.3	0.0205	5.8	6.3	0.01355	5.7	6.3	0.00940	7.7	6.4	0.00674	9.0	6.6
1.25	1.50	0.00711	9.3	6.4	0.00467	10.2	6.5	0.00319	11.5	6.5	0.00192	15.8	6.7	0.00141	21.1	6.9

p_T[GeV/c]		$2.0 < y < 2.2$			$2.2 < y < 2.4$			$2.4 < y < 2.6$			$2.6 < y < 2.8$			$2.8 < y < 3.0$		
min	max	$\frac{d^2n}{dy\,dp_T}$	σ_{stat}	σ_{sys}	$\frac{d^2n}{dy\,dp_T}$	σ_{stat}	σ_{sys}	$\frac{d^2n}{dy\,dp_T}$	σ_{stat}	σ_{sys}	$\frac{d^2n}{dy\,dp_T}$	σ_{stat}	σ_{sys}	$\frac{d^2n}{dy\,dp_T}$	σ_{stat}	σ_{sys}
0.00	0.05	0.1331	4.5	5.0	0.1144	5.0	5.5	0.0947	5.8	5.8	0.0855	5.5	5.8	0.0594	7.1	5.4
0.05	0.10	0.3661	2.6	4.9	0.3088	2.9	5.1	0.2739	2.8	5.3	0.2139	3.4	5.3	0.1586	3.9	5.1
0.10	0.15	0.517	2.2	4.7	0.433	2.3	4.6	0.3465	2.5	4.6	0.2690	2.8	4.6	0.2110	3.2	4.6
0.15	0.20	0.592	1.9	4.8	0.4835	2.1	4.5	0.3956	2.3	4.4	0.2831	2.7	4.4	0.2055	3.6	4.6
0.20	0.25	0.581	1.9	5.1	0.4458	2.2	4.8	0.3529	2.4	4.7	0.2512	2.8	4.7	0.1918	3.9	4.9
0.25	0.30	0.500	2.1	5.4	0.3807	2.2	5.3	0.2850	2.6	5.2	0.2112	3.2	5.3	0.1231	5.6	5.4
0.30	0.35	0.4070	2.4	5.6	0.3240	2.4	5.6	0.2260	3.0	5.6	0.1554	3.5	5.6	0.0798	6.5	5.7
0.35	0.40	0.3554	2.3	5.7	0.2533	2.8	5.8	0.1924	4.5	5.8	0.1199	5.4	5.8	0.0521	13.7	5.8
0.40	0.45	0.2847	2.7	5.6	0.2048	3.5	5.8	0.1312	4.3	5.9	0.0775	6.0	5.9			
0.45	0.50	0.2224	3.1	5.5	0.1570	4.1	5.7	0.0971	5.4	5.8	0.0578	8.2	5.9			
0.50	0.55	0.1923	3.5	5.5	0.1181	4.1	5.6	0.0706	6.7	5.8	0.0343	18.7	5.9			
0.55	0.60	0.1496	4.2	5.5	0.0994	4.8	5.6	0.0445	9.7	5.7						
0.60	0.70	0.0883	3.3	5.5	0.0532	5.1	5.6	0.0257	8.2	5.7						
0.70	0.80	0.0498	5.0	5.6	0.0295	8.0	5.7	0.0178	30.3	5.7						
0.80	0.90	0.0246	7.6	5.8	0.0162	14.8	5.9									
0.90	1.00	0.0113	11.8	6.3	0.0047	22.0	6.4									
1.00	1.25	0.00420	11.9	6.8	0.00148	36.9	6.9									
1.25	1.50	0.00086	51.6	7.2												

p_T[GeV/c]		$3.0 < y < 3.2$			$3.2 < y < 3.4$			$3.4 < y < 3.6$		
min	max	$\frac{d^2n}{dy\,dp_T}$	σ_{stat}	σ_{sys}	$\frac{d^2n}{dy\,dp_T}$	σ_{stat}	σ_{sys}	$\frac{d^2n}{dy\,dp_T}$	σ_{stat}	σ_{sys}
0.00	0.05	0.0422	7.7	5.0	0.0393	7.5	5.0	0.0280	17.4	5.0
0.05	0.10	0.1176	4.7	4.9	0.0900	4.9	5.0	0.105	23.4	5.0
0.10	0.15	0.1543	4.0	4.7	0.140	8.6	4.9	0.039	33.2	5.0
0.15	0.20	0.1590	4.2	4.8	0.0723	12.5	4.9			
0.20	0.25	0.0955	5.5	5.1						
0.25	0.30	0.078	26.2	5.5						

C.4 Rapidity spectra

This section presents numerical values of the rapidity spectra dn/dy.

y		p_{beam} = 20 GeV/c			p_{beam} = 31 GeV/c			p_{beam} = 40 GeV/c			p_{beam} = 80 GeV/c			p_{beam} = 158 GeV/c		
min	max	dn/dy	σ_{stat}	σ_{sys}	dn/dy	σ_{stat}	σ_{sys}	dn/dy	σ_{stat}	σ_{sys}	dn/dy	σ_{stat}	σ_{sys}	dn/dy	σ_{stat}	σ_{sys}
0.0	0.2	0.4184	2.0	4.7	0.4865	0.9	4.9	0.5200	0.6	3.3	0.6058	0.6	4.1	0.6781	0.5	5.8
0.2	0.4	0.3968	1.9	4.8	0.4713	0.8	5.1	0.5082	0.6	3.4	0.5939	0.5	4.2	0.6748	0.5	5.8
0.4	0.6	0.3770	1.8	5.0	0.4416	0.8	5.3	0.4859	0.6	3.5	0.5820	0.6	4.3	0.6485	0.4	5.9
0.6	0.8	0.3348	1.8	5.2	0.4113	0.8	5.4	0.4489	0.6	3.5	0.5328	0.6	4.4	0.6141	0.5	5.9
0.8	1.0	0.2817	2.0	5.2	0.3561	0.9	5.5	0.3978	0.7	3.6	0.4951	0.6	4.4	0.5790	0.4	5.9
1.0	1.2	0.2323	2.1	5.4	0.2957	1.0	5.6	0.3354	0.7	3.5	0.4442	0.6	4.4	0.5328	0.5	5.9
1.2	1.4	0.1793	2.5	5.5	0.2356	1.0	5.7	0.2805	0.7	3.5	0.3785	0.6	4.4	0.4857	0.5	5.8
1.4	1.6	0.1262	2.9	6.0	0.1837	1.2	5.8	0.2197	0.8	3.5	0.3225	0.6	4.3	0.4294	0.5	5.7
1.6	1.8	0.0978	3.0	6.1	0.1338	1.2	5.6	0.1617	0.8	3.5	0.2582	0.7	4.1	0.3693	0.5	5.5
1.8	2.0	0.0641	3.5	5.9	0.0977	1.5	5.5	0.1195	1.0	3.6	0.1978	0.8	3.8	0.3001	0.6	5.2
2.0	2.2	0.0446	4.3	5.8	0.0657	1.8	5.2	0.08159	1.2	3.5	0.1457	1.0	3.6	0.2340	0.7	4.8
2.2	2.4	0.0285	5.0	6.1	0.04339	2.1	5.2	0.05566	1.5	3.4	0.1043	1.2	3.5	0.1771	0.8	4.3
2.4	2.6	0.0160	7.0	6.5	0.02556	3.6	4.8	0.03409	2.0	3.5	0.0716	1.5	3.5	0.1327	1.1	4.0
2.6	2.8				0.01430	4.4	5.0	0.02103	2.5	4.1	0.0458	2.2	3.7	0.0921	1.3	4.6
2.8	3.0							0.01198	4.7	5.1				0.0582	1.8	5.9

C.5 Inverse slope parameter

This section presents numerical values of inverse slope parameter T [MeV/c^2] of the transverse mass spectra in rapidity bins (see Eq. (7.1)).

y		p_{beam} = 20 GeV/c			p_{beam} = 31 GeV/c			p_{beam} = 40 GeV/c			p_{beam} = 80 GeV/c			p_{beam} = 158 GeV/c		
min	max	T	σ_{stat}	σ_{sys}	T	σ_{stat}	σ_{sys}	T	σ_{stat}	σ_{sys}	T	σ_{stat}	σ_{sys}	T	σ_{stat}	σ_{sys}
0.0	0.2	149.1	3.3	3.2	153.3	1.4	0.8	157.7	1.1	1.3	159.9	1.0	2.5	159.3	0.8	1.7
0.2	0.4	159.1	3.1	3.0	156.1	1.4	1.1	159.2	1.1	1.0	159.2	1.0	1.9	160.7	0.8	1.3
0.4	0.6	158.4	3.0	2.2	156.2	1.4	1.9	155.0	1.0	1.0	158.1	1.0	1.7	158.3	0.8	1.4
0.6	0.8	149.8	3.0	2.5	152.2	1.3	1.9	152.7	1.1	1.2	159.0	1.0	1.8	157.2	0.8	1.5
0.8	1.0	148.5	3.3	2.1	152.5	1.5	2.0	150.1	1.1	2.7	152.8	1.0	2.1	153.7	0.7	1.8
1.0	1.2	140.1	3.7	2.9	143.5	1.6	1.8	146.6	1.2	2.7	151.6	1.0	2.0	156.3	0.7	1.3
1.2	1.4	135.6	4.2	4.4	136.4	1.6	3.6	142.8	1.2	2.7	149.8	1.0	1.1	153.8	0.8	0.9
1.4	1.6	106.8	4.7	5.8	126.3	1.8	5.0	133.3	1.2	1.2	146.7	1.0	2.2	153.0	0.8	1.0
1.6	1.8				118.7	2.0	8.7	119.8	1.4	1.0	141.1	1.1	2.7	152.6	0.9	1.5
1.8	2.0				93.1	2.3	10.0	104.5	1.8	0.9	128.8	1.2	3.7	145.0	1.0	3.0
2.0	2.2										115.4	1.6	3.0	137.6	1.1	3.5
2.2	2.4													125.9	1.4	4.2

C.6 Mean transverse mass

This section presents numerical values of the mean transverse mass $v = (\langle m_{\mathrm{T}} \rangle - m_{\pi})$ [GeV/c^2].

y		p_{beam} = 20 GeV/c			p_{beam} = 31 GeV/c			p_{beam} = 40 GeV/c			p_{beam} = 80 GeV/c			p_{beam} = 158 GeV/c		
min	max	v	σ_{stat}	σ_{sys}	v	σ_{stat}	σ_{sys}	v	σ_{stat}	σ_{sys}	v	σ_{stat}	σ_{sys}	v	σ_{stat}	σ_{sys}
0.0	0.2	0.2378	2.7	1.0	0.2461	1.1	0.4	0.2473	0.8	0.4	0.2535	0.7	0.4	0.2536	0.6	0.6
0.2	0.4	0.2487	2.4	0.9	0.2475	1.0	0.5	0.2495	0.8	0.4	0.2532	0.7	0.5	0.2564	0.6	0.6
0.4	0.6	0.2368	2.4	1.1	0.2405	1.1	0.6	0.2456	0.8	0.4	0.2484	0.8	0.5	0.2537	0.6	0.6
0.6	0.8	0.2387	2.3	1.3	0.2412	1.1	0.8	0.2410	0.8	0.4	0.2466	0.8	0.5	0.2533	0.6	0.6
0.8	1.0	0.2258	2.6	1.4	0.2342	1.2	1.2	0.2382	0.9	0.5	0.2407	0.7	0.4	0.2490	0.6	0.7
1.0	1.2	0.2108	2.9	1.8	0.2253	1.3	1.3	0.2267	1.0	0.6	0.2397	0.8	0.4	0.2463	0.6	0.7
1.2	1.4	0.1931	3.3	2.1	0.2063	1.3	1.5	0.2176	0.9	0.7	0.2312	0.8	0.4	0.2410	0.6	0.8
1.4	1.6	0.1673	3.6	3.8	0.1908	1.5	1.5	0.2004	1.0	0.7	0.2237	0.8	0.5	0.2358	0.6	0.7
1.6	1.8	0.1507	3.8	4.6	0.1715	1.6	1.5	0.1807	1.1	0.9	0.2122	1.0	0.7	0.2300	0.7	0.6
1.8	2.0	0.1249	4.7	4.4	0.1449	1.9	1.9	0.1583	1.3	1.2	0.1967	1.0	0.9	0.2209	0.8	0.5
2.0	2.2	0.1121	5.8	3.9	0.1262	2.3	2.5	0.1411	1.6	1.8	0.1764	1.3	0.9	0.2072	1.0	0.7
2.2	2.4	0.0942	6.8	5.7	0.1061	3.0	2.9	0.1196	2.0	2.7	0.1567	1.7	1.8	0.1893	1.2	1.1
2.4	2.6	0.0824	8.9	7.3	0.0923	4.0	3.2	0.1047	2.7	3.8	0.1359	2.2	2.2	0.1683	1.7	2.3
2.6	2.8				0.0752	5.8	4.0	0.0858	3.6	3.8	0.1176	3.8	3.7	0.1469	2.0	6.0
2.8	3.0							0.0791	7.9	4.8				0.1191	3.0	9.0

Bibliography

[1] M. Gaździcki. *On the history of multi-particle production in high energy collisions* 2012 [arXiv:hep-ph/1201.0485v1].

[2] E. Fermi. *High Energy Nuclear Events*. Prog. Theor. Phys. **5**(4):570 1950.

[3] R. Hagedorn. *Statistical thermodynamics of strong interactions at high-energies*. Nuovo Cim. Suppl. **3**:147 1965.

[4] K. Grebieszkow for the NA49 and the NA61 Collaborations. *NA49 and NA61/SHINE experiments: Results and perspectives*. Acta Phys. Polon. **B41**:427–440 2010.

[5] M. Gaździcki and M. Gorenstein. *On the early stage of nucleus-nucleus collisions*. Acta Phys. Polon. **B30**:2705 1999.

[6] R.V. Poberezhnyuk, M. Gaździcki, and M.I. Gorenstein. *Statistical Model of the Early Stage of nucleus-nucleus collisions with exact strangeness conservation* 2015 [arXiv:nucl-th/1502.05650v2].

[7] J. Beringer *et al.* (Particle Data Group). *Review of Particle Physics*. Phys. Rev. **D86**:010001 2012 and 2013 partial update for the 2014 edition.

[8] S.V. Afanasiev *et al.* (The NA49 Collaboration). *Energy dependence of pion and kaon production in central Pb+Pb collisions*. Phys. Rev. **C66**:054902 2002.

[9] C. Alt *et al.* (The NA49 Collaboration). *Pion and kaon production in central Pb+Pb collisions at 20A and 30A GeV: Evidence for the onset of deconfinement*. Phys. Rev. **C77**:024903 2008.

[10] F. Becattini, J. Cleymans, A. Keränen, E. Suhonen, and K. Redlich. *Features of particle multiplicities and strangeness production in central heavy ion collisions between 1.7A and 158A GeV/c*. Phys. Rev. **C64**(2):024901 2001.

[11] F. Becattini, J. Manninen, and M. Gaździcki. *Energy and system size dependence of chemical freeze-out in relativistic nuclear collisions*. Phys. Rev. **C73**:044905 2006.

[12] M. Gaździcki, M. Gorenstein, and P. Seyboth. *Onset of deconfinement in nucleus-nucleus collisions: Review for pedestrians and experts*. Acta Phys. Polon. **B42**:307–351 2011.

[13] K. Grebieszkow. *Lecture on Introduction to Heavy Ion Collisions* 2010–2011. `http://if.pw.edu.pl/kperl/HIP/hip.html`.

[14] Y. Itow *et al.* (T2K Collaboration). *The JHF-Kamioka neutrino project* 2001 arXiv:0106019 [hep-ex].

[15] K. Abe *et al.* (T2K Collaboration). *The T2K experiment*. Nucl. Instrum. Meth. **A659**(1):106–135 2011.

[16] N. Abgrall *et al.* (NA61/SHINE Collaboration). *NA61/SHINE plans beyond the approved program*. Technical Report CERN-SPSC-2012-022. SPSC-P-330-ADD-6 CERN Geneva 2012.

[17] K. Abe *et al.* (T2K Collaboration). *The T2K neutrino flux prediction*. Phys. Rev. **D87**:012001 2013.

[18] J. Abraham *et al.* (Pierre Auger Collaboration). *Properties and performance of the prototype instrument for the Pierre Auger Observatory*. Nucl. Instrum. Meth. **A523**(1–2):50–95 2004.

[19] T. Antoni *et al.* (KASCADE Collaboration). *The cosmic-ray experiment KASCADE*. Nucl. Instrum. Meth. **A513**(3):490–510 2003.

[20] *NA61/SHINE image library*.

[21] E. Kaptur for the NA61/SHINE Collaboration. *Is Beryllium heavy? The first results on Be+Be collisions*. X Polish Workshop on Relativistic Heavy-Ion Collisions, Kielce, Poland 2013. `http://www.ujk.edu.pl/homepages/mryb/10thworkshop/files/slides/kaptur.pdf`.

[22] A. Rustamov. *The Horn, Kink and Step, Dale: from few GeV to few TeV*. Central Eur. J. Phys. **10**:1267–1270 2012.

[23] L. Kumar for the STAR collaboration. *Systematics of kinetic freeze-out properties in high energy collisions from STAR*. Nuclear Physics **A931**:1114–1119 2014.

[24] S. Das for the STAR collaboration. *Identified particle production and freeze-out properties in heavy-ion collisions at RHIC Beam Energy Scan program* 2014 [arXiv:nucl-ex/1412.0499].

[25] C. Alt *et al.* (The NA49 Collaboration). *Inclusive production of charged pions in p+p collisions at 158 GeV/c beam momentum*. Eur. Phys. J. **C45**:343 2006.

[26] T. Anticic *et al.* (The NA49 Collaboration). *Inclusive production of protons, anti-protons and neutrons in p+p collisions at 158 GeV/c beam momentum*. Eur. Phys. J. **C65**(1–2):9 2010.

[27] T. Anticic *et al.* (The NA49 Collaboration). *Inclusive production of charged kaons in p+p collisions at 158 GeV/c beam momentum and a new evaluation of the energy dependence of kaon production up to collider energies*. Eur. Phys. J. **C68**(1–2):1 2010.

[28] A.I. Golokhvastov. *Koba–Nielsen–Olesen scaling in isospin-coupled reactions*. Phys. Atomic Nuclei **64**(10):1841 2001.

[29] N. Abgrall *et al.* (The NA61/SHINE Collaboration). *Measurement of negatively charged pion spectra in inelastic p+p interactions at* p_{lab} *= 20, 31, 40, 80 and 158 GeV/c*. Eur. Phys. J. **C74**(3):2794 2014.
Numerical results: https://edms.cern.ch/document/1314605, http://hepdata.cedar.ac.uk/view/ins1257740.

[30] M. Gaździcki and G. Vesztergombi. *A new experimental programme with nuclei and proton beams at the CERN SPS* 2003. CERN-SPSC-2003-038, SPSC-EOI-001.

[31] N. Antoniou *et al.* *Study of hadron production in collisions of protons and nuclei at the CERN SPS, NA49-future letter of intent* 2006. CERN-SPSC-2006-001, SPSC-P-329.

[32] N. Abgrall *et al.* (The NA61/SHINE Collaboration). *NA61/SHINE facility at the CERN SPS: beams and detector system*. J. Instrum. **9**(06):P06005 2014.

[33] S. Afanasiev *et al.* (The NA49 Collaboration). *The NA49 large acceptance hadron detector*. Nucl. Instr. Meth. Phys. Res. **A430**:210 1999.

[34] C. Bovet, S. Milner, and A. Placci. *The CEDAR (Cherenkov Differential Counters with Achromatic Ring Focus) Project*. IEEE Trans. Nucl. Sci. **25**:572 1978.

[35] N. Abgrall *et al.* (NA61/SHINE Collaboration). *Further information requested in the proposal review process*. Technical Report CERN-SPSC-2007-019 CERN Geneva 2007.

[36] A. Ivashkin *et al.* *Hadron calorimeter with MAPD readout in the NA61/SHINE experiment* 2012 [arXiv:physics.ins-det/1205.4864v2].

[37] F. Sauli. *Gaseous radiation detectors: Fundamentals and applications*. Cambridge University Press 2014.

[38] J.G. Layter. *Results from PEP-4 TPC*. In Harvey B. Newman, editor, *Electroweak Effects at High Energies* pages 201–213. Springer US 1985.

[39] A. Barbaro-Galtieri. *Tracking with the PEP-4 TPC*. Proceedings from International Conference on Instrumentation for Colliding Beam Physics **SLAC-250** 1982.

[40] D. Decamp *et al.* (ALEPH Collaboration). *ALEPH: A detector for electron-positron annihilations at LEP*. Nucl. Instrum. Meth. **A294**(1–2):121–178 1990.

[41] P. Aarnio *et al.* (DELPHI Collaboration). *The DELPHI detector at LEP*. Nucl. Instrum. Meth. **A303**(2):233–276 1991.

[42] M. Anderson *et al.* *The STAR Time Projection Chamber: a unique tool for studying high multiplicity events at RHIC*. Nucl. Instrum. Meth. **A499**(2–3):659–678 2003.

[43] J. Alme *et al.* *The ALICE TPC, a large 3-dimensional tracking device with fast readout for ultra-high multiplicity events*. Nucl. Instrum. Meth. **A622**(1):316–367 2010.

[44] S. Amerio *et al.* *Design, construction and tests of the ICARUS T600 detector.* Nucl. Instr. Meth. Phys. Res. **A527**(3):329 2004.

[45] E. Aprileaet *al.* (XENON100 Collaboration). *The XENON100 Dark Matter Experiment* 2011 [arXiv:astro-ph.IM/1107.2155].

[46] K. Nakamura *et al.* (Particle Data Group). *Review of Particle Physics.* J. Phys. **G37**:075021 2010.

[47] F. Sauli. *Principles of operation of multiwire proportional and drift chambers.* CERN **77-09**:41 1977.

[48] S. Puławski. *private communication.*

[49] P. Seyboth. *Numbering conventions for NA49 TPC's* 1994. NA49 internal note.

[50] A. Peisert and F. Sauli. *Drift and diffusion of electrons in gases: a compilation.* CERN **84-08**:29 1984.

[51] T. Alber, V. Eckardt, H. Fessler, S. Schönfelder, and P. Seyboth. *A study of argon, neon and helium based gas mixtures for improving the spatial resolution in time projection chambers.* Nucl. Instr. Meth. Phys. Res. **A349**(1):56–61 1994.

[52] J. Bartke *et al.* *RD-32 Final Report.* CERN LHCC **96–16**.

[53] A. Aduszkiewicz. *Operation and performance of Time Projection Chambers of SHINE/NA61 experiment at CERN.* Master's thesis University of Warsaw, Poland 2008. `https://edms.cern.ch/document/936393`.

[54] N. Abgrall *et al.* (The NA61/SHINE Collaboration). *Measurements of cross sections and charged pion spectra in proton-carbon interactions at 31 GeV/c.* Phys. Rev. **C84**:034604 2011.

[55] M. Unger for the NA61/SHINE Collaboration. *Results from NA61/SHINE.* EPJ Web Conf. **52**:01009 2013.

[56] M. Unger for the NA61/SHINE Collaboration. *Hadron production at fixed target energies and extensive air showers.* PoS **ICHEP2010**:449 2010.

[57] A. Ilnicka. *Comparison of hadron production in Monte-Carlo models and experimental data in p+p interactions at the SPS energies.* Master's thesis University of Warsaw, Poland 2013. `https://edms.cern.ch/document/1319366`.

[58] K. Werner. *The hadronic interaction model EPOS.* Nucl. Phys. B (Proc. Suppl.) **175–176**:81 2008.

[59] K. Werner. *Strings, pomerons and the VENUS model of hadronic interactions at ultrarelativistic energies.* Phys. Rep. **232**(2–5):87 1993.

[60] R. Brun and F. Carminati and S. Giani. *GEANT Detector Description and Simulation Tool.* CERN **W5013** 1994.

[61] A. Aduszkiewicz for the NA61/SHINE Collaboration. *New results of NA61/SHINE at the CERN SPS*. 2nd European Nuclear Physics Conference, Bucharest 2012. Numerical results:
https://twiki.cern.ch/twiki/bin/viewauth/NA61/Hminus_pp20_158.

[62] S. Puławski. *PID in relativistic rise for p+p at SPS energies*. NA61/49 Collaboration meeting, CERN 2012. Numerical results:
https://twiki.cern.ch/twiki/bin/viewauth/NA61/Dedx_pp158_80_40.

[63] M. Gaździcki. *A compilation of pion multiplicities in p+p interactions and central Au+Au collisions at RHIC*. Frankfurt 2005.

[64] M. Gaździcki and D. Röhrich. *Strangeness in nuclear collisions*. Z. Phys. **C71**:55 1996.

[65] R. Zybert and P. Buncic. *DSPACK: Object manager for high energy physics*. Proc. **CHEP95**:345 1995.

[66] *ROOT61*. https://na61bq.web.cern.ch/na61bq/pages/root61/.

[67] *ROOT*. http://root.cern.ch/.

[68] M. Haug. *Messung des Wirkungsquerschnitts von Pion-Kohlenstoff-Wechselwirkungen mit Hilfe des NA61 Detektors*. Master's thesis Karlsruhe Institute of Technology, Germany 2012.

[69] R. Trzeciak. *Determination of momentum resolution in the NA61 time projection chambers for p+p interactions at 158A GeV*. Master's thesis Warsaw University of Technology, Faculty of Physics, Poland 2011.

[70] M. Ruprecht. *Measurement of the spectrum of charged hadrons in π^-+C interactions with the NA61 experiment*. Master's thesis Karlsruhe Institute of Technology, Germany 2012.

[71] E.E. Zabrodin *et al. Inclusive spectra of charged particles in pp and $\overline{p}p$ interactions at 32 GeV/c*. Phys. Rev. **D52**:1316 1995.

[72] V. Blobel *et al. Multiplicities, topological cross sections, and single particle inclusive distributions from pp interactions at 12 and 24 GeV/c*. Nucl. Phys. **B69**:454 1974.

[73] H. Bøggild *et al. The inclusive single-particle spectra of π^-, K^0 and Λ in proton-proton collisions at 19 GeV/c*. Nucl. Phys. **B57**:77 1973.

[74] J. Benecke, T. T. Chou, C. N. Yang, and E. Yen. *Hypothesis of limiting fragmentation in high-energy collisions*. Phys. Rev. **188**:2159–2169 1969.

[75] V.V. Ammosov *et al. A study of π^+, π^- and proton production in pp interactions at 69 GeV/c*. Nuovo Cim. **A40**:237 1977.

[76] J.L. Klay *et al. Charged pion production in 2A to 8A GeV central Au+Au Collisions*. Phys. Rev. **C68**:054905 2003.

[77] L. Ahle *et al.* (E-802 Collaboration). *Particle production at high baryon density in central Au+Au reactions at 11.6A GeV/c.* Phys. Rev. **C57**:R466 1998.

[78] B.B. Back *et al.* (PHOBOS Collaboration). *Comparison of the total charged-particle multiplicity in high-energy heavy ion collisions with e^+e^- and $pp/\overline{p}p$ data* 2003 arXiv:0301017 [nucl-ex].

[79] K. Adcox *et al.* (PHENIX Collaboration). *Single identified hadron spectra from* $\sqrt{s_{NN}}$ = 200 *GeV Au+Au collisions.* Phys. Rev. **C69**:024904 2004.

[80] S.S. Adler *et al.* (PHENIX Collaboration). *Identified charged particle spectra and yields in Au+Au collisions at* $\sqrt{s_{NN}}$ = 200 *GeV.* Phys. Rev. **C69**:034909 2004.

[81] J. Adams *et al.* (STAR Collaboration). *Identified particle distributions in pp and Au+Au collisions at* $\sqrt{s_{NN}}$ = 200 *GeV.* Phys. Rev. Lett. **92**:112301 2004.

[82] I.G. Bearden *et al.* (BRAHMS Collaboration). *Charged meson rapidity distributions in central Au+Au collisions at* $\sqrt{s_{NN}}$ = 200 *GeV.* Phys. Rev. Lett. **94**:162301 2005.

[83] S. Puławski. *Identification and analysis of charged hadrons in p+p interactions from NA61/SHINE experiment at CERN SPS energies.* PhD thesis University of Silesia, Poland 2015.